

Øystein Fure

Characterisation of pyrrhotite-bearing concrete aggregates

Using conventional techniques in combination with SEM-based Automated Mineralogy

Master's thesis in Geology

Supervisor: Kurt Aasly

Co-supervisor: Nikolas Oberhardt

May 2021

Øystein Fure

Characterisation of pyrrhotite-bearing concrete aggregates

Using conventional techniques in combination with
SEM-based Automated Mineralogy

Master's thesis in Geology
Supervisor: Kurt Aasly
Co-supervisor: Nikolas Oberhardt
May 2021

Norwegian University of Science and Technology
Faculty of Engineering
Department of Geoscience and Petroleum



Kunnskap for en bedre verden

Abstract

Pyrrhotite-bearing concrete aggregates have in recent years been associated with deleterious effects on hardened concrete due to oxidation reactions and the formation of expanding secondary minerals. In Trois-Rivières, Canada, more than 1000 concrete structures have been exposed to serious deterioration reactions related to sulfide-bearing aggregates, while indications of pyrrhotite in excavated rocks from the 20 km Follo Line railroad Tunnel (Norway) lead to the rejection of this material for use in concrete linings. Detection of pyrrhotite in concrete aggregates is challenging and associated with uncertainty due to the low concentrations (<1 wt%) and difficulties with exact discrimination between the sulfides. The concrete aggregate standard NS-EN12620 states that the total sulfur limit is lowered from 1 wt% to 0,1 wt% if pyrrhotite is indicated in the aggregate sample through Differential Thermal Analysis (DTA).

In this study, concrete aggregates from the Follo Line Tunnel and Trois-Rivières are characterised by relevant techniques comprising LECO analysis for total sulfur, XRF, XRD, DTA, Optical Microscopy, EPMA, and SEM-based Automated Mineralogy (AM). These were evaluated on their suitability of total sulfur determination and pyrrhotite detection. Average sulfide contents in the Follo Line aggregates are 0,172 wt% pyrite, 0,009 wt% chalcopyrite and 0,006 wt% pyrrhotite, according to AM analysis. DTA indicates pyrite and pyrrhotite in all samples but provide no clue of the large difference in pyrite and pyrrhotite contents. Sulfides in the Trois-Rivières aggregates comprise on average 0,604 wt% pyrrhotite, 0,596 wt% pyrite, 0,136 wt% pentlandite, and 0,061 wt% chalcopyrite. Pyrrhotite is extensively weathered, especially in liberated grains in the finest fraction (0,045/1mm). More significant evidence of pyrrhotite oxidation (iron sulfate and -oxides) in smaller fractions compared to bigger fractions suggest that pyrrhotite-bearing aggregates in fractions <1 mm are the most harmful concerning concrete deterioration. The best mineral recipe for iron sulfide discrimination with AM involved classification of pyrrhotite and pyrite based on iron content above or below 58 wt%, respectively. This study shows that AM analysis on particulate sections probably is the most precise approach for pyrrhotite detection and quantification. The test regime relying solely on detection by DTA is especially vulnerable in cases where pyrite is the dominant sulfide and pyrrhotite barely occurs due to overlapping DTA characteristics. Implementation of AM analysis in the concrete standard will provide better ground for whether sulfide-bearing aggregates should be prohibited for use in concrete or not. Considering the scarcity of aggregate sources and the benefits of local use of rocks in infrastructure projects, rejection of aggregates due to inaccurate test methods is unfortunate. Conversely, correct detection is crucial to avoid serious deterioration in concrete structures.

Sammendrag

Magnetkis (Fe_{1-x}S) i betongtilslag har fått økt oppmerksomhet de siste årene grunnet potensielt skadelige effekter på betongs bestandighet. Deler av overskuddsmassene fra tunnelbyggingen ved Follobanen var tiltenkt å gjenbrukes i betongsegmenter, men ble avvist til dette formålet som følge av indikasjoner på magnetkis og overskridende svovelverdier. I Trois-Rivières, Canada, har mer enn 1000 betongfundamenter blitt utsatt for omfattende skader som følge av høyt sulfidinnhold, spesielt i form av magnetkis. Ifølge Norsk standard for betongtilslag NS-EN12620, senkes den opprinnelige grenseverdien for svovel fra 1 wt% til 0,1 wt% dersom det foreligger indikasjoner på magnetkis i tilslaget. Påvisning av magnetkis i betongtilslag er ofte forbundet med stor usikkerhet på grunn av de små mengdene som kan være tilstede og vanskeligheter med å skille mineralet fra svovelkis (pyritt).

Denne oppgaven presenterer karakterisering av betongtilslag fra Follobanetunnelen og en tilslagsprodusent i Trois-Rivières, utført ved hjelp av LECO-analyse for totalt svovelinnhold, XRF, XRD, DTA, optisk mikroskopi, EPMA og SEM-basert Automatisk Mineralogisk (AM) analyse. De ulike metodenes egnethet og evne til å bestemme svovelinnhold og detektere magnetkis er videre evaluert og sammenlignet. Ifølge AM-analyse inneholder tilslaget fra Follobanen gjennomsnittlig 0,172 wt% svovelkis, 0,009 wt% kobberkis og 0,006 wt% magnetkis. DTA indikerer svovelkis og magnetkis i alle prøvene fra Follobanen, men gir ingen informasjon om mengdeforholdet. Sulfidinnholdet i tilslaget fra Trois-Rivières består gjennomsnittlig av 0,604 wt% magnetkis, 0,596 wt% svovelkis, 0,136 wt% pentlanditt og 0,061 wt% kobberkis. Magnetkisen i dette tilslaget er betydelig forvitret, mens svovelkisen fremstår uforvitret. Ettersom de finere fraksjoner (0,045/1mm) inneholder mer frimalt og oksidert magnetkis enn de grovere fraksjonene (>1mm), tyder det på at magnetkis-holdig betongtilslag i fraksjoner <1mm er mest skadelig ved bruk i betong. Mineraloppskriften som gir mest optimal kvantifisering av magnetkis og svovelkis med AM-analyse er basert på jerninnhold henholdsvis over eller under 58 wt%. Oppgaven viser at AM-analyse på prøver av knust tilslag antakelig er den beste måten for påvisning og kvantifisering av magnetkis i små mengder. En svakhet med dagens testregime er at påvisning av magnetkis kun skal foregå med DTA, uten noen form for verifikasjon. Dette er uheldig ettersom DTA ofte ikke gir entydige svar på om tilslag med lavt totalt sulfidinnhold består av svovelkis, magnetkis eller begge mineraler. Implementering av AM-analyse i NS-EN12620 vil gi et bedre beslutningsgrunnlag for hvorvidt tilslag med lavt sulfidinnhold og usikre påvisninger fra DTA, skal tillates for bruk i betong. Det er svært ugunstig dersom gode tilslagsforekomster blir avvist for bruk i betong som følge av unøyaktige testmetoder. Samtidig er korrekt påvisning av magnetkis helt avgjørende for å unngå store skader i betongfundamenter.

Preface

The work with this thesis was conducted during the last year of the master's degree in Geology at the Institute of Geoscience and Petroleum, NTNU Trondheim.

First, I want to thank Associate Professor Kurt Aasly for introducing me to the topic and many exciting discussions on Automated Mineralogy and mineral characterisation. My gratitude also goes to all technical staff working with the analytical apparatuses at the institute, always eager to help me out with my analyses. My deepest gratitude goes to PhD candidate Nikolas Oberhardt for teaching me how to work and write scientifically and for the excellent proofreading of my thesis. I wish him all the best with his ongoing work and look forward to seeing how his project develops in the coming years.

Finally, I want to thank all my classmates for five brilliant years studying geology in Trondheim, and fantastic excursions all around the world. It's been a pleasure looking at rocks with you.

Contents

Abstract	i
Sammendrag	iii
Preface	v
1 Introduction	1
1.1 Motivation	1
1.2 Objectives and structure of thesis	3
2 Background	5
2.1 Geological settings of the sample origin	5
2.1.1 Follo Line Tunnel	5
2.1.2 Trois-Rivières, Canada	6
2.2 Iron sulfides	7
2.3 Pyrrhotite mineralogy	9
2.3.1 2C - Troilite	11
2.3.2 4C - Monoclinic pyrrhotite	11
2.3.3 NC - Intermediate pyrrhotites	13
2.4 Formation and appearance of pyrrhotite	14
2.5 Previous studies on the characterisation of pyrrhotite	16
2.6 Differential Thermal Analysis (DTA)	19
2.6.1 DTA apparatus at the Dept. of Geoscience and Petroleum (IGP)	21
2.7 Automated Mineralogy (AM)	24
2.7.1 Measurement modes	26
2.7.2 General background for sampling and prep. for AM	27
2.7.3 Resolution and detection capability	29
3 Materials and methods	30
3.1 Materials	30
3.1.1 Follo Line samples	30
3.1.2 Trois-Rivières samples	31
3.1.3 Sample splitting and selection	32
3.1.4 Preparation for XRD, XRF, DTA and LECO	32

3.2	Analytical tools for characterisation of pyrrhotite and sulfur	34
3.2.1	LECO for total sulfur content	34
3.2.2	X-Ray Fluorescence (XRF)	34
3.2.3	X-Ray Diffraction (XRD)	35
3.2.4	Differential Thermal Analysis (DTA)	36
3.2.5	Optical microscope	36
3.2.6	Electron Probe Micro Analysis (EPMA)	37
3.2.7	Automated Mineralogy (AM) on Mineralogic Mining	38
4	Results	44
4.1	Characterisation of Follo Line aggregates	45
4.1.1	LECO for total sulfur content	45
4.1.2	X-Ray Fluorescence (XRF)	45
4.1.3	X-Ray Diffraction (XRD)	46
4.1.4	Differential Thermal Analysis (DTA)	47
4.1.5	Optical microscopy investigations	49
4.1.6	Electron Probe Micro Analysis (EPMA)	52
4.1.7	Automated Mineralogy (AM)	52
4.1.8	Petrological classification	58
4.2	Characterisation of Trois-Rivières aggregates	59
4.2.1	LECO for total sulfur content	59
4.2.2	X-Ray Fluorescence (XRF)	59
4.2.3	X-Ray Diffraction (XRD)	60
4.2.4	Differential Thermal Analysis (DTA)	61
4.2.5	Optical microscopy investigations	63
4.2.6	Electron Probe Micro Analysis (EPMA)	67
4.2.7	Automated Mineralogy (AM)	68
4.2.8	Petrological classification	74
4.3	Discrimination of pyrrhotite and pyrite with Automated Mineralogy mapping	75
4.3.1	Element maps on a pyrite cluster with Electron Probe Micro Analysis (EPMA)	80
5	Discussion	85
5.1	Follo Line material	85
5.1.1	Sulfide mineralogy and pyrrhotite appearance	85
5.1.2	Bulk mineralogy estimations	90
5.2	Trois-Rivières material	94
5.2.1	Sulfide mineralogy and pyrrhotite appearance	94

5.2.2	Pyrrhotite oxidation and weathering products	96
5.2.3	Bulk mineralogy and rock classification	98
5.3	Pyrrhotite petrogenesis and mineralogy	100
5.4	Evaluation of techniques for analysing pyrrhotite and sulfur in aggregates for concrete	103
5.4.1	Total sulfur content by LECO and XRF	103
5.4.2	X-Ray Diffraction (XRD)	105
5.4.3	Optical Microscopy (OM)	105
5.4.4	Differential Thermal Analysis (DTA)	106
5.4.5	Automated Mineralogy (AM)	108
6	Conclusions	114
6.1	Recommendations for further research	116
	Bibliography	126
	Appendices	127
A	Sample preparation	129
B	Summary of optical microscope observations	131
C	Accessory mineralogy for Follo Line samples by 20 μ m AM mapping	134
D	Accessory mineralogy for Trois-Rivières samples by 20 μ m AM mapping .	135
E	False color mineral maps from 20 μ m AM mapping on Follo Line sections .	136
F	False color mineral maps from 20 μ m AM mapping on Trois-Rivières sections	150
G	Diffraction patterns from XRD analyses	155

List of Figures

2.1	The NiAs unit cell viewed from two directions.	9
2.2	Illustration of the pyrrhotite superstructure nomenclature.	10
2.3	Illustration of proposed vacancy structures in 4C and 5C pyrrhotites.	12
2.4	Fe-S phase diagram	15
2.5	DTA curves of pyrite in different grain size and amounts.	20
2.6	Illustration of the DTA apparatus at IGP.	21
2.7	Interpretation of DTA results.	23
2.8	Flowsheet of sample preparation procedures for AM analysis.	28
3.1	Sample splitting and Fly Press crushing.	33
4.1	XRD results on Follo Line samples.	46
4.2	DTA diagrams from analyses on the Follo Line samples.	48
4.3	Sulfide phases in Follo Line stub samples observed under reflected light.	50
4.4	Sulfide phases in Follo Line thin sections observed under reflected light.	51
4.5	Bulk mineralogy for all Follo Line samples by 20 μm AM mapping.	53
4.6	False color map by AM of iron sulfides from the Follo Line samples I	55
4.7	False color map by AM of iron sulfides from the Follo Line samples II	56
4.8	Pyrrhotite mineral associations in Follo Line samples by AM Mapping.	57
4.9	Streckeisen classification for the Follo Line aggregates.	58
4.10	XRD results on Trois-Rivières samples.	60
4.11	DTA diagrams from analyses on the Trois-Rivières samples.	62
4.12	Sulfide phases in Trois-Rivières stub samples observed under reflected light.	64
4.13	Sulfide phases in Trois-Rivières thin sections observed under reflected light.	66
4.14	Bulk mineralogy for all Trois-Rivières samples by 20 μm AM mapping.	68
4.15	Weathered pyrrhotite in TR0,045/1mm	71
4.16	Weathered pyrrhotite in TR1/8mm	72
4.17	Pyrrhotite mineral associations in Trois-Rivières samples by AM mapping	73
4.18	Streckeisen classification for the Trois-Rivières aggregates.	74
4.19	Strategies for discrimination between pyrite and pyrrhotite with AM.	75

4.20	Discrimination of pyrrhotite and pyrite with AM I	76
4.21	Discrimination of pyrrhotite and pyrite with AM II	77
4.22	Discrimination of pyrrhotite and pyrite with AM III	78
4.23	Discrimination of pyrrhotite and pyrite with AM IV	79
4.24	Discrimination of pyrrhotite and pyrite with EPMA I	80
4.25	Discrimination of pyrrhotite and pyrite with EPMA II	82
4.26	Discrimination of pyrrhotite and pyrite with EPMA III	83
4.27	Discrimination of pyrrhotite and pyrite with EPMA IV	84
5.1	Pyrrhotite content in the Follo Line stub- and thin sections by AM mapping	87
5.2	Iron sulfide content in the Follo Line stub- and thin sections by AM mapping	88
5.3	Correlation of biotite classification by AM and OM scan I.	92
5.4	Correlation of biotite classification by AM and OM scan II.	93
5.5	Sulfide content in Trois-Rivières stub- and thin sections by AM mapping. .	94
5.6	False color mineral maps from AM mapping on Trois-Rivières stub samples.	99
5.7	Pyrrhotite chemistry in the Follo Line- and Trois-Rivières material by EPMA.	102
5.8	Total wt% sulfur by LECO and XRF on Follo Line samples in 2019 and 2021.	104
5.9	Wt.% pyrrhotite in Follo Line- and Trois-Rivières aggregates by AM mapping.	111

List of Tables

2.1	Mineral compositions and metamorphic grade of Follo Line gneisses. . . .	6
2.2	Generalised composition for naturally occurring pyrrhotite superstructures. .	11
2.3	Summary of opaque mineral quantification by Rodrigues (2016) on the Trois- Rivières aggregates.	18
2.4	Characteristic temperature ranges for iron sulfides on the DTA apparatus at IGP.	22
3.1	Sample material overview	31
3.2	Mineral classification recipe for Follo Line material.	40
3.3	Mineral classification recipe for Trois-Rivières material I	41
3.4	Mineral classification recipe for Trois-Rivières material II	42
4.1	LECO results on Follo Line samples.	45

4.2	Selected XRF results on the Follo Line material.	45
4.3	DTA results from Follo Line samples.	47
4.4	Sulfides in Follo Line stub samples detected with reflected light microscopy	49
4.5	Sulfides in Follo Line thin sections detected with reflected light microscopy	50
4.6	EPMA results for Follo Line sulfides.	52
4.7	Amount of unclassified area in % for all Follo Line samples by AM mapping.	53
4.8	Wt% and average chemistry of iron sulfides in the Follo Line samples by AM mapping.	54
4.9	LECO results on Trois-Rivières samples.	59
4.10	Selected XRF results on Trois-Rivières material.	59
4.11	DTA results from Trois-Rivières samples.	61
4.12	Sulfides in Trois-Rivières stub samples detected with reflected light microscopy	63
4.13	Sulfides in Trois-Rivières thin sections detected with reflected light microscopy.	65
4.14	EPMA results for Trois-Rivières sulfides.	67
4.15	Area-% unclassified for Trois-Rivières samples from AM mapping.	69
4.16	Average wt% and chemistry of sulfur phases for all Trois-Rivières samples, by 20 μm AM mapping.	69
4.17	Wt% and average chemistry of sulfur phases for the Trois-Rivières samples gathered by 20 μm AM mapping.	70
5.1	Indications of pyrrhotite in Follo Line samples by DTA, OM and AM analyses.	86
5.2	Comparison of wt% biotite estimations by AM and XRD analyses on the Follo Line material.	93
5.3	Summary of average Fe-content in pyrrhotite and pyrite in the Follo Line and Trois-Rivières samples by AM and EPMA.	109

Abbreviations

NTNU = Norwegian University of Science and Technology
IGP = Department of Geoscience and Petroleum
NPRA = Norwegian Public Road Administration
NBTL = Norwegian Concrete and Aggregate Laboratory
DTA = Differential Thermal Analysis
TGA = Thermogravimetric Analysis
SEM = Scanning Electron Microscope
AM = Automated Mineralogy
EDS = Energy Dispersive Spectrometry
BSE = Back Scattered Electrons
FEG = Field Emission Gun
BPS = Bright Phase Search
XRD = X-Ray Diffraction
XRF = X-Ray Fluorescence
LOI = Loss On Ignition
EPMA = Electron Probe Micro Analysis
EBSD = Electron Backscatter Diffraction FB = Follo Line
TR = Trois-Rivières
OM = Optical Microscopy
RF = Reflected Light
PPL = Plane-Polarised Light
XPL = Cross-Polarised Light
AMD = Acid Mine Drainage
MLA = Mineral Liberation Analyser
QEMSCAN = Quantitative Evaluation of Mineralogy by a Scanning electron microscope
TIMA = TESCAN Integrated Mineral Analyser
PSV = Polished Stone Value
TBM = Tunnel Boring Machine

Mineral abbreviations are according to Whitney and Evans (2010).

Chapter 1

Introduction

1.1 Motivation

Sulfide minerals in concrete aggregates have in recent years experienced increasing attention concerning their destructive impact on hardened concrete. In Norway, this issue was seriously introduced during the construction of the Follo Line railroad tunnel. The intended usage of local excavation material was prohibited for the production of concrete linings due to exceeding sulfur concentrations and indications of pyrrhotite (Ytterdal, 2019). This led to drastic economic consequences for the project-owner forced to buy and convey aggregates from commercial producers, as well as finding suitable landfill areas for the surplus material. In Trois-Rivières (Canada) and Eastern Connecticut (USA), deterioration appeared at an even bigger magnitude. Thousands of concrete fundamentals in domestic houses were exposed to extensive cracking due to disregarded iron-sulfide concentrations in the aggregates (Rodrigues, 2016; Jana, 2018).

Back in Norway, the Norwegian University of Science and Technology (NTNU), National Public Roads Administration (NPRA) and Bane NOR initiated in 2018 a project to learn more about the effect pyrrhotite and other sulfide minerals have on concrete, and how these minerals can be characterised and quantified. A pre-project report by Danielsen et al. (2019) summarises the state of the art in this topic and defines the objectives for the coming research project. This M.Sc. study will focus on the characterisation, the formation, and appearance of pyrrhotite in different rocks. For these purposes, aggregate samples from the Follo Line

tunnel and the Trois-Rivières area in Canada, both related to pyrrhotite problems, are characterised using in-depth analytical techniques.

Acceptance limits for the total sulfur in concrete aggregates is 1 wt% (NS-EN12620, 2006). If however pyrrhotite is indicated in a sample, limit value is lowered to 0.1 wt%, without any further requirements for petrographic investigations. The Norwegian addition to the European standard specifies that investigation for pyrrhotite shall be carried out in all cases where total sulfur content exceeds 0.1 wt% by the aid of Differential Thermal Analysis (DTA). In practise, the sulfur limit is lowered to 0,144 wt% since only one decimal is specified in the standard. Concentrations of sulfur and pyrrhotite in such low ranges are in general challenging to determine and distinguish from other iron sulfides. The motivation for this study is therefore to investigate how precise and accurate different test methods are for the quantification and characterisation of sulfur and pyrrhotite in rock samples.

Challenges with pyrrhotite commence with the instability of this mineral when exposed to oxygen and water (Rodrigues, 2016). Pyrrhotite reportedly has an oxidation rate 20-100 times faster than that of pyrite, primarily due to larger surface area and iron vacancies in the crystal structure (Nicholson and Scharer, 1994; Belzile et al., 2004). The iron sulfide forms sulfate ions (SO_3), sulfuric acid (H_2SO_4) and iron hydroxide ($\text{Fe}(\text{OH})_3$) by oxidation (Jana, 2018). This may lead to internal sulfate attack in the concrete and expansion reactions, where detrimental secondary minerals such as ettringite and thaumasite induce map cracking and premature disintegration of the concrete structure (Danielsen et al., 2019; Jana, 2018). Thaumasite formation is a consequence of sulfate attack on the cement which may turn concrete into a non-cohesive mass as binding and load-carrying capacity are significantly reduced (Rahman and Bassuoni, 2014).

Statistics on sulfur and pyrrhotite test results in Norwegian aggregates presented by SINTEF in Danielsen et al. (2019), suggest that sulfur content and pyrrhotite appearance in general are higher in crushed rock compared to natural sand and gravel. This is especially unfortunate considering that natural sand and gravel deposits are limited, and also important for other purposes such as ground water reservoirs. According to the recently finished *Kortreist Stein* (short-travelled rock) project report by Rise et al. (2019), Norwegian sand- and gravel deposits are gradually getting emptied out.

It seems reasonable that most of the pyrrhotite in natural sand and gravel already is decomposed due to the long travel time in an oxidising atmosphere. On the other hand, pyrrhotite in crushed rock may be preserved during the short exposure until it is tested for use in con-

crete. Together, the findings from SINTEF and Kortreist Stein indicates that increased use of crushed rock in concrete could lead to more difficulties with pyrrhotite in aggregates in the coming years.

Good utilisation of local rock in large infrastructure projects have become higher prioritised during the last years, with the increased focus on sustainability. Aggregate materials represent finite resources that must be extracted and managed carefully (Fladvad, 2020). Many coming tunneling projects are likely to be judged on how well the excavated rock is utilised. The *Kortreist Stein* project emphasised the importance of using as much of excavated rocks as possible by pointing out some key areas that must be succeeded with, to achieve a *sustainable use of excavated rocks*. Good planning and geological mapping is necessary to reveal the rock qualities expected during excavation, and the following possibilities for usage of this material.

Aasly et al. (2019) created a guide on when necessary pre-investigations should be carried out, and what these should include. Knowledge on rock quality can best be utilised when gathered early in the planning of a project. The value of this knowledge presupposes that we can rely on our analytical methods when they give us decisive results for the applicability of excavated rocks. This thesis therefore aims to give an evaluation on relevant analytical techniques for the detection of sulfur and pyrrhotite, which are highly decisive for the value and applicability of rock materials.

1.2 Objectives and structure of thesis

The main objective of this study is to characterise pyrrhotite and associated sulfides in two different concrete aggregate types. Suitability of standardised test methods recommended in the technical specifications NS-EN1744-1 (2009) will be compared to advanced mineralogical techniques. Extra effort will be dedicated to the use of a SEM-based Automated Mineralogy system for discrimination between pyrite and pyrrhotite. Another motivation with this analytical tool is to demonstrate its applicability to deliver accurate quantitative mineralogy on particulate- and hard rock samples. Material from the Follo Line Tunnel in Norway and Trois-Rivières in Canada will be analysed for these purposes.

Chapter 2 comprises a literature review on geological settings of sample material, pyrrhotite mineralogy and geological processes that decides formation and preservation of pyrrhotite

in different rocks. Fundamentals of Differential Thermal Analysis (DTA) and Automated Mineralogy (AM) systems and their suitability for iron sulfide characterisation are determined. Chapter 3 describes materials and methods used in the study. This involves sample preparation for the various analyses and procedures in all analytical techniques. Chapter 4 presents characterisations of both materials with focus on pyrrhotite appearance and sulfide mineralogy, and different approaches for discrimination of pyrrhotite and pyrite. The results are further discussed in Chapter 5, where the suitability of the different analytical techniques performed during this work is evaluated. Chapter 6 concludes the main findings of the study.

Chapter 2

Background

This chapter comprises information on the geological settings of sample materials, general information on iron sulfides and pyrrhotite mineralogy, and a review of previous studies on pyrrhotite characterisation. Fundamentals of Differential Thermal Analysis (DTA) are presented as this method is the Norwegian standard industrial method for pyrrhotite detection. Additionally, a review on the Automated Mineralogy (AM) analysis is included to familiarise the reader with the technique and possibilities of this relatively new method.

2.1 Geological settings of the sample origin

2.1.1 Follo Line Tunnel

From 2016 to 2019, close to 20 km of the Follo Line Tunnel were excavated by several Tunnel Boring Machines (TBM) between Oslo to Ski. Parts of the excavated tunnel rock were intended to be used in concrete segments, but were rejected when 30% of the samples analysed during aggregate testing did not fulfill the requirements in NS-EN 12620+NA. 60 % of these samples contained pyrrhotite (Ytterdal, 2019; Danielsen et al., 2019).

According to bedrock maps from Norwegian Geological Survey, the tunnel mainly runs through Precambrian tonalitic to granitic gneisses (NGU, 2020). The geology and structural evolution of the area was described by Graversen (1984), who placed the area in the eastern

subprovince of the Sveconorwegian orogenic belt.

Ytterdal (2019) stated that the tunnel runs through different types of gneiss with intersecting amphibolite and diabase intrusions of varying thickness and shape. According to the report on ground conditions by Jernbaneverket (2011), the gneisses were divided into 3 main types based on mineral contents determined by Graversen (1984). All of the gneisses are predominantly composed of quartz, feldspars and biotite, with several accessory minerals. Opaque minerals were only registered as such, without any further description of e.g. sulfides. Compositions and metamorphic grade for the gneisses occurring in the Follo Line Tunnel are summarised in Table 2.1 below.

Table 2.1: Summary of the mineral compositions and metamorphic grade of the gneisses present where the Follo Line Tunnel was excavated. Determined during thin section examination by Graversen (1984). Mineral abbreviations after Whitney and Evans (2010).

Mineral composition in %		Quartz	Feldspar		Biotite	Accessory minerals, (-) is rare	Metamorphic grade
			(Pl)	(Kfs)			
Tonalitic to granitic gneiss	Tonalitic	30	40	0	20	Alm, Ap, Chl, Ms, Ttn, Zrn, + "opaque minerals"	Amphibolite facies
	Granitic	30	30	35	5	Alm, Ap, Cal, Chl, Ep, Ms, Zrn,+ "opaque minerals"	Amphibolite facies
Quartz-feldspar- rich gneiss		40	20	30	"dominant mafic mineral"	Alm, Ap, Cal, Chl, Ep, Ms, Ttn, Zrn, Rt, Hem, (Ky, Sil)	Amphibolite facies
Biotite-rich augen gneiss		25	20	40	10	Grt, Ap, Ms, Ttn, Zrn, + "opaque minerals"	Amphibolite facies

2.1.2 Trois-Rivières, Canada

The St. Boniface Quarry is situated North-West of the province Trois-Rivières, between Québec and Montréal in Canada. The quarry is subdivided into the B&B and Maskimo pits, located a couple of hundred meters apart. The problematic material causing concrete deterioration were produced from both quarries, within the same geological unit; an intrusive anorthositic gabbro (norite or hypersthene gabbro) with a varying degree of metamorphism (Rodrigues, 2016; Jana, 2018). Obtainable background information on this rock type is limited to this simple rock classification.

2.2 Iron sulfides

Iron sulfide is a generic term for crystalline compounds of iron and sulfur. The ones that are most abundant and relevant for characterisation of pyrrhotite are presented here, along with distinguishing features in hand specimen and optical microscope.

Pyrrhotite is the second-most common iron sulfide after pyrite, and is most often found in basic igneous rocks. It has the non-stoichiometric composition Fe_{1-x}S , where x can vary from 0 (FeS) to 0.125 (Fe_7S_8) (Deer et al., 2013; Zapletal, 1993). Pyrrhotite has a density around 4.5 - 4.8 and hardness around 3.5 - 4.5 (Marshall et al., 2004). Pyrrhotite usually appears in massive or granular aggregates and has a bronzy, brown-yellow color in hand specimen, which may easily tarnish and show other colors. It can be quite difficult to differentiate from other iron sulfides, but its bronze-brown stain in color compared to brass-yellow coloring of other iron-sulfides is a characteristic determination feature under the microscope. Many pyrrhotites are ferromagnetic, unlike other iron sulfides (Marshall et al., 2004). In reflected light (rf) microscopy, pyrrhotite has a creamy pinkish brown color under plane-polarised light (ppl) and shows strong anisotropy in cross-polarised light (xpl) varying from red to yellowish brown. Marcasite is the only other anisotropic iron sulfide, but is easily distinguishable from pyrrhotite, due its much higher bireflectance.

Pyrite is the most common sulfide mineral, appearing with the uniform composition FeS_2 . It commonly occurs as an accessory mineral in all types of rocks - sedimentary, metamorphic and magmatic, or more massive especially when related to hydrothermal systems (Deer et al., 2013). In hand specimen pyrite is often easily identified due to its characteristic cubic shape and brassy yellow color. In polished section under ppl, pyrite has a pale yellowish white color and is isotropic. Crystal faces or cubic shapes are also common under the microscope.

Marcasite is the orthorombic polymorph of pyrite and may be difficult to distinguish from pyrite in hand specimens (Marshall et al., 2004; Deer et al., 2013). It commonly occurs in replacement deposits in carbonate rocks, and may precipitate from acidic solutions in low-temperature environments. In polished sections, it has a yellowish white color with slight pinkish/ greenish tint. Marcasite can be distinguished from pyrite due to its distinct bireflectance and strong anisotropy.

Chalcopyrite is the most abundant copper-bearing mineral, and has the composition CuFeS_2 . It mainly occurs in mafic and ultramafic igneous rocks, hydrothermal deposits and stratiform

sedimentary environments (Deer et al., 2013). Chalcopyrite has a darker brass yellow color than pyrite and is also much softer, 3,5-4,5 in Mohs scale (Marshall et al., 2004). In ppl, chalcopyrite shows a distinct yellow color much stronger than that of pyrite.

Pentlandite is an iron-nickel sulfide with composition $(\text{Fe,Ni})_9\text{S}_8$. It is predominantly found in mafic and ultramafic igneous rocks and is often associated with pyrrhotite due to the similar chemistry (Marshall et al., 2004). In hand specimen it may look similar to pyrrhotite and pyrite with a metallic and a brass yellow color. Pentlandite can easily be recognised in ppl when occurring together with pyrrhotite, where flame-like lamellae of pentlandite can be seen in pyrrhotite due to exsolution. This exsolution happens in nickeliferous pyrrhotite when nickel is substituting iron in such an extent that crystallisation of pentlandite is possible during cooling (Francis et al., 1976). If no exsolution textures is present, pentlandite can be distinguished from pyrrhotite with a lighter creamy yellowish color and no anisotropy.

2.3 Pyrrhotite mineralogy

The pyrrhotite group comprises a complex group of slightly different minerals with stoichiometry close to FeS (Deer et al., 2013). The variations among pyrrhotite polytypes originate first and foremost from different ordering of iron vacancies in the mineral lattice (Wuensch, 1963b). The pyrrhotite family is based on the unit cell parameters from NiAs (nickeline/niccolite), illustrated in Figure 2.1. Pyrrhotites are made up of superstructures based on this unit cell, in different ordering of the iron vacancies, which allow many varieties to be formed. The NiAs unit cell parameters are $a = 3.618 \text{ \AA}$ and $c = 5.034 \text{ \AA}$ (Lide, 2004). The physical, chemical and magnetic properties of pyrrhotites vary with the number of iron vacancies in the superstructure and how they are ordered (Zapletal and Janák, 1972).

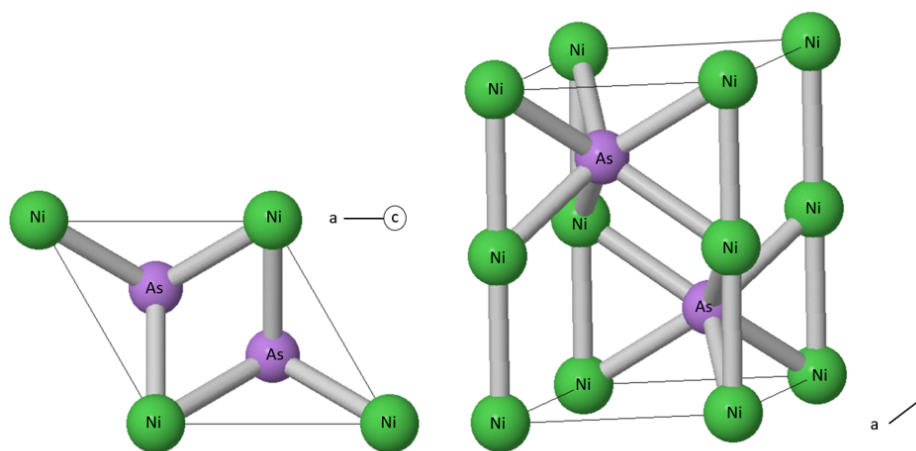


Figure 2.1: The NiAs unit cell viewed from two directions. Modified after Mindat (2020).

Pyrrhotites have been intensively studied during the last century due to their unusual, non-stoichiometric chemical formulas, varying properties and abundance in base metal sulphide ores. In 1925, Alsén was one of the first to describe the chemistry and crystallography of pyrrhotite. Since then, several pyrrhotite superstructures, both naturally occurring and synthetic ones, have been discovered and described.

Wuensch (1963a) suggested the system where pyrrhotite superstructures are described by repeating the NiAs unit cell dimensions along the a -axis or c -axis. In this system, the dimensions of a 1C pyrrhotite structure reassembles the NiAs unit cell, while dimensions of a 2C pyrrhotite equals two NiAs unit cells stacked along their c -axis. Henceforth, the c -axis in a 4C pyrrhotite unit cell exhibits four times the c -axis in the NiAs unit cell, as illustrated

in Figure 2.2. The nomenclature system of Wuensch (1963a) will primarily be used in this study for the characterisation of different pyrrhotite types.

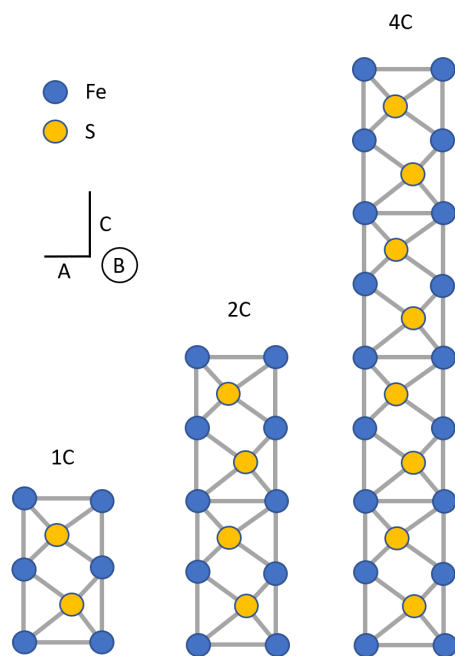


Figure 2.2: Illustration of the nomenclature suggested by Wuensch (1963a), describing pyrrhotite superstructures by NiAs unit cell multiplication along the C-axis. 2C and 4C pyrrhotites are naturally occurring, while 1C pyrrhotite only is a high-temperature synthetic phase (Becker, 2009). The sketch only depicts the principle repetitive sequence, not the specific vacancy configurations of sub-layers, illustrated in Figure 2.3

Pyrrhotites were for a long time claimed to crystallise in either the monoclinic or the hexagonal crystal systems, and have been classified thereafter. Becker (2009) claims that "hexagonal" pyrrhotites may possess a more complex crystal structure than first assumed, and are actually orthorhombic. Varying magnetic properties are also used for the differentiation of pyrrhotite polytypes. The two most common natural occurring types, 4C- and NC pyrrhotites, do respectively display ferromagnetic and anti-ferromagnetic behavior (Wang and Salveson, 2005; Gordon and McDonald, 2015). NC pyrrhotites comprise 5C, 6C and 11C pyrrhotites, which are commonly referred to as one phase due to very small compositional differences.

In the following we will elevate the three different naturally occurring types of pyrrhotite: 2C (Troilite), 4C pyrrhotite and NC pyrrhotites (Carpenter and Desborough, 1964; von Gehlen and Pillier, 1965; Corlett, 1968). Structural information for the natural occurring pyrrhotites are summarised in Table 2.2. It should be noted that pyrrhotite usually comprise mixtures of

4C and NC superstructures, which gives intermediate overall compositions (Dekkers, 1988).

Table 2.2: Generalised composition for naturally occurring pyrrhotite superstructures. Modified after Multani and Waters (2018).

Type	Ideal Composition	Proposed Formula for Charge Neutrality	$\frac{\text{Fe}^{3+}}{\text{Tot Fe}} \%$	Ideal Atomic %		Ideal Weight %	
				Fe	S	Fe	S
2C	FeS	$\text{Fe}^{2+}\text{S}^{2-}$	0.0	50.00	50.00	63.53	36.47
NC (6C)	$\text{Fe}_{11}\text{S}_{12}$	$\text{Fe}_2^3+\text{Fe}_9^2+\text{S}_{12}^{2-}$	18.2	47.83	52.17	61.49	38.51
NC (11C)	$\text{Fe}_{10}\text{S}_{11}$	$\text{Fe}_2^3+\text{Fe}_8^2+\text{S}_{11}^{2-}$	20.0	47.62	52.38	61.29	38.71
NC (5C)	Fe_9S_{10}	$\text{Fe}_2^3+\text{Fe}_7^2+\text{S}_{10}^{2-}$	22.2	47.37	52.63	61.05	38.95
4C	Fe_7S_8	$\text{Fe}_2^3+\text{Fe}_5^2+\text{S}_8^{2-}$	28.6	46.67	53.33	60.38	39.62

2.3.1 2C - Troilite

Troilite, FeS, is the stoichiometric end member in the pyrrhotite group, crystallising in the hexagonal system (Deer et al., 2013). It appears to have no iron deficiencies in its crystal structure and equal proportions of iron and sulfur, and is therefore non-magnetic (Arnold, 1967; Wang and Salveson, 2005). In the nomenclature system denoted by Wuensch (1963a), is Troilite often referred to as 2C. Troilite is rarely found in nature, and is probably most known for its presence in meteorites and lunar samples (Evans, 1970; Becker, 2009).

2.3.2 4C - Monoclinic pyrrhotite

The monoclinic pyrrhotite has the ideal composition Fe_7S_8 and represents the most iron deficient end-member of the FeS - Fe_7S_8 system (Nakazawa and Morimoto, 1971). According to Wuensch (1963a) it is referred to as 4C pyrrhotite, and due to its ferromagnetic properties often called "magnetic pyrrhotite" (Deer et al., 2013). The 4C pyrrhotite constitutes of superstructures with alternating layers of fully occupied metal sites and layers with a varying number and ordering of vacant sites (Tokonami et al., 1972). Fe-vacant, incomplete layers are suggested to appear in four different configurations, illustrated in Figure 2.3, modified after Vaughan et al. (1971). Becker et al. (2010) investigated the reactivity of pyrrhotite types in connection with flotation performance, and found that magnetic pyrrhotite(Fe_7S_8) was the most reactive type, while non-magnetic(Fe_9S_{10}) pyrrhotite was relatively unreactive.

To obtain charge neutrality, despite iron deficiency, Vaughan and Craig (1978) suggested that

ferric iron (Fe^{3+}) is present in the vacancy layers, giving the valence formula $\text{Fe}_2^{\text{Fe}^{3+}}\text{Fe}_5^{\text{Fe}^{2+}}\text{S}_8^{2-}$. Whether ferric iron is present in the sublayers of 4C-types or not is still debated and the literature is quite contradictory on this matter. Pratt et al. (1994) and Letard et al. (2007) respectively found evidence for ferric iron, and no ferric iron at all in the 4C pyrrhotite.

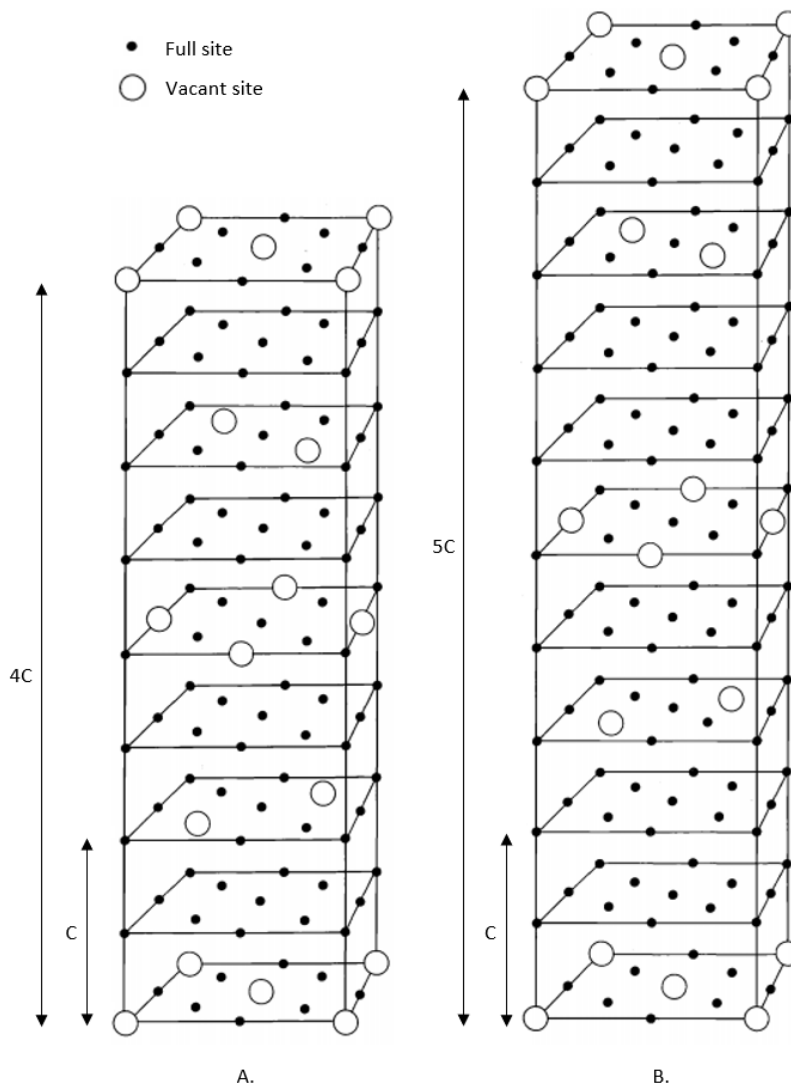


Figure 2.3: **A.:** Illustration of the proposed vacancy arrangements in the superstructure of 4C magnetic pyrrhotite. **B.:** Illustration of the proposed vacancy arrangements in the superstructure of 5C pyrrhotite. Sulfur sites are omitted for clarity in these figures. After the proposed vacancy arrangements of 4C and 5C pyrrhotites by Vaughan et al. (1971).

2.3.3 NC - Intermediate pyrrhotites

The intermediate pyrrhotites comprise three naturally occurring polytypes with ideal compositions Fe_9S_{10} (5C), $\text{Fe}_{10}\text{S}_{11}$ (6C), and $\text{Fe}_{11}\text{S}_{12}$ (11C), placing them in between end members of the $\text{FeS} - \text{Fe}_7\text{S}_8$ system (Vaughan and Craig, 1978). The repeat distance of the NiAs unit cell *c*-axis varies from 5 to 11, and is denoted N for the intermediate pyrrhotites. In literature, these minerals are treated as one phase because their composition falls within a very narrow range, ideally 47.37-47.84 % atomic Fe (Wang and Salveson, 2005). The NC pyrrhotites are antiferromagnetic and can be distinguished from the ferromagnetic 4C pyrrhotite based on this.

It appears there are far more uncertainties regarding crystal structure for the NC pyrrhotites than for 2C and 4C pyrrhotites. The suggested vacancy structures are based on filling in some of the iron vacancies from the 4C structure, until the absolute number of vacancies for the NC pyrrhotites is reached. A proposal by Vaughan et al. (1971) for 5C pyrrhotite, suggested a vacancy structure with alternating layers of one and two fully occupied metal sites between the vacancy layers, shown in Figure 2.3. According to Becker (2009), no complete crystal structure exist for NC pyrrhotites in the literature, and their crystallography is still debated.

NC pyrrhotites were for a long time considered to have hexagonal crystallography, and are therefore in many papers referred to as hexagonal pyrrhotites (Morimoto et al., 1975). According to Vaughan and Craig (1978), 5C- and 6C pyrrhotites are hexagonal, while 11C pyrrhotite is orthorhombic. On the other hand, Morimoto et al. (1975) and Koto et al. (1975) describes 5C- and 6C pyrrhotites as orthorhombic and monoclinic (pseudo-orthorhombic), respectively. Becker (2009) also describes the 5C pyrrhotite as orthorhombic.

2.4 Formation and appearance of pyrrhotite

Pyrrhotite is most often found in basic igneous rocks such as gabbros and basalts, hydrothermal deposits or metamorphic rocks, and can also be present in pegmatites or stratiform sedimentary environments (Deer et al., 2013; Marshall et al., 2004). However, according to analyses by SINTEF (Haugen and Lindgård, 2019) and NBTL (Jensen, 2019), small amounts of pyrrhotite may occur in most rock types. Although pyrite overall is the most abundant sulfide mineral, pyrrhotite is commonly more abundant in ultramafic and mafic rocks (Deer et al., 2013).

The abundance of sulfur in a rock or a magma is normally decisive for pyrrhotite to be formed, because the earth's crust on an average estimate is made up of only 0,035% sulfur and 5,6% iron (Lide, 2004; Mauk et al., 2020). For a comprehensive review on the sulfur budget and the solubility in magmas is the reader encouraged to have a look at Wallace and Edmonds (2011) and Baker and Moretti (2011). Although ore forming processes generate most massive formations and occurrences of pyrrhotite, are these rocks rather irrelevant for the concrete problem. In the following we will therefore focus on generic processes of pyrrhotite formation as accessory minerals in rocks that may be suitable for use in concrete aggregates.

In igneous rocks, pyrrhotite mainly forms as a result of immiscibility between silicate and sulfide melts, occurring when a melt becomes saturated in sulfur (Deer et al., 2013; Robb, 2005). Small globules of sulfur-rich melt will appear disseminated in the magma attracting chalcophile elements, which are elements with higher affinity for sulfur than silica. The sulfide globules either accumulate and crystallise in layers, possibly creating ore deposits, or crystallise disseminated in the cooling magma. The latter is probably the most important magmatic process responsible for formation of the accessory pyrrhotite in rocks that may be used as concrete aggregate. In a review on sulfur-bearing magmatic accessory minerals, Parat et al. (2011) stated that these are common in mafic and silicic arc-related igneous rocks, ocean island basalts and mid-ocean ridge basalts. Sulfides are in general less common in alkaline magmas, but pyrrhotite, pyrite and molybdenite are likely to appear here as well. For instance, was pyrrhotite detected in peralkaline rhyolite on Gran Canaria and in syenite on the Canary Islands (Crisp and Spera, 1987; Rodríguez-Losada and Martínez-Frias, 1998). Indications of pyrrhotite in the felsic gneisses surrounding the Follo Line Tunnel also belong to the story (Graversen, 1984; Ytterdal, 2019). Parat et al. (2011) points out pyrrhotite as the most abundant sulfide in continental arc-related magmatic rocks, and in island arc basalts

and andesites. Regarding texture, the magmatic accessory sulfides usually occur as isolated globules/blebs embedded in other mineral phases or as isolated crystals in glass. They rarely form euhedral crystals.

Pyrrhotite precipitates also in hydrothermal systems when Fe- and S-solubility in the fluid is sufficiently reduced (Robb, 2005). Solubility primarily depends on temperature, pH and oxygen- and sulfur fugacity in the fluid solution. Metamorphism of pyrite-bearing rocks may contribute to formation of pyrrhotite due to S^{-2} release from pyrite (Toulmin and Barton, 1963; Craig and Vokes, 1993). Conversely, during retrograde metamorphism, release of sulfur from pyrrhotite is assumed to result in pyrite recrystallisation. The amount of sulfur release and recrystallisation is in coherency with pyrite sulfur release during prograde metamorphism and pyrrhotite sulfur release during retrograde metamorphism (Craig and Vokes, 1993). Common alteration products of pyrrhotite comprise pyrite, marcasite and other sulfides, while pyrrhotite oxidation products include iron sulfates, carbonates and oxides (Deer et al., 2013).

According to the Fe-S phase relations in Figure 2.4, originally determined by Kullerud and Yoder (1959), and reproduced from Deer et al. (2013), pyrite will melt incongruently to pyrrhotite and liquid sulfur at around 742 °C. Also, as illustrated in Figure 2.4, pyrrhotite shows increasing iron deficiency with increasing temperature when in equilibrium with pyrite. Below 350 °C, the phase relations of pyrrhotite is very complex as the already described superstructures will begin to develop and create pyrrhotites with marginally varying compositions (Nakazawa and Morimoto, 1971; Kissin and Scott, 1982).

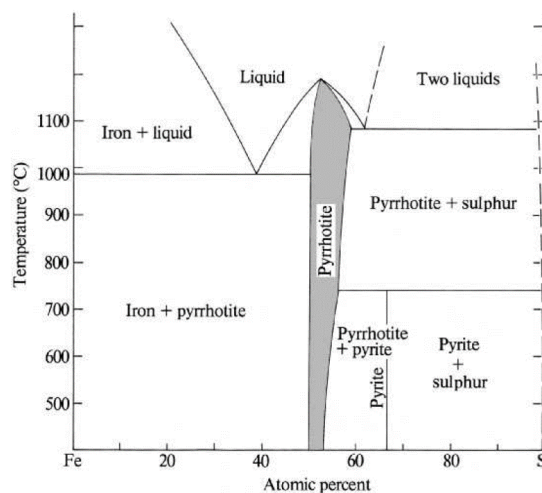


Figure 2.4: Fe-S phase diagram showing the relations between pyrite and pyrrhotite above 400 °C. Determined by Kullerud and Yoder (1959), reproduced from Deer et al. (2013).

2.5 Previous studies on the characterisation of pyrrhotite

So far, little research has been conducted on the characterisation of very low amounts of pyrrhotite in concrete aggregates. Most of the previous research on pyrrhotite characterisation is related to metallurgical purposes such as ore recovery and Acid Mine Drainage (AMD) (Moncur et al., 2009; Duffy et al., 2015). Mineral reactions between different pyrrhotite variations and neighbouring associations indicate comparable behavior across different fields of interest. Durability studies and deterioration research of concrete therefore benefits from these related topics. Becker (2009) and Bunkholt (2014) contributed with their research on the characterisation of different pyrrhotite types using modern analytical tools. Their studies focused on identifying different types of pyrrhotites rather than detection of very low pyrrhotite contents.

Becker (2009) managed to differentiate between magnetic- and non-magnetic pyrrhotite with QEMSCAN, an automated mineralogy solution based on Scanning Electron Microscopy (SEM). It was also proven that the magnetic type has higher iron deficiency than non-magnetic polytypes. According to Becker (2009), it is theoretically possible to differentiate between pyrrhotites based on Back Scattered Electron (BSE) imaging. The BSE grey level is 43.33 for Fe_9S_{10} pyrrhotite and 43.16 for Fe_7S_8 pyrrhotite. This difference is too narrow for discriminating with routine operating settings on a SEM. Note that the BSE grey level of minerals is relative, and changes with brightness and contrast adjustments.

After many iterations and careful adjustments in brightness and contrast settings, Becker (2009) eventually did manage to differentiate between the pyrrhotite types based on BSE. BSE imaging is influenced by crystal orientation and surface quality of the sample specimen, which could interfere with the back scatter signals. After personal correspondence in September 2020, Becker suggested that today's modern Field Emission Guns (FEG) are likely to produce better results for the mineral's characterisation. Becker (2009) stated that the x-ray spectra captured from different pyrrhotite phases with the Energy Dispersive Spectrometer (EDS) was not enough to differ the types based on composition. Becker (2009) also distinguished pyrrhotite types with powder XRD analysis, but this method is less relevant for pyrrhotite in aggregate materials due to their low concentrations.

Bunkholt (2014) distinguished between two pyrrhotite phases with BSE imaging on an ordinary SEM (Hitachi SU6600). It was emphasised that the different grey levels within pyrrhotite were not visible immediately, but after numerous adjustments of brightness and contrast. To determine which grey levels correspond with the iron-rich and iron-poor pyrrhotite, spot analyses with Electron Micro Probe Analysis (EPMA) were performed on both phases. This showed that the brighter BSE phase on average was 0,6% richer in iron than the darker phase. Due to the very small differences in chemical content, EPMA requires accurate calibration to succeed. Bunkholt (2014) used a pyrite standard for calibration, but denotes that a pyrrhotite standard would have been the ideal choice. Bunkholt (2014) also tried to differentiate the pyrrhotites with an Electron Backscatter Diffraction (EBSD) technique. This was only partly successful, and further work was recommended.

Furthermore, Bunkholt (2014) tested the accuracy of XRF and LECO by analysing respectively Fe and S in spiked samples composed of 98% calcite and 2% sulfides, in which compositions were predefined to certain contents of pyrite and pyrrhotite. Fe and S contents were calculated based on the known sulfide concentration and composition, and compared to XRF and LECO analysis. It turned out that XRF and LECO were well suited for analysing low concentrations of sulfides. In the case with sulfides in aggregates, the verification of LECO as an accurate method for sulfur analysis is promising. XRF can not be used for Fe analysis with the purpose of iron sulfide quantification, since Fe is common among other rock forming minerals typically present in aggregates.

With focus on the concrete durability problem, **Rodrigues (2016)** developed a performance test for sulfide bearing aggregates in her PhD work. The research covers mineralogical investigations on the aforementioned sulfide-bearing aggregates used in Trois-Rivières (Canada). Petrographic analyses on the materials were carried out with optical microscope, and SEM- and EPMA imaging. The aggregates consist of anorthositic, ortho-pyroxene-rich gabbro, called norite (Winter, 2013). The observed sulfides in the Trois Rivières aggregates were pyrrhotite, pyrite and chalcopyrite, along with pentlandite exsolutions in pyrrhotite. These appeared closely associated with each other and well disseminated among the silicates. Chalcopyrite was also observed as scattered inclusions within pyrrhotite and pyrite. Pyrrhotite was reported as the most abundant sulfide mineral, see Table 2.3. It was also observed that iron carbonate (siderite, FeCO_3) often were surrounding sulfides and filling cracks within sulfides.

Rodrigues (2016) performed optical microscopy point-counting and made petrographic descriptions of aggregates from Maskimo (MSK) and B&B quarries in St Boniface, Trois-Rivières. The results were reported as % of opaques, further divided into composition of the opaques in each sample, Table 2.3. For an easier comparison with results obtained in the current study, the original values from Rodrigues (2016) are calculated to % of total mineral content.

Table 2.3: Summary of the mineral quantifications by Rodrigues (2016) on coarse aggregates from Maskimo (MSK) and B&B quarries in Saint-Boniface, Trois-Rivières. The results were obtained with point counting on thin sections with optical microscopy. % of opaque minerals was reported by Rodrigues (2016), while % of total mineral content is calculated in the current study for easier comparison. x = observed, not quantified.

Sample	Opaques %	% of opaque minerals					% of total mineral content				
		Pyrrhotite	Pyrite	Chalcopyrite	Pentlandite	Magnetite	Pyrrhotite	Pyrite	Chalcopyrite	Pentlandite	Magnetite
MSK-1	6,2	95	4	1	x		5,9	0,2	0,1	x	0,0
MSK-2	1,4	45	50	5	x		0,6	0,7	0,1	x	0,0
MSK-3	4,3		95	3		2	0,0	4,1	0,1	0,0	0,1
MSK-4	0,5		x		x		0,0	x	0,0	x	0,0
MSK-5	43	65	32	3	x		28,0	13,8	1,3		0,0
BB-1	10,3	50	45	5			5,2	4,6	0,5	0,0	0,0
BB-2	7,7	90	8	2			6,9	0,6	0,2	0,0	0,0
BB-3	12,4	55	40	5			6,8	5,0	0,6	0,0	0,0
BB-4	17,8	50	45	5	x		8,9	8,0	0,9	x	0,0
BB-5	2,7		95	3	2		0,0	2,6	0,1	0,1	0,0

In the damaged concrete, several secondary reaction products were observed, such as ferric oxyhydroxides (goethite, limonite), gypsum and solid solution ettringite-thaumasite phases. Macroscopic examinations of the concrete samples revealed that pyrrhotite surfaces were strongly oxidised compared to the seemingly unaltered pyrite. Cracks in the concrete were predominantly observed in close contact with sulfide-bearing aggregate particles. Rodrigues (2016) suggested that formation of thaumasite may be facilitated by carbonate minerals in the aggregate, or by limestone filler from the cement.

2.6 Differential Thermal Analysis (DTA)

Differential Thermal Analysis (DTA) refers to the measurement of temperature differences between a sample material and a thermally inert reference material during heating or cooling (Smykatz-Kloss, 2012). Phase changes in minerals provoked by heating or cooling trigger measurable exothermal and endothermal reactions. The temperatures of these reactions provide characteristic curves for qualitative identification of minerals (Smykatz-Kloss, 1982).

When a reaction in the sample material releases heat (exothermic) or requires heat (endothermic), a potential between the sample and the thermally inert reference material will appear (Smykatz-Kloss, 2012). The DTA curve represents the differential voltage appearing between sample and reference, and is plotted as deviations from the normal-curve of the inert material. The peak temperature and the peak height on DTA curve deviations represent the two most important characteristics for mineral identification (Smykatz-Kloss, 1982). A natural first step when analysing a DTA curve is therefore to compare the peak shape from the unknown sample with existing curves of known minerals.

Iron sulfides exhibit strong exothermic peaks, due to oxidation reactions (Smykatz-Kloss, 1982). Földvári (2011) stated that pyrite and pyrrhotite oxidise between 350-600°C, simultaneously emphasising the large inconsistency in literature on temperature ranges for sulfide oxidation in air.

Kopp and Kerr (1958) investigated peak characteristics of pyrite and marcasite through variations in sample weight and grain size. Their study showed that the first exothermic peak temperature decreased with grain size reduction. It was proposed that a respective temperature decrease with grain size correlates to an increase in surface area available for oxidation. Also, the total peak area, or deviation from the normal curve, was found to increase when the amount of sample was increased. The pyrite DTA curves obtained by Kopp and Kerr (1958) are presented in Figure 2.5.

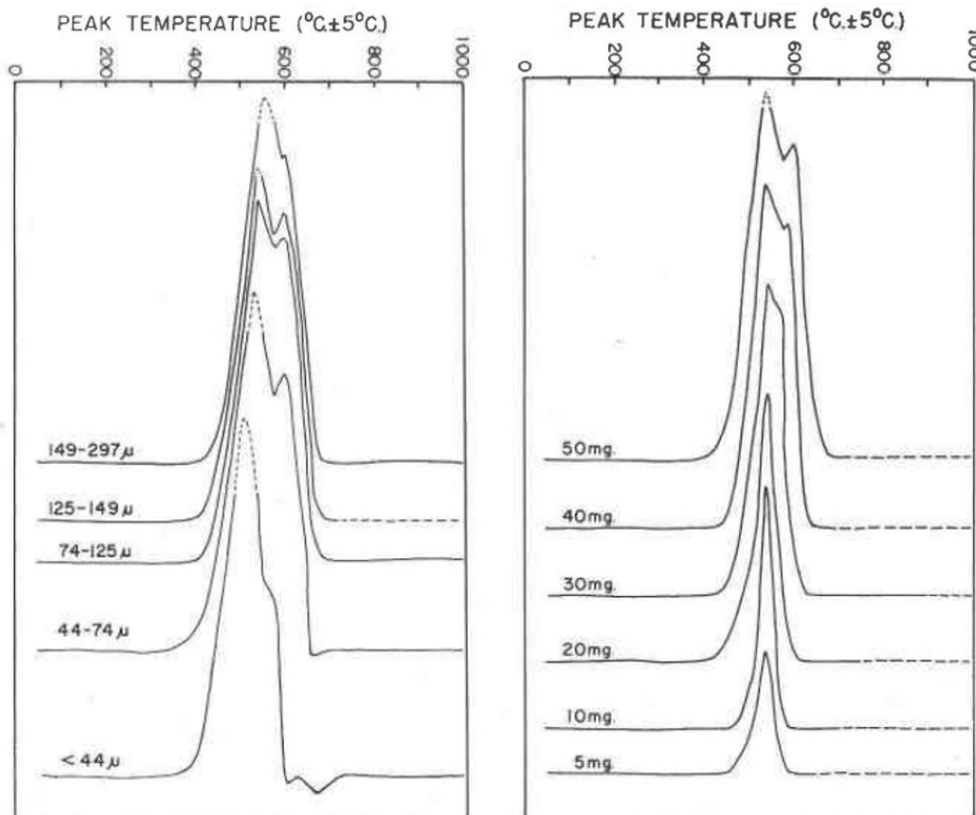


Figure 2.5: **Left:** DTA curves of pyrite in different grain sizes. The first exothermic peak temperatures decrease with grain size reduction. **Right:** DTA curves of pyrite in different sample amounts. Total peak areas, or magnitudes, increase with sample amounts. Reproduced after Kopp and Kerr (1958).

In addition to the influence of grain size and sample amount, DTA curves are found to depend on packing density, furnace atmosphere and sample preparation (Smykatz-Kloss, 2012). Detailed descriptions of preparations and the analytical conditions are therefore in particular important to report along with DTA results.

According to Mackenzie and Mitchell (1962), many laboratories have constructed their own DTA apparatus due to the apparent simplicity of the method. This has resulted in little commercial development and a low degree of standardisation. Although several manufacturers offer solutions, home-built versions, also in combination with Thermogravimetric Analysis (TGA), are still common. Since DTA curves are influenced by so many variables it is difficult to compare results from different studies and laboratories (Smykatz-Kloss, 2012). Berg and Shlyapkina (1975) emphasised the bad reproducibility of DTA results. Various factors, influencing oxidation and difficulties with stabilising them, were stated in this study.

2.6.1 DTA apparatus at the Dept. of Geoscience and Petroleum (IGP)

The DTA available at the IGP was built by Prof. Rolf Selmer Olsen back in 1957, and has later been modernised and automatised on several occasions. It is co-owned and operated by NTNU and SINTEF, and regularly used for commercial testing of pyrrhotite in concrete aggregates by the latter. The following technical descriptions and procedures in this section are taken from the local DTA operation manual compiled by SINTEF, and the chapter on DTA from the booklet on geological laboratory investigations compiled by Sørlokk et al. (2007).

Sample preparation involves micronisation of 40g sample material to approximately 75% 8 - 10 μm and 15% $<2\mu\text{m}$. Two samples can be analysed simultaneously, and are placed in Nickel crucibles along with two thermometers and Al_2O_3 -powders, illustrated in Figure 2.6. The two crucibles with Al_2O_3 -powders next to the samples contain thermo elements coupled to each sample. Al_2O_3 will not undergo any phase transitions in the temperature range of the analysis. The two thermometers above and within Al_2O_3 are for keeping track of temperature development in air and within a sample.

The thermal reactions that occur in a sample during heating are transmitted by a thermocouple (Pt-Pt 10% Rh) covered with sample powder. Electric pulses (μV) generated during the phase reactions are registered and plotted against temperature development.

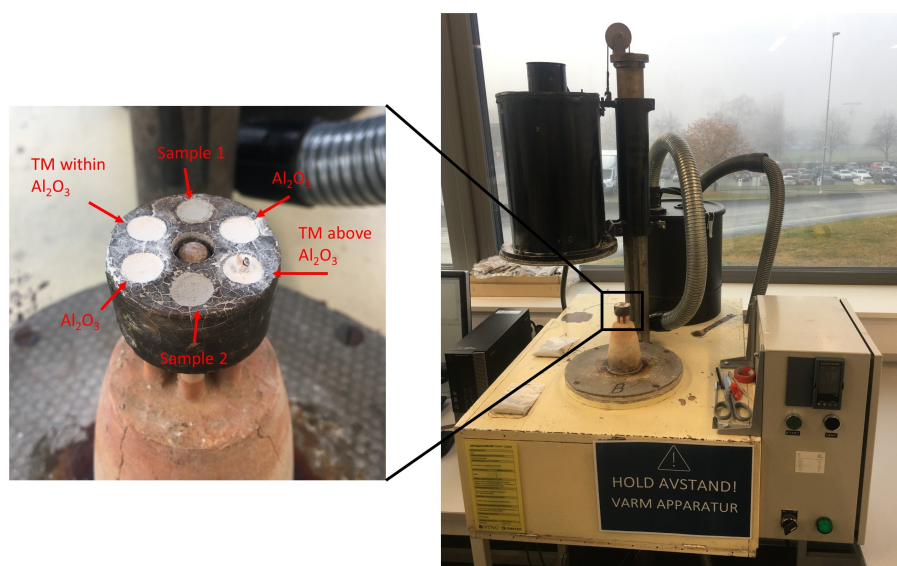


Figure 2.6: The home-built DTA machine at the institute can analyse two samples simultaneously. TM = Thermometer.

When sudden heat changes occur in one of the samples due to phase reactions, a potential is established between the couples in sample and in Al_2O_3 , and a current between the sample and the Al_2O_3 -powder can be registered. Exothermal phase reactions will give a positive voltage anomaly, while endothermal reactions results in a negative anomaly. Since oxidation reactions are used to identify sulfides, the exothermal reactions that are most relevant for this purpose.

The machine can be calibrated with a reference material if it is desirable to quantify a phase that undergoes thermal reactions. This require a reference material with known concentrations of the mineral phase that is to be quantified in the unknown sample. Grain shape and -size must also be defined and consistent, since these parameters largely influence on the surface area on minerals in the sample. Since no reference material for iron sulfides is available at the institute, the method on this apparatus is not suited to perform quantitative determination of sulfide phases. Overlapping curves among the common iron sulfides also makes it very difficult to distinguish between these minerals with DTA.

According to the operation manual at IGP pyrite, chalcopyrite and pyrrhotite may oxidise between 380°C and 520°C , as shown in Table 2.4.

Table 2.4: Temperature ranges where oxidation and characteristic DTA signature takes place for the common iron sulfides. Obtained from the operation manual at the institute, and from the booklet compiled by Sørlokke et al. (2007).

	Chalcopyrite	Pyrite	Pyrrhotite
Temperature range	380-420°C	430-450°C	480-520°C

The output from a DTA analysis at IGP comprises a print of the temperature development and electrical pulses generated during the elapsed time in a test. This is illustrated in Figure 2.7 along with a common iron sulfide curve pattern.

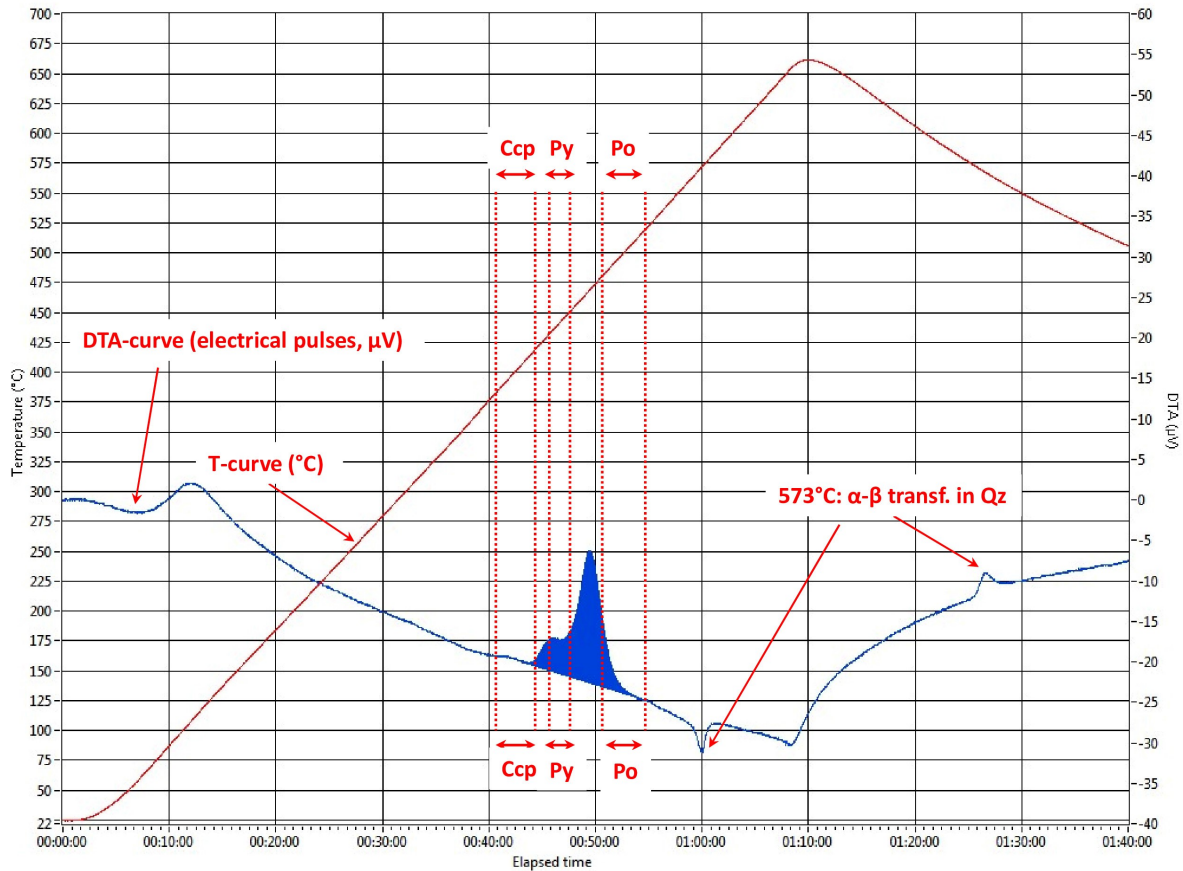


Figure 2.7: Example of an output sheet from DTA analysis with a typical iron sulfide signature, where the main peak falls between pyrite and pyrrhotite temperature ranges. The iron sulfide oxidation intervals are obtained from the operation manual from the DTA at the institute, and from the booklet compiled by Sørlokk et al. (2007).

2.7 Automated Mineralogy (AM)

Automated Mineralogy (AM) determines a multi- instrumental approach of different automatised techniques for the textural and quantitative analyses of rock samples, based on e.g. Optical Microscopy (OM), X-Ray Diffraction (XRD) or Scanning Electron Microscopy (SEM) (Sandmann, 2015; Young, 2019). This section presents the fundamentals of the SEM-based technique, referred to as AM in the following.

SEM-based AM systems consist of a hardware platform and a specific image analysis and processing software solution (Gottlieb et al., 2000; Schulz et al., 2020). The technique comprises scanning of a specimen surface with a traditional SEM, followed by automatic quantification, processing and interpretation of collected signals through a specific software. The use of automated electron beam methods for mineral identification has been initially developed to optimise mineral processing operations and characterisation of metal-bearing ores in the 1970s (Sutherland and Gottlieb, 1991; Pirrie and Rollinson, 2011). Another motivation was the possibility to obtain statistically significant sets of data without performing labour-intensive manual viewing of particles (Fandrich et al., 2007). Today, AM systems are mostly used in the mining industry for routine characterisation of particulate samples of ore feed, products and tailings (Warlo et al., 2019). For a comprehensive review on development in AM methodology, the reader is recommended to have a look at the PhD thesis by Sandmann (2015).

Back Scattered Electron (BSE) imaging and Energy Dispersive Spectrometry (EDS) detectors are the two main electron beam instruments used in most AM systems (Gottlieb, 2008). BSE imaging measures the average atomic number of minerals, used to discriminate phases in a sample. This allows for preliminary differentiation of epoxy resin as background in particulate samples, and rapid discrimination between minerals with different average atomic number. One or several EDS detectors are used to acquire X-ray spectra at selected points in the sample, providing a measure on chemical compositions (Pirrie and Rollinson, 2011). More than one EDS detector is an advantage since this will reduce the time consumption during a scan.

All AM-systems have in common that recorded X-ray signals are matched with a database of classification criteria, for mineral identification (Warlo et al., 2019). QEMSCAN (Quantitative Evaluation of Mineralogy by a SCANNing electron microscope) (Gottlieb et al., 2000) and MLA (Mineral Liberation Analyser) (Gu, 2003) represent the two most widely applied

AM systems today, although production of both currently have stopped (Warlo et al., 2019). Two of the most prominent systems distributed today are the ZEISS Mineralogic Mining system (Graham et al., 2015) and the TESCAN Integrated Mineral Analyser (TIMA) (Hrstka et al., 2018). The former being operated at the Dept. of Geoscience and Petroleum (IGP), and is used in the current study.

On Zeiss Mineralogic, measured X-ray spectra from EDS is classified with user defined mineral recipes based on the mineral chemistry, enabling a detailed and quantitative chemical-mineralogical classification throughout the sample (Zeiss, 2017). Mineral recipes consist of max- and min values for elements making up each mineral and/or element ratios within a mineral. The latter is especially useful when distinguishing between solid solution minerals or minerals with close compositions, such as the plagioclase solid-solution series or pyrrhotite and pyrite (Zeiss, 2017).

Desired outputs from AM analysis vary with the purpose of investigation. Additional to bulk mineralogy, one can get statistics on e.g. grain sizes, mineral associations, mineral liberation and elemental deportment (Graham et al., 2015). After all signals are gathered, adjustments on the mineral recipe can be made to optimise the classification. *Retrospective analysis* allows to detect unclassified phases and adjust the recipe thereafter (Zeiss, 2017). When new premises are implemented during re-processing, updated output sets based on the original analysis data will be generated.

Over the last decades, the use of AM has increased also in other geoscientific areas. Scott and Rollinson (2015) performed AM analyses with QEMSCAN on whole rock thin sections from crushed rock aggregate quarries in the UK. AM was used to describe the mineralogy and texture of different rock types, which in turn relate to the physical properties of aggregates, e.g. PSV (Polished Stone Value). It was suggested that this method has potential to be used by companies when formally describing their aggregate products. Although the amount of deleterious minerals, e.g. sulfides, were not considered in this study, it was suggested that presence and distribution of these easily could be established with AM. However, sample representativeness is a remaining problem for the analysis with AM, comparable with OM. The significant petrographic variations that may occur within an aggregate quarry will demand examination of multiple samples.

2.7.1 Measurement modes

A number of different measurement modes are possible with AM, and possibilities vary between manufacturers. The preferred mode usually depends on the purpose of investigation, sample format, desired level of resolution and acceptable time consumption. The following five analysis modes are possible with Zeiss Mineralogic Mining (Graham et al., 2015).

- **Mapping mode** is dividing the sample into pixels, or a grid, of a certain resolution and will work its way through the sample by scanning and measuring the chemistry of every pixel with EDS detectors. Since time consumption is largely dependant on the number of EDS measurements, this method may be slow or fast depending on what step size is chosen.
- **Spot Centroid mode** is first using the BSE signal to identify each individual mineral grain in the sample. The geometric centre of each grain is calculated, and analysed by the EDS. This method does not recognise compositional variations within a grain, as the centre-measurement is assigned to the whole grain. Spot Centroid is normally considered to be one of the fastest mode, but this is largely dependant on the BSE-identification of grain boundaries. If grain boundaries are complex, or lots of small grains are present, time consumption may increase drastically.
- **Feature Scan** also uses the BSE signal to identify each grain, but makes several EDS measurements within each grain to give an average composition which is assigned to the whole grain.
- **Line Scan** creates a line across the center of each particle, where EDS measurements are performed at a chosen step size. This method is fast, and provides a statistically valid impression of the bulk mineralogy.
- **Back Scatter Electron mode** is only using BSE signal to create a grey-scale from 0-255 corresponding to the average atomic numbers on the present phases. Mineral phases with a high portion of heavy elements will return the most electrons and create a stronger and brighter signal than phases with lighter elements which appear darker. This method may be combined with mapping mode in a so called Bright Phase Search (BPS), where phases with a certain back scatter signature is selected for further mapping with EDS.

2.7.2 General background for sampling and prep. for AM

Sampling for AM analyses is not different from most other analytical techniques, requiring random selection of each sample from a population and unbiased preparation (Whateley and Scott, 2006). In principle, two types of sample materials can be analysed with AM; granular materials such as aggregates or non-granular materials such as drill core samples (Sandmann, 2015). Since only a few grams of material are required, smaller amounts must be extracted and partitioned in a way that keeps the extracted parts as representative as possible for the total sample volumes. Sample split can be achieved with several methods. Scoop sampling, coning and quartering, chute splitter, table splitter and rotary riffler are the common procedures (Allen, 2003).

Sandmann (2015) outlined a couple of crucial prerequisites regarding sample preparation for quantitative SEM analyses. A well-polished and planar specimen surface is crucial to avoid shadowing effects in uneven surfaces that may lead to lower X-ray detection in some areas of the sample surface. For the case with granular samples, it is also a challenge to ensure an even dispersion of particles throughout the sample without segregation caused by differing size or density.

Pooler and Dold (2017) tested different sample preparation protocols in order to reduce the effect of segregation during waste rock characterisation with AM. Transverse cut thin sections exposed that sulfide-rich particles tended to sink towards bottom of the section. Furthermore, it was concluded that particle size reduction down to $<212 \mu\text{m}$ and preparation of a transversely-mounted polished section is the most effective and accurate methodology to avoid segregation.

Røisi and Aasly (2018) investigated how segregation and number of touching particles in a sample of quartz and iron sulfide were influenced by the amount and grain size of graphite additive. Also here it was emphasised that transverse sections are the best way to reduce the effect of segregation, although this method requires more time to the sample preparation process. The results of Røisi and Aasly (2018) indicated that mixing graphite with sample material not necessarily prevent segregation, but reduced the amount of touching particles, which is crucial for AM liberation analyses.

The use of transverse-cut sections, exposing the vertical section of a particulate epoxy resin mould, appear to be the most promising way of minimising effects of segregation (Craig et al., 1981; Kwitko-Ribeiro, 2012; Blaskovich, 2013; Grant et al., 2016). Use of sized

samples rather than unsized samples are also suggested to reduce segregation, due to less particle size differences. Minimising segregation is important regarding the potential use of AM for iron sulfide detection, since these are heavier than most silicate minerals. The flowsheet in Figure 2.8 illustrates the most common sample preparation procedures for AM analyses on particulate samples according to Sandmann (2015).

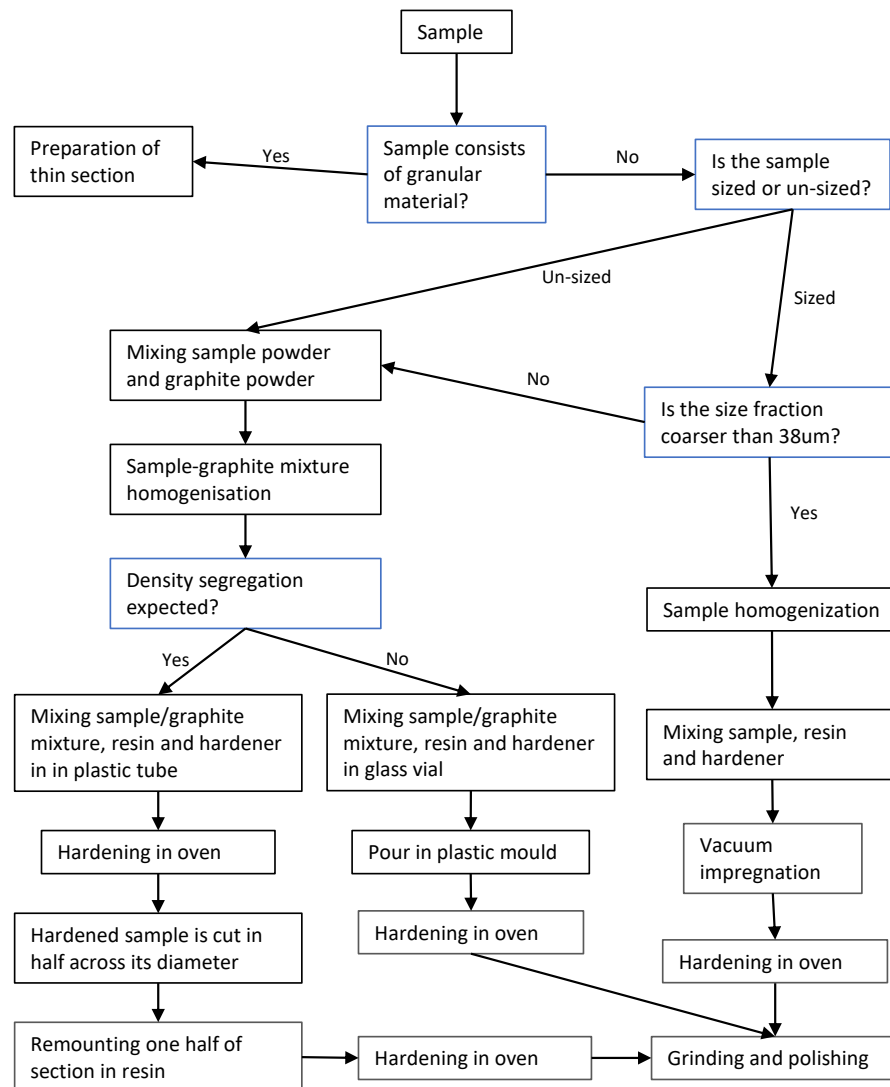


Figure 2.8: Flowsheet of sample preparation procedures for AM analysis on particulate samples. Modified after Sandmann (2015).

2.7.3 Resolution and detection capability

A general detection limit for AM systems is difficult to define since it depends on several factors like measurement mode of analysis, electron beam settings and spectral resolution of EDS and BSE detectors. EDS detectors are typically able to detect phases with elemental concentrations $>0,1-1\%$ (Hjelen, 1989; Reed, 2005). Andersen et al. (2009) used QEM-SCAN to characterise Ni-rich ores, and estimated a lower limit of detection for NiO around 3.8 wt% with minimum 5000 counts per pixel and 1.8 wt% with minimum 16000 counts.

The type of measurement mode is probably most decisive for the mineral phase detection ability. If mapping mode is chosen, it follows that mineral phases smaller than the measurement step size may not be properly recognised. The excitation volume of beam electrons in the sample is another decisive factor regarding detection limit (Warlo et al., 2019; Kenis et al., 2020). Depth of excitation increases with acceleration voltage of the electron beam (Hjelen, 1989). Mineral phases smaller than the excitation volume of the electron beam will be difficult to identify due to mixed signals (Warlo et al., 2019).

Reed (2005) suggested to not use pixels smaller than $1\ \mu\text{m}$, since this typically represents the X-ray source region. Boni et al. (2013) performed $10\ \mu\text{m}$ and $1\ \mu\text{m}$ scans with QEM-SCAN on bauxite deposits and experienced that differences between these resolutions were marginal from a bulk mineralogy point of view. The most appropriate resolution during mapping mode must therefore be adjusted according to the time budget of the analysis and what mineral phases to operator expect to find.

The large potential, and uncertainties, with mineral phase detection on AM mapping may be illustrated in an example: If a mineral A is present at 1 ppm (0,0001%), and the AM is scanning an area of 1000×1000 pixels, the AM will find that single pixel and report the very low content of mineral A. Detection of mineral A in this case however assumes that it becomes the dominating part of a pixel in a way that the EDS picks up composition of mineral A and not a mixture of different phases. The latter is typically happening if mineral A is split between several pixels, resulting in mixed signals and low influence from mineral A on the chemistry in each pixel.

Chapter 3

Materials and methods

3.1 Materials

3.1.1 Follo Line samples

Sample material from the Follo Line project was received at NTNU Trondheim in big bags in 2019. This material had been randomly sampled from different stockpiles in spoil sheds where TBM excavated material was temporary stored outside the tunnel. The rocks reportedly originate from parts of the bedrock that have been exposed to weathering, with probable contents of iron sulfides. Beyond this, no information exist on where in the tunnel the material is excavated. Rock material from TBM excavations is produced by disc-cutters which break rocks away from the tunnel face by applying compressive stress.

Sample selection from the big bags was done prior to this study. Hand specimens were picked out of the big bags by hand and crushed subsequent to gravel size sample material. Five polished stub samples were produced in 2019 from each of the Follo Line hand pieces, by Postdoctor Ben Snook and Associate Professor Kurt Aasly. These samples are well suited for investigations with SEM, but have limited value under optical microscope since only opaque phases can be identified. The sample basis before the current study was five plastic bags (FB-A1, FB-B, FB-C, FB-D and FB-E) with 250g-900g gravel size material, and five polished whole-rock stub samples.

3.1.2 Trois-Rivières samples

Sample material from the Maskimo pit, St. Boniface quarry, in Trois-Rivières, was received at NTNU in 2019, sent from the University of Laval, Quebec. The samples consisted of crushed and screened rock material in fractions <8mm, 1/8mm and >8mm from the quarry. These are reportedly taken directly from aggregate products at the St Boniface Quarry, which is one of the aggregate-suppliers to the problematic Trois-Rivières concrete. Prior to this study it was produced one polished stub sample from 1/8mm and >8mm fractions, plus a 0,045/1mm fraction screened from the <8mm sample.

Table 3.1 show all samples and sample formats from the Follo Line and Trois Rivières aggregates used in the current study.

Table 3.1: Overview of all sample material and analyses conducted in the study. Follo Line samples to the left and Trois Rivières samples to the right. All stub samples were produced during the pre-project work in 2019.

Sample	Format	Analyses	Sample	Format	Analyses
FB-A1	Stub	AM, OM	TR-0,045/1mm	Stub	AM, OM
	Powder	XRD, XRF, DTA, LECO		Powder	XRD, XRF, DTA, LECO
FB-B	Stub	AM, OM	TR<8mm	Thin section	AM, OM, EPMA
	Powder	XRD, XRF, DTA, LECO		Stub	AM, OM
	Thin section(2)	AM, OM		Powder	XRD, XRF, DTA, LECO
FB-C	Stub	AM, OM	TR1/8mm	Thin section(2)	AM, OM, EPMA
	Powder	XRD, XRF, DTA, LECO		Stub	AM, OM
	Thin section(2)	AM, OM, EPMA		Powder	XRD, XRF, DTA, LECO
FB-D	Stub	AM, OM	TR>8mm	Stub	AM, OM
	Powder	XRD, XRF, DTA, LECO		Powder	XRD, XRF, DTA, LECO
	Stub	AM, OM			
FB-E	Powder	XRD, XRF, DTA, LECO			
	Thin section(2)	AM, OM			
FB-F	Thin section	AM, OM			
FB-G	Thin section	AM, OM			
FB-H	Thin section	AM, OM			
FB-I	Thin section	AM, OM			
FB-J	Thin section	AM, OM, EPMA			
FB-K	Thin section	AM, OM			

3.1.3 Sample splitting and selection

Gravel material from Follo Line and Trois-Rivières was divided into smaller samples with an *Eriez Macsalab* rotary sample splitter, Figure 3.1. This resulted in 10 smaller samples of each size fraction. Each sample was weighed before and after splitting, to give a measure on how even the splitting was executed. Samples with weight closest to average within each sample split were considered to be most representative, and selected for further preparation into thin section. Excel sheets from splitting, weighing and sample selection can be found in Appendix A.

Kjetil Eriksen, the thin section preparator at the Dept. of Geoscience and Petroleum (IGP), prepared six polished thin sections from Follo Line hand pieces, four polished thin sections from the Follo Line gravel samples and two polished thin sections from the Trois-Rivières gravel, all with dimensions 28x48mm. Preparation of gravel thin sections involved extracting 20-40g from each sub-sample, placing it into plastic cylinders and mixing with epoxy resin. After hardening, a thin section was produced by cutting a transverse section from each cylinder. The remaining half-part of each cylinder is shown in Appendix A. From the Follo Line hand pieces, small rectangular blocks were cut out by a diamond cutter for further preparation to whole-rock thin sections.

3.1.4 Preparation for XRD, XRF, DTA and LECO

XRD, XRF, DTA and LECO analyses do all require powder <125 μm in minor quantities. Material was crushed and ground in the same operation for these analyses. A *Fly Press Rock Crusher*, Figure 3.1, was used to crush the material down to <4 mm. This crusher is operated without external power, and crushes material by raising and lowering a steel disc above another steel disc until the desired size reduction is achieved.

A *Retsch RS 200 disc mill* was used to grind the material further down. The sample size requirements for disc milling is 15-50 ml and grain size <5 mm. Each sample was ground with 1200 rpm in 90 seconds, providing suitable grain size for XRD, XRF and DTA. Over-milling could make it difficult for the XRD to recognise crystal lattice distances, while too coarse milling could lead to over-representation of some mineral grains in both XRD and XRF. The disc mill material was wolfram carbide. After disc milling, material for XRD-analysis was further micronised to avoid flat-lying grains which may cause over-exposure of

some minerals. Micronisation was performed by using a *McCrone Micronising Mill* for 120 seconds in a chamber with agate and 10 ml ethanol. All crushing and grinding equipment was cleaned between every sample, to avoid cross-contamination.



Figure 3.1: Left: Sample separation with the 10-way rotary splitter. Right: Crushing of small samples with the Fly Press Crusher.

3.2 Analytical tools for characterisation of pyrrhotite and sulfur

3.2.1 LECO for total sulfur content

LECO analysis for total sulfur were assigned to the Norwegian Concrete and Aggregate Laboratory (NBTL), in Trondheim. All Follo Line (FB-A1, FB-B, FB-C, FB-D, FB-E) and Trois-Rivières (TR<8mm, TR1/8mm, TR>8mm) samples were analysed by this method, involving combustion of a powder sample and detection of the gaseous SO₃ phase.

15-200 mg of each sample was placed in a porcelain crucible. Iron and LECOCEL powders were used as accelerators. The oxygen flow was 3,25 L/min. Temperature during analysis was 1700-1800°C. No detection limits are reported for these analyses. The apparatus delivers results with four decimals, which are rounded to two decimals for reporting.

3.2.2 X-Ray Fluorescence (XRF)

The five Follo Line samples (FB-A1, FB-B, FB-C, FB-D, FB-E) and the three Trois-Rivières samples (TR<8mm, TR1/8mm, TR>8mm) were analysed by XRF with main- and trace element analyses. The XRF at the institute, operated by technical engineer Torill Sørlokk, was installed and set up during the fall of 2020, and is a *Zetium XRF Spectrometry* delivered by *Malvern Panalytical*.

The main element analysis was performed on a glass pellet made up by sample powder and a flux material consisting of lithium tetraborat/metaborat. The first step in this preparation was to measure the Loss On Ignition (LOI) on 2,5 g sample material. The material was heated to 1000 °C. This gives a controlled measure on the removal of volatiles and organic phases. Based on this, the LOI can be calculated and incorporated into the results. This value can give indications on the amount of lost phases, but provides no specifics on what these may be.

In the next step, 0,5g (+/-0,0005g) material was extracted from each sample and put in glass containers. This was mixed with 5,0g (+/-0,0002g) flux material. The flux material lowers the melting temperature of all minerals throughout the sample in such a degree that all will

melt when heated to 1050°C. The high proportion of flux relative to sample material ensures that no mineral crystallization occurs during cooling and that the elements solidify evenly distributed throughout the glass pellet. The mixture of sample and flux was put into melting crucibles (Pt+5%Au), along with 60 μ l lithium iodide for better consistency of the final glass pellets and easier removal from the crucibles. All samples were melted in a *Claisse TheOx Advanced* fusion oven for 24 minutes and 45 seconds up to 1050°C.

The trace element analysis required preparation of pressed pellets, which involved mixing of 9,6 g sample material with 2,4 g of a wax binder (Licowax). This was well mixed with a *Fluxana MUK* mixer, and compressed with 200 kN into pellets on a *Herzog* manual pellet press. In addition to the trace element analysis, it was performed a semi-quantitative analysis on the pressed pellets which measured all elements without any reference. This method is considered as semi-quantitative because it is not calibrated for the elements that are measured. On the other hand, trace- and main element analyses are both calibrated for each element they measure. The semi-quantitative analysis is of particular interest for the sulfur content, which may have been significantly reduced during preparation for the main element analysis.

3.2.3 X-Ray Diffraction (XRD)

Follo Line samples (FB-A1, FB-B, FB-C, FB-D, FB-E) and Trois-Rivières samples (TR<8mm, TR1/8mm, TR>8mm) were analysed with XRD, by a *Bruker D8 Advance XRD* operated by senior engineer Laurentius Tijhuis at the IGP. A couple of grams of the powder material, described in Section 3.1.4, were extracted from each sample by a spoon. This powder was further micronized, aforementioned in Chapter 3.1, for the avoidance of over-exposing flat-lying grains. The samples then dried on 60°C for approximately 12 hours, compressed in sample holders and made ready for XRD analysis.

The software *DIFFRAC.EVA* was used to identify minerals based on the registered peak intensities from the analyses. This program seeks through a mineral database with the experimental diffraction peak patterns, ranked in a list with the minerals most likely present in the sample. Quantification of the identified mineral phases was carried out by the *TOPAS* software, using Rietveld refinement to fit the experimental diffraction pattern to a theoretical pattern.

The results are presented in Chapter 4, while the diffractograms from each analysis is listed in Appendix G. Since the detection limit of XRD analyses is as high as 1%, the reported results for minerals quantified below 1% yield large uncertainties. The reason why some minerals below the detection limit are reported is that certain characteristic peaks could be strong evidence, despite low contents. Broad and rounded peaks in the diffractogram are likely due to disturbed and irregular crystal structures which often is related to weathered mineral phases.

3.2.4 Differential Thermal Analysis (DTA)

Differential Thermal Analysis (DTA) was performed on all Follo Line (FB-A1, FB-B, FB-C, FB-D, FB-E) and Trois-Rivières (TR<8mm, TR1/8mm, TR>8mm) samples, by Laboratory Technician Kevin Aaserud Dahlen on the DTA apparatus at IGP/SINTEF. Further details on this apparatus and method were presented in 2.6.

Two samples were analysed simultaneously. Temperature was evenly raised from room temperature to approximately 660 °C at a heating rate of 10 °C/min. Cooling happened naturally as the apparatus cooled down. Differential voltage measurements were started when the heating began and went on for 1 hour and 40 minutes. All samples reached maximum temperature after approximately 1 hour.

3.2.5 Optical microscope

A *Nikon Eclipse E600* polarisation microscope was used for the petrographic investigation of thin sections and polished stub samples. In thin sections, opaque minerals were analysed in epi-illumination, while anisotropic minerals were studied in transmitted light. Photomicrographs were acquired with the *SPOT 5.3* imaging software. All thin- and stub samples were scanned by a *Olympus BX51* microscope. These full-sample scans are very useful for comparison and verification of false color mineral maps produced by Automated Mineralogy (AM) mapping. The samples were scanned at 5x magnification and resolution 1688x1352 (Binning 2x2) pixels per field. Image processing and automatic field stitching were done with the *Olympus Stream Motion* software.

The optical microscopy investigations in this study focused primarily on the iron sulfide

appearances. Investigations of translucent minerals in thin sections were limited to identification and verification of AM false color maps.

3.2.6 Electron Probe Micro Analysis (EPMA)

Selected iron sulfide phases in FB-J, FB-C, TR1/8mm and TR<8mm thin sections were point-analysed with a JEOL JXA8500 probe, operated at the IGP by Postdoctoral Researcher Kristian Drivenes. The purpose of EPMA analysis was to investigate narrow chemical differences in the already identified sulfides in the Follo Line and the Trois-Rivières material. Some unknown phases related to pyrrhotite weathering in the Trois-Rivières samples were attempted analysed as well.

Analytical settings comprised 2 μm probe diameter, 15 kV acceleration voltage and 20 nA probe current. The element recipe consisted of the most common elements in sulfides; Se, As, Fe, Mn, Mo, Co, S, Cu, Ni, Zn. Calibration was done on standards of natural minerals and pure heavy metals from Astimex. Re-analyses of chalcopyrite, marcasite, pentlandite and sphalerite standards were carried out for every 20 analysis point, to make sure that operating conditions remained stable.

Element map analysis on a pyrite cluster in FB-K was also carried out to control the pyrrhotite-pyrite discrimination delivered by AM mapping. Selected areas with potential misidentified pyrrhotite pixels within pyrite were analysed for Fe, S, Ni, Co and Si. If the pyrrhotite pixels within pyrite truly were pyrrhotite inclusions, one would see increased Fe-values and decreased S-values in these areas. Operational settings for these analyses were 100 nA probe current, 15 kV acceleration voltage and 500 ms dwell time per pixel. 1 μm , 2 μm and 10 μm probe diameter/pixel size were used in dependence to the size of the selected areas.

3.2.7 Automated Mineralogy (AM) on Mineralogic Mining

All Follo Line and Trois-Rivières stub samples and thin sections were analysed with 20 μm mapping on a *Zeiss Sigma 300 VP* field emission electron microscope with a Bruker Quantax EDS, configured to operate with Mineralogic Mining software. The analyses were set up in cooperation with the operator of the AM system at IGP, Associate Professor Kurt Aasly.

Prior to analysis, all stub samples and thin sections were carbon coated to approximately 20 nm to ensure sufficient conductivity on the sample surfaces. Standard SEM settings were used; 20 kV acceleration voltage, 8,5mm working distance and aperture 120 μm . X-ray measurement settings were initially set to 0,004 seconds mapping dwell time and minimum 1000 spectrum counts in each pixel. Removal of background epoxy within particulate sections and around whole-rock sections was achieved using a BSE-threshold on 35-255. All samples were analysed with similar settings, except from different sample holders for stub samples and thin sections, and different adjustments of brightness and contrast among stub sample and thin section analyses. Brightness and contrast is decisive for grey phase contrasts in the BSE images produced along with mineral maps.

After the initial analyses on stub samples, some problems regarding detection of aluminium (Al) appeared. Pixels within the same phase seemed to contain around 10% Al or no Al at all in alternating patterns. This effect was primarily observed in orthopyroxene and K-feldspar phases. It was suggested by Mineralogic technical support and supervisor Kurt Aasly to raise mapping dwell time and minimum spectrum counts to resolve this. Mapping dwell time was raised from 0,004 to 0,01 seconds and spectrum counts was raised from minimum 1000 to 1500 per pixel. This turned out to be the correct solution as the Al-effect disappeared after all samples were analysed again with adjusted settings.

Dwell time per pixel decides how long the EDS analyse a pixel before moving to the next. *Minimum spectrum counts* sets the threshold for the number of counts required for a pixel to be classified. Number of spectrum counts represent the number of characteristic photons sent out from the elements and detected by the EDS. Pixels with elements that deliver less than 1000 spectrum counts are considered not to be sufficiently statistical representative, and are categorised as *Non Classified*. This category may be confused with the *Unclassified*-category, representing pixels with enough counts, but not caught up by the mineral classification.

Average time consumption for 20 μm mapping on the different sample formats was:

- Particulate stubs: 7 hours
- Intact rock stubs: 9 hours
- Particulate thin sections: 10 hours
- Intact rock thin sections: 11 hours

The two data programs *Mineralogic* and *Mineralogic Explorer* were used for mineral classifications and retrospective analyses on the chemical data gathered by SEM. Mineral phases were identified by the aid of the online mineral search database, *Athena*, by Perroud (2021). This page allows to include and exclude elements from a search, which narrows down the search significantly. Another online mineral database, *Webmineral*, by Barthelmy (2021), was used to find the ideal atomic- and weight percentage of minerals, which is useful when adjusting element limits in the recipe and in general identifying unknown phases.

Mineral recipes for classification

Adjustments of mineral classifications and retrospective analysis were performed to detect all phases and reduce the amount of unclassified pixels to <3% of total mapped area. It is essential to note all mineral recipe changes during re-processing, and pay close attention to bulk mineralogy changes during this process.

Minerals with relatively complicated and similar chemistry are listed first in the mineral recipe, e.g. pyroxenes, chlorite, while simpler minerals, e.g. quartz, calcite, are listed at the bottom. The AM system works through this list from the top and classifies every single EDS analysis to the first fitting mineral criteria. This prioritisation ensures e.g. plagioclase is classified before quartz. This allows for overlapping criterias for oxygen and silicon between these minerals, which is necessary since both contain considerable amounts of oxygen and silicon. In cases where different minerals have partly similar and overlapping chemistry, it is crucial to find characteristic parameters with high consistency and stable EDS quantification. Mineral classification recipes for the Follo Line material and Trois-Rivières material are presented in Table 3.2, 3.3 and 3.4.

Table 3.2: Mineral classification recipe for Automated Mineralogy analysis on the Follo Line material. SG = Specific Gravity. RGB = Red Green Blue, colour code.

Colour	Mineral	RGB	SG	O	Al	Si	K	Mg	Fe	Ti	Ca	Mn	F	Ba	Na	S	Cu	Ni	Zn	P	Ce	Y	Zr
	Biotite	154; 85; 39	3,09	25-50	0-20	5-30	5-20	0-15	8-40	0-20													
	Almandine	255; 128; 64	4,19	20-45	9-22	15-25	0-4	0-6	23-45		0-7												
	Chlorite	128; 255; 128	3,2	30-55	5-15	5-16	0-3	0-15	20-45		0-1	0-1											
	Muscovite	171; 147; 7	2,82	20-50	16-30	15-35	7-16		0-7				0-15	0-9									
	K-feldspar	7; 112; 99	2,52	25-43	0-18	25-60	12-25								0-6								
	Plagioclase	94; 174; 255	2,67	25-60	5-25	20-60	0-3	0-2	0-2		0-20				0-15								
	Sericite	0; 255; 255	2,82	35-50	10-27	20-40	1-15	0-2	0-6		0-6				0-10								
	Amphibole	0; 215; 0	3,23	20-50	5-22	13-30	0-1	0-15	4-15		10-30				0-1								
	Pyrrhotite	255; 255; 0	4,61						58-70							30-45							
	Chalcopyrite	247; 199; 9	4,19						25-55							18-40	18-45						
	Pentlandite	169; 255; 83	4,8						15-55							15-50		10-50					
	Sphalerite	255; 255; 170	4,05													10-40			30-70				
	Pyrite	225; 215; 9	5,01						35-58							40-65							
	Po rand effect	255; 255; 0	4,61						65-90							5-30							
	Fe sulfate	128; 128; 0	1,89	5-40		0-5		0-1	30-80							5-40							
	Ca sulfate	72; 72; 0	2,71	15-60							20-55					10-50							
	Al-silicate	0; 64; 128	3,60	30-50	15-40	10-40	0-5		0-10														
	Apatite	255; 0; 255	3,19	0-50							30-75									10-30			
	Ce-Monazite	159; 6; 49	5,15	10-75																10-40	0-10		
	Y-Monazite	128; 0; 0	5,15	10-75																10-40		0-10	
	P-Si-O phase	255; 128; 166	2,6	25-40		20-36														35-45			
	Zirkon	255; 0; 128	4,65	10-35		10-30																	40-70
	Calcite	202; 228; 255	2,71	35-60		0-1					35-60												
	Carbonate	128; 128; 255	2,71	30-65	0-1	0-9		0-20	0-8		23-60												
	Titanite	206; 157; 157	3,48	30-45		10-20			0-3	17-30	17-30												
	Ilmenite	128; 0; 128	4,72	10-35					25-40	35-50													
	Rutile	230; 0; 0	4,25	0-60					0-10	35-100													
	Fe-oxides	83; 41; 0	5,3	10-60		0-5			4-90	0-11													
	Quartz	255; 204; 230	2,62	30-60	0-3	35-70		0-3	0-3		0-3			0-3		0-3							
	TS-glass	255; 255; 255	2,6	20-50	0-01	10-60			0-0,1		2-15			5-20									
	Background	0; 0; 0	2,6		85-100																		

Table 3.3: Part 1 of 2 - Mineral classification recipe for Automated Mineralogy analysis on the Trois-Rivières material. SG = Specific Gravity. RGB = Red Green Blue, colour code.

Colour	Mineral	RGB	SG	O	Na	Mg	Si	K	Ca	Fe	Al	S	Ti	F	Ca/Na	Cu	Ni	Zn	Zr	P
	Orthopyroxene	88; 111; 68	3,55	20-60	0-2	5-30	10-40	0-0,1	0-4	5-35	0-7									
	Clinopyroxene	0; 149; 0	3,4	20-60	0-2	0-30	10-50	0-0,1	4-45	0-35	0-7	0-5								
	Chlorite	0; 255; 64	3,2	30-50		5-25	7-16	0-3	0,3	7-45	0-20									
	Amphibole	0; 215; 0	3,23	10-50	0-5	0-15	5-40	0-2	3-15	5-20	2-8									
	Biotite	196; 98; 0	3,09	25-50		0-20	5-30	5-20		1-38	0-20		0-20							
	Almandine	255; 128; 0	4,19	20-50	0-5	0-8	16-30		0-8	20-45	0-20									
	K-feldspar	0; 147; 147	2,56	25-55	0-6		25-60	5-25			5-20									
	Muscovite	175; 179; 62	2,82	25-50		0-4	17-35	5-15		0-4	17-27			0-10						
	Anorthite	23; 139; 255	2,73	25-50	0-15		16-45	0-5	0-25	0-10	7-25				>1					
	Albite	12; 211; 202	2,62	30-50	0-15		25-45	0-5	0-15	0-1	5-20				<1					
	Pumpellyite	128; 128; 255	3,2	30-45	0-1	0-1	15-25	0-1	15-25	4-11	11-19									
	Dolomite	0; 0; 255	2,84	30-65		5-20	0-2		23-60	0-25										
	Chalcopyrite	250; 194; 3	4,19							20-45		20-45				20-45				
	Pentlandite	190; 237; 3	4,8							15-55		15-50					10-50			
	Pyrrhotite	255; 255; 0	4,61							57-70		30-45								
	Po rand-effect	255; 255; 0	5,0							65-90		5-30								
	Pyrite	230; 213; 0	5,01							35-57		40-65								
	Sphalerite	255; 255; 164	4,05									10-40						40-70		
	Fe-sulfate	164; 164; 0	1,89	5-40		0-1				30-80		5-40	0-1							
	Ca-sulfate	111; 111; 0	2,71	15-60					20-55			10-50								

Table 3.4: Part 2 of 2 - Mineral classification recipe for Automated Mineralogy analysis on the Trois-Rivières material. SG = Specific Gravity. RGB = Red Green Blue, colour code.

Colour	Mineral	RGB	SG	O	Na	Mg	Si	K	Ca	Fe	Al	S	Ti	F	Ca/Na	Cu	Ni	Zn	Zr	P
	Rutile	174; 0; 0	4,25	0-60						0-10			35-100							
	Ilmenite	101; 50; 50	4,72	0-40						10-55			15-50							
	Fe-oxide	168; 84; 0	5,3	10-60						40-90			0-11							
	Fe-Mg-oxide	128; 64; 0	4,65	35-55		15-40				15-40										
	Spinel	193; 0; 0	4,39	20-50			0-2			15-40	25-55									
	Al-oxide	152; 138; 230	3,95	40-60			0-2			0-15	45-85									
	Al-silicate	255; 72; 72	3,24	35-50			15-35				25-45									
	Titanite	177; 101; 101	3,48	0-55			5-25		10-45	0-3	0-5		10-45	0-10						
	Zirkon	255; 128; 255	4,65	10-35			10-30												45-70	
	Apatite	255; 0; 255	3,19	25-50					30-55											10-28
	Calcite	210; 240; 255	2,71	30-65			0-10		23-65			0-5								
	Quartz	255; 196; 225	2,62	25-50	0-2		15-65	0-7	0-2		0-2			0-10						
	Background	255; 255; 255	2,6								85-100									
	TS-glass	255; 255; 255	2,6	20-50	5-20		10-60		2-15	0-0,5	0-0,5									

Discrimination between pyrite and pyrrhotite with Bright Phase Search (BPS) + 5 μm mapping

Comparisons of reflected light microscopy, BSE imaging and chemical data by EDS were made to find the optimal mineral recipe for discrimination between pyrite and pyrrhotite with AM. In addition to the 20 μm mapping analysis on all samples, a Bright Phase Search (BPS) followed by 5 μm mapping was performed on thin sections FB-B, FB-C, FB-E, FB-I, FB-J, TR<8 mm, and TR1/8 mm. This was done to get an even higher chemical resolution on pyrite and pyrrhotite grains. BPS thresholding was done to reduce time consumption, since common rock forming minerals were left out of the high resolution analysis. The BPS range and brightness and contrast settings were adjusted to make sure all pyrite and pyrrhotite grains were included in the analysis. Phases with more or less similar atomic densities would also be included.

Three strategies were tested during re-processing. Discrimination based on,

1. element ratio Fe/S above or below 1.2, respectively pyrrhotite or pyrite
2. Fe content above or below 58 wt%, respectively pyrrhotite or pyrite
3. Fe content above 58 wt% or below 54%, respectively pyrrhotite or pyrite

Discrimination based on Fe/S element ratio was suggested by Postdoc. Ben Snook during the pre-project work, and can thus be regarded as a personal comment from him. The two other strategies focusing on Fe content were created in the current study. These are developed based on the chemistry in unclassified or misclassified pixels, and how the strategy with Fe/S-ratio performed.

The purpose of this test is to establish a mineral recipe that in the best way quantifies and separates between pyrite and pyrrhotite. A collection of mineral grains with seemingly clean pyrite and pyrrhotite, without inclusions of each other, was identified with microscope and BSE imaging. Each discrimination technique was evaluated on how correct these grains were classified.

Chapter 4

Results

The first two parts of this chapter present results from the investigations on the Follo Line and Trois Rivières aggregates. Results from analyses on bulk powder samples are presented first, comprising LECO for total sulfur, X-Ray Fluorescence (XRF), X-Ray Diffraction (XRD), and Differential Thermal Analysis (DTA). Furthermore, stub- and thin section investigations by Optical Microscopy (OM), Electron Probe Micro Analysis (EPMA) and Automated Mineralogy (AM) are presented. Petrological classification based on XRD and AM bulk analyses comes in the end of each part. The third and last part of the chapter presents results from the testing of three mineral recipes for best possible discrimination between pyrrhotite and pyrite with AM mapping.

4.1 Characterisation of Follo Line aggregates

4.1.1 LECO for total sulfur content

Results from total sulfur (S) analysis with LECO on the Follo Line samples are presented in Table 4.1. If pyrrhotite is indicated in FB-A1 by DTA (Chapter 4.1.4), this sample will not meet the requirements stated in NS-EN12620 (2006). Indications of pyrrhotite will lower the total sulfur limit from 1 wt% to 0,1 wt%, in practise 0,144 wt%. The other samples have acceptable concentrations of S regardless of pyrrhotite indications.

Table 4.1: Results from LECO analysis on total sulfur concentration in the Follo Line samples.

Sample	FB-A1	FB-B	FB-C	FB-D	FB-E
Total S (wt%)	0,15	0,11	0,05	0,11	0,09

4.1.2 X-Ray Fluorescence (XRF)

Relevant results for iron sulfide mineralogy from main element and trace element analyses are presented in Table 4.2. It was also performed a semi-quantitative analysis on the pressed pellets with the purpose to detect sulfur concentration in unfused samples. Unfortunately, these analyses resulted in total elemental sums below 80% and were therefore not considered as statistically valid. Sulfur concentrations reported by main element analysis are likely to be under-represented due to sulfur escape during heating in the sample preparation process. The LOI is calculated to catch up the mass that escapes during heating, but provides no information on which phases escaped.

Table 4.2: Selected results from main- and trace element X-Ray Fluorescence (XRF) analysis on the Follo Line samples. Values shown in the table are calculated from oxides reported from the XRF apparatus with conversion factors: S = 0.400459, Fe = 0,699433, Ni = 0,785845, Cu = 0,798865. The SO_3 detection limit for main element XRF analysis was 22 ppm.

	LOI 1000°C	S	Fe	Ni		Cu	
me = main element tr = trace element	me	me	me	me	tr	me	tr
	wt%	wt%	wt%	wt%	wt%	wt%	wt%
FB-A1	1,200	0,003	3,441	0,000	0,001	0,002	0,003
FB-B	1,154	0,002	3,373	0,000	0,001	0,001	0,001
FB-C	0,647	0,001	3,487	0,000	0,001	0,000	0,001
FB-D	0,700	0,004	5,676	0,002	0,002	0,001	0,002
FB-E	0,648	0,002	3,105	0,000	0,001	0,002	0,002

4.1.3 X-Ray Diffraction (XRD)

Bulk mineralogy from XRD analysis on the Follo Line samples is illustrated in Figure 4.1 below. The results show that all samples consist of more than 80% quartz, plagioclase and K-feldspar. According to XRD analysis, pyrrhotite seem more prominent than pyrite in all samples except FB-B, where indications of neither were present.

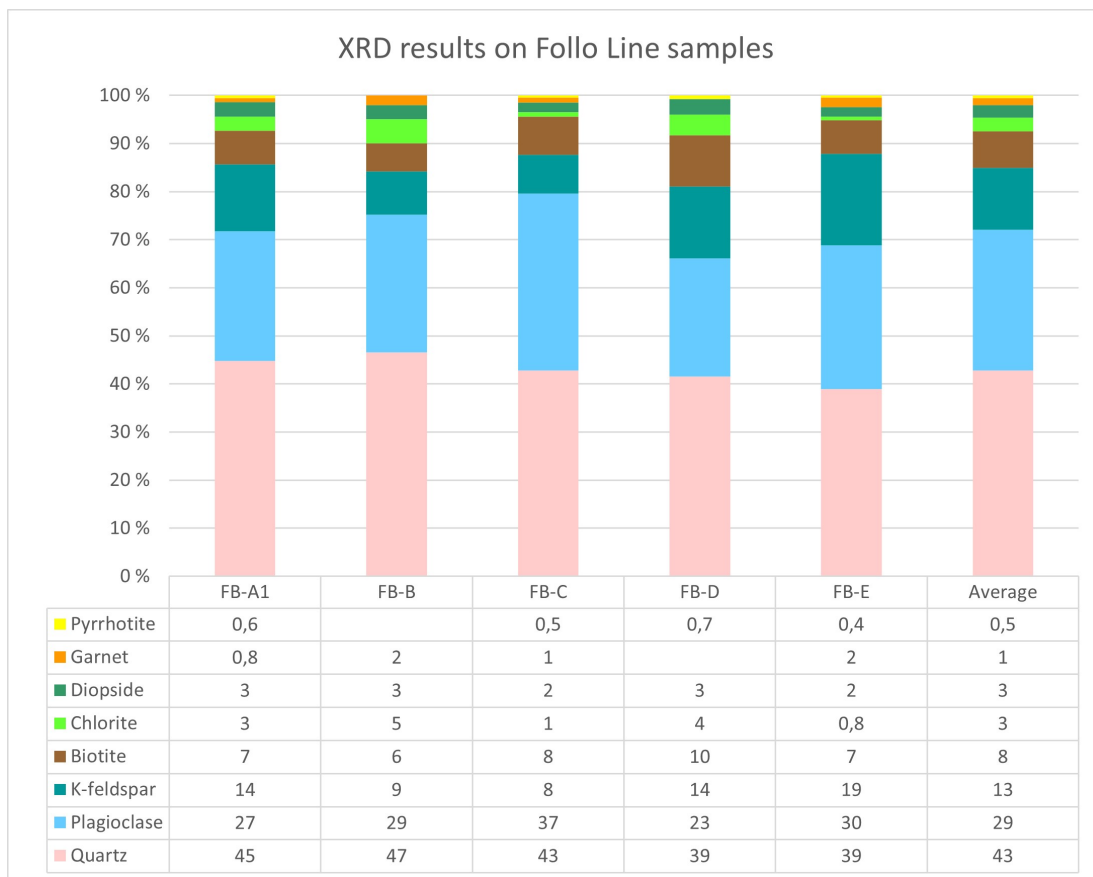


Figure 4.1: Results from X-Ray Diffraction (XRD) analysis on bulk mineralogy in Follo Line samples, FB-A1, FB-B, FB-C, FB-D and FB-E. Mineral quantities less than 1% are uncertain, but are included due to some characteristic peaks indicating that these minerals are present at some extent.

4.1.4 Differential Thermal Analysis (DTA)

DTA on the Follo Line material indicates that pyrrhotite and pyrite are present in all samples. Analyses from unpublished work by Postdoc. Ben Snook and Associate Professor Kurt Aasly in 2019 on the same samples are also presented here for comparison. These results indicate pyrrhotite in all samples as well, but no pyrite in FB-B and FB-C. Results from the current study and the unpublished work by Aasly and Snook are compiled in Table 4.3. Since pyrrhotite is indicated by DTA in FB-A1, and the total sulfur by LECO exceeds the lowered limit value on 0,1 wt%, this sample would fail acceptance for use in concrete according NS-EN12620 (2006).

Table 4.3: Compilation of Differential Thermal Analysis (DTA) results from unpublished work in 2019 by Kurt Aasly and Ben Snook, and the current MSc. study from 2020. The sulfide peaks represent the temperatures of primary and secondary peaks in the iron sulfide region on the DTA curve.

Year of analysis	2019 (Pre-project)			2020 (MSc. study)		
	Indications	Sulfide peaks (°C)		Indications	Sulfide peaks (°C)	
		1.	2.		1.	2.
FB-A1	Po + Py	470	435	Po + Py	465	420
FB-B	Po	474	–	Po + Py	470	–
FB-C	Po	475	–	Po + Py	465	–
FB-D	Po + Py	477	451	Po + Py	465	–
FB-E	Po + Py	475	–	Po + Py	470	–

Output diagrams from analyses in the current study are shown in Figure 4.3. Broad peaks within the typical oxidation ranges of pyrrhotite and pyrite makes it difficult to exclude one or the other. The primary sulfide peak in all samples falls between the ranges of typical pyrite and pyrrhotite oxidation, respectively 430-450°C and 480-520°C. The different peak magnitudes within the iron sulfide range show the sudden temperature increases, and gives an impression on the extent of oxidation in each sample. FB-A1 experienced the greatest oxidation while FB-C barely experienced any oxidation in the iron sulfide range. All samples exhibit characteristic endothermal peaks at 573°C, proving the presence of quartz and thermometric stability in the apparatus.

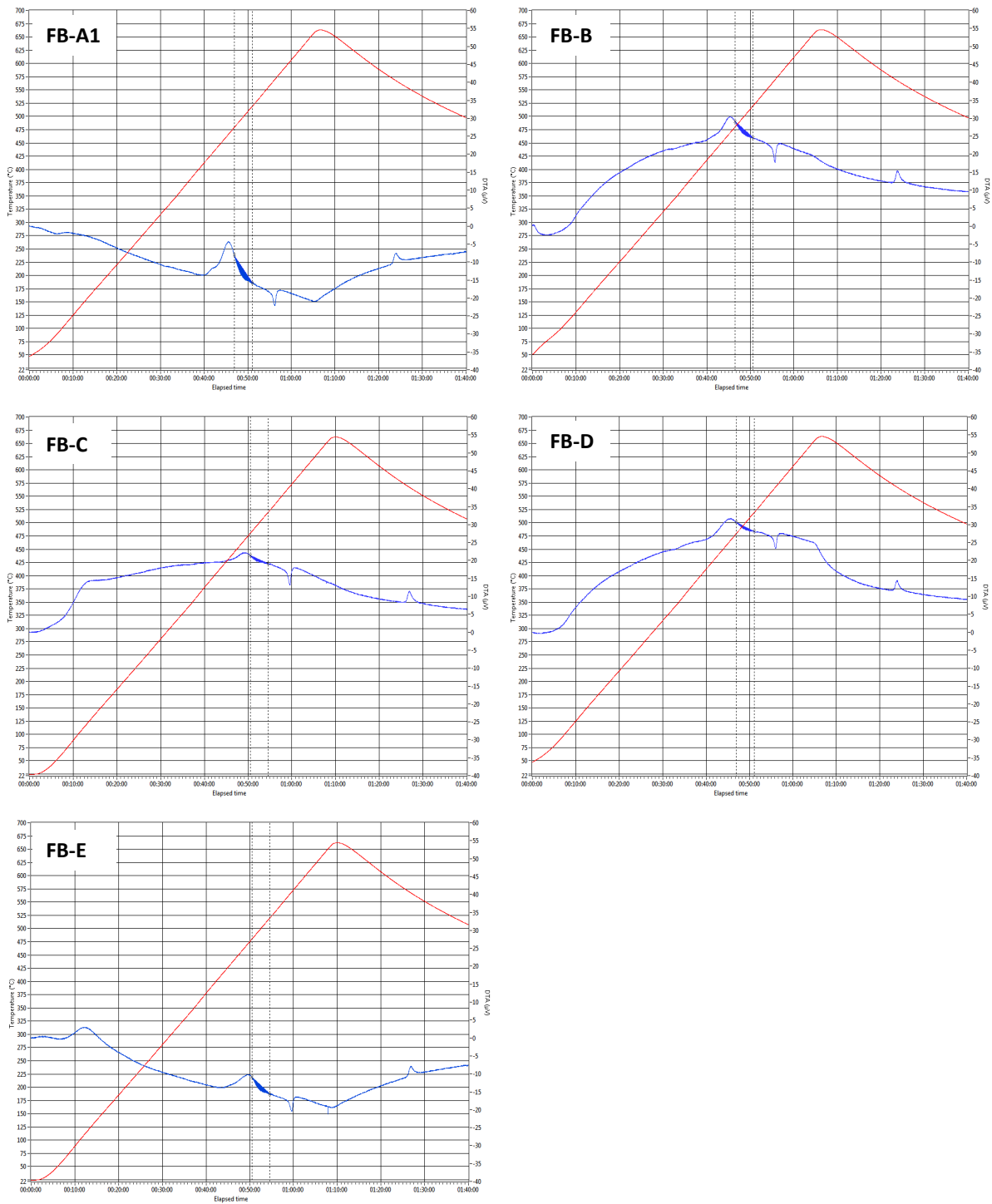


Figure 4.2: DTA diagrams from analyses on the Folio Line samples. Stippled lines and blue-filled areas represent the range of characteristic pyrrhotite oxidation at 480-520°C. Although the magnitudes vary, all samples show typical iron oxidation peaks, with the primary peak between the typical ranges of pyrite and pyrrhotite oxidation, respectively 430-450°C and 480-520°C.

4.1.5 Optical microscopy investigations

Stub samples (FB-A1, FB-B, FB-C, FB-D, FB-E)

All stub samples from Follo Line have less than 1% sulfides, with pyrite as the most common sulfide, while pyrrhotite and chalcopyrite barely occur. The sulfides appear well disseminated in all samples, and tend to occur associated with each other, as shown in Figure 4.3, A). The largest pyrrhotite appearance is 3-4 grains with size up to 200 μm in FB-B. Pyrrhotite is barely appearing in FB-D and FB-E, as 20-50 μm inclusions within pyrite on two occasions. Other opaque minerals observed comprise ilmenite and iron oxides. Table 4.4 below summarises the sulfides observed in all samples. Further observations on grain size and textures can be found in Appendix B.

Table 4.4: Sulfides in Follo Line stub samples detected with reflected light microscopy. Mineral abbreviations after Whitney and Evans (2010)

Sample	FB-A1	FB-B	FB-C	FB-D	FB-E
Sulfides	Py, Ccp, Sp	Py, Po, Ccp	Py	Py, Po	Py, Po, Ccp

Thin sections (FB-B2, FB-C2, FB-E2, FB-F, FB-G, FB-H, FB-I, FB-J, FB-K)

Common rock forming minerals quartz, plagioclase and K-feldspar dominates the Follo Line thin sections. Biotite and muscovite are also present in all sections, but to a smaller extent. All sections exhibit more or less lepidoblastic texture, where predominantly biotite appear irregularly banded and aligned next to quartz, plagioclase and K-feldspar in various thickness. Feldspars are often extensively sericiticised. Fine-grained mica appears within or along boundaries of weathered feldspars. Biotite is mainly observed in two distinctly different ways; bright brown colored in ppl with distinct pleochroism and cleavage or dark brown colored without the characteristic pleochroism and cleavage.

All Follo Line thin sections have small portions of pyrite, displayed in Table 4.5, appearing as disseminated vein fills, anhedral clusters or euhedral grains. The pyrite varies from appearing as fully intact to extensively weathered and perforated, shown in Figure 4.4, A). Chalcopyrite is present in almost all sections, but to a significantly lesser extent than pyrite. Pyrrhotite is only present in three of the total nine sections, and its largest appearance is a few 150 μm grains in FB-J, seen in Figure 4.4, E). The other pyrrhotite appearances are two 50 μm grains within silicate minerals in FB-C2 (Figure 4.4, C) and FB-I. Further observations on sulfide mineralogy and identification of translucent minerals can be seen in Appendix B.

Table 4.5: Sulfides in Follo Line thin sections detected with reflected light microscopy. Mineral abbreviations after Whitney and Evans (2010)

Sample	FB-B(2)	FB-C(2)	FB-E(2)	FB-F	FB-G	FB-H	FB-I	FB-J	FB-K
Sulfides	Py, Ccp	Py, Po, Ccp	Py, Ccp	Py, Ccp	Py, Ccp	Py, Ccp	Py, Ccp, Po	Py, Po, Ccp	Py, Ccp

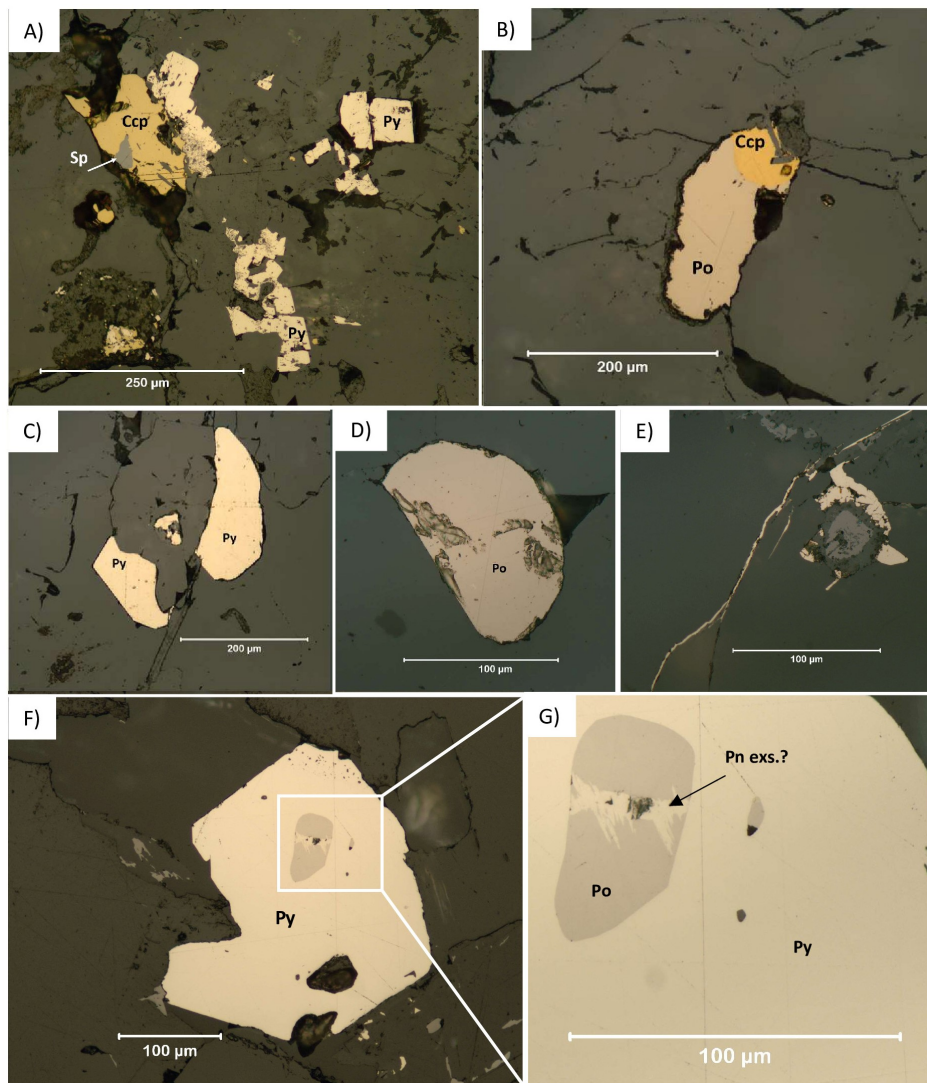


Figure 4.3: Sulfide phases in Follo Line stub samples observed under reflected light. Mineral abbreviations after Whitney and Evans (2010). **A):** Weathered pyrite cubes next to chalcopyrite and sphalerite in sample FB-A1. **B):** Subhedral, probably hexagonal, pyrrhotite grain with chalcopyrite intergrowth in sample FB-B. Weathered grain boundaries, but internal is intact. **C):** Pyrite in sample FB-B. **D):** Pyrrhotite grain in FB-B. **E):** Sulfide fill in cracks in FB-C. Most likely pyrite. **F):** Subhedral pyrite with pyrrhotite inclusion in sample FB-D. **G):** Close up on pyrrhotite inclusion with characteristic flame-like exsolutions. Possibly pentlandite.

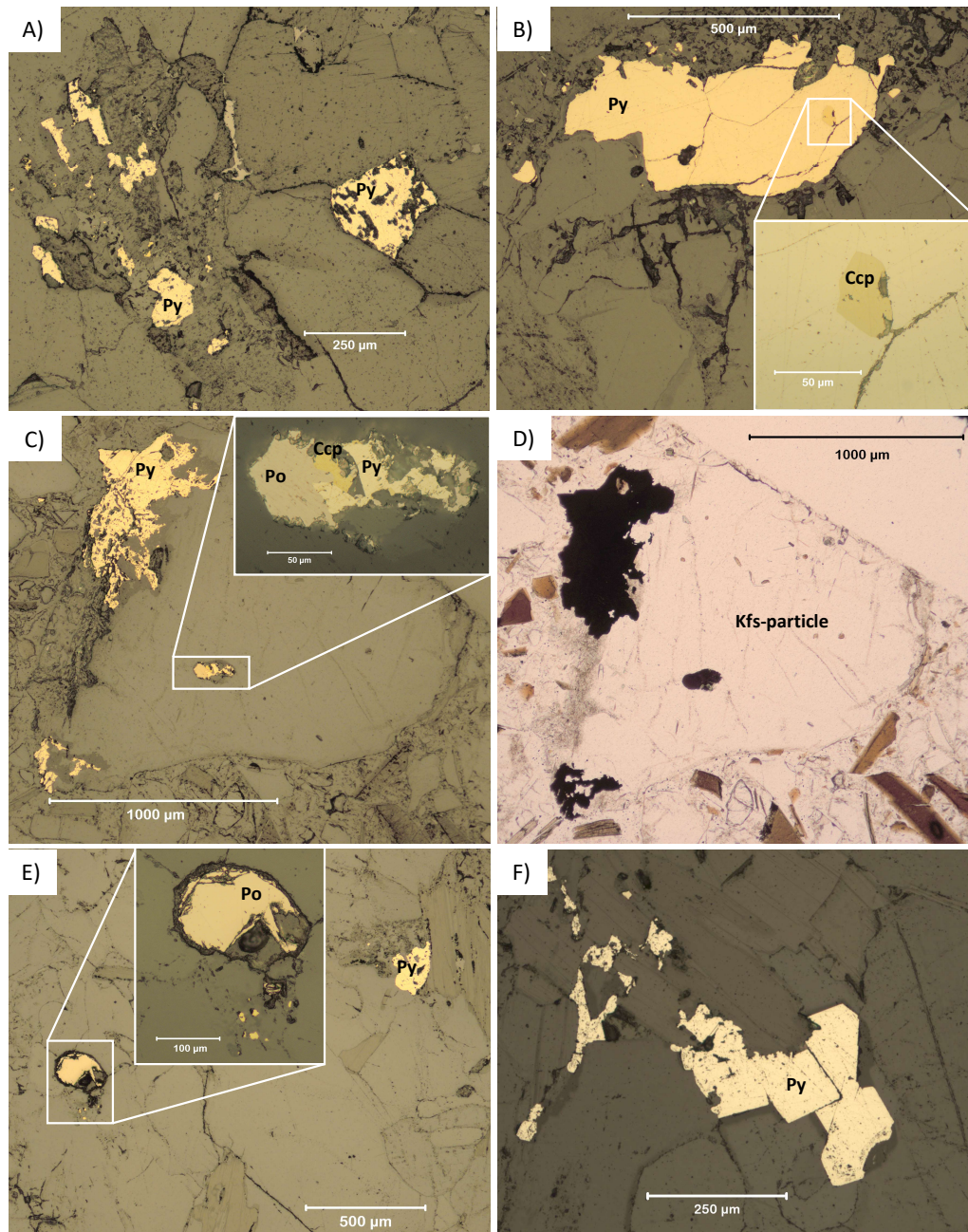


Figure 4.4: Sulfide phases in Follo Line thin sections observed under reflected light. Mineral abbreviations after Whitney and Evans (2010). **A)** Cluster with Py and highly weathered subhedral Py grain in FB-H. This is a common appearance of Py in all Follo Line thin sections, with various amounts of Py. **B)** Anhedra Py grain with Ccp inclusion in FB-B-1. This inclusion was initially misidentified as Po during microscopy, but was corrected with Automated Mineralogy (AM) mapping. **C)** and **D)**: Py aggregate attached to a Kfs-particle respectively under reflected light and transmitting light microscopy in FB-C2. Reflected light microscopy is crucial to discriminate between the opaque minerals. An assemblage of Po, Ccp and Py appear as inclusion within the Kfs-particle. **E)** Po and Py grains in FB-J. Notice the smooth and matte appearance of Po, compared to the brighter and glossier Py. **F)** Clusters of anhedra and euhedral Py in FB-I.

4.1.6 Electron Probe Micro Analysis (EPMA)

Estimations of average composition based on point analysis on the iron sulfides in FB-J and FB-C thin sections are shown in Table 4.6. The average pyrite and chalcopyrite compositions are close to those suggested by ideal mineral formulas. Average pyrrhotite compositions are close to the iron-deficient pyrrhotite end member, 4C pyrrhotite. Pyrrhotite analyses show the highest average sum and the lowest standard deviation for Fe- and S measurements.

Table 4.6: Electron Probe Micro Analysis (EPMA) results for Follo Line sulfides from FB-J and FB-C thin-sections. Blanks are below detection limit. Ideal formula represents ideal mineral formula compositions, obtained from the online mineralogy database, Webmineral.com, by Barthelmy (2021). Ideal compositional ranges of pyrrhotite, as described in the literature, were presented in Table 2.2, obtained from Multani and Waters (2018).

Mineral (no. analyses)		As	Fe	Mo	Co	S	Cu	Ni	Zn	Total
Pyrrhotite (14)	Ideal formula		62,33			37,67				100
	Average wt%	0,07	59,59	0,06	0,13	39,61		0,16		99,62
	St. dev	0,14	0,54	0,03	0,04	0,24		0,07		0,64
	Min-max	0,00-0,33	58,40-60,21	0,00-0,09	0,07-0,19	39,31-40,12		0,00-0,24		98,16-100,31
Pyrite (14)	Ideal formula		46,55			53,45				100
	Average wt%	0,05	45,74		0,09	53,20		0,29	0,01	99,37
	St. dev	0,13	1,03		0,11	0,49		0,61	0,02	1,01
	Min-max	0,00-0,36	43,28-47,01		0,04-0,45	51,72-53,72		0,00-1,95	0,00-0,07	96,47-100,75
Chalcopyrite (6)	Ideal formula		30,43			34,94	34,63			100
	Average wt%		29,73	0,01	0,01	34,55	33,42		0,07	97,79
	St. dev		0,55	0,02	0,02	0,37	0,30		0,06	0,60
	Min-max		29,08-30,17	0,00-0,06	0-0,05	33,89-35,02	33,05-33,73		0,00-0,15	96,69-98,25

4.1.7 Automated Mineralogy (AM)

The amount of significant data and results generated by AM analyses exceed the scope of this study by far, as detailed imaging and chemical analyses on all phases in the samples were obtained. In correlation with the defined motivation of this study, focus was primarily on the iron sulfide mineralogy and in particular the detection of pyrrhotite. All data presented in the subsequent section was therefore aligned and results concentrated to answer the previously determined research goals. False color mineral maps on all Follo Line samples can be found in Appendix E.

Bulk mineralogy

According to bulk mineralogy estimations by 20 μm AM mapping, the Follo Line samples are predominantly made up of quartz, plagioclase and biotite, with varying amounts of K-feldspar and muscovite. Only small variations between the samples can be seen in the bar diagram in Figure 4.5. Note that FB-B2, -C2 and E2 are gravel-versions of the intact-rock samples FB-B, -C and -E. Table 4.7 lists the amounts of unclassified area in % on all sample surfaces, all well below the <3% target. Accessory minerals, in this case defined as minerals which on average constitute less than 1,0 wt%, are shown in Appendix C.

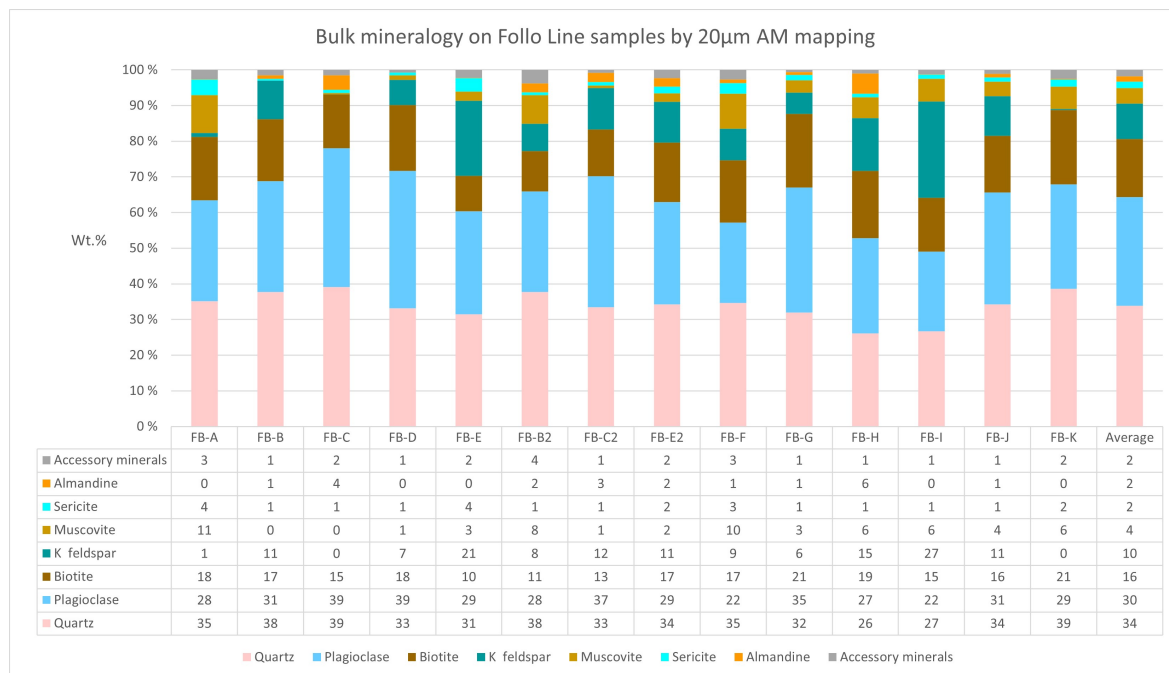


Figure 4.5: Bulk mineralogy for all Follo Line samples by 20 μm Automated Mineralogy (AM) mapping.

Table 4.7: Amount of unclassified area in % for all Follo Line samples by AM mapping.

Sample	FB-A	FB-B	FB-C	FB-D	FB-E	FB-B2	FB-C2	FB-E2	FB-F	FB-G	FB-H	FB-I	FB-J	FB-K	Average
Unclassified, % area	1,90	0,55	0,98	0,56	0,96	2,11	1,08	1,94	1,66	1,15	0,92	0,80	0,92	2,26	1,27

Iron sulfide mineralogy

According to results from 20 μm AM mapping, pyrite, pyrrhotite and chalcopyrite occur in all Follo Line samples except for FB-C where only pyrite is reported. Pyrite is the most common iron sulfide in all samples. The greatest pyrrhotite appearances are 0,022 wt% in

FB-B and 0,015 wt% in FB-J, while all other samples contain less than 0,010 wt% pyrrhotite. Average pyrrhotite content in all 14 samples is 0,006 wt%. However, the validity of low-content pyrrhotite detection must be evaluated with respect to how well pyrrhotite have been detected and discriminated from pyrite.

Table 4.8 below shows wt% and average chemistry for the iron sulfides in all Follo Line samples. Average chemistry provides statistics on the average elemental composition of each mineral classification. When compared to ideal mineral formulas, these values could indicate the accuracy of the mineral classification and eventual trends in the collection of EDS spectra. Pyrrhotite (Po) rand effect was also classified by AM as pixels on weathered pyrrhotite grain boundaries, typically containing Fe >65 wt% and S <30 wt%. FB-B contained 0,005 wt% of this Po rand effect, while all the other samples had $\leq 0,001$ wt%.

Table 4.8: Wt% and average chemistry of iron sulfides in the Follo Line samples gathered by 20 μ m Automated Mineralogy mapping.

Sample	Mineral	Wt%	Average chemistry			Sample	Mineral	Wt%	Average chemistry		
			Fe	S	Cu				Fe	S	Cu
FB-A1	Pyrite	0,309	50,05	49,95		FB-F	Pyrite	0,451	49,64	50,36	
	Pyrrhotite	0,006	61,06	38,94			Pyrrhotite	0,007	60,94	39,06	
	Chalcopyrite	0,016	35,40	31,48	33,12		Chalcopyrite	0,022	36,08	30,98	32,94
FB-B	Pyrite	0,102	50,16	49,84		FB-G	Pyrite	0,062	49,59	50,41	
	Pyrrhotite	0,022	62,77	37,23			Pyrrhotite	0,001	59,63	40,37	
	Chalcopyrite	0,029	37,69	31,45	30,86		Chalcopyrite	0,005	35,16	31,38	33,46
FB-C	Pyrite	0,001	46,26	53,73							
FB-D	Pyrite	0,053	49,8	50,2		FB-H	Pyrite	0,126	50,14	49,86	
	Pyrrhotite	0,001	61,56	38,44			Pyrrhotite	0,003	61,23	38,77	
	Chalcopyrite	0,003	36,43	30,51	33,06		Chalcopyrite	0,004	35,5	31,67	32,83
FB-E	Pyrite	0,168	50,42	49,58		FB-I	Pyrite	0,090	50,04	49,96	
	Pyrrhotite	0,006	61,73	38,27			Pyrrhotite	0,004	61,47	38,53	
	Chalcopyrite	0,005	35,41	32,06	32,53		Chalcopyrite	0,012	35,55	31,17	33,28
FB-B2	Pyrite	0,258	49,6	50,4		FB-J	Pyrite	0,149	49,66	50,34	
	Pyrrhotite	0,005	62,12	37,88			Pyrrhotite	0,015	62,66	37,34	
	Chalcopyrite	0,004	35,51	31,81	32,68		Chalcopyrite	0,003	36,08	31,7	32,22
FB-C2	Pyrite	0,105	49,78	50,22		FB-K	Pyrite	0,424	49,55	50,45	
	Pyrrhotite	0,004	61,86	38,14			Pyrrhotite	0,005	60,76	39,24	
	Chalcopyrite	0,004	35,16	31,47	33,37		Chalcopyrite	0,004	35,18	31,22	33,59
FB-E2	Pyrite	0,112	49,85	50,15		Average	Pyrite	0,172	49,61	50,39	
	Pyrrhotite	0,002	62,19	37,81			Pyrrhotite	0,006	61,54	38,46	
	Chalcopyrite	0,005	36,05	30,69	33,26		Chalcopyrite	0,009	35,78	31,35	32,86

As seen below in Figure 4.6, 20 μm AM mapping discriminates well between iron sulfides in the FB-D stub sample. Brightness and contrast settings applied for the analyses in Figure 4.6 makes discrimination based on BSE imaging difficult. Pyrrhotite, pyrite and chalcopyrite are all displaying the same, bright BSE tone.

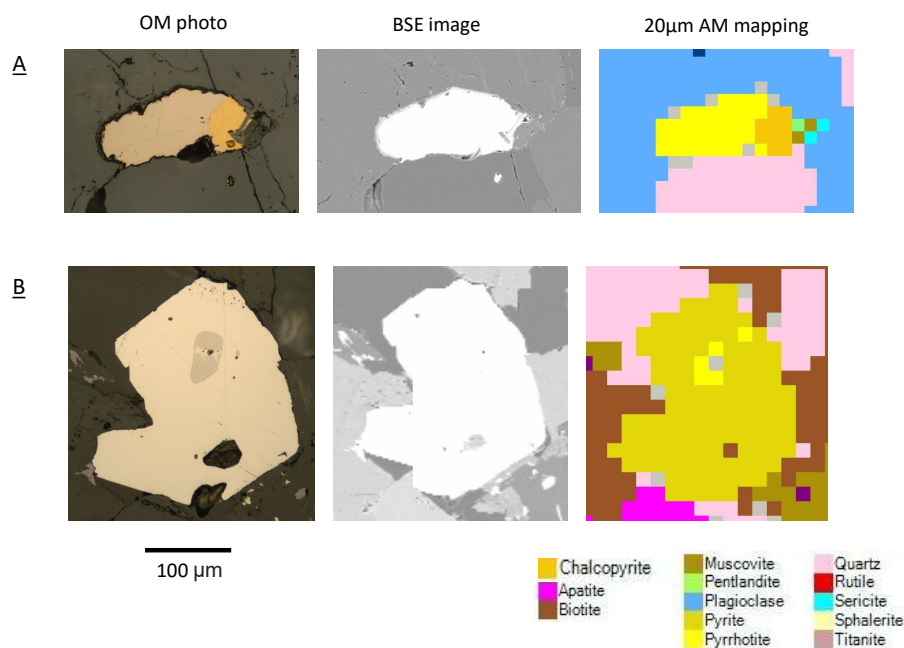


Figure 4.6: **A:** From left: Pyrrhotite and chalcopyrite in FB-B stub sample under reflected light microscope, back-scatter imaging (BSE) and 20 μm Automated Mineralogy mapping. **B:** From left: Pyrite with pyrrhotite inclusion in FB-D under reflected light microscope, back-scatter imaging (BSE) and 20 μm Automated Mineralogy mapping.

Stub samples and thin sections from the Follo Line material were analysed on different occasions, with different adjustments in brightness and contrast on the SEM. The analysis on stub samples had poor brightness/contrast settings with respect to iron sulfide differentiation (Figure 4.6), while the thin sections analysis (Figure 4.7) had much better settings for this purpose. Examples from pyrrhotite/pyrite discrimination in Chapter 4.3 stem entirely from thin section analysis, carried out with brightness/contrast settings that enabled discrimination based on BSE contrast.

Figure 4.7 shows a minor assemblage of pyrrhotite, pyrite and chalcopyrite from FB-C thin section, analysed with 5 μm and 20 μm AM mapping. This sample was analysed with brightness/contrast settings enabling pyrrhotite-pyrite discrimination based on BSE contrast. Pyrrhotite and chalcopyrite have significantly brighter grey shades than pyrite.

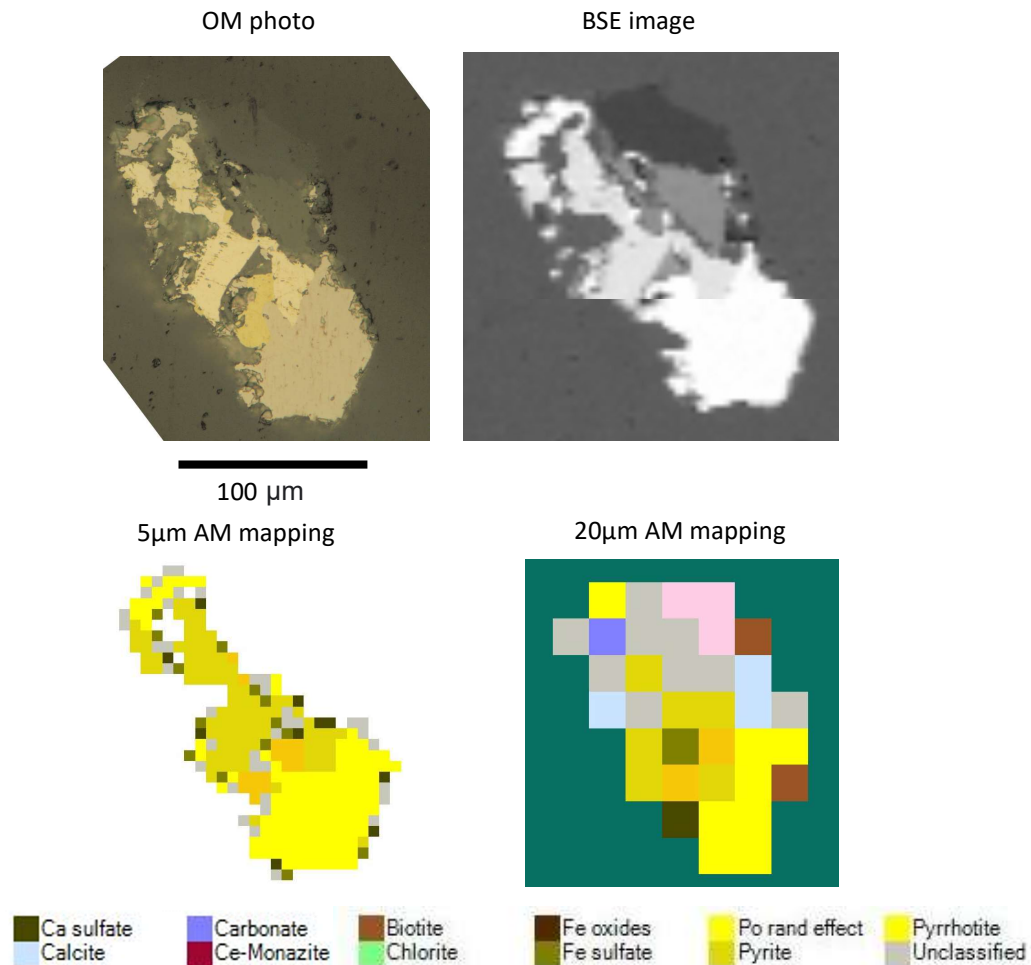


Figure 4.7: Assemblage of pyrrhotite, chalcopyrite and pyrite in FB-C thin section under reflected light microscope, Back-Scatter Electron (BSE) imaging, and Bright Phase Search (BPS) + 5 μm and 20 μm Automated Mineralogy (AM) mapping. The horizontal lag-line in the BSE image is due to an error with the automatic image stitching in the AM software.

Pyrrhotite mineral associations

Mineral associations are calculated by the *Mineralogic* software as percentage of minerals most frequently appearing next to the mineral of interest, in this case pyrrhotite. Figure 4.8 shows that pyrrhotite in Follo Line samples is often associated with pyrite. However, considering the low amounts of pyrrhotite in most of the Follo Line samples, association statistics may be influenced by wrong classifications such as misclassified pyrrhotite pixels within pyrite.

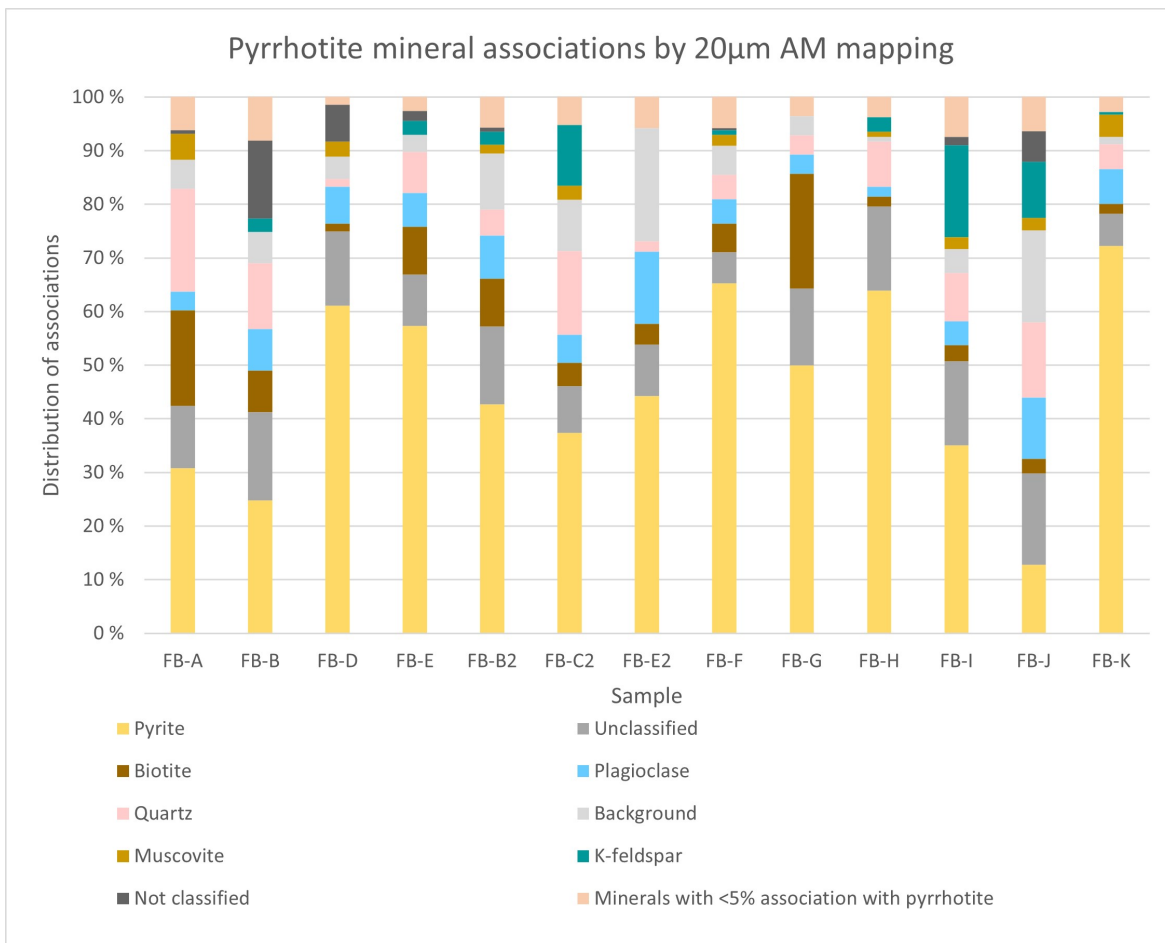


Figure 4.8: Pyrrhotite mineral associations in Follo Line samples acquired with 20 μm Automated Mineralogy mapping.

4.1.8 Petrological classification

Petrological classification of the Follo Line material is carried out with the classification system developed by the International Union of Geological Sciences (IUGS) (Streckeisen, 1976). According to Figure 4.9, the composition varies from granitic to tonalitic. The majority of samples are within the granodioritic field. Bulk mineralogy of 19 samples by XRD and AM were used for the classification.

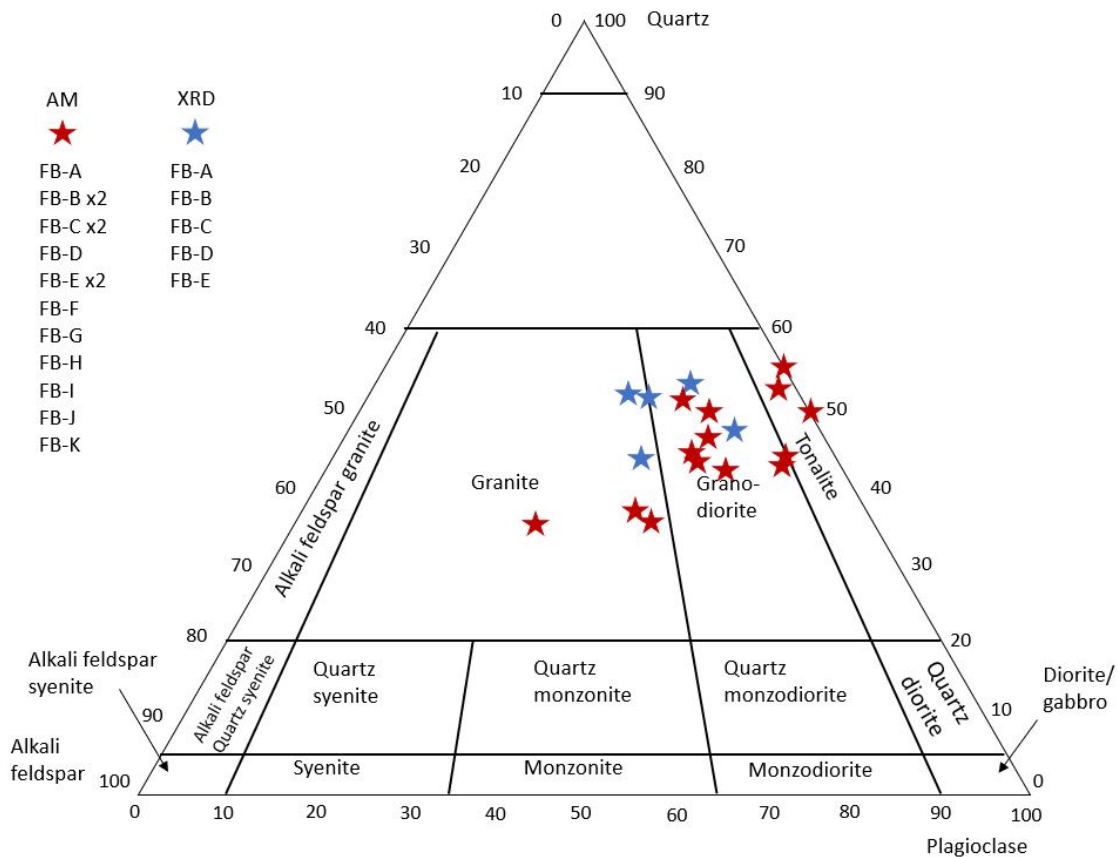


Figure 4.9: The composition of the Follo Line aggregates is classified as granodioritic with granitic-tonalitic variations according the classification system by the International Union of Geological Sciences (IUGS) (Streckeisen, 1976), based on X-Ray Diffraction (XRD) and 20 μm Automated Mineralogy (AM) bulk analyses. Plagioclase was not differentiated by XRD or AM, which means that the Alkali feldspar component is entirely made up of K-feldspar and no Albite.

4.2 Characterisation of Trois-Rivières aggregates

4.2.1 LECO for total sulfur content

Results from total S analysis with LECO on the Trois-Rivières samples are presented in Table 4.9. All fractions exceed the 0,1 wt% sulfur limit in NS-EN12620 (2006) if pyrrhotite is indicated by DTA (Chapter 4.2.4). TR<8mm exceeds the 1 wt% sulfur limit value and is rejected regardless indications of pyrrhotite.

Table 4.9: Results from LECO analysis on total sulfur content in Trois-Rivières samples.

Sample	TR<8mm	TR1/8mm	TR>8mm
Total S (wt%)	1,14	0,96	0,84

4.2.2 X-Ray Fluorescence (XRF)

Relevant results for iron sulfide mineralogy from main element and trace element XRF analyses are presented in Table 4.10. Sample TR>8mm show the highest sulfur (S) concentration with 0,217 wt%. Note that sulfur concentrations reported by main element analysis are likely to be under-represented due to sulfur escape during fusion in the preparation process.

Table 4.10: Selected results from main- and trace element X-Ray Fluorescence (XRF) analysis on the Trois-Rivières material. Values shown in the table are calculated from oxides reported from the XRF apparatus with conversion factors: S = 0.400459, Fe = 0,699433, Ni = 0,785845, Cu = 0,798865. SO_3 detection limit for the XRF analysis was 22 ppm.

	LOI 1000°C	S	Fe	Ni		Cu	
me = main element tr = trace element	me	me	me	me	tr	me	tr
	wt%	wt%	wt%	wt%	wt%	wt%	wt%
TR<8mm	2,265	0,050	6,507	0,084	0,071	0,036	0,036
TR1/8mm	3,218	0,122	6,349	0,060	0,052	0,032	0,032
TR>8mm	2,571	0,217	4,919	0,056	0,046	0,028	0,027

4.2.3 X-Ray Diffraction (XRD)

Bulk mineralogy estimations from XRD on the Trois-Rivières samples are illustrated in Figure 4.10 below. Plagioclase makes up approximately 50% in each of the samples. Enstatite, quartz, chlorite and diopside are present with $\geq 5\%$ in all samples. According to the XRD analysis, indications of pyrite are more prominent than pyrrhotite in all samples.

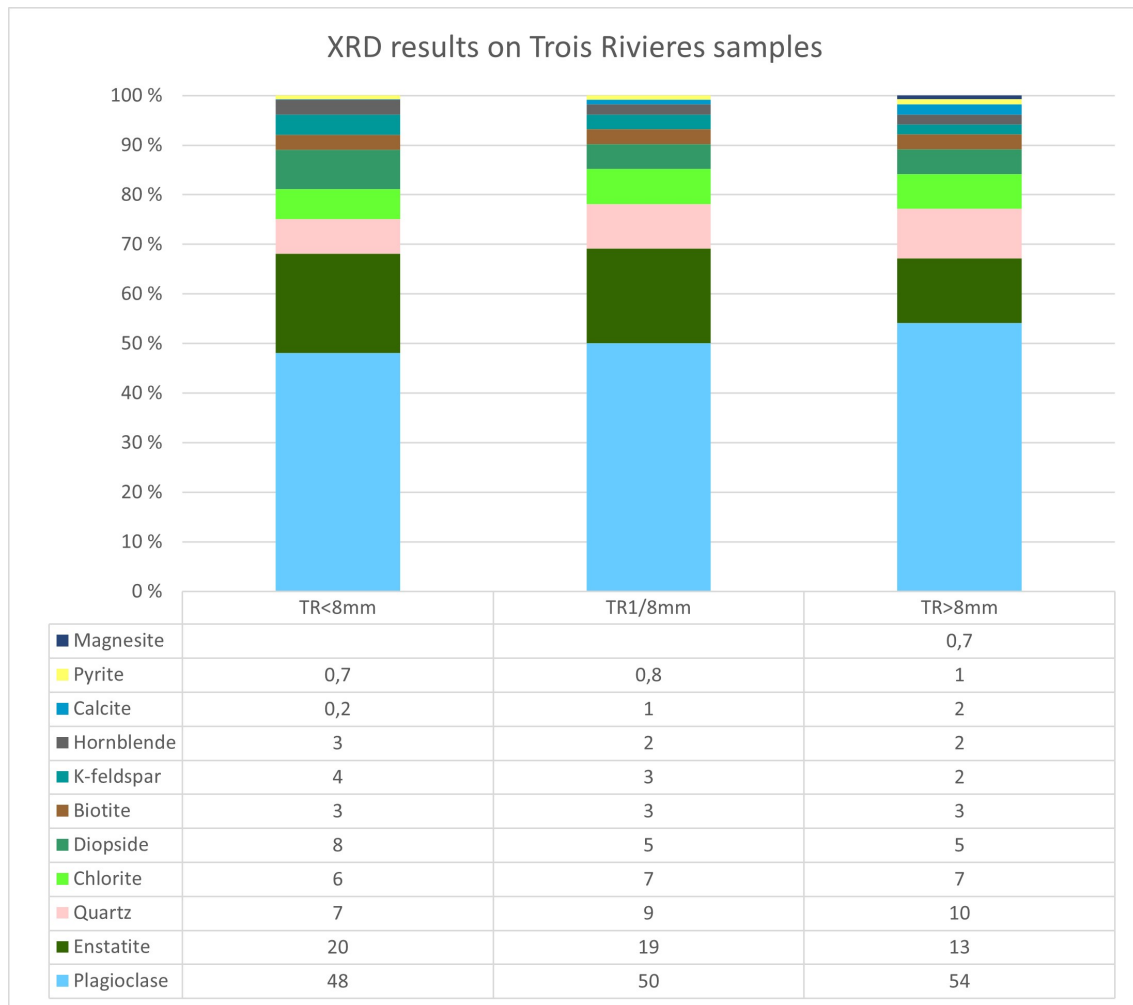


Figure 4.10: Results from XRD analysis on bulk mineralogy in the Trois-Rivières samples, TR <8mm, TR 1/8mm and TR >8mm. Mineral quantities less than 1% are uncertain, but are included due to some characteristic peaks which indicate that these minerals are present at some extent.

4.2.4 Differential Thermal Analysis (DTA)

The DTA analyses on the Trois-Rivières material from this study, and from unpublished work by Postdoctoral Ben Snook and Associate Professor Kurt Aasly in 2019 on the same material, are reported in Table 4.11. Pyrrhotite is indicated by both analyses in all three fractions. The primary sulfide peaks in all analyses on this material falls within the pyrrhotite oxidation range, 480-520°C. The primary and secondary peak registrations occur in general on higher temperatures in the current study compared to the pre-project results from 2019. According NS-EN12620 (2006), all samples would have been rejected for use in concrete due to indications of pyrrhotite and total sulfur contents exceeding 0,1 wt% (Chapter 4.2.1).

Table 4.11: Compilation of the DTA results from unpublished work by Kurt Aasly and Ben Snook in 2019, and the current MSc. study from 2020. The sulfide peaks represent the temperatures of primary and secondary peaks in the iron sulfide region on the DTA curve. ” - ” is not analysed.

Year of analysis	2019 (Pre-project)			2020 (MSc. study)		
	Indicated sulfides	Sulfide peaks (*C)		Indicated sulfides	Sulfide peaks (C*)	
Sample material		1.	2.		1.	2.
TR-0,045/1mm	Po (or sulfides)	489	445	-	-	-
TR-<8mm	-	-	-	Po + Py	510	445
TR-1/8mm	Po (or sulfides)	484	445	Po + Py	510	455
TR->8mm	Po (or sulfides)	497	433	Po + Py	515	465

The interpretations in Table 4.11 are based on the DTA diagrams in Figure 4.11 on the next page. Note that the middle fraction, TR1/8mm, was analysed twice since the DTA apparatus needs two samples per run. The DTA curves from all Trois-Rivières samples show way taller and broader peaks than the curves from the Follo Line material did. This implies that all Trois-Rivières samples experienced a significantly greater extent of iron sulfide oxidation. None of the samples show the characteristic quartz peak at 573 °C.

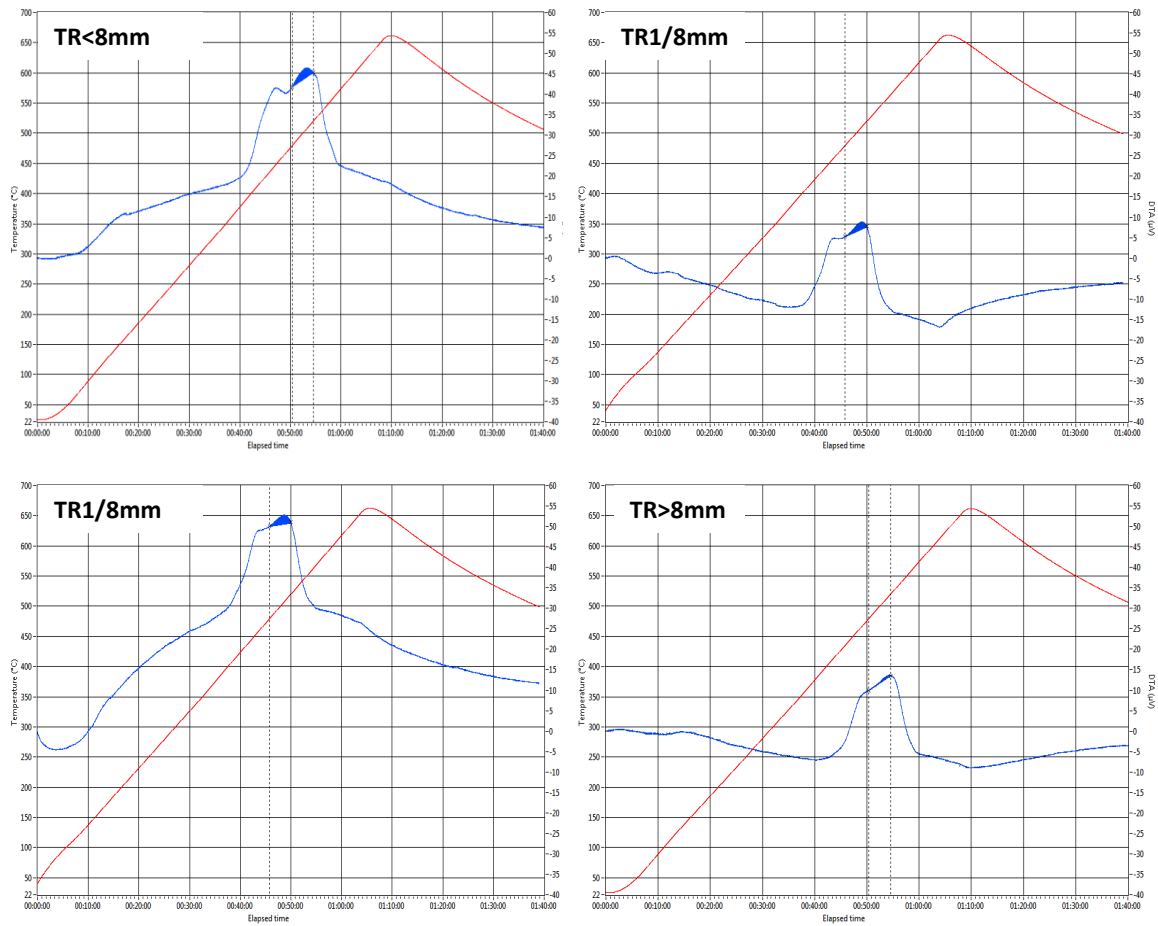


Figure 4.11: DTA diagrams from analyses on the Trois-Rivières samples. The stippled lines and blue-filled areas represent the range of characteristic pyrrhotite oxidation at 480-520°C. All samples exhibit main sulfide peaks within the range of pyrrhotite oxidation.

4.2.5 Optical microscopy investigations

Stub samples (TR0,045/1mm, TR1/8mm, TR>8mm)

The three Trois-Rivières stub samples all contain various amounts of pyrrhotite, pyrite, pentlandite and chalcopyrite. Overall far more sulfides than the Follo Line samples. Pentlandite occurs mainly as exsolution in pyrrhotite. In the smallest fraction, TR0,045/1mm, about 5-10% of particles contain iron sulfides. This sample exhibits the highest amount of liberated sulfide grains among the Trois-Rivières samples. Free pyrrhotite grains are heavily weathered, as shown in Figure 4.12. The grey phase occurring within weathered pyrrhotite, Figure 4.12, A), seems to replace the pyrrhotite within the grain boundaries. In Figure 4.12, B), a brighter grey phase can be seen seemingly "leaching out" from a heavily weathered pyrrhotite grain. This feature is seen around several liberated, extensively weathered pyrrhotite grains in TR0,045/1mm. These phases are probably iron oxide/hydroxide oxidation products of pyrrhotite. Thin bands of another grey phase, surrounds pyrite with coronas on several occasions, e.g. Figure 4.12, D).

The two samples with larger fractions, TR1/8mm and TR>8mm, contain a higher share of sulfide bearing particles, but far less sulfides are liberated. Pyrrhotite is weathered also when appearing inside particles, however less than in TR0,045/1mm. Pyrite is the least weathered iron sulfide, while chalcopyrite overall appears to be more intact than pyrrhotite. Other opaque minerals observed comprise ilmenite and iron oxides. Further observations on grain size and textures in the Trois-Rivières stub samples are listed in Appendix B.

The extent and appearance of pyrrhotite weathering can be divided into two categories,

1. The greatest extent of weathering has removed continuous parts of the grain boundaries as well as the interior of the grain. This is most frequently observed among pyrrhotites in TR0,045/1mm, Figure 4.12 A) and B).
2. The less critical weathering appearance can be described as elongated "carve-outs" of the pyrrhotite internal. This is most frequently observed among pyrrhotites in TR>8mm, Figure 4.12 E) and F).

Table 4.12: Sulfides in Trois-Rivières stub samples detected with reflected light microscopy. Mineral abbreviations after Whitney and Evans (2010).

Sample	TR0,045/1mm	TR1/8mm	TR>8mm
Sulfides	Py, Po, Ccp, Pn	Py, Po, Ccp, Pn	Po, Py, Ccp, Pn

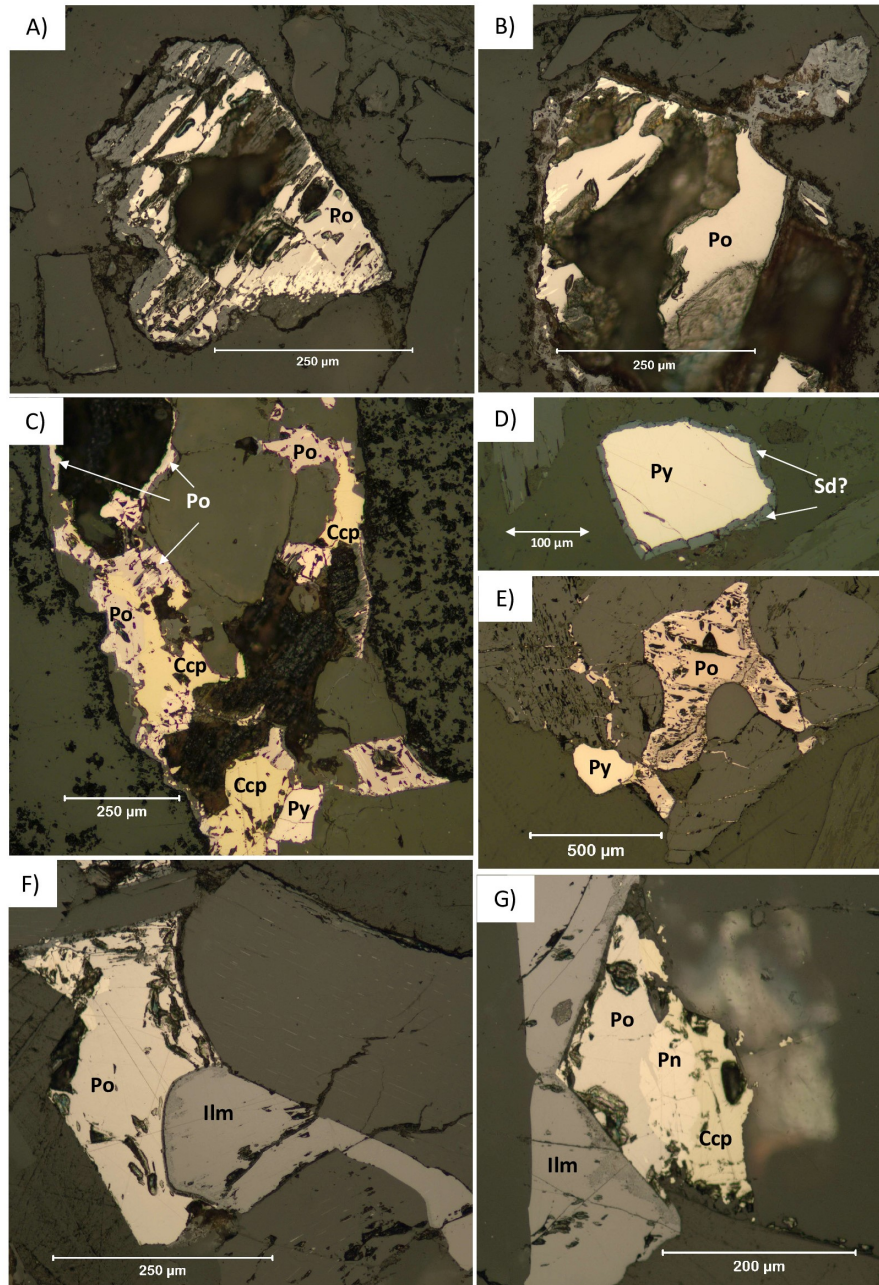


Figure 4.12: Sulfide phases in Trois-Rivières stub samples observed under reflected light. Mineral abbreviations after Whitney and Evans (2010). **A) and B):** Relatively large, liberated and heavily weathered pyrrhotite grains in TR0,045/1mm. The original crystal faces are more or less preserved in both cases. Both have characteristic exsolution patterns, probably pentlandite, near grain boundaries. The grey phase in A) is mainly enclosed within former pyrrhotite grain boundaries, while it in B) seems to "leach out" from the pyrrhotite grain. **C):** Pyrrhotite, chalcopyrite and pyrite disseminated throughout an aggregate particle in TR1/8mm. Pyrrhotite is heavily weathered, and it looks like the weathered, dark areas are results of pyrrhotite weathering. **D):** Intact pyrite in TR0,045/1mm surrounded by a grey phase corona, possibly iron carbonate. **E):** Weathered pyrrhotite next to intact pyrite in TR1/8mm. **F):** Euhedral pyrrhotite grain partly overgrown by ilmenite in TR>8mm. **G):** A sequence of pyrrhotite, pentlandite and chalcopyrite next to ilmenite in TR>8mm.

Thin sections (TR<8mm, TR1/8mm)

The Trois-Rivières thin sections are predominantly composed of plagioclase and pyroxenes, with lesser amount of biotite and quartz. Exsolution patterns are observed in many of the pyroxenes as slightly elongated dark-red patches.

Opaque phases make up a considerable share of the sections, comprising various iron sulfides, displayed in Table 4.13, ilmenite, and iron oxides. Pyrrhotite appears with anhedral grains up to 1000 μm , while pyrite is often subhedral-euhedral and more fine-grained. Pyrite flame-like exsolution textures appear within pyrrhotite, Figure 4.13: C and D, on the next page.

Pyrrhotite shows highest degree of weathering among the sulfides. Some grains are nearly intact with few carve-outs, while others appear perforated or with almost unrecognisable interior. This is well illustrated in Figure 4.13 where heavily weathered pyrrhotite contain pyrite and chalcopyrite inclusions (B), and mineralisation of a grey opaque phase, probably iron oxide/hydroxide, next to the pyrrhotite particle in A. Like observed in the stub sample, this grey phase seems to leach out from the weathered pyrrhotite. These phases are investigated further by Automated Mineralogy (AM) in Chapter 4.2.7, and discussed in Chapter 5.2.2.

Another grey phase in reflected light, is in some places surrounding pyrrhotite and pyrite with thin grey bands, e.g. Figure 4.13 C) and D). This mineral is translucent and have a bright, white color under plane-polarised light (ppl) and show high order interference colors under crossed polars (xpl). Tiny appearances (<20 μm) makes proper identification difficult, but it could be a carbonate mineral based on high interference colors.

Table 4.13: Sulfides in Trois-Rivières thin sections detected with reflected light microscopy. Mineral abbreviations after Whitney and Evans (2010).

Sample	TR<8mm	TR1/8mm
Sulfides	Po, Py, Pn, Ccp	Po, Py, Pn, Ccp

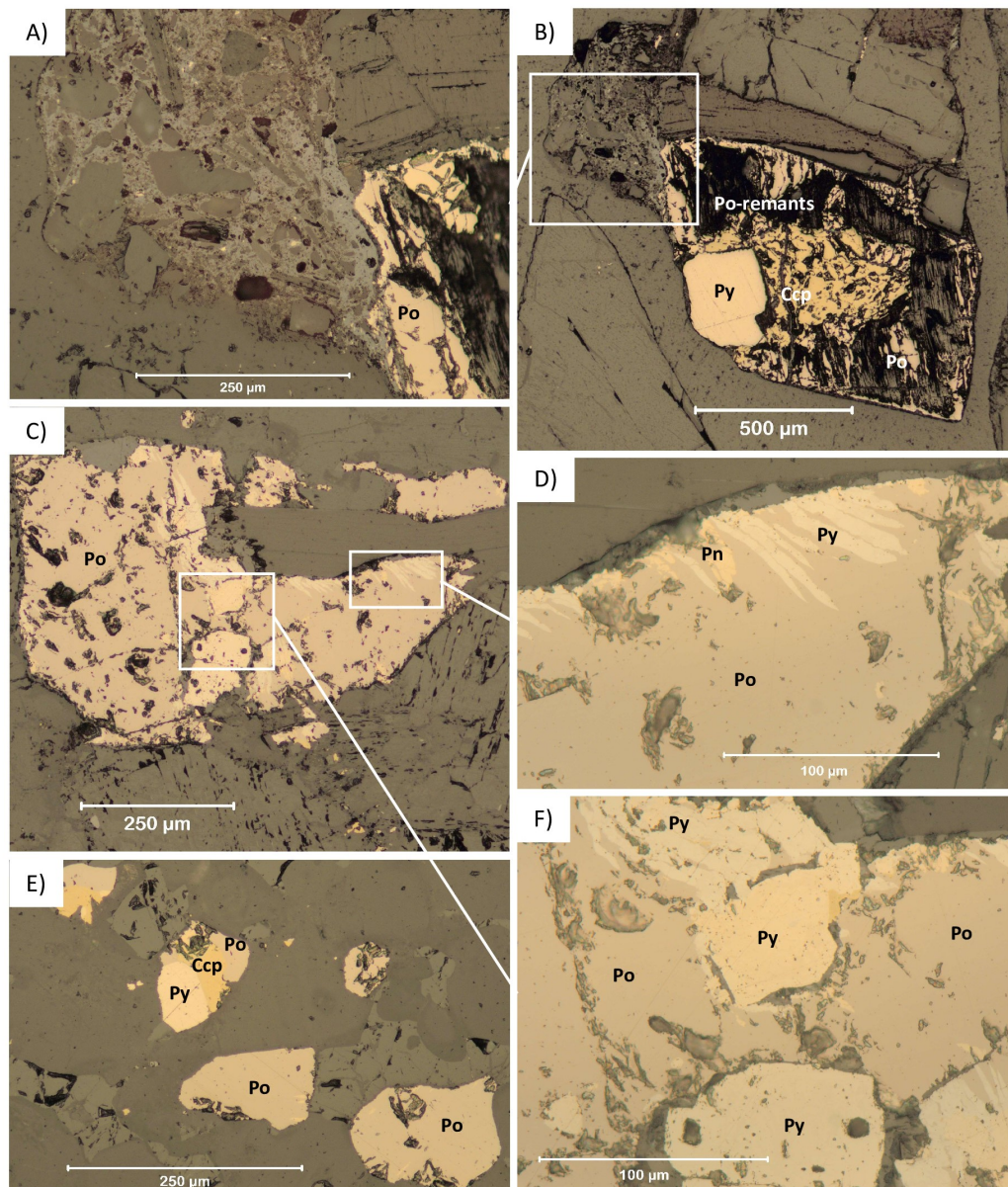


Figure 4.13: Sulfide phases in Trois-Rivières thin sections TR<8mm and TR1/8mm observed under reflected light. Mineral abbreviations after Whitney and Evans (2010). **A):** Close-up on the light-grey matrix phase, which appear to have leaked out from the weathered pyrrhotite in B), TR1/8mm. The larger grains within light-grey matrix are feldspar and quartz. **B):** Extensively weathered, subhedral pyrrhotite grain with euhedral pyrite and weathered chalcopyrite inclusions in TR1/8mm. **C):** Moderately weathered iron sulfide cluster, dominated by pyrrhotite, in TR<8mm. **D):** Close-up on pyrite exsolution patterns along the pyrrhotite boundary. The grey phase surrounding the pyrrhotite boundary is probably iron carbonate (siderite). **E):** Pyrrhotite is the dominating iron sulfide in TR<8mm. **F):** Close-up on an aggregate of iron sulfides within the pyrrhotite from C).

4.2.6 Electron Probe Micro Analysis (EPMA)

Estimations on average composition based on point analysis on iron sulfides in TR<8mm and TR1/8mm thin sections are shown in Table 4.14. Average pyrite composition is close to the ideal formula, and show small substitutions of nickel (Ni) and cobalt (Co) for iron (Fe). The average Fe content in pyrrhotite is less than the suggested contents of ideal pyrrhotite types. Average total sum for pyrrhotite is the lowest among all sulfides.

The analyses of unknown phases related to pyrrhotite weathering resulted in low total sums (<70 wt.%), and are therefore discarded from the results. These low sums were probably due to contents of elements not analysed by the method (e.g. oxygen) and topography on the sample surface resulting in bad signals.

Table 4.14: Electron Probe Micro Analysis (EPMA) results for Trois-Rivières sulfides from TR<8mm and TR1/8mm thin-sections. Blanks are below detection limit. Ideal formula represents ideal mineral formula compositions, obtained from the online mineralogy database, Webmineral.com, by Barthelmy (2021). Ideal compositional ranges of pyrrhotite, as described in the literature, were presented in Table 2.2, obtained from Multani and Waters (2018).

Mineral (no. analyses)		Fe	Mo	Co	S	Cu	Ni	Zn	Total
Pyrrhotite (6)	Ideal formula	62,33			37,67				100
	Average wt%	59,53	0,04	0,06	38,80		0,46		98,88
	St. dev	0,57	0,05	0,02	0,37		0,13		0,34
	Max-min	58,64-60,19	0,00-0,10	0,04-0,09	38,40-39,33		0,39-0,72		98,49-99,26
Pyrite (12)	Ideal formula	46,55			53,45				100
	Average wt%	45,28		0,47	53,09		0,65		99,49
	St. dev	1,02		0,35	0,69		0,84		0,25
	Max-min	43,28-46,53		0,04-1,14	50,96-53,58		0,98-1,95		99,09-99,86
Chalcopyrite (5)	Ideal formula	30,43			34,94	34,63			100
	Average wt%	30,10	0,019	0,04	34,68	34,14	0,02	0,03	99,04
	St. dev	0,34	0,03	0,01	0,13	0,65	0,03	0,05	0,61
	Max-min	29,72-30,57	0,00-0,05	0,04-0,05	34,55-34,85	33-34,26	0,00-0,08	0,00-0,09	98,16-99,89
Pentlandite (4)	Ideal formula	32,56			33,23		34,21		100
	Average wt%	31,02		2,14	33,39	0,02	32,77	0,25	99,59
	St. dev	2,39		0,91	0,35	0,05	3,45	0,49	0,58
	Max-min	29,21-34,53		1,38-3,24	33,13-33,91	0,00-0,09	27,77-35,33	0,00-0,99	98,74-100,02

4.2.7 Automated Mineralogy (AM)

Bulk mineralogy

Bulk mineralogy estimations by 20 μm AM mapping suggest that the Trois-Rivières samples mainly consist of plagioclases and pyroxenes, with less quartz and biotite. According to the mineral classification for this material (Table 3.3), plagioclase discrimination is simplified to anorthite or albite based on a Ca/Na ratio above or below 1. Pyroxenes are discriminated based on their Ca-content, where clinopyroxene require $>4\text{wt}\%$ Ca and orthopyroxene $<4\text{wt}\%$ Ca. Hence, it can be seen that almost all plagioclase is Ca-rich, while the majority of pyroxenes are Fe- and Mg-rich rather than Ca-rich. Accessory minerals, in this case defined as minerals which on average constitute less than 1,0 wt%, are shown in Appendix D. False color mineral maps on all Trois-Rivières samples can be found in Appendix F.

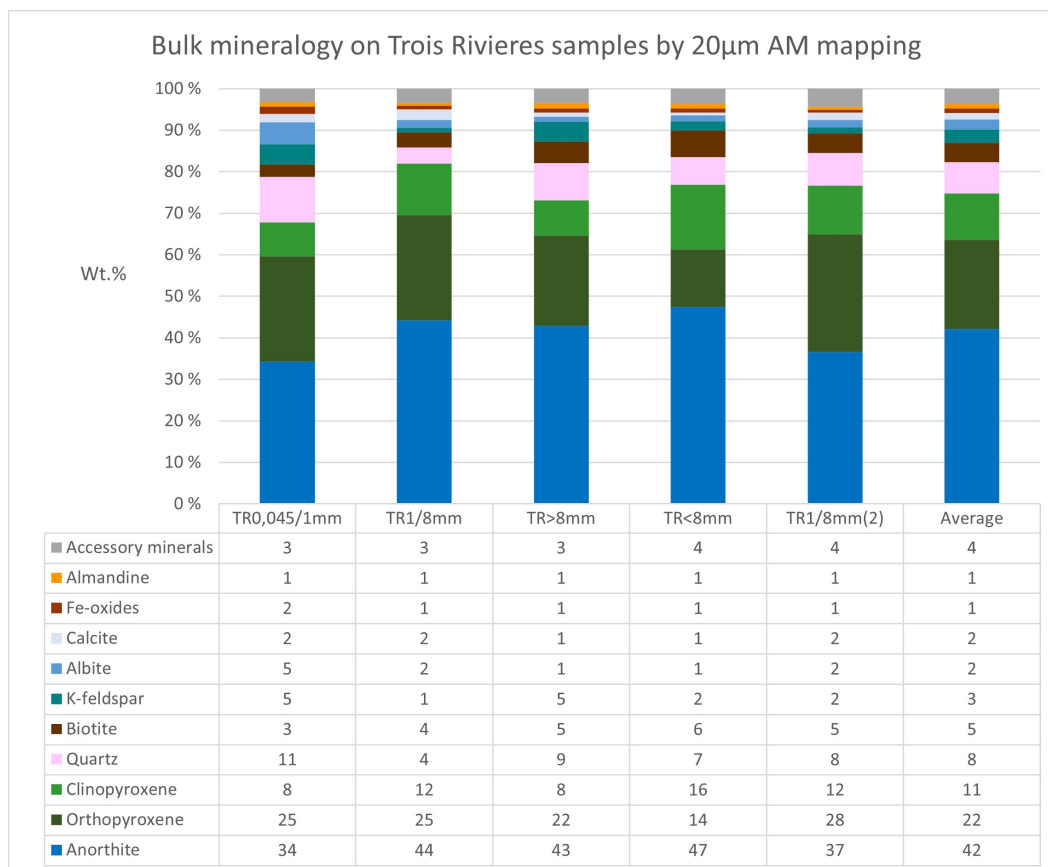


Figure 4.14: Bulk mineralogy for all Trois-Rivières samples by 20 μm Automated Mineralogy mapping.

Unclassified area/pixels on all sample surfaces are shown in Table 4.15. For the finest fraction, TR0,045/1mm, %- unclassified is not below the <3% target. After reviewing all particles in this fraction, it could be seen that grain boundaries often lead to several unclassified pixels due to mixed signals of epoxy and sample material. This effect is also visible among the other fractions, where the lowest amount of unclassified pixels is found in the coarser fractions, containing fewest grain boundaries.

Table 4.15: Area-% unclassified for Trois-Rivières samples from AM mapping.

Sample	TR0,045/1mm	TR1/8mm	TR>8mm	TR<8mm	TR1/8mm(2)	Average
Unclassified, % area	4,09	2,00	1,08	1,55	2,17	2,18

Sulfur-phase mineralogy

According to AM analyses on the Trois-Rivières aggregates, sulfur phases comprise pyrrhotite, pyrite, chalcopyrite, pentlandite, sphalerite, Fe sulfate/oxide and Ca-sulfate. Average wt% and chemistry of sulfides among all Trois-Rivières samples are shown in Table 4.16, while specific contents for each sample are presented in Table 4.17. Pyrrhotite concentration varies from 0,291 wt% to 0,915 wt% in all samples. Pyrrhotite and pyrite appear on average with almost equal contents among the samples, respectively 0,604 wt% and 0,596 wt%.

Table 4.16: Average wt% and chemistry of the sulfur phases in all Trois-Rivières samples gathered by 20 μm Automated Mineralogy mapping.

Sample	Mineral	Weight%	Average chemistry						
			Fe	S	Ni	Cu	Zn	Ca	O
Average TR-samples	Pyrrhotite	0,604	62,81	37,19					
	Pyrite	0,596	49,49	50,51					
	Pentlandite	0,136	38,61	31,15	30,23				
	Chalcopyrite	0,061	35,31	31,94		32,74			
	Sphalerite	0,008		31,07			68,93		
	Fe-sulfate/oxide	0,078	56,43	21,92					21,64
	Ca-sulfate	0,039		22,22				36,98	36,90
	Po rand-effect	0,126	80,81	19,19					

Table 4.17: Wt% and average chemistry of the sulfur phases in each Trois-Rivières sample gathered by 20 µm Automated Mineralogy mapping.

Sample	Mineral	Weight%	Average chemistry						
			Fe	S	Ni	Cu	Zn	Ca	O
TR0,045/1mm	Pyrrhotite	0,291	63,29	36,71					
	Pyrite	0,397	49,55	50,45					
	Pentlandite	0,107	39,11	29,33	31,56				
	Chalcopyrite	0,038	35,77	31,36		32,87			
	Sphalerite	0,001		30,12			69,88		
	Fe-sulfate/oxide	0,151	59,46	16,37					24,16
	Ca-sulfate	0,185		21,88				36,76	21,88
	Po rand-effect	0,334	84,88	15,12					
TR1/8mm	Pyrrhotite	0,430	62,45	37,55					
	Pyrite	0,630	49,41	50,59					
	Pentlandite	0,167	36,96	31,66	31,39				
	Chalcopyrite	0,106	35,3	32,07		32,62			
	Sphalerite	0,006		32,47			67,53		
	Fe-sulfate/oxide	0,103	56,54	19,97					23,48
	Ca-sulfate	0,004		21,29				37,8	40,91
	Po rand-effect	0,132	82,73	17,27					
TR>8mm	Pyrrhotite	0,915	62,62	37,38					
	Pyrite	0,336	49,79	50,21					
	Pentlandite	0,095	40,32	32,27	27,41				
	Chalcopyrite	0,043	34,76	32,37		32,880			
	Sphalerite	0,016		29,77			70,23		
	Fe-sulfate/oxide	0,033	56,31	23,16					20,53
	Ca-sulfate	0,001		21,3				35,54	43,16
	Po rand-effect	0,044	78,79	21,21					
TR<8mm	Pyrrhotite	0,717	62,79	37,21					
	Pyrite	0,650	49,4	50,6					
	Pentlandite	0,111	38,85	31,63	29,51				
	Chalcopyrite	0,026	35,13	32,25		32,610			
	Sphalerite	0,013		31,43			68,57		
	Fe-sulfate/oxide	0,030	54,8	23,53					21,67
	Ca-sulfate	0,003		25,06				37,93	37
	Po rand-effect	0,038	76,89	23,11					
TR1/8mm(2)	Pyrrhotite	0,666	62,88	37,12					
	Pyrite	0,968	49,28	50,72					
	Pentlandite	0,200	37,83	30,87	31,3				
	Chalcopyrite	0,092	35,6	31,67		32,73			
	Sphalerite	0,004		31,56			68,44		
	Fe-sulfate/oxide	0,072	55,04	26,59					18,35
	Ca-sulfate	0,002		21,57				36,87	41,56
	Po rand-effect	0,082	80,78	19,22					

Possible products and remnants of pyrrhotite weathering are classified as Fe oxides and Fe sulfate/oxide by 20 μm AM mapping. Several examples of weathered pyrrhotite particles from TR0,045/1mm and TR1/8mm samples are illustrated in Figure 4.15 and 4.16, with reflected light microscopy, BSE imaging and 20 μm AM mapping. Average chemical composition of the Fe sulfate/oxide classification can be seen in Table 4.16 and 4.17. Average composition of the Fe oxide classification is not specified in these tables, but involves 65-75 wt.% iron and 25-35 wt.% oxygen in all samples.

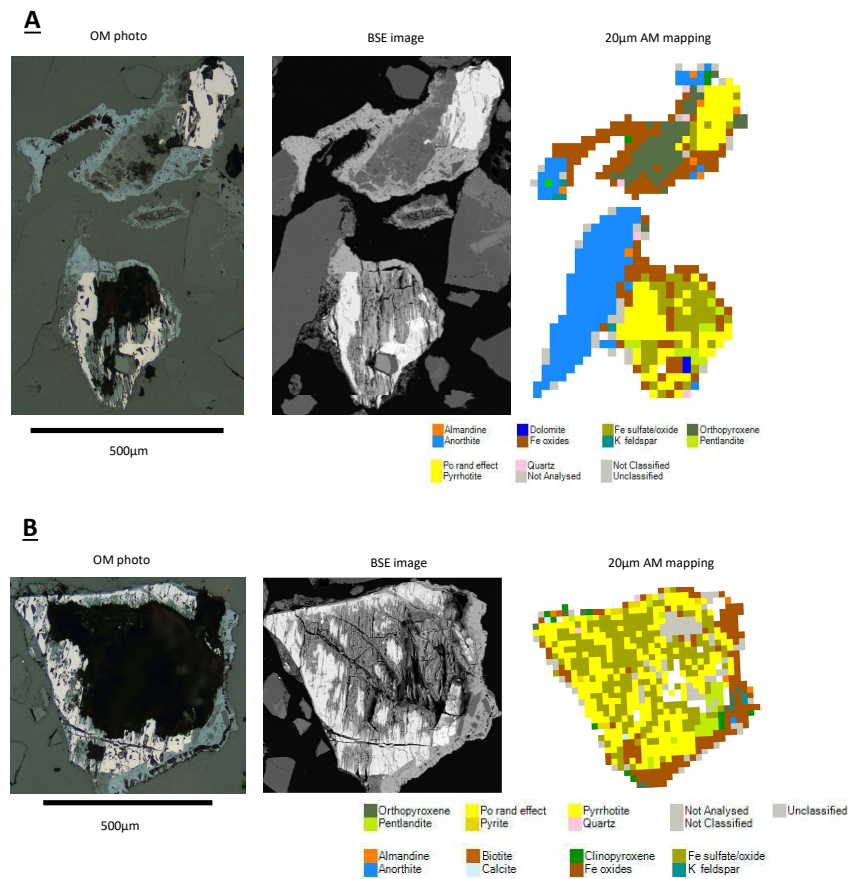


Figure 4.15: Weathered pyrrhotite associated with Fe-oxides in TR0,045/1mm, displayed with reflected light under optical microscope (OM), Back Scattered Electron (BSE) imaging and 20 μm Automated Mineralogy (AM) mapping.

The weathering process removes major parts of the pyrrhotite interior, while grains retain intact at mineral boundaries. This tendency is evident in Figure 4.15, B and Figure 4.16, A, B and C. The remnant phase within weathered pyrrhotite seems to possess an entirely different relief than the intact parts. Completely intact pyrite appears together with weathered

pyrrhotite in all examples in Figure 4.16. Chalcopyrite and pentlandite appear moderately weathered in all cases.

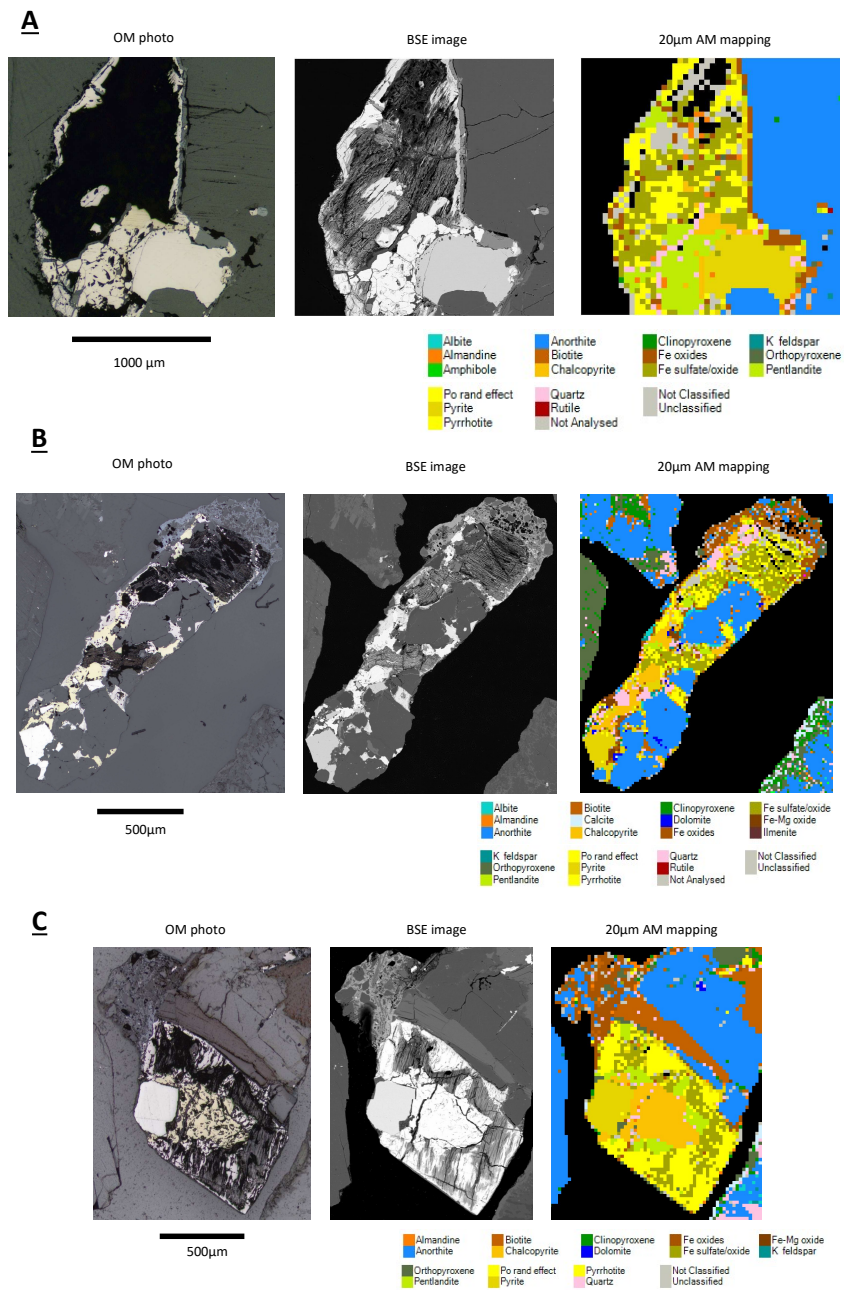


Figure 4.16: Weathered pyrrhotite associated with Fe-oxides in TR1/8mm, displayed with reflected light under optical microscope (OM), Back Scattered Electron (BSE) imaging and 20 µm Automated Mineralogy (AM) mapping. **A** and **B** are from the TR1/8mm stub sample, while **C** is from the TR1/8mm(2) thin section.

Pyrrhotite mineral associations

Mineral associations are calculated as percentage of minerals that most frequently appear next to the mineral of interest, in this case pyrrhotite. Figure 4.17 shows that the Trois-Rivières pyrrhotite first and foremost is associated with the other sulfides, and the most abundant silicates in the samples.

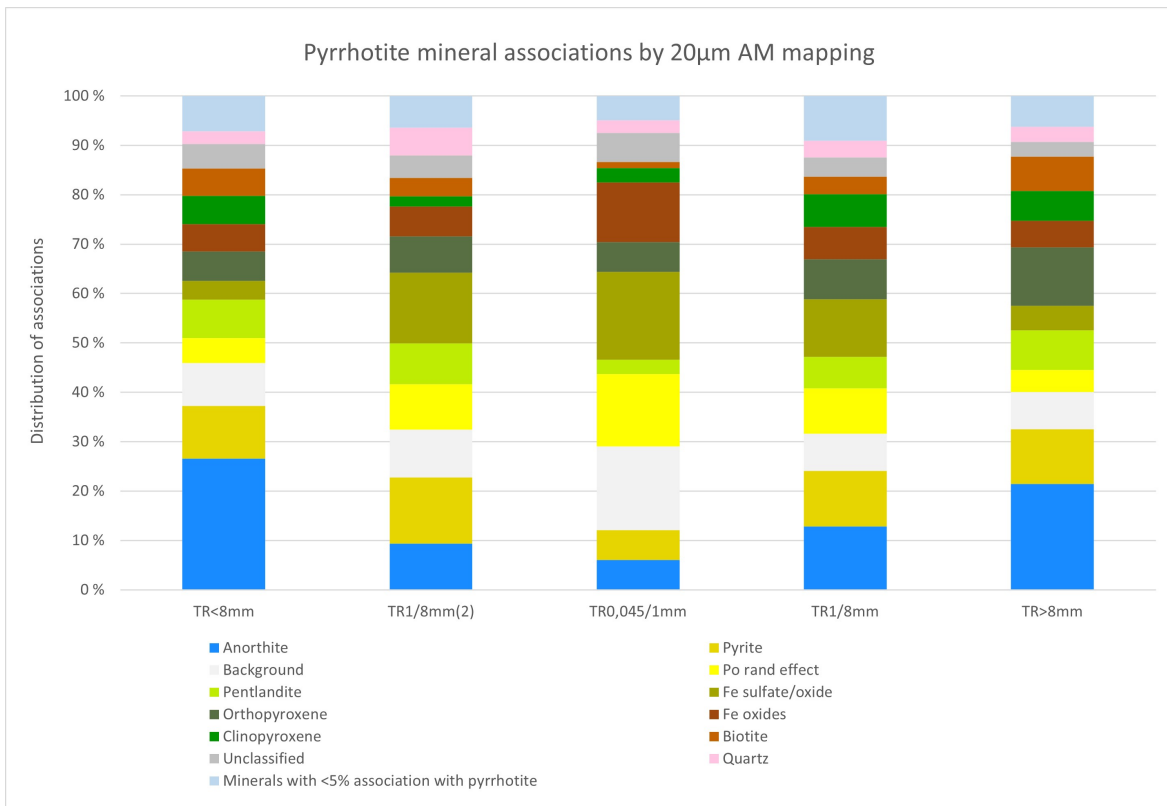


Figure 4.17: Pyrrhotite mineral associations in Trois-Rivières samples acquired with 20 μ m Automated Mineralogy (AM) mapping.

4.2.8 Petrological classification

The Trois-Rivières material was classified according to the system by the International Union of Geological Sciences (IUGS) (Streckeisen, 1976). Although some variations occur among the samples, was the material classified as a clinopyroxene-norite. Eight samples were analysed by XRD and AM, as presented in Figure 4.18.

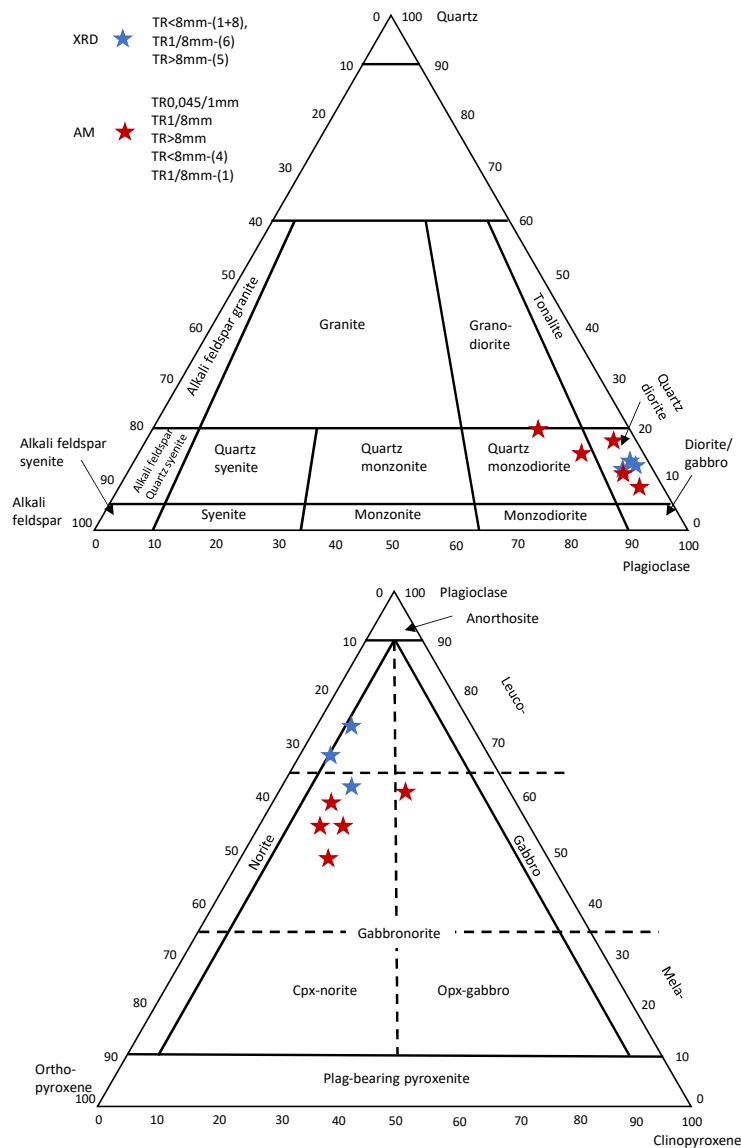


Figure 4.18: The Trois-Rivières aggregates were classified as a Clinopyroxene-Norite (Cpx-Norite) according to the classification system by the International Union of Geological Sciences (IUGS) (Streckeisen, 1976), based on X-Ray Diffraction (XRD) and 20 μm Automated Mineralogy (AM) bulk analyses. Albite and K-feldspar were merged for the Alkali feldspar component from the AM analyses. Plagioclase was not differentiated by the XRD analyses.

4.3 Discrimination of pyrrhotite and pyrite with Automated Mineralogy mapping

Mineral recipes tested for best possible discrimination between pyrite and pyrrhotite with Automated Mineralogy (AM) are illustrated in Figure 4.19. Three strategies are named after their characteristics, e.g. the main discriminating factor in **2. Fe content** is wt% Fe above or below 58. The strategies are judged on how well they discriminate between pyrite and pyrrhotite in a selection of pyrite and pyrrhotite grains from Follo Line and Trois-Rivières samples. Bright Phase Search (BPS) followed by $5\mu\text{m}$ AM mapping were used for testing the recipes.

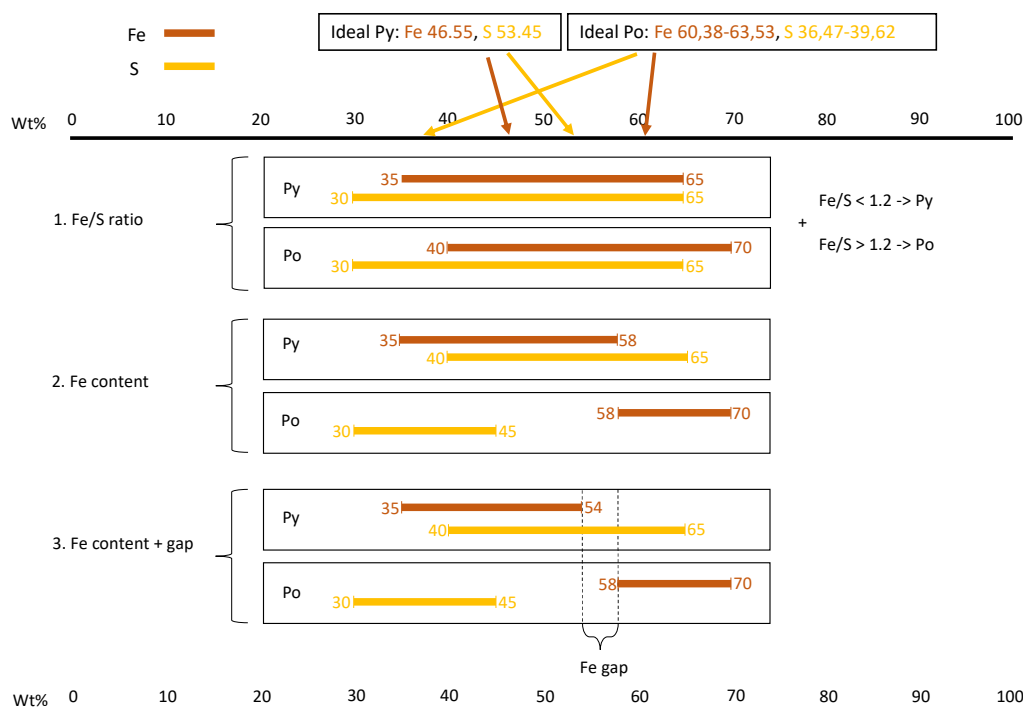


Figure 4.19: Three strategies were tested for discrimination between pyrite (py) and pyrrhotite (po) with Automated Mineralogy mapping. **1. Fe/S ratio** accepts wide variations of iron (Fe) and sulfur (S) contents in both minerals, and uses elemental ratio Fe/S to discriminate between pyrite (Fe/S < 1,2) and pyrrhotite (Fe/S > 1,2). **2. Fe content** tolerates less variation of Fe and S contents, and discriminates mainly based on Fe content above or below 58 wt%, respectively into pyrrhotite or pyrite. Max 45 wt% S for pyrrhotite, and min 40 wt% S for pyrite are also decisive factors in this recipe. **3. Fe content + gap** uses the same limits as 2. Fe content, but is not tolerating Fe content above 54wt% in pyrite. This means that eventual pyrite or pyrrhotite with 54-58wt% Fe content will remain unclassified. This recipe is the best approximation with respect to ideal formulas of pyrite and pyrrhotite.

Differentiation of an intact pyrrhotite grain and a moderately weathered pyrite cluster, both without inclusions of each other, from FB-J thin section is illustrated in Figure 4.20. A small difference in brightness can be seen in the two BSE images. Pyrrhotite is expected to have slightly brighter BSE signature due to a larger Fe content, resulting in higher average atomic number. Since no mixing of the two brightness grades can be seen, the pyrite and pyrrhotite is most likely clean without mixed features. All three techniques determine pyrrhotite well, with only a few misclassified pixels by Fe content and Fe content + gap. The scars and marks of weathering in the pyrite cluster is more challenging. The Fe/S ratio classifies many pyrrhotite pixels within the pyrite cluster, and Fe content + gap returns several pixels as unclassified (grey). Overall, the recipe based on Fe content appear to discriminate best among pyrite and pyrrhotite for these grains.

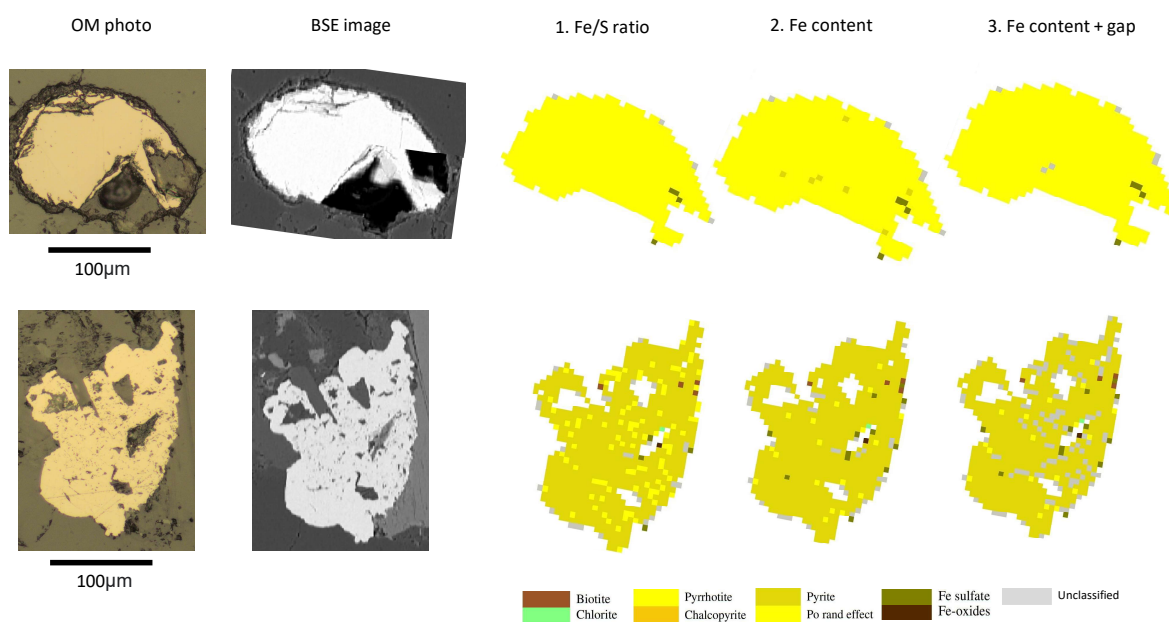


Figure 4.20: Discrimination of pyrrhotite and pyrite with three different mineral recipes by Back-Scatter Electron (BSE) imaging and Bright Phase Search (BPS) + 5 μ m Automated Mineralogy (AM) mapping. Sample: FB-J thin section.

The differentiation of another moderately weathered pyrite cluster, also from FB-J thin section, is shown in Figure 4.21 on the next page. A significant variation in BSE signature can be observed between the massive pyrite and the minor chalcopyrite grain to the right. Since brightness and contrast settings used in this case were similar those displayed in to Figure 4.20, the pyrite seems to be clean without pyrrhotite inclusions. These should eventually be visible as brighter patches within the pyrite. A small Fe oxide inclusion in the pyrite is visible under reflected light and also detected by AM, but is not distinguished from

surrounding pyrite by BSE imaging.

Also in this example, the recipe based on Fe content in the middle seems to yield the best classification scheme of pyrite. A similar trend like in Figure 4.20 can be seen, where Fe/S ratio returns a high amount of misclassified pyrrhotite pixels within pyrite. Many pixels with 54-58 wt% Fe content are not classified by the Fe content + gap, and remain unclassified.

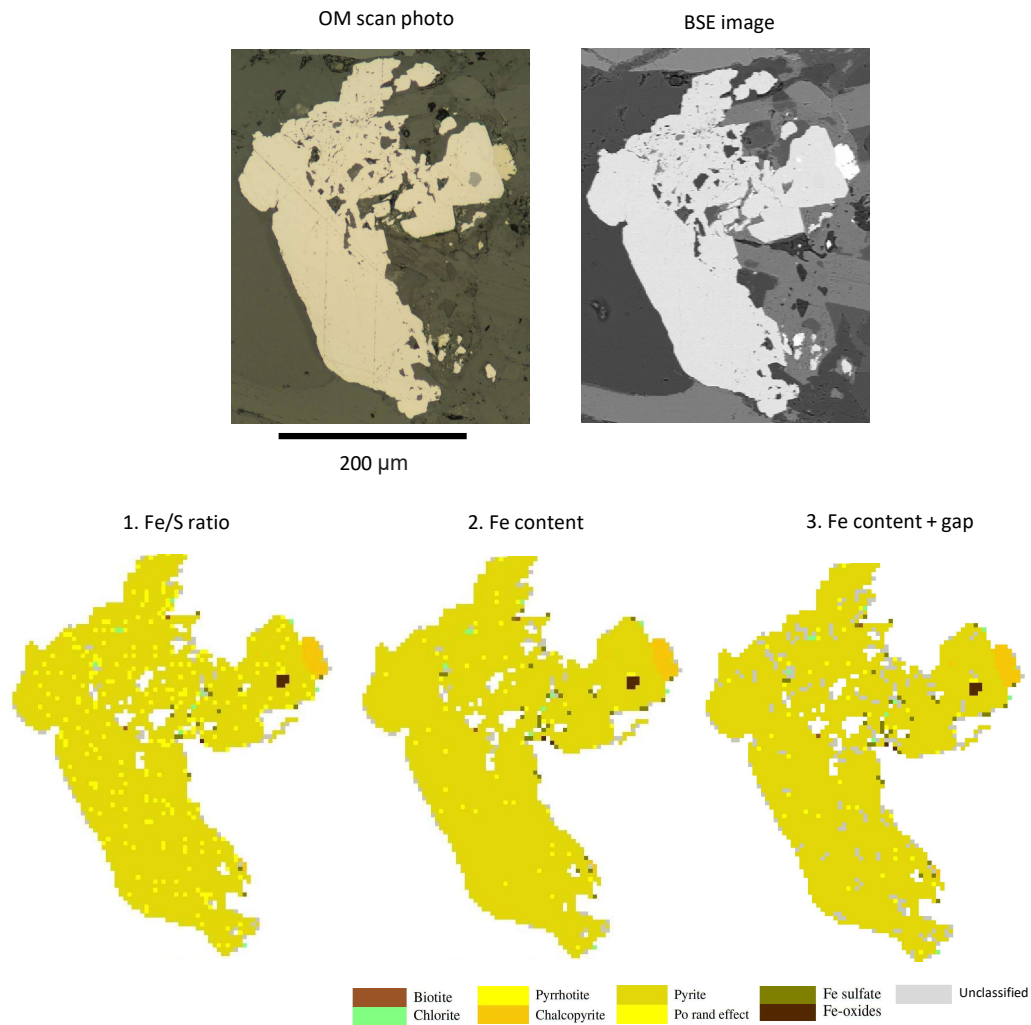


Figure 4.21: Discrimination of pyrrhotite and pyrite with three different mineral recipes by Back-Scatter Electron (BSE) imaging and Bright Phase Search (BPS) + 5µm Automated Mineralogy (AM) mapping. Sample: FB-J thin section.

Aggregates from Trois-Rivières contain generally more, and larger pyrrhotite and pyrite appearances than Follo Line aggregates. Figure 4.22 on the next page, shows massive pyrite with chalcopyrite inclusions, next to pentlandite and pyrrhotite. The BSE image reflects significant brightness contrasts between pyrite and the other sulfides. Pyrrhotite, chalcopyrite

and pentlandite display similar brightness. A correct discrimination within pyrite remains the challenge, where iron-rich pixels commonly are misclassified as pyrrhotite.

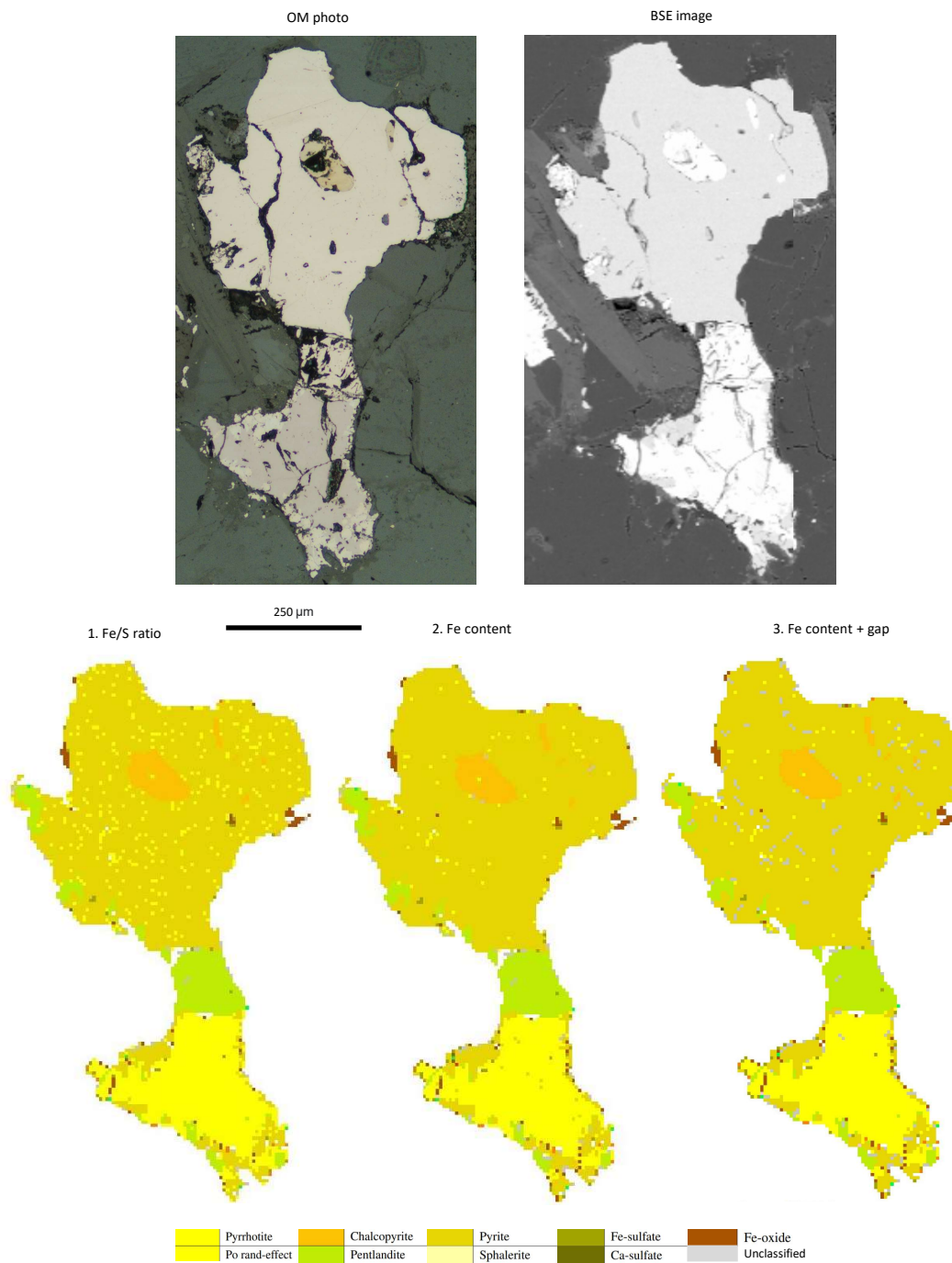


Figure 4.22: Discrimination of pyrrhotite and pyrite with three different mineral recipes by Back-Scatter Electron (BSE) imaging and Bright Phase Search (BPS) + 5µm Automated Mineralogy (AM) mapping. Sample: TR1/8mm thin section.

Yet again, the recipe based on Fe content seems to produce the classification with least misclassified or unclassified pixels. Pyrite exsolution patterns surrounding the pyrrhotite grain in Figure 4.22 are correctly classified by all discrimination strategies.

In Figure 4.23, a large pyrrhotite grain with several pyrite inclusions was analysed with both BPS + 5 μm mapping and 20 μm mapping. Both analyses discriminate between pyrrhotite and pyrite with the most promising recipe so far, based on whether Fe content exceeds, or is below, 58 wt%. The 20 μm mapping result displayed on the right side in Figure 4.23 is included for comparison on how pixel size affect the classification. The analysis with larger pixel size discriminates well among larger pyrrhotite grains and pyrite inclusions, but struggles with fine-grained pyrite exsolution along pyrrhotite boundaries.

BSE imaging discriminates pyrrhotite repeatedly as the brighter phase compared to pyrite, as depicted in Figure 4.23. Flame-like exsolution patterns of pyrite along the pyrrhotite boundary occur in several places and are illustrated well by BSE contrasts.

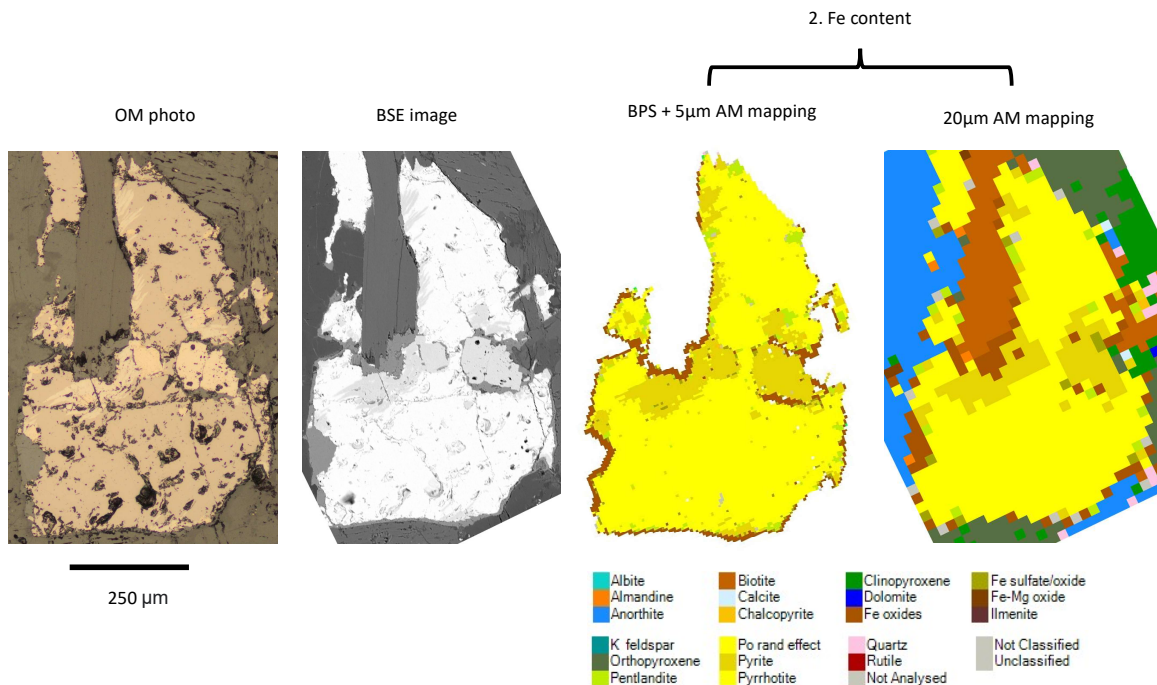


Figure 4.23: Discrimination of pyrrhotite and pyrite with Back-Scatter Electron (BSE) imaging, Bright Phase Search (BPS) + 5 μm and 20 μm Automated Mineralogy (AM) mapping. Both AM analyses are performed with the 2. Fe content-recipe, discriminating pyrrhotite and pyrite based on Fe content above or below 58wt%. Sample: TR < 8mm.

4.3.1 Element maps on a pyrite cluster with Electron Probe Micro Analysis (EPMA)

Although the discrimination criteria of 58 wt% Fe-content seems most suitable for quantifying pyrrhotite and pyrite, several pyrrhotite pixels still occur within apparently clean pyrite. These pixels are most likely misidentified pyrrhotite caused by cracks, holes or sudden iron enrichment in the pyrite. For further investigation of this issue, element maps for Fe and S were produced with Electron Probe Micro Analysis (EPMA) on a pyrite cluster in FB-K. Based on Optical Microscopy (OM) and Back-Scatter Electron (BSE) imaging, this cluster consists of pure pyrite, as seen in Figure 4.24. However, the 20 μm AM analysis shows several potentially misidentified pyrrhotite pixels within pyrite. The OM photo and BSE image in Figure 4.24 reveal that the pyrite cluster is irregularly weathered with a varying degree of cracks and holes.

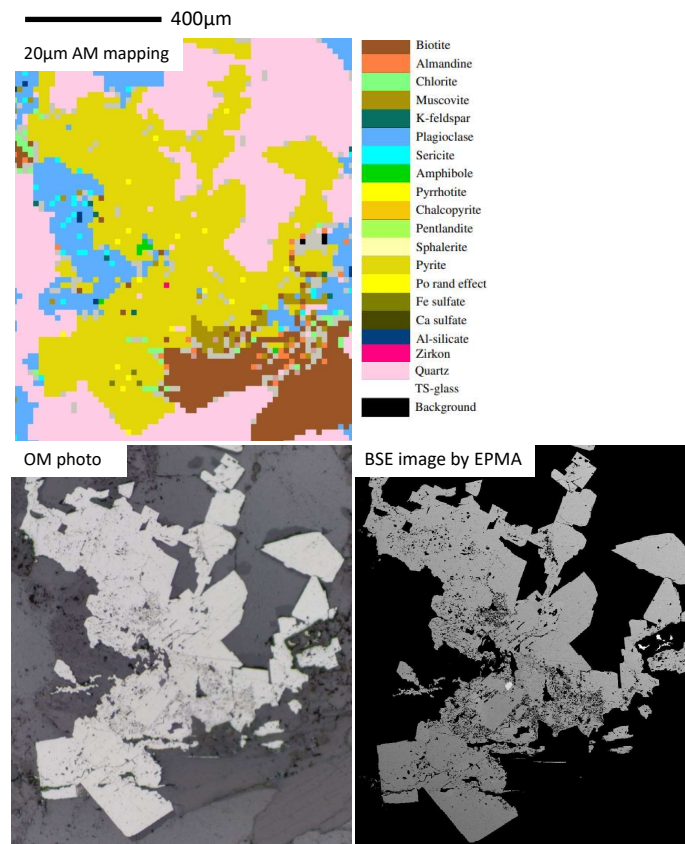


Figure 4.24: Compilation of 20 μm Automated Mineralogy (AM) mapping, Optical Microscopy (OM) photo and Back-Scatter Electron (BSE) imaging of a pyrite cluster in FB-K thin section. The false color mineral map classifies the cluster as pyrite, but with several pyrrhotite pixels within. Two brighter phases can be seen in the pyrite cluster; A little Zirkon inclusion, which is also indicated by AM, and minor disseminated chalcopyrite to the right in the image, only indicated by AM with one pixel.

Figure 4.25 on the next page depicts 20 μm AM false color map and 10 μm EPMA elemental maps of Fe, S, Co, Si and Ni on the pyrite cluster in FB-K. The Fe- and S-map show that the strongest intensity, dark-orange color, is covering the majority of the pyrite cluster. Some areas related to weathering and grain boundaries, seen in Figure 4.24, show weaker intensity with a more yellow color. No abrupt areas with stronger Fe-intensity can be seen in the areas where pyrrhotite is indicated by 20 μm AM mapping. Co- and Ni-intensities vary slightly across the cluster, but do not correlate with the pyrrhotite pixels. Different intensities in the Si-map are in accordance with expected amounts of Si in the silicates classified by AM mapping.

Figure 4.26 and 4.27 in the following pages, display 1 μm EPMA elemental maps of two selected areas with several pyrrhotite pixels within the same pyrite cluster in FB-K. Both examples have even Fe- and S-intensities without sudden intensity differences, which would have been more distinct if the indicated pyrrhotite pixels really were representing pyrrhotite inclusions. Linear structures of Ni-enrichment are observed in both examples, Figure 4.26 and 4.27. Figure 4.27 shows BSE contrast between a brighter patch and darker surroundings within the pyrite. This contrast is not caused by any of the mapped elements, and can definitely not be a pyrrhotite inclusion.

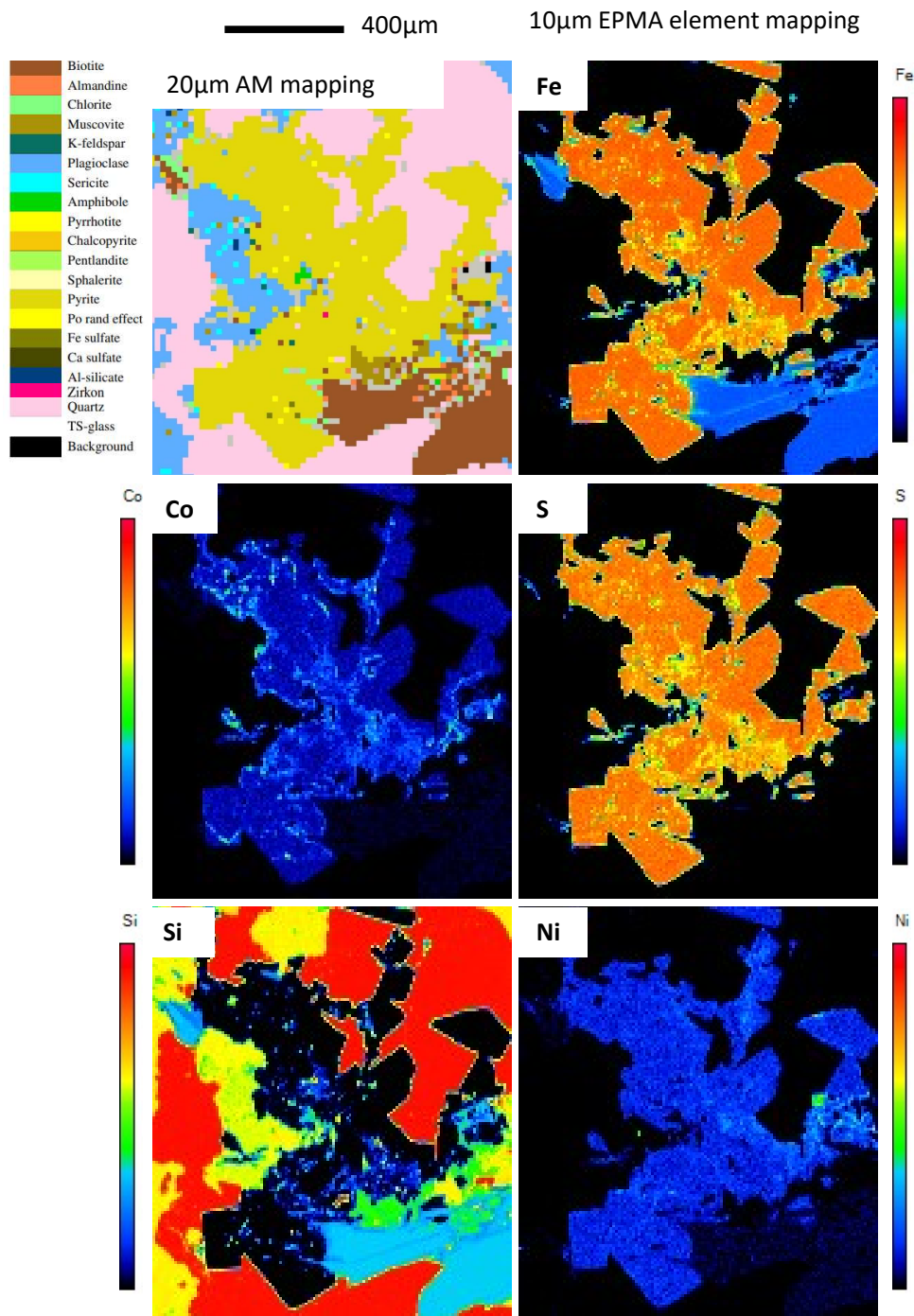


Figure 4.25: 20µm Automated Mineralogy (AM) mapping and 10µm element maps by Electron Probe Micro Analysis (EPMA) of the pyrite cluster in FB-K thin section. The elemental maps are based on spectrum counts and illustrate relative intensity of the actual element. Red color represents the strongest intensity, while dark-blue represents the weakest intensity.

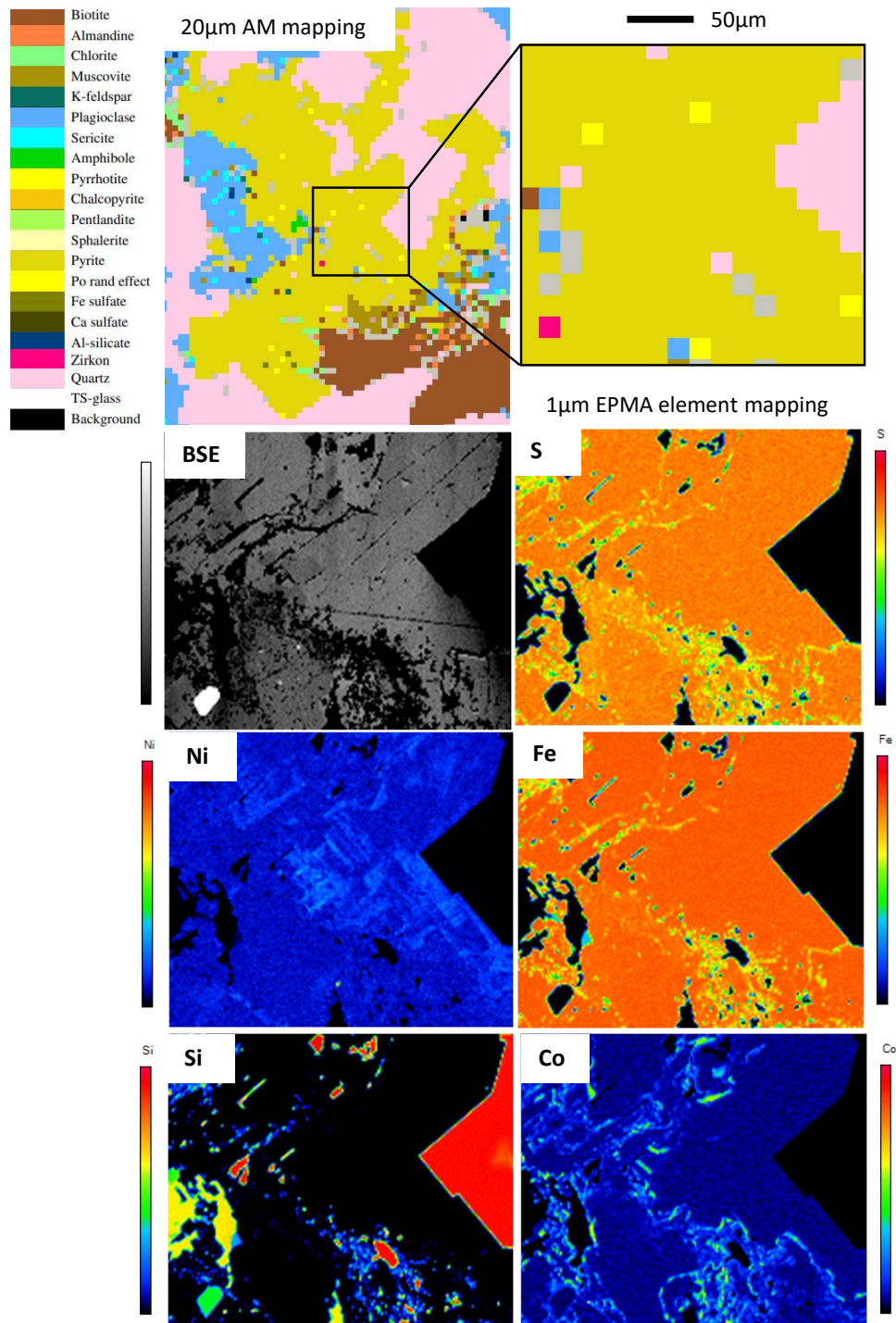


Figure 4.26: 20µm Automated Mineralogy (AM) mapping and 1µm element maps by Electron Probe Micro Analysis (EPMA) on a selected area within a pyrite cluster in FB-K thin section. The elemental maps are based on spectrum counts and illustrate relative intensity of the actual element. Red color represents the strongest intensity, while dark-blue represents the weakest intensity. Fe- and S-intensities are even throughout the area, except for reduced intensities in cracks and holes. A true pyrrhotite inclusion would have resulted in relative increase of Fe-intensity and reduction of S-intensity.

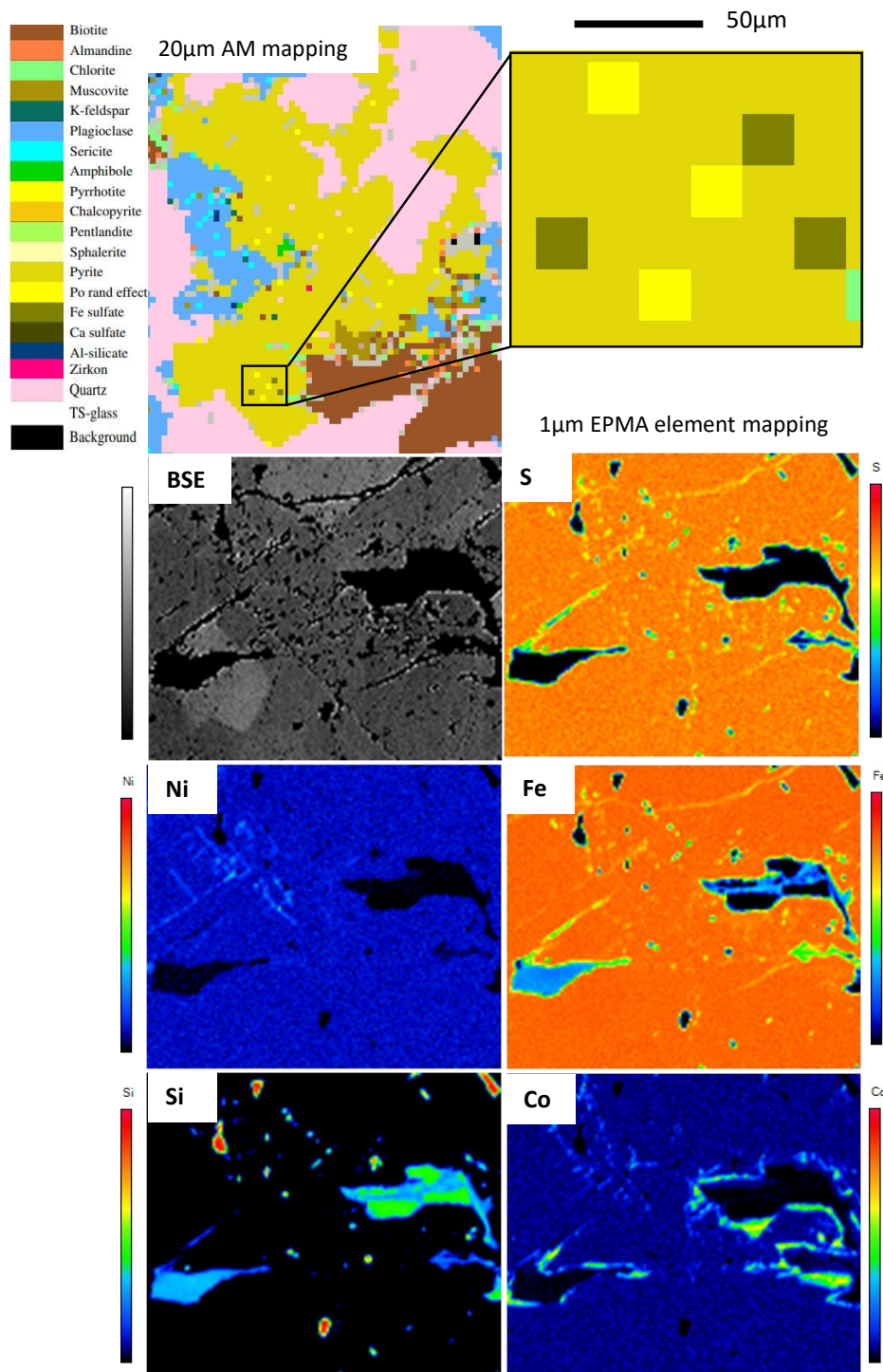


Figure 4.27: 20µm Automated Mineralogy (AM) mapping and 1µm element maps by Electron Probe Micro Analysis (EPMA) on a selected area within a pyrite cluster in FB-K thin section. The elemental maps are based on spectrum counts and illustrate relative intensity of the actual element. Red color represents the strongest intensity, while dark-blue represents the weakest intensity. None of the indicated pyrrhotite pixels by AM corresponds with abrupt changes in Fe- and S-intensities.

Chapter 5

Discussion

The first two parts of the chapter discuss mineralogical characteristics of the Follo Line and Trois Rivières aggregates, with focus on sulfur-phase mineralogy and pyrrhotite weathering-appearance in the samples. A comprehensive comparison of the analytical techniques and results presented in this study and previous studies are discussed in coherency. The third part elaborates the pyrrhotite mineralogy and petrogenesis of the two materials investigated. The fourth and final part of the discussion comprises an overall evaluation on how each analytical technique used in this work is suited for detecting and quantifying pyrrhotite and sulfur in rock samples in minor concentrations.

5.1 Follo Line material

5.1.1 Sulfide mineralogy and pyrrhotite appearance

Previous characterisations of the Follo Line gneisses are to the current knowledge limited to Graversen (1984), who stated that opaque minerals were present as accessories. Of other relevant knowledge, there is of course the basis for rejection of this material for use in concrete in the Follo Line Tunnel. It was prohibited due to exceeding sulfur concentrations and indications of pyrrhotite, lowering the sulfur acceptance limit from 1 wt% to 0,1 wt% NS-EN12620 (2006).

According to NS-EN12620 (2006), standard for concrete aggregates, eventual indications of pyrrhotite should be proven by Differential Thermal Analysis (DTA). In the current study, the DTA analysis suggested indications of pyrrhotite in all five Follo Line gravel samples; FB-A1, FB-B, FB-C, FB-D and FB-E. The pyrrhotite indications by DTA are compared with indications by optical microscope (OM) and Automated Mineralogy (AM) in Table 5.1.

Table 5.1: Indications of pyrrhotite in Follo Line samples by Differential Thermal Analysis (DTA), Optical Microscope (OM) and 20 μm Automated Mineralogy (AM) mapping. Samples marked in yellow have confirmed indications of pyrrhotite based on OM and AM. All samples analysed by OM and AM are whole rock sections except gravel sections in FB-B2, FB-C2 and FB-E2. n/a = not analysed.

	FB-A1	FB-B	FB-C	FB-D	FB-E	FB-B2	FB-C2	FB-E2	FB-F	FB-G	FB-H	FB-I	FB-J	FB-K
Differential Thermal Analysis	x	x	x	x	x	x	x	x	n/a	n/a	n/a	n/a	n/a	n/a
Optical Microscope		x		x	x		x					x	x	
Automated Mineralogy mapping	x	x		x	x	x	x	x	x	x	x	x	x	x

Under the optical microscope (OM), 3-4 pyrrhotite grains with size 10-200 μm were detected in FB-B, while one single 20-50 μm pyrrhotite grain was found in each of the FB-D, FB-E and FB-C2 sections. Pyrrhotite was also detected in FB-I and FB-J thin sections, but these are not directly related to the samples analysed by DTA. According to 20 μm AM mapping, all Follo Line samples except FB-C contain traces of pyrrhotite. However, only minimal amounts (<0,010 wt%) of pyrrhotite were indicated in 11 of 14 samples.

Figure 5.1 on the next page shows that the certain pyrrhotite appearances in FB-B and FB-J suggested by OM are confirmed by AM mapping as the two samples with most pyrrhotite, respectively 0,022 wt.% and 0,015 wt%. With minor pyrrhotite indications from OM and low pyrrhotite contents from AM, the other samples may contain minimal amounts of pyrrhotite or nothing at all. One single 20-50 μm pyrrhotite grain was found in each of the samples FB-D, FB-E, FB-C2 and FB-I by optical microscopy and was later confirmed by 20 μm AM mapping. The low pyrrhotite contents reported by AM in these samples are therefore probably representing these minor grains.

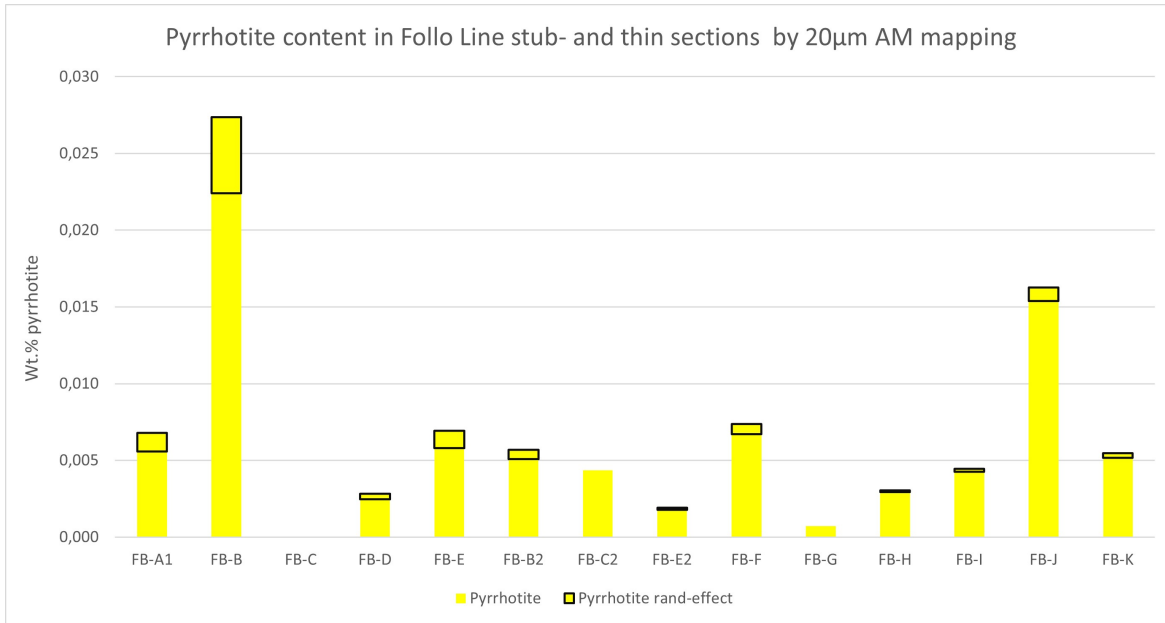


Figure 5.1: Pyrrhotite content in the Follo Line stub- and thin sections by 20 μm Automated Mineralogy (AM) mapping. The results suggest an analytical, or experience-based, detection limit for pyrrhotite in the range 0,004-0,007 wt% with this analysis.

Output graphs from DTA analyses (Figure 4.2) suggest that FB-A1 contains the most significant amount of iron sulfides among samples analysed by DTA, while FB-C barely exhibits any iron sulfide signature. This correlates well with the quantification from AM, where FB-A1 contains most iron sulfides (0,309 wt% Py, 0,006 wt% Po and 0,016 wt% Ccp) and FB-C the least (0,001 wt% Py) among samples analysed by both DTA and AM, displayed in Figure 5.2. The 0,006 wt% pyrrhotite in FB-A1 could not be verified by optical microscopy, and must therefore be considered as uncertain. In this case, the challenge with DTA analysis is that the main sulfide peaks in both FB-A1 and FB-C fall between the typical oxidation ranges for pyrite and pyrrhotite. Therefore, such results are interpreted as indications of both pyrite and pyrrhotite, since none of them can be excluded based on the main peak between typical oxidation ranges. Taking into account the results by AM and OM, it seems evident that the iron sulfides virtually only consist of pyrite (Figure 5.2), although pyrrhotite is indicated in all samples analysed by DTA (Table 5.1).

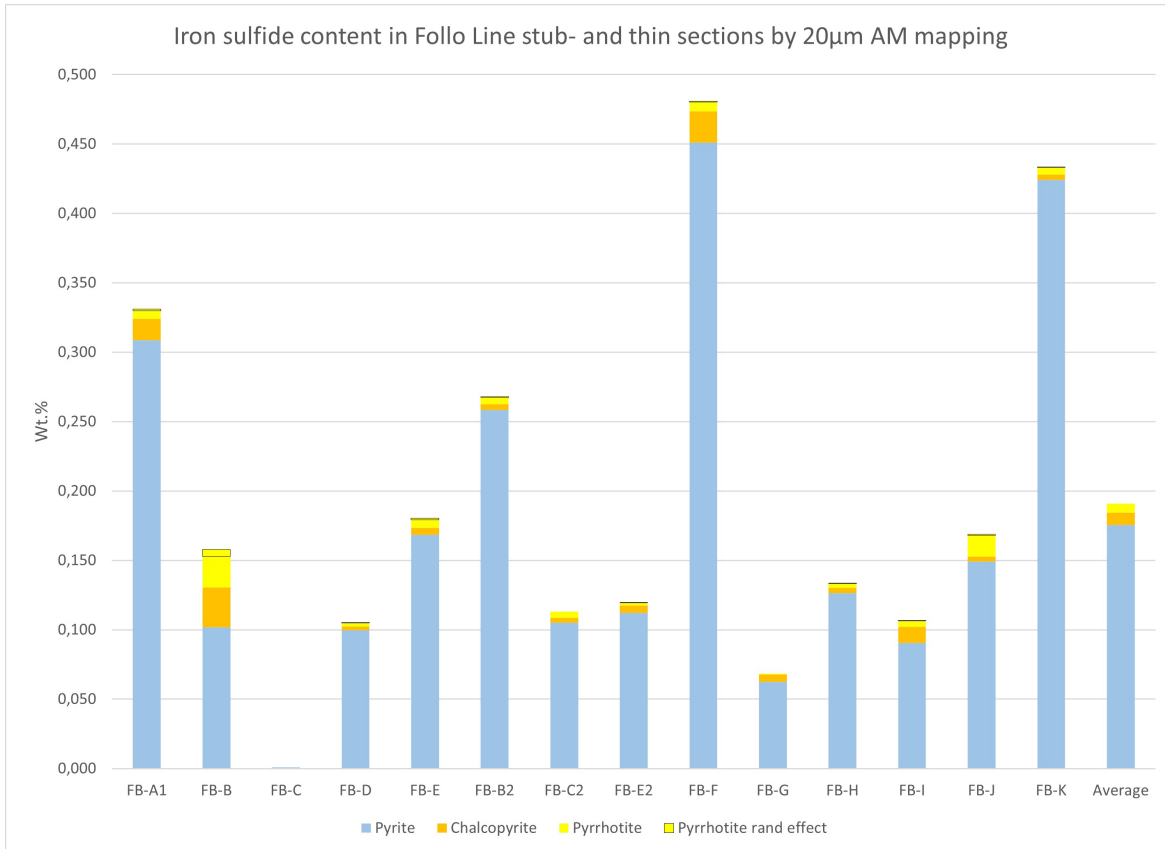


Figure 5.2: Distribution of iron sulfides among all Follo Line stub- and thin sections by 20 µm Automated Mineralogy (AM) mapping. Pyrite is light-blue for better visualisation along with the yellow pyrrhotite.

When comparing DTA and AM/OM results, one must be aware that sample formats are widely different concerning grain size and representativeness. Methods based on sample surface analysis are also limited to a 2D impression, which represents an evident limitation due the possible ignoring of spatial characteristics. AM analysis deliver mineral wt.% based on the area of minerals on a 2D surface and the specific gravity of each mineral. This is of course a considerable simplification, but also probably the best way of estimating mineral amounts based on 2D sections.

While whole-rock sections portray small windows in a rock, bulk samples consist of random fragments from potentially larger volumes. Crushed-rock thin sections, made from bulk samples, are probably the most representative samples available for AM/OM analysis, and the most comparable with DTA results. Thus, comparisons of DTA results with OM and AM, for Follo Line gravel samples (FB-B2, FB-C2, FB-E2) especially, underline the uncertainty in pyrrhotite detection by DTA.

The low contents of pyrrhotite detected in the Follo Line samples may suggest an analytical, or experience-based, detection limit for pyrrhotite. The pyrrhotite contents 0,004 wt% in FB-I and 0,015 wt% in FB-J, were verified by visual detection with OM. On the other hand, the contents 0,007 wt% in FB-F and 0,005 wt% in FB-K could not be verified by OM. The result from FB-I suggest that AM is able to detect pyrrhotite contents down to 0,004 wt%, while the result from FB-F shows that 0,007 wt% may be false. These results suggest that an analytical detection limit for pyrrhotite is in the range 0,004-0,007 wt% with the current mineral recipe. Lower contents are uncertain due to possible pyrrhotite misclassifications within pyrite. However, if a sample contains more pyrite than the Follo Line samples did, a potentially higher amount of pixels is likely to be misclassified as pyrrhotite. This will lead to more uncertainty related to the pyrrhotite contents, and hence increase the analytical detection limit for pyrrhotite. Conversely, lower amounts of pyrite are likely to result in better detection, and more correct quantification of pyrrhotite. The mineral assemblage must therefore always be considered when detection capability is estimated based on AM results.

The element maps by EPMA (Chapter 4.3) on a pyrite cluster in FB-K showed that AM mapping indicated several pyrrhotite pixels within pure pyrite. This misclassification happens because the EDS is analysing Fe wt% >58 within pyrite. Since no pyrrhotite were detected by OM in the rest of FB-K, the 0,005 wt% content in this sample is probably wrong and not credible. Many of the misclassified pyrrhotite pixels appeared near cracks and holes in the pyrite, without any visible Fe-enrichment seen in Fe-elemental maps, or atomic number increase in BSE imaging. If pyrrhotite was present, this should have been visible in both these maps considering that pyrrhotite contains >10 wt% more Fe than pyrite. Therefore, it is probable that such misclassified pyrrhotite pixels within pyrite are due cracks and holes in the pyrite, resulting in disturbed EDS signals.

Chalcopyrite is much easier to discriminate from pyrite due to the characteristic copper (Cu)-content, requiring >18 wt% Cu to be classified (mineral recipe in Table 3.2). According to Figure 5.2, chalcopyrite appeared approximately in the same degree as pyrrhotite. Since many pyrrhotite pixels probably originated from misclassified holes and cracks within pyrite, chalcopyrite is most likely more common in the Follo Line samples than pyrrhotite after all.

The iron sulfides appeared predominantly in clusters or associated with each other, and pyrite occurred in cracks and veins on some occasions. Crystal faces were visible on some of the pyrrhotite grains, which overall appeared relatively intact and unweathered. On the other hand, pyrite varied from being extensively weathered and perforated to almost intact, euhedral grains (Figure 4.3). This relationship between pyrite and pyrrhotite weathering is the

opposite of what is expected considering that pyrrhotite reportedly has a 20-100 times faster oxidation rate than pyrite (Nicholson and Scharer, 1994; Belzile et al., 2004). However, the basis for deciding the grade of pyrrhotite weathering in Follo Line samples is insufficient, with the very few grains present in only some of the samples.

Mineral association output from AM suggested that pyrrhotite most often was associated with pyrite in the Follo Line samples. If pyrrhotite content in general is low, as in all Follo Line samples, mineral association data will be highly influenced by misclassified pixels (Chapter 4.3). A typical example of this is when several pyrrhotite pixels have been misclassified within seemingly pure pyrite, like in the pyrite cluster in FB-K (Figure 4.24). This sample contained 0,424 wt% Pyrite and only 0,005 wt% Pyrrhotite. The highest pyrrhotite association with pyrite, just above 70% (Figure 4.8), was also indicated in this sample. Since pyrrhotite was not found in the rest of the sample analysed by optical microscope, the high pyrite mineral association for pyrrhotite is probably artificial due to misclassified pyrrhotite pixels within pyrite.

5.1.2 Bulk mineralogy estimations

The thin section investigations and petrological classification suggest that the Follo Line material mainly consists of granodioritic gneiss, with variations ranging from granitic to tonalitic. This classification agrees well with earlier work by Graversen (1984) and geological maps compiled by NGU (2020). All thin sections showed characteristic gneissic structures with felsic and mafic bands of varying thickness.

Graversen (1984) classified the gneiss into four types based on quartz, feldspar and biotite content, where 5wt% biotite represented granitic and 20wt% represented tonalitic. Biotite concentrations in the present study are estimated by X-Ray Diffraction (XRD), Figure 4.1, and Automated Mineralogy (AM), Figure 4.5. On average, AM reported more than twice as much biotite as XRD, respectively 16 wt% and 8 wt%. Although these values are in agreement with results from Graversen (1984) on biotite variations within the gneisses, the deviations between XRD and AM analyses are above what should be expected. XRD also reported 9wt% higher quartz content than AM. Muscovite was not reported by XRD at all, while AM, on average reported 4 wt% muscovite and 2 wt% of the micro- to cryptocrystalline muscovite sericite in feldspar alterations. Because AM detects far more accessory mineral phases than XRD, it is expected that wt% by XRD is a bit higher than by AM for the domi-

nating minerals. If, for example, true wt% of quartz in a rock is 50 wt%, and XRD estimates 55 wt% quartz, it could be because XRD ignored several accessory minerals. The detected phases will be normalised to making up 100 wt% of the sample by both XRD and AM, but the consequences of normalising is more prominent in XRD due to fewer detected phases than in AM.

Sample preparation and format could also be part of the explanation for these differences. The AM results are based on 11 intact-rock sections and three particulate sections, while XRD results are based on five powder samples. Intact-rock sections are likely to be cut in orientations that may cause over-representation of biotite and micas. These minerals appear aligned in specific orientations and irregularly banded next to quartz and feldspars in the Follo Line gneisses, Figure 5.3. During sample preparation, all intact-rock sections were cut more or less perpendicular to the foliation to avoid over-representing specific bands in the rock. If sections were cut parallel to the foliation, sections would almost entirely be made up of either mica bands or quartz and feldspars. Such preparation would definitely have caused over-representation of certain minerals.

The average biotite content is 14 wt% for the three AM analyses on gravel sections and 17 wt% for the 11 intact-rock sections. Although the average from gravel sections is closer to the 8 wt% biotite average from XRD, the difference is still significant.

Wrong biotite classification in the AM mineral recipe is another possible error source. Cross-checking false-colour mineral maps from AM with optical microscope scans make it possible to get an approximation of how accurate the classification is. Figure 5.3 shows a cropped-out area from FB-K as optical microscope photos under crossed-polarised light (xpl), plane-polarised light (ppl), and false-colour AM map. This sample has 21wt% biotite, according to AM analysis. Biotite is easy to identify under plane-polarised light (ppl) due to its color and pleochroism, and it seems that the obvious appearances under ppl match quite well with the false colour map from AM.

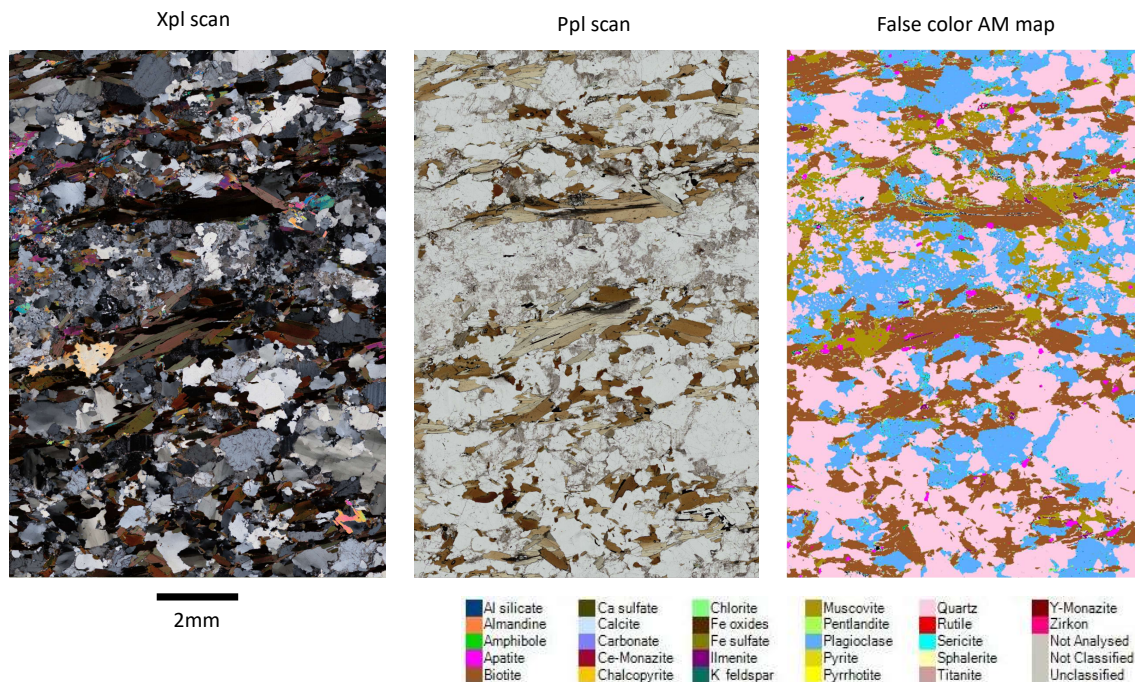


Figure 5.3: Compilation of optical microscope photos under cross-polarised light (xpl) and plane-polarised light (ppl), and false color mineral map by 20 μm Automated Mineralogy mapping of cropped-out area in sample FB-K. The biotite classification by AM appear to correlate well with biotite identification from optical microscope.

Material for the three grain mount thin sections was extracted from similar samples as the material for XRD analyses. AM analyses on particulate sections should be more representative than intact-rock sections and thus more comparable with XRD analyses. The compilation of OM photos and false colour AM map in Figure 5.4 on the next page show high variation of biotite abundance among the sectioned particles. This suggests a more representative mineral quantification than the intact-rock section in Figure 5.3. Finally, in Table 5.2, all biotite wt% acquired by AM and XRD on the three sample materials analysed on stub samples and particulate thin sections by AM, and on powder by XRD, are compared. Almost no coherency among these values makes it difficult to conclude on the reasons for significant biotite variations between XRD and AM.

Table 5.2: Comparison of wt% biotite estimations by Automated Mineralogy (AM) and X-Ray Diffraction (XRD) on three samples from the Follo Line material.

Analysis	Sample format	wt.% biotite		
		FB-B	FB-C	FB-E
AM	Intact-rock stub samples	17	15	10
	Particulate thin sections	11	13	17
XRD	Powder	6	8	7

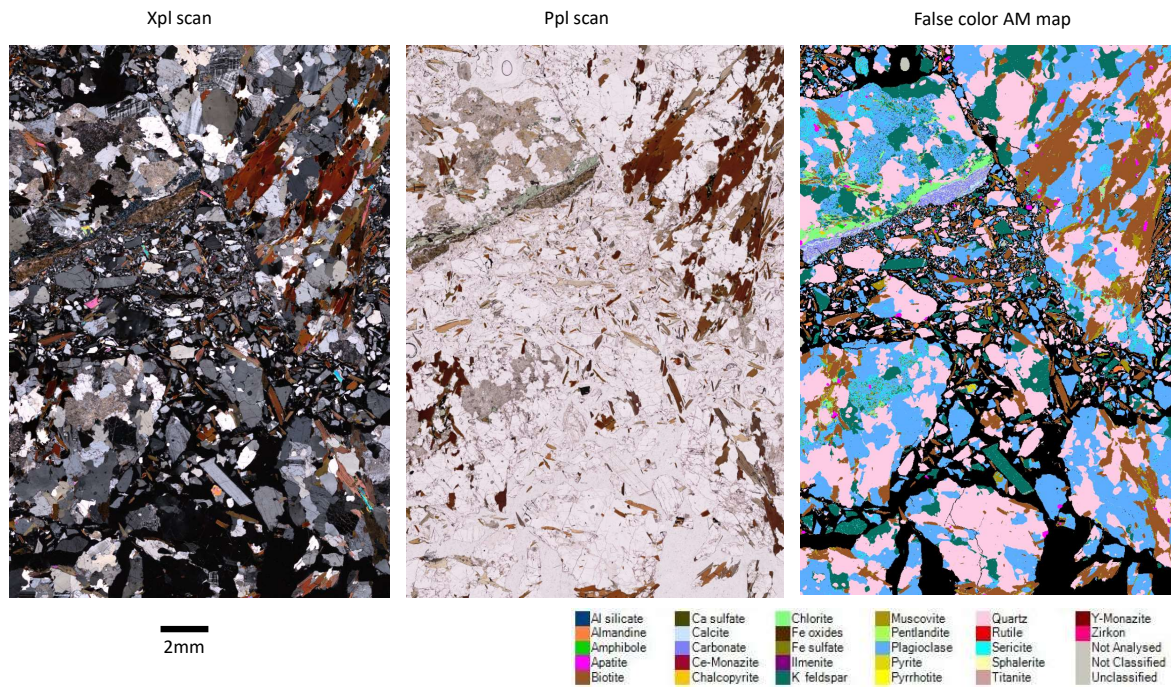


Figure 5.4: Compilation of optical microscope photos under cross-polarised light (xpl) and plane-polarised light (ppl), and false color mineral map by 20 μ m Automated Mineralogy mapping of a cropped-out area in FB-E(2).

5.2 Trois-Rivières material

5.2.1 Sulfide mineralogy and pyrrhotite appearance

The relatively large amount of various iron sulfides in the Trois-Rivières aggregates were previously determined through microscopy point counting as part of the PhD work by Rodrigues (2016), and is further established through analyses with OM, AM mapping and DTA in the current study. Pyrrhotite, pyrite, pentlandite and chalcopyrite were all identified by OM and AM. Small portions of sphalerite, Fe-sulfate and Ca-sulfate were also detected by OM and AM. Small portions of sphalerite, Fe-sulfate and Ca-sulfate were also detected by AM, displayed in Figure 5.5.

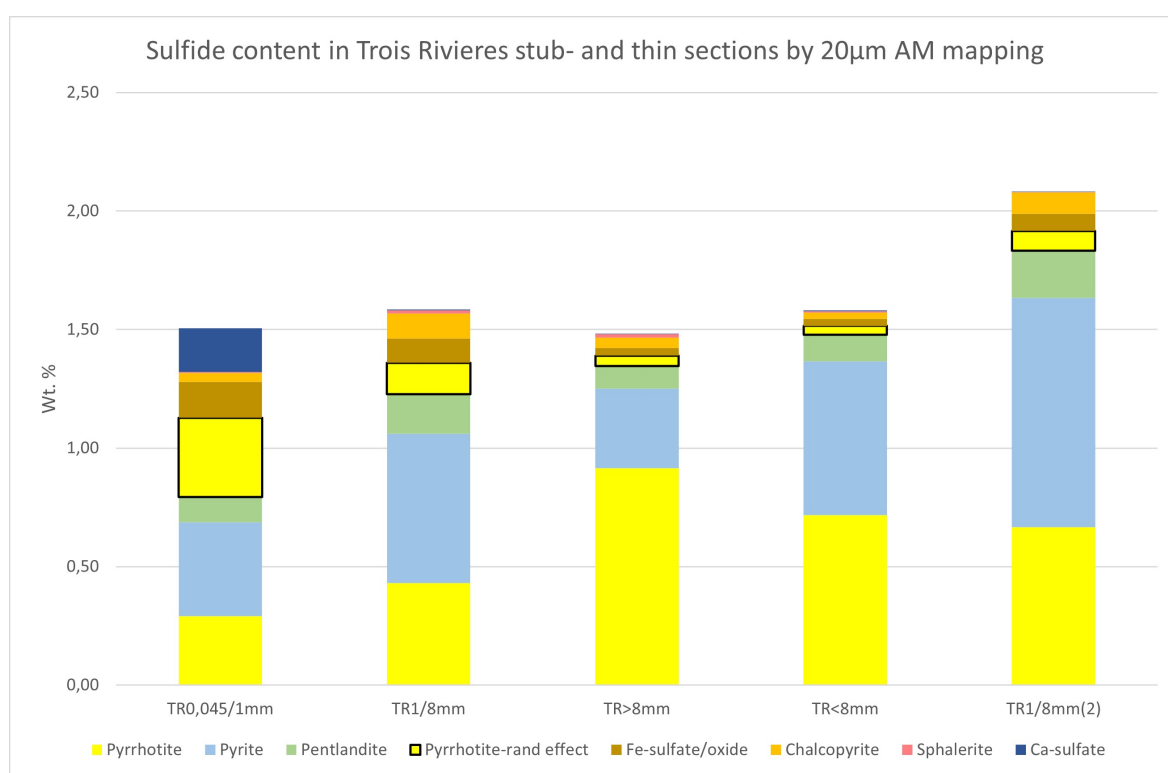


Figure 5.5: Sulfide content in the Trois-Rivières stub- and thin sections by 20 µm Automated Mineralogy (AM) mapping. Pyrite is light-blue for better visualisation along with the yellow pyrrhotite.

Pyrrhotite amounts estimated by AM varied from 0,291 wt.% to 0,915 wt.% for all Trois-Rivières samples. Po (pyrrhotite) -rand effect was also quantified to catch up pixels on weathered pyrrhotite grain boundaries, which typically contained Fe >65 wt.% and S <30 wt.%. This classification varied among the samples with the highest amount in TR0,045/1mm on 0,334 wt.%, and the smallest in TR<8mm with 0,038 wt.%. DTA analyses on the Trois-

Rivières material showed solid primary sulfide peaks within the typical range of pyrrhotite oxidation in all samples. In other words, the indication of pyrrhotite in these samples is undisputable, and much clearer than the primary peaks between pyrite and pyrrhotite in the Follo Line material. The total sulfide peak areas were also much larger than for the Follo Line material, confirming the greater sulfide content in the Trois-Rivières material.

Rodrigues (2016) quantified opaques as one phase and specified the amount of different sulfides as % of the opaques in each sample. For easier comparison with results from the current study, % of opaques from Rodrigues (2016) is transformed to % of total mineral content in Table 2.3. Quantifications by the point counting from Rodrigues (2016) resulted in 3/10 samples without pyrrhotite, 1/10 sample with 0,6 wt.%, 5/10 samples with 5-9 wt.% and 1/10 sample with 28 wt.% pyrrhotite. In other words, quite large variations, and overall much higher pyrrhotite contents compared to the AM analysis from the current study with average 0,604 wt% pyrrhotite.

Manual point counting with OM involves interpretation of mineral characteristics consecutively during the counting session, while AM analysis interprets all the acquired data points with a classification file. Hence, both methods are based on the basic principles of point counting, step size and mineral classification. The amount of data is probably the big difference since an AM analysis often has higher resolution and much more data is stored in each point. When similar sample formats are used, fairly equal results should be expected from the two methods. Since Rodrigues (2016) not specified the number of points counted per sample, a comparison of the statistical validity of her results with the results from AM analysis in the current study seems difficult. Anyway, it is notable that Rodrigues (2016) did not identify ilmenite as part of the opaques in any of the samples, while it was identified in all five samples in the current study by OM. Results from AM analysis suggests 0,336-0,767 wt.% ilmenite in all samples (Appendix D). Although these values are far from enough to fill in the gaps between the pyrrhotite quantification from Rodrigues (2016) and the current study, a misidentification by Rodrigues (2016) of ilmenite as being pyrrhotite could be part of the picture. Under reflected light, ilmenite and pyrrhotite are often both brownish with a purple/pink tint and both show strong anisotropism. However, when both are present, it should be possible to discriminate based on the higher reflectance of pyrrhotite, resulting in brighter appearance compared to ilmenite.

Iron carbonate (siderite) was frequently observed related to sulfides according Rodrigues (2016). A similar appearance was also observed in the current study as a bright-grey phase surrounding pyrrhotite and pyrite in thin bands. Certain identification with the optical micro-

scope was difficult due to the very thin, cryptocrystalline bands. However, based on the high order interference color, a carbonate mineral seem plausible. Due to carbon coating for SEM analyses, carbon is ignored by AM analysis. The possible iron carbonate phase consisted of 65-75 wt.% iron and 25-35 wt.% oxygen in all samples, and was therefore picked up by the iron oxide classification with AM. However, due to the translucency under the optical microscope, it could not be one of the common iron oxides/hydroxides since these are opaque (hematite, magnetite, goethite, lemonite). As suggested by Rodrigues (2016), siderite sticks out as a probable identification.

Statistics on pyrrhotite mineral associations by AM for the Trois-Rivières material (Figure 4.17) are much more valid than for the Follo Line material due to less influence from misclassified pixels within pyrite. The previous impression of highest pyrrhotite liberation in the finest fraction, TR0,045/1mm, is further supported by these statistics. Anorthite is the main constituent of the rock. Pyrrhotite appears in TR0,045/1mm as least associated with anorthite, and highest affiliated with the background (epoxy resin) among the samples. This relationship suggests high degree of pyrrhotite liberation. TR0,045/1mm also shows the highest pyrrhotite association for Fe sulfate/oxide, Fe oxides and Pyrrhotite (Po) rand-effect. This suggest that pyrrhotite in this fraction has been most exposed to weathering among the samples. Apart from that, no particular association is discovered through these statistics beyond what is expected from well disseminated pyrrhotite among silicates.

5.2.2 Pyrrhotite oxidation and weathering products

The substantial weathering of pyrrhotite in the Trois-Rivières aggregates was in this study confirmed by OM and AM analyses. Examples of more or less completely weathered pyrrhotites were shown in Figure 4.15 and 4.16.

Liberated pyrrhotite grains seemed to be far more weathered than the ones incorporated in aggregate particles. This observation becomes emphasised when comparing the great share of liberated pyrrhotite in TR0,045/1mm with the less liberated pyrrhotite in TR>8mm, displayed in Figure 5.6. According to AM analysis, TR0,045/1mm contained the lowest amount of pyrrhotite (0,291 wt.%), and the highest amount of Fe-sulfate/oxide (0,151 wt.%) among Trois-Rivières samples (Figure 5.5). The largest fraction, TR>8mm, contained the highest amount of pyrrhotite (0,915 wt.%), and the second-lowest amount of Fe-sulfate/oxide (0,033 wt.%). TR0,045/1mm also had the largest amount of Pyrrhotite rand-effect (0,334

wt.%), a classification created to catch up Fe-rich and S-poor pixels on weathered pyrrhotite grain boundaries.

The observations and values mentioned above suggest that pyrrhotite is much more oxidised, and to a larger extent transformed into Fe-sulfate/oxide, in finer ground fractions. Furthermore, this implies that pyrrhotite in finer aggregate fractions will oxidise more rapidly than in coarser fractions. Easier access to oxygen and water, due to surface exposure for liberated pyrrhotite grains, seem to be a sensible explanation. Concerning the use of pyrrhotite-bearing aggregates in concrete, this suggests the finest fractions (<1mm) to be most harmful due to their increased prominence to oxidation reactions.

Overall, pyrite appeared quite intact, with no signs of weathered interior or secondary mineral surroundings, while pyrrhotite was extensively weathered in the Trois-Rivières samples. This relationship between pyrite and pyrrhotite weathering agrees with the findings of Rodrigues (2016), and supports the laboratory studies by Nicholson and Scharer (1994), suggesting a significantly higher oxidation rate of pyrrhotite compared to pyrite.

AM analysis classified oxidised pyrrhotite interior as Fe sulfate/oxide, on average consisting of 56,43 wt.% iron, 21,92 wt.% sulfur and 21,64 oxygen (Chapter 4.2.7). This interior phase did not disappear after polishing, as typical surface oxidation of iron sulfides in sample sections would. These pyrrhotite grains have also quite recently been cut through at random planes during preparation of the sections. Since the majority of pyrrhotite grains in TR0,045/1mm comprise similar weathering degree, despite being cut through differently, this feature is most likely present throughout the grains. Considering the much greater extent of pyrrhotite weathering in the smallest fraction compared to the largest fraction, the oxidation process was most likely initiated after crushing and screening in the St.Boniface quarry. Unfortunately, for the current study, no record exist on the time span and storage conditions for the Trois-Rivières aggregates.

An iron oxide matrix with silicate mineral fragments appeared in a fluid-like, erupting way in close proximity to grain boundaries of oxidised pyrrhotite, e.g. Figure 4.12 B), 4.13 A) and 4.15. This iron oxide phase is opaque, and must not be confused with the thin layers of translucent iron carbonate, seen surrounding both pyrite and pyrrhotite in thin layers. Oxidation of pyrrhotite where oxygen is the primary oxidising agent is likely to cause formation of secondary minerals such as goethite ($\text{Fe}^{3+}\text{O}(\text{OH})$) and ferrihydrite ($\text{Fe}_{10}^{3+}\text{O}_{14}(\text{OH})_2$) (Nicholson and Scharer, 1994; Chinchón et al., 1995; Belzile et al., 2004). The fluid-like iron oxides around weathered pyrrhotite is therefore most likely a result of ferric iron precipitation after

pyrrhotite oxidation.

The occurrence of thin iron carbonate layers surrounding pyrite and pyrrhotite grains with coronas do not seem to be particularly constrained to weathered grains, (Figure 4.12 D) and 4.13 D). Iron carbonates have previously been found to be related to iron sulfide weathering, e.g. Lara et al. (2015) studied weathering processes of pyrite and pyrrhotite under simulated calcareous soil conditions, and experienced formation of a siderite-like compound in both mineral systems. However, the iron sulfides surrounded by siderite in Trois-Rivières aggregates are not among those exposed to the heaviest weathering.

5.2.3 Bulk mineralogy and rock classification

The aggregate material from St. Boniface Quarry, Trois-Rivières, is referred to as an anorthositic gabbro (norite or hypersthene-gabbro) by Rodrigues (2016) and Jana (2018). According to the petrological classification based on bulk mineralogy analyses (XRD and AM) in the current study, the rock is classified as a gabbronorite or more specific, a clinopyroxene-norite.

Estimations of bulk mineralogy by XRD and AM analyses showed more coherency than the same analyses did for the Follo Line material. Biotite content is 3 wt.% in all samples from XRD analyses, and varies between 3 and 6 wt.% from AM analyses. However, the AM analysis on the smallest fraction, TR0,045/1mm, gave the same result as the XRD analyses, namely 3 wt.%. This is expected, since TR0,045/1mm should be the most representative Trois-Rivières sample, with least influence of how larger particles are cut in the sections. This is well illustrated in Figure 5.6 on the next page, where the presence or absence of large particles with certain minerals may influence bulk mineralogy estimations.

The false color maps also give clear indications on mafic and felsic mineral assemblages. Anorthite, pyroxenes and sulfides dominate the mafic particles, while quartz, K-feldspar, and albite are more prominent in felsic particles. More examples of this tendency can be seen in the other false color maps in Appendix F.

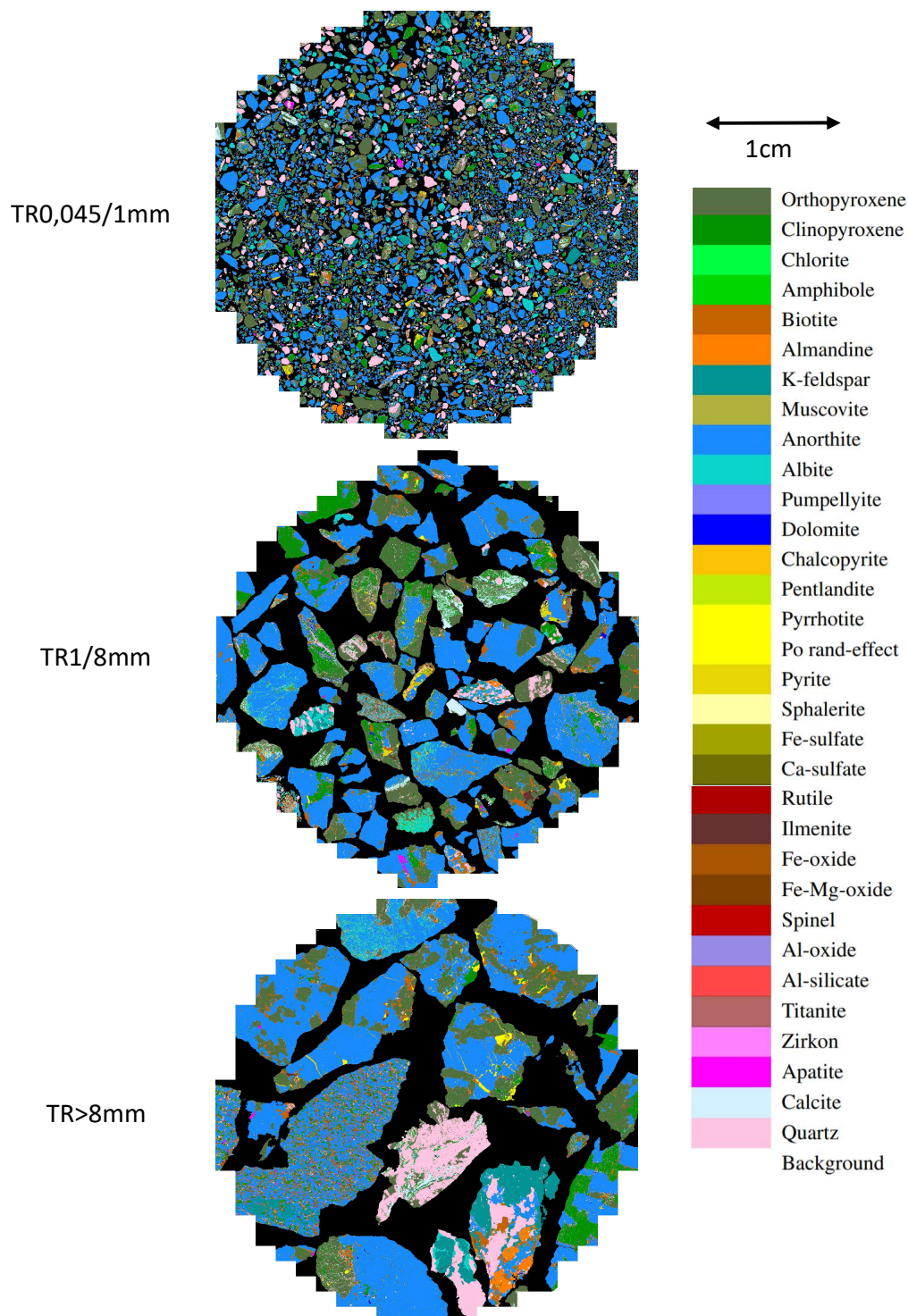


Figure 5.6: False color mineral maps from 20 μ m Automated Mineralogy (AM) mapping on TR0,045/1mm, TR1/8mm and TR>8mm stub samples. Presence or absence of larger particles dominated by certain minerals could be decisive for the bulk mineralogy estimation.

5.3 Pyrrhotite petrogenesis and mineralogy

The occurrence of pyrrhotite is not particularly constrained by the literature, as it may appear in basic igneous rocks, hydrothermal deposits, metamorphic rocks, pegmatites and sedimentary environments (Deer et al., 2013; Marshall et al., 2004). In other words, pyrrhotite can be present in most rock types. Concerning the use of rocks as aggregate in concrete, the possible presence of this mineral in all rocks is challenging. As mentioned, current regulations prohibit usage of the rock if indications of pyrrhotite are present and total sulfur content is above 0,1 wt%, in practise 0,144 wt%. Indications of pyrrhotite in some sample batches of an entire deposit could represent the largest appearances, or simply just a tip of the iceberg.

One of the objectives of the project on pyrrhotite in concrete aggregates, is to investigate if the particular genesis of a rock can indicate whether it contains traces of pyrrhotite or not (Danielsen et al., 2019). The disseminated traces of pyrrhotite in the Follo Line granodioritic gneisses demonstrate how pyrrhotite may appear in very small amounts in felsic rocks, where pyrite normally is the most common sulfide. According to Toulmin and Barton (1963); Craig and Vokes (1993), pyrrhotite possibly generates due to sulfur release during metamorphism in pyrite-bearing rocks. Since pyrite commonly occurs as an accessory mineral in all types of rocks, traces of pyrrhotite may, in principle, occur in all metamorphic rocks. Hence, predicting traces of pyrrhotite based on the geological history in metamorphic rocks seems very difficult.

Sulfides in the Follo Line gneisses may originate from the crystallisation of the protolith or may have formed later during metamorphism or hydrothermal activity. Sulfur-silica immiscibility, followed by the development of small sulfur-rich melt globules, is pointed out as a major formation process of pyrrhotite in igneous rocks by Deer et al. (2013); Robb (2005). Such a process seems very likely to have been responsible for the embedded assemblage of pyrrhotite, chalcopyrite and pyrite in a K-feldspar grain, Figure 4.4. According to the ground condition report for the Follo Line Tunnel by Jernbaneverket (2011), diabase intrusions and amphibolite lenses are cutting through the gneisses at several locations. Hydrothermal activity related to such intrusions could be another source of iron sulfide formation in the felsic gneiss, since mafic rocks in general are richer in iron sulfides than felsic rocks.

The general assumption that mafic rocks tend to exhibit more indications of pyrrhotite than felsic rocks, is well confirmed by this study. The Trois-Rivières gabbro norite contained significantly larger amounts of pyrrhotite than the Follo Line granodioritic gneisses. In the gabbro norite from Canada, pyrrhotite also is the most abundant iron sulfide. This relation supports the claim from Deer et al. (2013) that pyrrhotite is more common than pyrite in ultramafic and mafic rocks. On the other hand, pyrite is much more abundant than pyrrhotite in felsic gneisses from the Follo Line Tunnel.

The appearance of pyrrhotite relative to other minerals and structures in the gabbro norite could not be investigated thoroughly in this study since sample material was limited to gravel samples. However, based on the larger particles in TR > 8mm (Figure 5.6), formation through hydrothermal precipitation seems likely for the pyrrhotite in cracks and veins. Sulfur-silica immiscibility has probably been responsible for the sulfide assemblages with pyrrhotite, pyrite, chalcopyrite and pentlandite, embedded in silicate minerals. By studying the false colour maps in Figure 5.6, pyrrhotite seems to solely appear in particles with mafic minerals, e.g. anorthite, pyroxenes, and rarely in particles dominated by felsic minerals like quartz, albite, and K-feldspar. This confirms the mafic mineral association for pyrrhotite.

Parat et al. (2011) stated that magmatic accessory sulfides rarely form euhedral crystals. Optical microscope investigations in this study showed that pyrite and pyrrhotite are likely to form euhedral crystals in a gabbro norite, Figure 4.12. Chalcopyrite and pentlandite were mostly anhedral. Hints of pyrrhotite crystal faces were also observed in the Follo Line gneisses, Figure 4.3 and 4.4.

According to Table 2.2 (composition in pyrrhotite types from Multani and Waters (2018)), and Table 4.6 and 4.14 (EPMA results), pyrrhotite in the Follo Line- and Trois-Rivières aggregates exhibit on average a composition closest to the 4C pyrrhotite (Fe_7S_8), illustrated in Figure 5.7 on the next page. These results suggest that both of the aggregates contain arguably the most reactive, 4C, ferrimagnetic pyrrhotite type. (Becker et al., 2010). The small amounts of impurities/substitutions for the Fe-component (As, Co, Ni) measured by EPMA were added for better comparison with ideal formulas in Figure 5.7. Small amounts of molybdenum (Mo) were added to the S-component since these Mo-values most likely were measured as a result of overlapping signals between Mo and S.

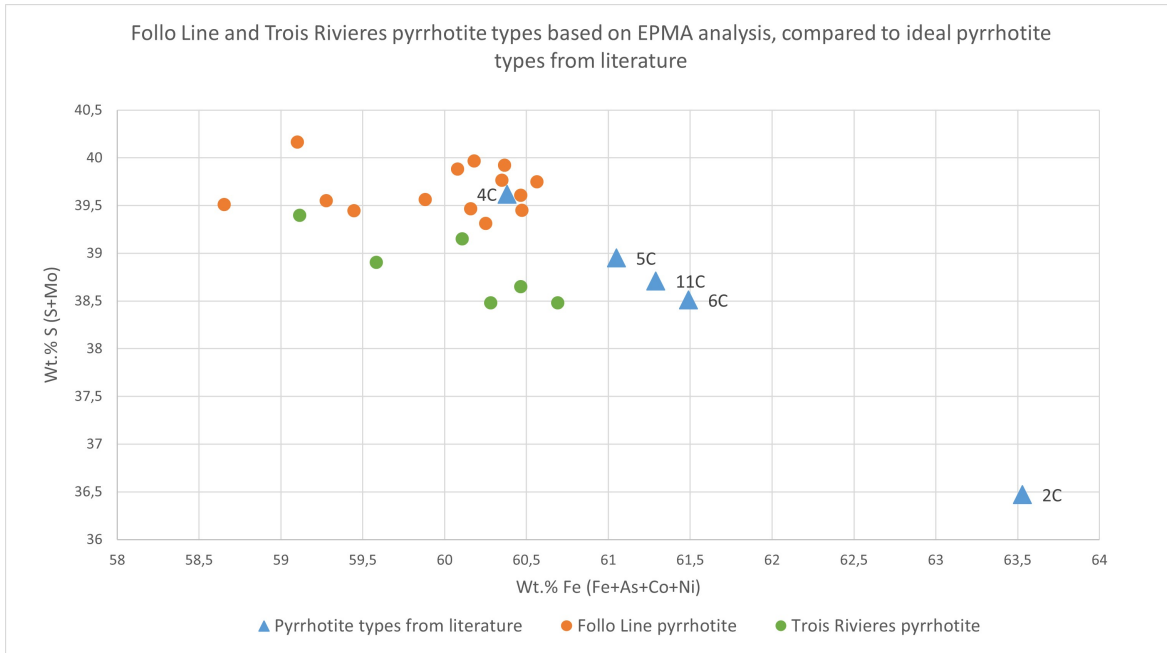


Figure 5.7: Pyrrhotite chemistry in the Follo Line- and Trois-Rivières aggregates by Electron Probe Micro Analysis (EPMA), compared to ideal pyrrhotite compositions obtained from Multani and Waters (2018).

5.4 Evaluation of techniques for analysing pyrrhotite and sulfur in aggregates for concrete

5.4.1 Total sulfur content by LECO and XRF

In coherency with this study's motivation, also commercial analytical techniques for the detection of total sulfur concentration were tested. The Norwegian standard on aggregate for concrete sets an upper limit on 1 wt% sulfur (S) (NS-EN12620, 2006). If there are indications of pyrrhotite, this limit is lowered to 0,1 wt%, or in practise 0,144 wt% since only one decimal is specified in the standard. LECO is recognised as an alternative method to acid digestion analysis for total sulfur determination in the standard. The analyses with LECO in this study was conducted externally at NBTL, which also delivers commercial testing of total sulfur for the majority of concrete aggregate producers in Norway.

Bunkholt (2014) tested the applicability of LECO and XRF on low concentrations of sulfides by analysing respectively S and Fe in spiked samples, and found that LECO was well suited for analysing low concentrations of sulfides. A similar approach was not possible in this study due to unknown sample material, with unknown elemental department of S and Fe. Although XRF is not suited for sulfur analysis due to sulfur escape during preparation, it is possible to compare results from XRF and LECO to investigate how consistent the sulfur escape is. Since results from previous XRF and LECO analyses on the Follo Line material also were available, it is possible to make comparisons with results from the current study on similar sample material, and evaluate the consistency of these techniques. Results from unpublished work by Postdoc Ben Snook and Associate Professor Kurt Aasly from the NTNU, are correlated with results from the current study in Figure 5.8. The 2019 LECO analysis was performed at the same apparatus externally at NBTL, but the 2019 XRF analysis was performed on a XRF apparatus (BRUKER S8 Tiger) that was replaced in 2020.

The plots in Figure 5.8 show a certain coherency between total S by LECO and XRF, despite the way too low values from XRF due to sulfur escape triggered by LOI. Also, the use of two different XRF apparatuses clearly affects the S analysis. A relative consistent deviation can be seen between the two XRF analyses from different year and apparatus, where the analysis from 2021 gave 0,002-0,004 wt% S less than in 2019. Note that the measured contents from XRF in 2021 were just above the SO₃ detection limit on 22 ppm (0,0022%). The values in the table are converted from oxides, as reported from the apparatus, with conversion factor 0.400459.

The LECO analyses from different occasions show very good consistency for samples FB-B, FB-C, FB-D and FB-E, which all are below the 0,1 wt% (in practise 0,144) S limit stated in NS-EN12620 (2006) if pyrrhotite is present. FB-A1 is above 0,144 wt% S on both occasions, and would have caused rejection of the aggregate for use in concrete if pyrrhotite were present. Based on LECO analyses, FB-A1 apparently lost sulfur from 2019 to 2021, while all other samples seemingly increased their sulfur content marginally in the same period. The situation for FB-A1 with decreasing sulfur content makes sense with respect to oxidation of sulfide minerals and gaseous sulfur escape. According to AM analyses, FB-A1 also had the largest sulfide content among the samples, which facilitates for the greatest reduction of S through oxidation between 2019 and 2021. The very small differences among the other samples are probably more related to analytical conditions and calibrations.

Overall, the LECO results from 2019 and 2021 are promising with respect to consistency of low sulfur analysis with this method. The case with FB-A1 also exemplifies the difficulties with sulfur analysis on powder material, where the oxidation of sulfide minerals followed by sulfur escape represents an uncontrollable factor.

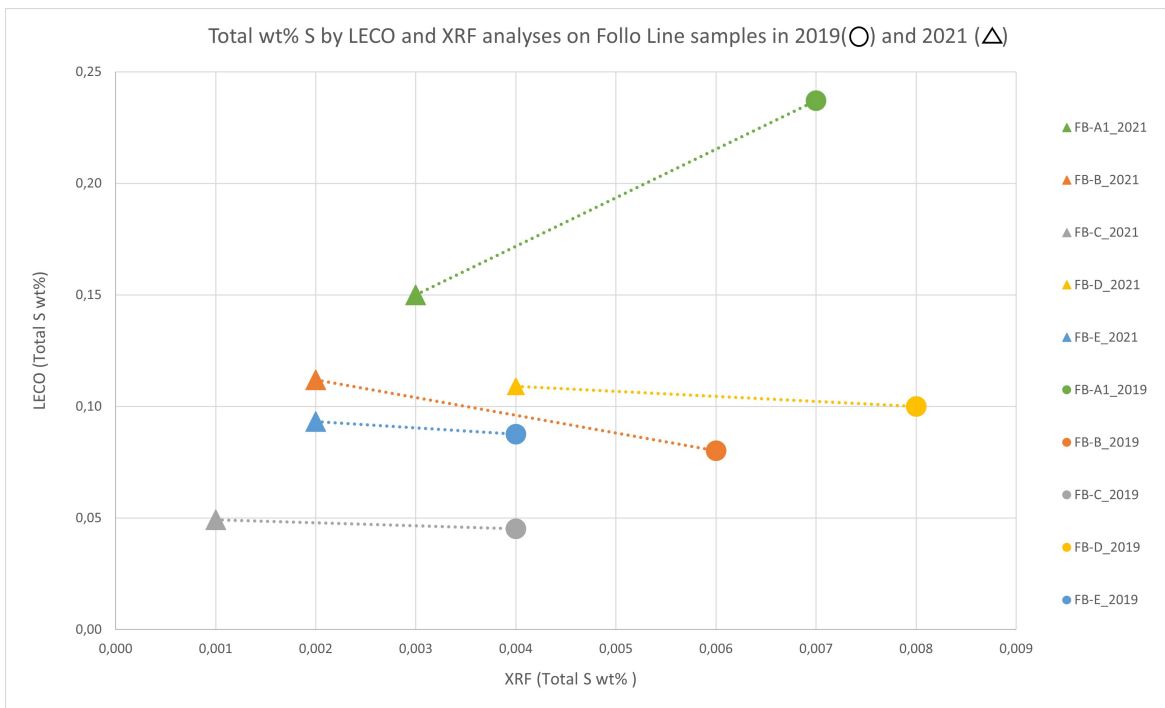


Figure 5.8: Total wt% sulfur by LECO and X-Ray Fluorescence (XRF) analyses on similar sample material from the Follo Line aggregates in 2019 and 2021. The analyses from 2019 are from the unpublished work by Postdoc Ben Snook and Associate Professor Kurt Aasly, and are included for comparison with results obtained in the current study.

5.4.2 X-Ray Diffraction (XRD)

Because of the general assumption of 1% detection limit with XRD analysis, this method is in principle not suited for quantification of pyrrhotite in low concentrations. It was attempted to quantify pyrite and pyrrhotite in the two materials investigated in this study anyway, since this method also was needed for bulk mineralogy estimations (Table 4.1 and 4.10). No clear evidence for pyrite or pyrrhotite was found in the two materials, but some characteristic peaks indicated pyrite in the Trois-Rivières material and pyrrhotite in the Follo Line material. These indications are contradictory to AM and OM analyses, which suggested far more pyrite than pyrrhotite in the Follo Line material, and more pyrrhotite than pyrite in the Trois-Rivières material. However, all iron sulfide concentrations reported by XRD were ≤ 1 wt%, and are therefore not considered any further.

5.4.3 Optical Microscopy (OM)

Small, but distinct differences in color make it possible to discriminate between the iron sulfides based on color without much experience on the optical microscope. Nevertheless, this will be far more easier to do if both pyrrhotite and pyrite are present and one is able to compare the colors. Fine-grained iron sulfides are difficult to discriminate properly with microscopy, due to limitations with magnification and clarity. This is especially an issue regarding aggregates for concrete, since these often may contain small amounts of very fine-grained and disseminated sulfides. For example, a minor chalcopyrite inclusion within pyrite in FB-B2 (Figure 4.4), was initially misidentified as pyrrhotite with optical microscopy, and corrected by AM afterwards.

If pyrrhotite-pyrite discrimination is difficult with color, the strong anisotropy of pyrrhotite gives a solid answer in most cases. However, one must be aware that not all pyrrhotite will show this anisotropy due to crystal orientations. If a mineral phase looks like pyrrhotite based on its smooth texture and creamy pale brown color, but lacks the characteristic anisotropy, it is most likely a pyrrhotite. In the Trois-Rivières material especially, several cases of pyrrhotite without visible anisotropy were observed. Pentlandite exsolution patterns are another common feature of pyrrhotite, which makes it easy to distinguish from pyrite. This flame-like feature was observed in almost all the Trois-Rivières pyrrhotite, but only once in the Follo Line pyrrhotite. Occurrence of pyrite flame-like exsolution within the Trois-Rivières pyrrhotite may easily be confused with the characteristic pentlandite structures. Be-

cause these types of exsolution not seem to be that common within pyrite, they nevertheless provide a solid indication towards pyrrhotite.

Exact discrimination of iron sulfides is certainly possible with OM, due to its different optical properties. However, the acquisition of statistically valid data through point counting is very time consuming, and may also suffer from subjective mineral identification errors. Concerning the issue with pyrrhotite in aggregate, OM investigations could still contribute as quality assurance for other techniques. This is especially useful with AM, since the same sample formats can be investigated by both techniques. Also, if pyrrhotite is indicated with DTA on a sample material, it should be possible to find pyrrhotite with OM in gravel sections from the same material.

5.4.4 Differential Thermal Analysis (DTA)

In Norway, Differential Thermal Analysis (DTA) plays a crucial role for the approval or rejection of aggregate for concrete if total S is above 0,144wt%. If so, DTA determines whether indications of pyrrhotite are present or not, with consequences whether the aggregate should be prohibited or allowed for use in concrete. This decision is based on interpretation of the DTA curve, where iron sulfides are indicated through strong exothermic signature peaks, due to oxidation reactions of the sulfides (Smykatz-Kloss, 1982).

Since pyrite represents the most common and widespread occurring sulfide mineral, it is likely that this mineral is present in a rock with more than 0,144% S. Overlapping peak characteristics for pyrite and pyrrhotite makes it very difficult to determine if only pyrite, pyrrhotite or both are present in a material. In all Follo Line samples analysed by DTA in this study, indications of pyrite and pyrrhotite were interpreted due to primary sulfide peaks at 460-470°C, between the typical oxidation ranges of pyrite (430-450°C) and pyrrhotite (480-520°C). The analyses on similar samples from unpublished work in 2019, resulted in primary sulfide peaks on temperatures 470-480°C. Although there is a 10-20 °C deviation between the analyses on different occasions, results still range between the typical pyrite and pyrrhotite temperature intervals, and a certain degree of reproducibility is proven. Oxidation of pyrrhotite during the time between the two analyses is a possible explanation of why sulfide peaks were closer to the typical pyrite-range in 2020 than in 2019.

All analyses on Trois-Rivières samples from 2019 and 2020 showed primary and secondary

peaks within the typical oxidation ranges of respectively pyrrhotite and pyrite (Table 4.11). This shows that material with larger amounts of pyrite and pyrrhotite will exhibit clearer signals, which in turn becomes easier to interpret. However, unlike with the Follo Line samples, primary and secondary peaks were registered at higher temperatures in 2020 than in 2019. This difference are probably not caused by pyrrhotite oxidation, but could be due to variations in sample amount and grain size. Kopp and Kerr (1958) used pyrite and marcasite to show that the first exothermic peak temperature decreased with grain size reduction and that total peak area increased with sample amount.

Such exact oxidation ranges as the ones used for interpretation at IGP/SINTEF could not be found elsewhere in the literature. This issue is recognised by e.g. Berg and Shlyapkina (1975) and Smykatz-Kloss (2012), emphasising the bad reproducibility and comparability of DTA results between different apparatuses and laboratories.

The knowledge and procedures on the apparatus and method used in this study, and in commercial testing for aggregate producers, seem to be largely based on experience transferred through generations at NTNU/SINTEF. The device undoubtedly has a high detection capability for low iron sulfide contents, proved by e.g. the indications in Follo Line samples, containing <0,35 wt% iron sulfides according to AM analyses. However, the discrimination between these sulfides with DTA seems to involve a great deal of uncertainty. The narrow, typical oxidation ranges suggested by the user manual at IGP are probably correct for that particular apparatus. However, there is a need for a method to validate the results from DTA, with less impact from subjective operator interpretations. Especially since this method alone, without any alternative or reference method, is trusted for delivering grounds for the decision on whether a deposit is allowed for use as concrete aggregate or not. It is regrettable if promising aggregate resources, where pyrite is the dominant sulfide mineral, become rejected due to diffuse results and interpretations influenced by a desire to *be on the safe side*.

5.4.5 Automated Mineralogy (AM)

The current study shows that the Zeiss Mineralogic Mining (AM) system has great ability for detection and quantification of iron sulfides in low concentrations. This is promising concerning the need for verification of results from DTA, which nowadays carry all the responsibility for detection of possibly deleterious pyrrhotite in concrete aggregates. In line with the objectives for this study, AM analyses were used for the characterisation of iron sulfides in two pyrrhotite-bearing aggregate materials.

A great advantage with AM is that mineral identification can be verified by optical microscope (OM), since the same sections can be investigated by both techniques. These techniques complement each other in the way that minerals with similar optical properties can be distinguished with AM, and minerals with similar chemical properties can be distinguished with OM. If a section is prepared for AM analysis, the obtained results can more or less be verified with OM. Iron sulfide identification with OM does not require thin sections, and can therefore be carried out on block samples. On the other hand, DTA do not allow such verification since this method involves destruction of the actual sample batch by oxidation reactions.

Discrimination between pyrrhotite and pyrite

The decisive factors of this operation were accuracy and consistency of EDS analyses in each pixel, and a mineral recipe that to the greatest extent classified the collected spectra from these pixels correctly into pyrrhotite or pyrite. The mineral recipe leading to fewest unclassified or misclassified pixels turned out to be the one based on iron(Fe)-content above or below 58 wt%, respectively classifying pyrrhotite or pyrite (Chapter 4.3). Note that this was the ideal distinguishing threshold with the analytical settings applied, described in Chapter 3.2.7. Different settings for e.g. dwell time per pixel and minimum spectrum counts are expected to influence the collection of spectra, used for mineral classification.

Difficulties with the discrimination involved some apparently Fe-rich areas within pyrite, ending up as misclassified pyrrhotite pixels. Based on BSE imaging and the elemental maps from EPMA, these areas did not seem to be local Fe-enrichments, but rather holes, cracks and irregularities in the pyrite. These features probably caused uneven collection of EDS spectra, which again resulted in artificially higher Fe measurements. The trick was therefore

to tolerate as much Fe as possible in pyrite, while simultaneously avoiding that too many pixels within real pyrrhotite were classified as pyrite. The best Fe-threshold for this purpose seemed to be 58 wt%. This content is considerably closer to the actual wt.% Fe in pyrrhotite than in pyrite. Table 5.3 show average Fe contents in pyrrhotite and pyrite from AM and EPMA, and those suggested by ideal formula. On average, AM measured 2-3 wt% higher Fe-content in pyrrhotite and pyrite compared to EPMA, which delivered contents not far from those suggested by ideal formulas. Due to this over-representation of Fe by AM, the discriminating threshold between pyrrhotite and pyrite had to be set as high as 58 wt% Fe.

Table 5.3: Summary of average Fe-content in pyrrhotite and pyrite in the Follo Line and Trois-Rivières samples by Automated Mineralogy (AM) mapping and Electron Probe Micro Analysis (EPMA). Ideal formula Fe-content for pyrite is obtained from Webmineral.com, by Barthelmy (2021). Ideal formula Fe- content range for pyrrhotite is from Multani and Waters (2018), and were presented in Table 2.2.

	Sample	Average Fe content (wt.%)		Fe content in ideal formula
		AM	EPMA	
Pyrrhotite	FB	61,54	59,59	60,38-63,53
	TR	62,81	59,53	
Pyrite	FB	49,61	45,74	46,55
	TR	49,49	45,28	

Since these minerals only consist of Fe and sulfur (S) and the collected spectra from each pixel always is normalised to 100, this Fe over-representation comes at the expense of S. Vice versa, this issue may also be caused by under-representation of S. Nevertheless, this skewness is probably caused by the much shorter dwell time per pixel in AM compared to point analyses by EPMA. A possible explanation is that Fe generates more counts (X-ray emissions) than S, since Fe has a higher atomic weight. By looking at differences in pixel data for e.g. pyrite and quartz, it is clear that far more spectrum counts are registered in pyrite than in quartz.

Pyrrhotite-Pyrite differentiation would most likely be easier with increased dwell time per pixel, as this gives analyses closer to the correct compositions. However, increased dwell time per pixel will cause a drastic increase in time consumption for the analysis. Average time consumption for 20 μm AM analysis on particulate thin sections in this study was 10 hours. Hence, an increase of dwell time per pixel from 0,01 s to 0,1 s will result in at least 100 hours per analysis for each section.

Becker (2009) and Bunkholt (2014) managed to discriminate different pyrrhotite types with BSE imaging by tweaking brightness and contrast settings. As shown in the current study,

the BSE contrast of pyrite and pyrrhotite is sufficient for the discrimination without much effort adjusting brightness and contrast settings. The limitation for the discrimination based on BSE, is that back scattering only generates a grey scale image, corresponding to average atomic number. This does not compile any statistical, compositional data such as those acquired by EDS. It was attempted to systematise the grey values of pyrite and pyrrhotite pixels from an analysis that produced image where a clear difference could be seen. Unfortunately, these numbers did not make much sense in the current study. However, if different grey values are assigned pyrrhotite and pyrite and the discrimination based on EDS is correct, it should be possible to see a trend in the numbers behind the grey values (0-255).

Possible applications with Automated Mineralogy for pyrrhotite detection in the concrete aggregate standard NS-EN 12620

As stated in the concrete aggregate standard NS-EN12620 (2006), it is only an indication of pyrrhotite that decides if the sulfur limit value should be lowered, not the amount of pyrrhotite. In the Follo Line gneisses, indications of pyrrhotite were definitely present in some of the samples, proven by Optical Microscopy and Automated Mineralogy in this study. The potential harm these indications of pyrrhotite (<0,05 wt%) could cause in a concrete structure is simply not known today. However, we do know with some certainty that the 0,3-0,9 wt% pyrrhotite in the Trois-Rivières aggregates had severe deleterious effects on concrete structures (Rodrigues, 2016). The difference in pyrrhotite content for the Follo Line- and the Trois-Rivières aggregates is large, as shown in Figure 5.9 on the next page. If we are able to find out which amounts of pyrrhotite that are dangerous for concrete, an idea could be to allow amounts considered as harmless in the standard. Quantification of iron sulfides by the aid of AM analysis would in that case play a crucial role, as this probably is the most precise way of obtaining statistically valid data on low amounts of such minerals with similar chemistry.

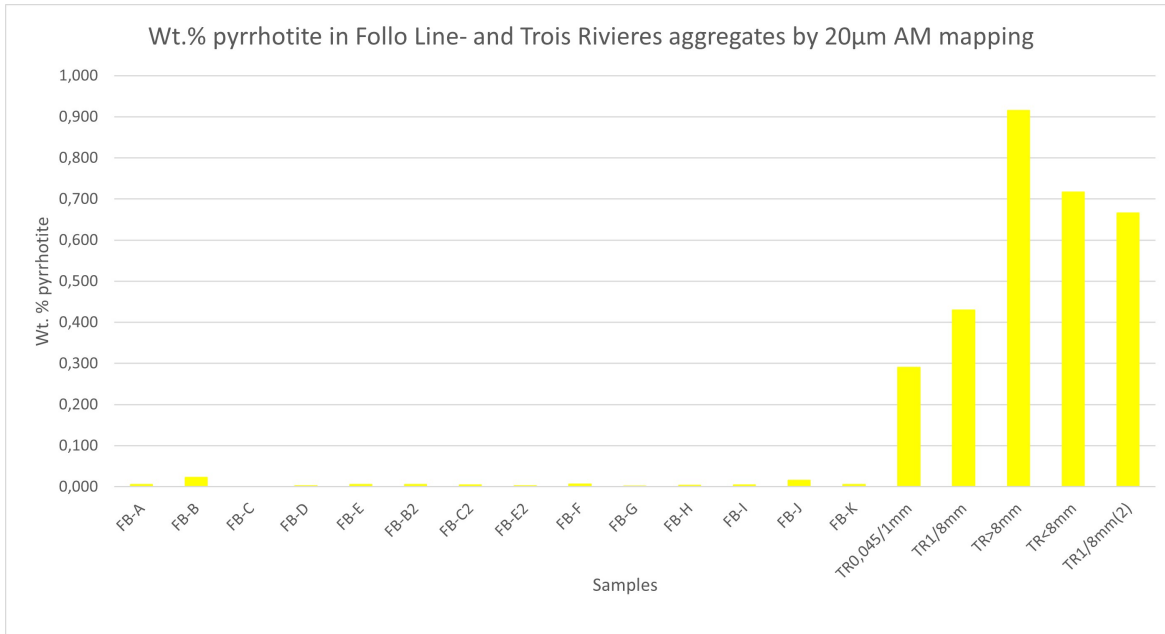


Figure 5.9: Wt.% pyrrhotite content in the Follo Line- and Trois-Rivières aggregates by 20 µm Automated Mineralogy (AM) mapping.

Scott and Rollinson (2015) performed AM analysis on aggregate material in whole-rock thin sections, and outlined the bad representativeness with these sections if petrographic variations occur in a quarry. Analyses on gravel/grain mounts or thin sections are probably more representative than whole-rock sections if crushing, sample splitting and preparation are performed properly. AM analysis on a certain number of blocks with different fractions, like in Figure 5.6, could for example be incorporated into the standard for detection of pyrrhotite when sulfur content is $>0,10\%$, and/or DTA deliver unclear results. Although this is a much more expensive and time consuming approach than only performing DTA, it provides a much better basis for approval or rejection on aggregate with sulfur content around the acceptance limit.

A possibility is to perform Bright Phase Search (BPS) to identify the iron sulfides and further high resolution mapping ($1-5\mu\text{m}$) to discriminate among these. This will significantly reduce time consumption of the analysis, since common rock forming minerals will not be analysed or incorporated in the mineral recipe. However, if the purpose is exact quantification of the iron sulfides, it would require additional work to create and adjust a customised mineral recipe that can catch up all minerals present in the rock. If the purpose only is to check if indications of pyrrhotite are present, like it is with the DTA, there is no need for such a detailed mineral recipe.

The considerations above lead forward to two possible applications with Automated Mineralogy mapping, that have potential to be implemented in the concrete aggregate standard.

1. Detection of pyrrhotite indications

- Purpose: Detection of pyrrhotite on occasions where DTA results are diffuse and difficult to interpret. Examples of such results are curve peaks within the typical range of sulfide oxidation, but outside, or between pyrite and pyrrhotite ranges (Figure 4.2).
- Resolution: Bright Phase Search (BPS) + high resolution (1-5 μm) mapping.
- Mineral Recipe: Limited to iron sulfides, or ultimately only pyrite and pyrrhotite.
- Sample format: Particulate stub- or thin section.

2. Detection and quantification of pyrrhotite

- Purpose: Quantification of the complete rock mineralogy is needed to estimate the pyrrhotite concentration. This estimation would be necessary if an upper limit of pyrrhotite content is discovered to be harmless and permitted for use in concrete.
- Resolution: Medium resolution (10-20 μm) mapping of entire samples.
- Mineral recipe: Customised and unique recipes are needed for each rock type in order to classify all minerals present. Petrographical variations within the deposit could require adjustments of the recipe.
- Sample format: Particulate thin section. Adjustments of the mineral recipe to classify translucent minerals require verification with transmitted light microscopy. Stub samples are limited to reflected light microscopy.

The first proposal may serve as an alternative, or as replacement of DTA, where the purpose is to deliver analyses that with accuracy and certainty can tell if pyrrhotite is present or not.

The second proposal is quite uncertain in the nearest future due to missing research basis on the deterioration potential of different amounts of pyrrhotite. Time consumption and labour intensive work with the complete mineral recipes are also drawbacks with this approach. Complex and fine-grained mineral distributions are likely to occur in most rock types, and represents a challenge for AM analyses. Sericitisation textures in plagioclase from the Follo

Line samples was for example way too fine-grained to achieve detailed imaging with 20 μm mapping. Such features often results in a mixture of signals from different phases, making the mineral classification difficult to resolve, which in turn increases time consumption. A sufficiently small pixel size could partly solve this issue, but this will also increase time consumption significantly. Resolution on 20 μm is probably sufficient for bulk mineralogy estimations, but not for catching up alteration textures or fine-grained accessory minerals.

Scott and Rollinson (2015) praised the objectivity of the AM-procedure compared to traditional mineral identification and quantification with optical microscopy. They further suggested that AM could be used by companies to formally describe their aggregate products. If such detailed mineral quantification is desirable and useful for the industry, then the comprehensive and time consuming rock quantification from the second proposal suddenly becomes more interesting.

Chapter 6

Conclusions

The main objectives for this study were to characterise two different pyrrhotite-bearing aggregate materials, and evaluate different test methods on their applicability for detection and discrimination of iron sulfides. Main findings of the study are summarised in the following.

- The iron sulfides in the Follo Line aggregates are predominantly made up of pyrite (0,172 wt%), with traces of chalcopyrite (0,009 wt%) and pyrrhotite (0,006 wt%) according to Automated Mineralogy (AM) analyses. Pyrrhotite shows low degree of weathering, and appear disseminated and in close association with the other sulfides. The composition of pyrrhotite is almost equivalent to the 4C type (Fe_7S_8), with average 59,59 wt% iron and 39,61 wt% sulfur, according to Electron Probe Micro Analysis (EPMA).
- The Trois-Rivières aggregates contain several metal-bearing sulfides, where the most prominent are pyrrhotite (0,604 wt%), pyrite (0,596 wt%), pentlandite (0,136 wt%) and chalcopyrite (0,061 wt%). Pyrrhotite is extensively weathered throughout grains in the finest fraction (0,045/1mm), which also shows the highest degree of pyrrhotite liberation. This fraction contains more oxidation products (Fe-sulfate and Fe-oxides) than the larger fractions. The sulfides appear predominantly in particles dominated by mafic minerals (e.g. anorthite, pyroxenes), while felsic particles (quartz, albite, K-feldspar) contain less sulfides. The composition of the Trois-Rivières pyrrhotite is most similar to 4C pyrrhotite (Fe_7S_8), with average 59,53 wt% iron and 38,80 wt% sulfur, according to Electron Probe Micro Analysis (EPMA).

- Based on the relation between pyrrhotite liberation and grade of weathering among the Trois Rivières samples, it is suggested that the finer fractions (<1mm) of pyrrhotite-bearing aggregates should be considered as the most harmful with respect to concrete deterioration.
- Differential Thermal Analysis (DTA) on the Follo Line aggregates shows broad curves within the sulfide oxidation range, and peaks between the typical oxidation ranges of pyrrhotite and pyrite. These results are difficult to interpret into certain indications of pyrrhotite and pyrite, and demonstrates the weakness and insecurity of the DTA method. Both sulfides were indicated in all samples, since neither of them could be excluded based on the intermediate peaks. DTA on the Trois-Rivières samples shows distinct peaks for pyrite and pyrrhotite in their respective oxidation ranges.
- One out of five Follo Line samples exceed the 0,144 sulfur limit stated in NS-EN12620 (2006), and would have been rejected for use in concrete due to possible indications of pyrrhotite by DTA. All three Trois-Rivières samples exceed the 0,144 sulfur limit and would have been rejected according to NS-EN12620 (2006) due to obvious indications of pyrrhotite from DTA.
- The most optimal mineral recipe for discrimination of pyrrhotite and pyrite with AM distinguishes based on iron content above (\geq) or below ($<$) 58 wt%, respectively. Only a few misclassified pyrrhotite pixels appeared within pyrite with this recipe. Note that this is the optimal threshold for the analytical settings applied in this study, and is likely to shift if e.g. dwell time per pixel is changed.
- Based on pyrrhotite detection in the Follo Line samples with 20 μ m AM mapping and verifications by optical microscopy, the analytical detection limit for pyrrhotite is in the range 0,004-0,007 wt%.
- Automated Mineralogy can be applied in the concrete aggregate standard NS-EN12620 (2006) for pyrrhotite detection and quantification in gravel samples. The diffuse results from DTA on pyrrhotite in low concentrations reveal the need for alternative methods with higher precision.
- LECO analysis for total sulfur content showed good correlation with previous results on the same sample material. Main element analysis with X-Ray Fluorescence (XRF) is not suited for total sulfur analysis due to sulfur escape during fusion in the sample preparation process.

- The unsuitability of X-Ray Diffraction (XRD) for detection of iron sulfides in low concentrations (<1 wt%) was confirmed in this study.
- Formation of pyrrhotite in the Follo Line granodioritic gneisses and the Trois-Rivières gabbro norite most likely happened through sulfur-silica immiscibility in melts, hydrothermal precipitation, and sulfur release from pyrite during metamorphism. These are probably the most important formation processes for the accessory pyrrhotite related to rocks used as concrete aggregates. Prediction of pyrrhotite traces based on the geological history of a rock seems unlikely due to the close relation of this mineral with pyrite, commonly occurring in all rock types.

6.1 Recommendations for further research

- The suggestions for implementing pyrrhotite detection by AM in the concrete aggregate standard need to be tested on different aggregate rock types. The proposal focusing on pyrrhotite detection with Bright Phase Search (BPS) is most realistic in the short term and should be prioritised.
- The AM mineral recipes from this study should be tested on other sample material with similar petrology, to investigate if it is possible to have all-round recipes that quantifies mineralogy in different rocks within the same domain. The Follo Line recipe should be tested on samples of other granitic-dioritic gneisses, while the Trois-Rivières recipe should be tested on other gabbros.
- Spiked samples with low-concentrations of pyrite, pyrrhotite, pentlandite and chalcopyrite should be analysed by DTA and AM to investigate how the DTA curve responds on different proportions of these minerals.
- Samples with pyrrhotite and pyrite should be analysed several times with different dwell time per pixel to see if the effect with over-representation of iron at the expense of sulfur gets smaller with increased dwell time. This effect was recognised in the current study, making pyrrhotite-pyrite discrimination more challenging.
- Chemical analyses for all pyrrhotite and pyrite pixels in a sample can be extracted and plotted in Fe/S diagrams. The resulting patterns will probably give good indications on how well the discrimination has been. With high resolution and a generous dwell time per pixel, it could be possible to indicate different pyrrhotite types on such plots.

During the work with the Mineralogic Mining system used in this study, some areas of improvement with the software were noticed:

- Higher efficiency and more help with mineral identification in the post-processing workflow is favourable. For example, automatic grouping of phases with similar chemistry based on selected premises could be incorporated to help the operator systematise the phases present.
- Data sets from the AM analysis takes up much space, and the following post-processing of many samples generate huge amounts of data. This makes the program and file management slower. Old re-processed data sets should be easier to delete from the system. In today's solution, each re-processed data set must be loaded before it can be deleted, which takes quite some time. A *select and delete* option would be a useful application.
- The chemical analyses of each pixel obtained from mapping on a whole section represents a huge database of detailed chemical information on all phases. Today's solution only offers an option to extract all pixel data into text files. Since this generates large data sets that may be difficult to maneuver, it should be possible to extract the pixel data of selected mineral classifications.

Bibliography

- Aasly, K. A., Margreth, A., Erichsen, E., Rise, T., and Alnæs, L.-I. (2019). Forundersøkelser og bruk av kortreist stein. En geologisk veileder. *Kortreist Stein*.
- Allen, T. (2003). *Powder Sampling and Particle Size Determination*. Elsevier.
- Alsén, N. (1925). Röntgenographische Untersuchung der Kristallstrukturen von Magnetkies, Breithauptit, Pentlandit, Millerit und verwandten Verbindungen. *Geologiska Föreningen i Stockholm Förhandlingar*, 47(1):19–72.
- Andersen, J. C., Rollinson, G. K., Snook, B., Herrington, R., and Fairhurst, R. J. (2009). Use of QEMSCAN® for the characterization of Ni-rich and Ni-poor goethite in laterite ores. *Minerals Engineering*, 22(13):1119–1129.
- Arnold, R. (1967). Range in composition and structure of 82 natural terrestrial pyrrhotites. *The Canadian Mineralogist*, 9(1):31–50.
- Baker, D. R. and Moretti, R. (2011). Modeling the Solubility of Sulfur in Magmas: A 50-year Old Geochemical Challenge. *Reviews in Mineralogy and Geochemistry*, 73(1):167–213.
- Barthelmy, D. (2021). Webmineral - Mineralogy Database. Available at <http://webmineral.com/> (2021/04/25).
- Becker, M. (2009). *The mineralogy and crystallography of pyrrhotite from selected nickel and PGE ore deposits and its effect on flotation performance*. PhD thesis, University of Pretoria, Pretoria.
- Becker, M., Ekmekci, Z., de Villiers, J., and Bradshaw, D. J. (2010). The mineralogy and reactivity of pyrrhotite from selected nickel ore deposits and its effect on flotation performance. In *XXV International Mineral Processing Congress 2010, IMPC 2010*, volume 4, pages 2785–2796. Australasian Institute of Mining and Metallurgy.

-
- Belzile, N., Chen, Y.-W., Cai, M.-F., and Li, Y. (2004). A Review on Pyrrhotite Oxidation. *Journal of Geochemical Exploration*, 84(2):65–76.
- Berg, L. and Shlyapkina, E. (1975). Characteristic features of sulphide mineral DTA. *Journal of thermal analysis*, 8(3):417–426.
- Blaskovich, R. J. (2013). Characterizing waste rock using automated quantitative electron microscopy. Master's thesis, University of British Columbia, Vancouver.
- Boni, M., Rollinson, G., Mondillo, N., Balassone, G., and Santoro, L. (2013). Quantitative mineralogical characterization of karst bauxite deposits in the southern Apennines, Italy. *Economic Geology*, 108(4):813–833.
- Bunkholt, I. O. (2014). *The implications of sulphides in GCC feed and the potential for their removal during alkaline amine flotation*. PhD thesis, Norwegian University of Science and Technology, Trondheim.
- Carpenter, R. H. and Desborough, G. A. (1964). Range in solid solution and structure of naturally occurring troilite and pyrrhotite. *American Mineralogist: Journal of Earth and Planetary Materials*, 49(9-10):1350–1365.
- Chinchón, J., Ayora, C., Aguado, A., and Guirado, F. (1995). Influence of weathering of iron sulfides contained in aggregates on concrete durability. *Cement and concrete research*, 25(6):1264–1272.
- Corlett, M. (1968). Low-iron polymorphs in the pyrrhotite group. *Zeitschrift für Kristallographie-Crystalline Materials*, 126(1-3):124–134.
- Craig, J. R., Vaughan, D. J., and Hagni, R. D. (1981). *Ore Microscopy and Ore Petrography*. Wiley, New York.
- Craig, J. R. and Vokes, F. M. (1993). The metamorphism of pyrite and pyritic ores: an overview. *Mineralogical Magazine*, 57(386):3–18.
- Crisp, J. A. and Spera, F. J. (1987). Pyroclastic flows and lavas of the Mogan and Fataga formations, Tejeda Volcano, Gran Canaria, Canary Islands: mineral chemistry, intensive parameters, and magma chamber evolution. *Contributions to Mineralogy and Petrology*, 96(4):503–518.
- Danielsen, S., Hagelia, P., Wigum, B., De Weerd, K., Aasly, K., Lindgård, J., and Pedersen, B. (2019). *Magnetkis i betongtilslag. Betydning for betongs bestandighet*. NPRA, State-of-the-art report.

- Deer, W., Howie, R., and Zussman, J. (2013). *An Introduction to the Rock-Forming Minerals*. The Mineralogical Society, London, 3 edition.
- Dekkers, M. (1988). Magnetic properties of natural pyrrhotite Part I: Behaviour. *Physics of the Earth and Planetary Interiors*, 52:376–393.
- Duffy, D., Garg, S., Washer, C., Grammatikopoulos, T., and Papangelakis, V. (2015). Mineralogical characterization of Sudbury pyrrhotite tailings: Evaluating the bioleaching potential. *COM 2015, The Conference of Metallurgists*, pages 1–10.
- Evans, H. T. (1970). Lunar troilite: Crystallography. *Science*, 167(3918):621–623.
- Fandrich, R., Gu, Y., Burrows, D., and Moeller, K. (2007). Modern SEM-based mineral liberation analysis. *International Journal of Mineral Processing*, 84(1-4):310–320.
- Fladvad, M. (2020). *Optimal utilisation of unbound crushed aggregates for road construction*. PhD thesis, Norwegian University of Science and Technology, Trondheim.
- Földvári, M. (2011). *Handbook of thermogravimetric system of minerals and its use in geological practice*. Geological Institute of Hungary Budapest.
- Francis, C., Fleet, M., Misra, K., and Craig, J. (1976). Orientation of exsolved pentlandite in natural and synthetic nickeliferous pyrrhotite. *American Mineralogist*, 61:913–920.
- Gordon, S. C. and McDonald, A. M. (2015). A Study of the Composition, Distribution, and Genesis of Pyrrhotite in the Copper Cliff Offset, Sudbury, Ontario, Canada. *Canadian Mineralogist*, 53(5):859–878.
- Gottlieb, P. (2008). The Revolutionary Impact of Automated Mineralogy on Mining and Mineral Processing. In *The XXIV International Mineral Processing Congress*, pages 165–174.
- Gottlieb, P., Wilkie, G., Sutherland, D., Ho-Tun, E., Suthers, S., Perera, K., Jenkins, B., Spencer, S., Butcher, A., and Rayner, J. (2000). Using Quantitative Electron Microscopy for Process Mineralogy Applications. *The Journal of the Minerals, Metals & Materials Society*, 52(4):24–25.
- Graham, S., Brough, C., and Cropp, A. (2015). An Introduction to ZEISS Mineralogic Mining and the correlation of light microscopy with automated mineralogy: a case study using BMS and PGM analysis of samples from a PGE-bearing chromitite prospect. *Zeiss Natural Resources Lab*.

-
- Grant, D., Goudie, D., Shaffer, M., and Sylvester, P. (2016). A single-step trans-vertical epoxy preparation method for maximising throughput of iron-ore samples via SEM-MLA analysis. *Applied Earth Science*, 125(1):57–62.
- Graversen, O. (1984). Geology and structural evolution of the Precambrian rocks of the Oslofjord-Øyeren area, Southeast Norway. *NGU Bulletin 398*.
- Gu, Y. (2003). Automated Scanning Electron Microscope Based Mineral Liberation Analysis: An Introduction to JKMRC/FEI Mineral Liberation Analyser. *Journal of Minerals and Materials Characterization and Engineering*, 2(1):33–41.
- Haugen, M. and Lindgård, J. (2019). Determination of total sulphur content in aggregates (2004-2018) - results from SINTEF. In *Magnetkis i betongtilslag. Betydning for betongs bestandighet*, pages 92–97. NPRA reports.
- Hjelen, J. (1989). Scanning elektron-mikroskopi. *Metallurgisk institutt, NTH*.
- Hrstka, T., Gottlieb, P., Skala, R., Breiter, K., and Motl, D. (2018). Automated mineralogy and petrology-applications of TESCAN Integrated Mineral Analyzer (TIMA). *Journal of Geosciences*, 63(1):47–63.
- Jana, D. (2018). Pyrrhotite Epidemic in Eastern Connecticut: Diagnosis and Prevention. *ACI Materials Journal*, 117:61–70.
- Jensen, V. (2019). Total S and Pyrrhotite in Norwegian concrete aggregate deposits. Statistical assessment from NBTLs database over projects. In *Magnetkis i betongtilslag. Betydning for betongs bestandighet*, pages 98–106. NPRA reports.
- Jernbaneverket (2011). Konsekvensutredning for Follobanen. Temarapport – Grunnforhold. HØRINGSUTGAVE.
- Kenis, P., Skurzyński, J., Jary, Z., and Kubik, R. (2020). A new methodological approach (QEMSCAN®) in the mineralogical study of Polish loess: Guidelines for further research. *Open Geosciences*, 12(1):342–353.
- Kissin, S. A. and Scott, S. (1982). Phase relations involving pyrrhotite below 350 degrees C. *Economic Geology*, 77(7):1739–1754.
- Kopp, O. C. and Kerr, P. F. (1958). Differential thermal analysis of pyrite and marcasite. *American Mineralogist: Journal of Earth and Planetary Materials*, 43(11-12):1079–1097.

- Koto, K., Morimoto, N., and Gyobu, A. (1975). The superstructure of the intermediate pyrrhotite. I. Partially disordered distribution of metal vacancy in the 6C type, $\text{Fe}_{11}\text{S}_{12}$. *Acta Crystallographica Section B: Structural Crystallography and Crystal Chemistry*, 31(12):2759–2764.
- Kullerud, G. and Yoder, H. S. (1959). Pyrite stability relations in the Fe-S system. *Economic Geology*, 54(4):533–572.
- Kwitko-Ribeiro, R. (2012). New Sample Preparation Developments to Minimize Mineral Segregation in Process Mineralogy. In *Proceedings of the 10th International Congress for Applied Mineralogy (ICAM)*, pages 411–417.
- Lara, R. H., Monroy, M. G., Mallet, M., Dossot, M., González, M. A., and Cruz, R. (2015). An experimental study of iron sulfides weathering under simulated calcareous soil conditions. *Environmental Earth Sciences*, 73(4):1849–1869.
- Letard, I., Saintavit, P., and Deudon, C. (2007). XMCD at Fe L2, L3 edges, Fe and SK edges on Fe_7S_8 . *Physics and Chemistry of Minerals*, 34(2):113–120.
- Lide, D. (2004). Handbook of chemistry and physics, 84th edition. *CRC Press*, page 2475.
- Mackenzie, R. and Mitchell, B. (1962). Differential Thermal Analysis. A Review. *Analyst*, 87(1035):420–434.
- Marshall, D., Anglin, C., and Mumin, H. (2004). *Ore Mineral Atlas*. Geological Association of Canada, Newfoundland, 1. edition.
- Mauk, J., Crafford, T., Horton, J., Carma, S., and Robinson Jr, G. (2020). Pyrrhotite Distribution in the Conterminous United States. *Mineral Resources Program*.
- Mindat (2020). Mindat. Available at <https://www.mindat.org/min-2901.html> (2020/10/05).
- Moncur, M., Jambor, J., Ptacek, C., and Blowes, D. (2009). Mine drainage from the weathering of sulfide minerals and magnetite. *Applied Geochemistry*, 24(12):2362–2373.
- Morimoto, N., Gyobu, A., Tsukuma, K., and Koto, K. (1975). Superstructure and non-stoichiometry of intermediate pyrrhotite. *American Mineralogist: Journal of Earth and Planetary Materials*, 60(3-4):240–248.
- Multani, R. S. and Waters, K. E. (2018). A review of the physicochemical properties and flotation of pyrrhotite superstructures ($4\text{C-Fe}_7\text{S}_8/5\text{C-Fe}_9\text{S}_{10}$) in Ni-Cu sulphide mineral processing. *The Canadian Journal of Chemical Engineering*, 96(5):1185–1206.

- Nakazawa, H. and Morimoto, N. (1971). Phase relations and superstructures of pyrrhotite, Fe_{1-x}S . *Materials Research Bulletin*, 6(5):345–357.
- NGU (2020). National bedrock database. Available at http://geo.ngu.no/kart/berggrunn_mobil/ (2020/10/01).
- Nicholson, R. V. and Scharer, J. M. (1994). Laboratory Studies of Pyrrhotite Oxidation Kinetics. *ACS Symposium Series*.
- NS-EN12620 (2006). Aggregates for concrete. Standard ICS 91.100.15/30, European Committee for Standardization (CEN), Brussels, Belgium.
- NS-EN1744-1 (2009). Test for chemical properties of aggregates – Part 1: Chemical analysis. Standard ICS 71.040.40;91.100.15, European Committee for Standardization (CEN), Brussels, Belgium.
- Parat, F., Holtz, F., and Streck, M. J. (2011). Sulfur-bearing Magmatic Accessory Minerals. *Reviews in Mineralogy and Geochemistry*, 73(1):285–314.
- Perroud, P. (2021). Athena - Mineral Search. Available at <http://athena.unige.ch/athena/mineral/search.html> (2021/04/25).
- Pirrie, D. and Rollinson, G. K. (2011). Unlocking the applications of automated mineral analysis. *Geology Today*, 27(6):226–235.
- Pooler, R. and Dold, B. (2017). Optimization and Quality Control of Automated Quantitative Mineralogy Analysis for Acid Rock Drainage Prediction. *Minerals*, 7(1):12.
- Pratt, A., Muir, I., and Nesbitt, H. (1994). X-ray photoelectron and Auger electron spectroscopic studies of pyrrhotite and mechanism of air oxidation. *Geochimica et Cosmochimica Acta*, 58(2):827–841.
- Rahman, M. and Bassuoni, M. (2014). Thauasite sulfate attack on concrete: Mechanisms, influential factors and mitigation. *Construction and Building Materials*, 73:652–662.
- Reed, S. J. B. (2005). *Electron Microprobe Analysis and Scanning Electron Microscopy in Geology*. Cambridge university press.
- Rise, T., Alæs, L., and Rambæk, I. (2019). Kortreist stein: Oppnådde resultater (2016-2019). *Kortreist Stein*.
- Robb, L. (2005). *Introduction to Ore-Forming Processes*. Blackwell, Oxford, 1. edition.

- Rodrigues, A. D. A. (2016). *Concrete deterioration due to sulfide-bearing aggregates*. PhD thesis, Université Laval, Québec.
- Rodríguez-Losada, J. A. and Martínez-Frías, J. (1998). Ancient oxide-and sulphide-mineralization in the islands of Tenerife and La Gomera (Canary Archipelago, Spain). *Mineralium Deposita*, 33(6):639–643.
- Røisi, I. and Aasly, K. (2018). The effect of graphite filler in sample preparation for automated mineralogy – a preliminary study. *Mineralproduksjon*, 8.
- Sandmann, D. (2015). *Method development in automated mineralogy*. PhD thesis, Technische Universitaet Bergakademie Freiberg Universitaetsbibliothek, Freiberg.
- Schulz, B., Sandmann, D., and Gilbricht, S. (2020). SEM-Based Automated Mineralogy and its Application in Geo-and Material Sciences. *Minerals*, 10(11):1004.
- Scott, P. and Rollinson, G. (2015). Crushed rock aggregates: Their mineralogy and textures using automated scanning electron microscope. *Proceedings of the 18th Extractive Industry Geology Conference, EIG conferences Ltd*.
- Smykatz-Kloss, W. (1982). Application of differential thermal analysis in mineralogy. *Journal of Thermal Analysis and Calorimetry*, 23(1-2):15–44.
- Smykatz-Kloss, W. (2012). *Differential Thermal Analysis: Application and Results in Mineralogy*. Springer Science & Business Media.
- Sørløkk, T., Rokoengen, K., and Nilsen, B. (2007). *Geologiske laboratorieundersøkelser*. NTNU - Institutt for Geologi og Bergteknikk.
- Streckeisen, A. (1976). To each plutonic rock its proper name. *Earth-science reviews*, 12(1):1–33.
- Sutherland, D. and Gottlieb, P. (1991). Application of automated quantitative mineralogy in mineral processing. *Minerals Engineering*, 4(7-11):753–762.
- Tokonami, M., Nishiguchi, K., and Morimoto, N. (1972). Crystal structure of a monoclinic pyrrhotite (Fe₇S₈). *American Mineralogist: Journal of Earth and Planetary Materials*, 57(7-8):1066–1080.
- Toulmin, P. and Barton, P. (1963). A thermodynamic study of pyrite and pyrrhotite. *Geochimica et Cosmochimica Acta*, 28(5):641–671.

- Vaughan, D. J. and Craig, J. R. (1978). *Mineral chemistry of metal sulfides*. Cambridge University Press, Cambridge, 1. edition.
- Vaughan, D. J., Schwarz, E. J., and Owens, D. R. (1971). Pyrrhotites from the Strathcona Mine, Sudbury, Canada; A thermomagnetic and mineralogical study. *Economic Geology*, 66(8):1131–1144.
- von Gehlen, K. and Pillier, H. (1965). Optics of hexagonal pyrrhotite (Fe_9S_{10}). *Mineralogical Magazine and Journal of the Mineralogical Society*, 35(270):335–346.
- Wallace, P. J. and Edmonds, M. (2011). The Sulfur Budget in Magmas: Evidence from Melt Inclusions, Submarine Glasses, and Volcanic Gas Emissions. *Reviews in Mineralogy and Geochemistry*, 73(1):215–246.
- Wang, H. and Salveson, I. (2005). A review on the mineral chemistry of the non-stoichiometric iron sulphide, Fe_{1-x}S ($0 \leq x \leq 0.125$): polymorphs, phase relations and transitions, electronic and magnetic structures. *Phase transitions*, 78(7-8), page 547–567.
- Warlo, M., Wanhainen, C., Bark, G., Butcher, A. R., McElroy, I., Brising, D., and Rollinson, G. K. (2019). Automated Quantitative Mineralogy Optimized for Simultaneous Detection of (Precious/Critical) Rare Metals and Base Metals in a Production-Focused Environment. *Minerals*, 9(7):440.
- Whateley, M. K. and Scott, B. C. (2006). Evaluation Techniques. In *Introduction to Mineral Exploration*, chapter 10, pages 199–252. Blackwell publishing, Malden, MA, USA.
- Whitney, D. L. and Evans, B. W. (2010). Abbreviations for Names of Rock-Forming Minerals. *American mineralogist*, 95(1):185–187.
- Winter, J. D. (2013). *Principles of Igneous and Metamorphic Petrology*. Cambridge University Press, New York.
- Wuensch, B. J. (1963a). On the superstructure and twinning of Pyrrhotite. *Mineralogical society of America, Special paper 1*, pages 157–162.
- Wuensch, B. J. (1963b). *The nature of the crystal structures of some sulfide minerals with substructures*. PhD thesis, Massachusetts Institute of Technology, United States of America.
- Young, C. A. (2019). *SME Mineral Processing and Extractive Metallurgy Handbook*. Society for Mining, Metallurgy & Exploration.

- Ytterdal, S. G. (2019). Lessons learned from the Follo Line Project. In *Magnetkis i betongtilslag. Betydning for betongs bestandighet*, pages 84–91. NPRA reports.
- Zapletal, K. (1993). Effect of intergrowths of the ferrimagnetic and antiferromagnetic phases on the rock magnetic properties of natural pyrrhotites. *Physics of the Earth and Planetary Interiors*, 76, pages 151–162.
- Zapletal, K. and Janák, F. (1972). On the magnetic phases of natural pyrrhotites. *Studia Geophysica et Geodaetica*, 16(2):167–176.
- Zeiss (2017). Zeiss Mineralogic Mining - Your Solution for Automated Mineral analysis 2.0. *Product Information, Carl Zeiss Microscopy*.

Appendices

A Sample preparation

Table 1: Summary of sample splitting, weighing and selection of subsamples for the gravel material from Follo Line and Trois-Rivières aggregates.

Sample FB-A1 Tot. weight before sample split = 313,8g						
Subsample	Subsample weight (g)	TS prep.	XRD	XRF	DTA	LECO
1	34,9					
2	31,2		x	x	x	x
3	27,1					
4	30,1					
5	30,8		x	x	x	x
6	31,5					
7	27,7					
8	32,4					
9	29,4					
10	35,5					
Sum	310,6					
Loss	3,2					
Mean	31,06					

Sample FB-B Tot. weight before sample split = 383,36g						
Subsample	Subsample weight (g)	TS prep.	XRD	XRF	DTA	LECO
1	37,24	x				
2	43,10					
3	30,30					
4	43,62					
5	41,04					
6	33,14					
7	40,62					
8	33,94					
9	44,88					
10	37,91		x	x	x	x
Sum	385,79					
Loss	0,57					
Mean	38,58					

Sample FB-C Tot. weight before sample split = 815,06g						
Subsample	Subsample weight (g)	TS prep.	XRD	XRF	DTA	LECO
1	95,24					
2	77,40					
3	89,08					
4	90,59					
5	63,69					
6	83,87		x	x	x	x
7	78,61	x				
8	73,29					
9	67,16					
10	93,95					
Sum	812,88					
Loss	2,18					
Mean	81,29					

Sample FB-D Tot. weight before sample split = 277,3g						
Subsample	Subsample weight (g)	TS prep.	XRD	XRF	DTA	LECO
1	28,1		x	x	x	x
2	29,9					
3	33,3					
4	33,3					
5	27,1		x	x	x	x
6	26,4					
7	21,8					
8	22,6					
9	23,5					
10	28,7					
Sum	274,7					
Loss	2,6					
Mean	27,47					

Sample FB-E Tot. weight before sample split = 522,13g						
Subsample	Subsample weight (g)	TS prep.	XRD	XRF	DTA	LECO
1	63,29					
2	50,97		x	x	x	x
3	60,81					
4	51,08	x				
5	54,39					
6	58,92					
7	45,44					
8	44,53					
9	42,90					
10	48,35					
Sum	520,68					
Loss	1,45					
Mean	52,07					

Sample TR<8mm Tot. weight before sample split = 200,04g						
Subsample	Subsample weight (g)	TS prep.	XRD	XRF	DTA	LECO
1	21,02		x	x	x	x
2	22,28					
3	22,55					
4	19,52	x				
5	16,62					
6	16,50					
7	18,14					
8	19,07		x	x	x	x
9	21,24					
10	22,71					
Sum	199,65					
Loss	0,39					
Mean	19,97					

Sample TRI/8mm Tot. weight before sample split = 436,71g						
Subsample	Subsample weight (g)	TS prep.	XRD	XRF	DTA	LECO
1	43,46	x				
2	37,80					
3	38,31					
4	37,20					
5	41,22					
6	43,26		x	x	x	x
7	45,95					
8	49,63					
9	50,82					
10	49,09					
Sum	436,74					
Loss	-0,03					
Mean	43,67					

Sample TR>8mm Tot. weight before sample split = 746,63g						
Subsample	Subsample weight (g)	TS prep.	XRD	XRF	DTA	LECO
1	76,22					
2	66,67					
3	48,32					
4	82,17					
5	74,92		x	x	x	x
6	88,42					
7	83,96					
8	79,50					
9	72,55					
10	73,26					
Sum	745,99					
Loss	0,64					
Mean	74,60					

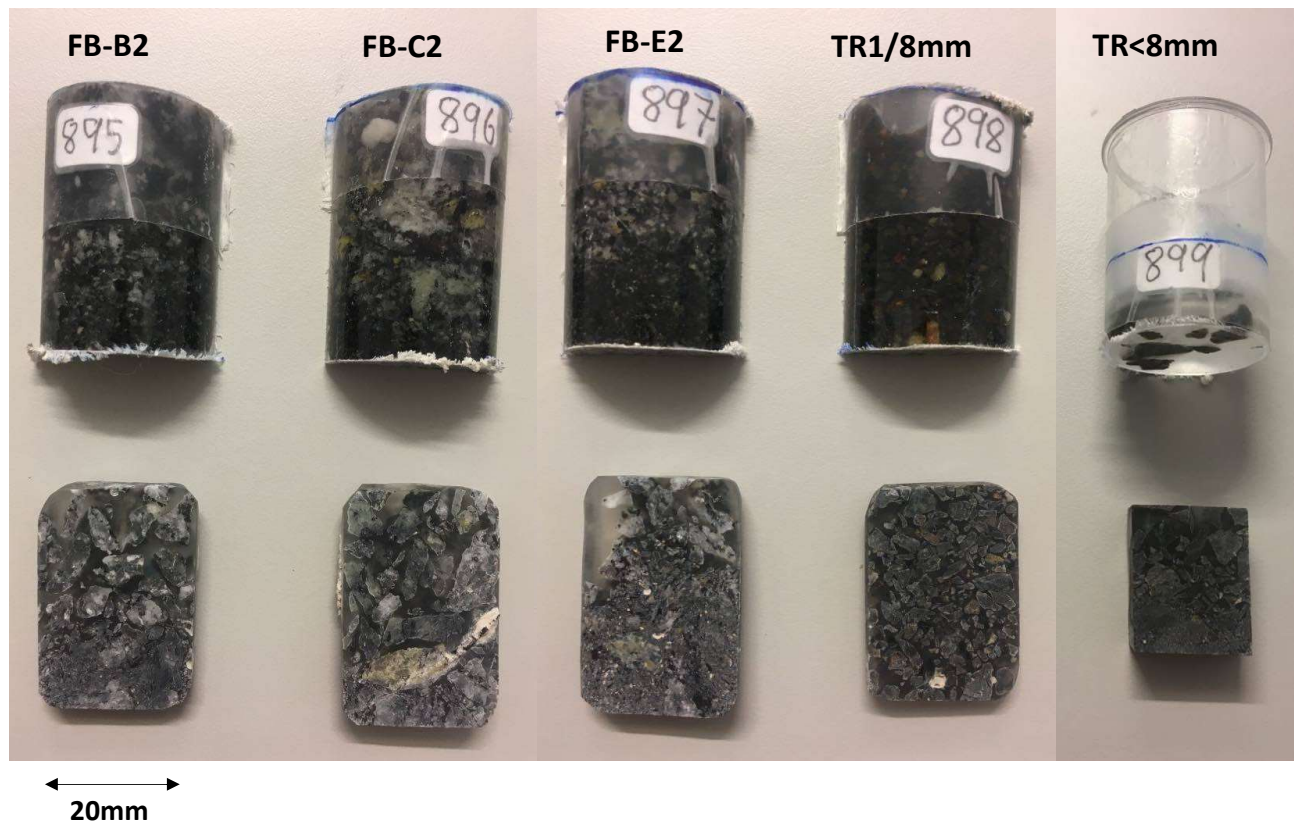


Figure 1: Residual half-parts from the preparation of particulate thin sections in plastic tubes with epoxy resin.

B Summary of optical microscope observations

Table 2: Optical microscopy descriptions of stub samples from the Follo Line and Trois-Rivières material. Abbreviations after Whitney and Evans (2010). n/a = not available.

Sample	Opaque minerals	Dominant sulfide	Iron sulfide texture		Pyrrhotite texture			Comments
			Grain size	Distribution	Grain shape	Grain Size	Weathering	
FB-A1	Py, Ccp, Hem, (Sp)	Py	10-200 μm	Disseminated and in veins.	n/a	n/a	n/a	Py is weathered, and appear as weathered subhedral cubes.
FB-B	Py, Po, (Ccp)	Py	50-200 μm	Disseminated and in veins.	Subhedral	50-200 μm	Low	Py is less weathered, and appear more intact than in FB-A1. 3-4 Po grains are present.
FB-C	Py, Ilm, Hem	Py	10-40 μm	Py appear as vein fill and in anhedral clusters.	n/a	n/a	n/a	Py is only iron sulfide present. Ilm have Hem/Mag lamellae. Hem appear as characteristic laths.
FB-D	Py, (Ccp), (Po)	Py	10-200 μm	Disseminated as subhedral grains and anhedral clusters.	n/a	n/a	n/a	Up to 1% Py. Appear as subhedral grains or in clusters. Po is minor and appear as inclusion within Py.
FB-E	Py, (Ccp), (Po)	Py	100-300 μm	Subhedral Py disseminated throughout the sample.	n/a	n/a	n/a	Some py is weathered, while some grains are intact. Minor Po within Py.
TR-0,045/1mm	Py, Po, Ccp, Pn, Ilm, Hem/Mag	Py	50-500 μm	Py is often liberated. Po and Ccp less liberated.	Subhedral	50-500 μm	Very high	Approx. 5-10% of all particles contains an Py, Po or Ccp. Py is not weathered.
TR-1/8mm	Py, Po, Ccp, Pn, Ilm, Hem/Mag	Po/Py	50-1000 μm	No iron sulfides completely liberated. They appear random disseminated in particles.	Subhedral	50-1000 μm	High	Approx. 50% of all particles contains Py, Po or Ccp. Py is not weathered.
TR->8mm	Po, Py, Ccp, Pn Ilm, Hem/Mag	Po	50-1000 μm	No iron sulfides completely liberated. Some particles are heavily dominated by iron sulfides.	Subhedral	50-1000 μm	Moderate	Some particles contains up to 30% iron sulfides, while some have less than 1%.

Table 3: Optical microscopy descriptions of thin section gravel samples from the Follo Line and Trois-Rivières material. Mineral abbreviations after Whitney and Evans (2010). n/a = not available.

Sample	Mineral content		Dominant sulfide	Iron sulfide texture		Pyrrhotite texture			Comments
	Transparent	Opaques		Grain size	Distribution	Grain shape	Grain Size	Weathering	
FB-B-1	Qz, Bt, Pl, Kfs Ms, Grt, Chl	Py, (Po)	Py	50-300 μm	Subhedral grains, evenly disseminated	n/a	n/a	n/a	Py is intact with low degree of weathering. Appear within particles and liberated. Bt appear in two ways: deep brown without pleochroism+cleavage, and bright with pleochroism+cleavage.
FB-C-7	Qz, Pl, Kfs, Bt Cpx, Grt, Ms, Chl	Py, Po, (Ccp)	Py	20-500 μm	2-3 disseminated clusters, subhedral grains.	Subhedral	60 μm	Moderate	Po appear within a Kfs- grain once. Py is perforated and weathered. Bt appear in the two described ways.
FB-E-4	Qz, Kfs, Pl, Bt Grt, Ms, Chl	Py, (Ccp)	Py	50-200 μm	Subhedral grains, disseminated.	n/a	n/a	n/a	Py is varying from subhedral and intact to moderately weathered/perforated. Some liberated py grains. Bt appear in the two described ways.
TR<8mm-4	Pl, Opx, Bt, Qz Cpx, Hbl	Po, Py, Ccp Pn, Ilm	Po/Py	50-1000 μm	Abundant, anhedral grains, disseminated and as crack/ vein fill. Lots of Pn-exsolution in Po.	Anhedral	50-1000 μm	High	Approx. 10% of the particles contain sulfides. Po is heavily perforated, but not completely altered like in TR1/8mm-1.
TR1/8mm-1	Pl, Opx, Bt, Cpx, Qz, Kfs, Grt	Po, Py, Ccp Pn, Ilm	Po	50-1500 μm	Abundant, subhedral grains, disseminated and as crack/vein fill.	Anhedral	50-1000 μm	Very high	Approx. 40% of the particles contain sulfides. Some Po-grains are completely altered. A grey phase is filling in many cracks through particles. Could originate from Po weathering. Py and Ccp intergrowth within Po.

Table 4: Optical microscopy descriptions of thin section whole-rock samples from the Folio Line material. Mineral abbreviations after Whitney and Evans (2010). n/a = not available.

Sample	Mineral content		Rock texture	Dominant sulfide	Iron sulfide texture		Pyrrhotite texture			Comments
	Transparent	Opagues			Grain size	Distribution	Grain shape	Grain Size	Weathering	
FB-F	Qz, Bt, Ms, Pl, Kfs, Chl, Grt	Py, Ccp	Gneissic, felsic and mafic banding.	Py	100-800 μm	4-5 subhedral Py clusters + smaller disseminated fragments.	n/a	n/a	n/a	Py is moderately weathered. Appear with 800um grains/ aggregates in the center. Ccp is minor. Bt appear in two ways: deep brown without pleochroism+cleavage, and bright with pleochroism+cleavage.
FB-G	Qz, Bt, Pl, Kfs, Grt, Ms	Py, Ccp, Hm	Gneissic, felsic and mafic banding.	Py	50-200 μm	5-6 anhedral Py clusters, disseminated.	n/a	n/a	n/a	Py is moderately weathered. Ccp is minor. Bt appear in the two described ways.
FB-H	Qz, Kfs, Bt, Pl, Chl, Grt, Ms, (Zrn)	Py, Ccp, Hm	Gneissic, felsic and mafic banding.	Py	50-150 μm	4-5 anhedral Py clusters + smaller fragments, disseminated.	n/a	n/a	n/a	6mm disintegrated Grt grain. Py is highly weathered/perforated. Hm is anhedral and in laths. Bt appear in the two described ways.
FB-I	Qz, Bt, Pl, Kfs, Ms, Chl	Py, Ccp, (Po)	Gneissic, felsic and mafic banding.	Py	100-200 μm	1 euhedral Py cluster + disseminated fragments.	n/a	n/a	n/a	Unweathered and weathered Py. Ccp appear close to Py. Bt appear in the two described ways.
FB-J	Qz, Pl, Kfs, Bt, Grt, Ms	Py, Ccp, Po	Gneissic, felsic and mafic banding.	Py	100-200 μm	Small clusters + subhedral grains disseminated evenly throughout the sample.	Anhedral	150 μm	Moderate	3-4 Po grains, anhedral with weathered boundaries and intact interior. Py is common and appear evenly disseminated and homogeneous. Bt appear in the two described ways.
FB-K	Qz, Pl, Kfs, Bt, Ms, Chl, (Zrn)	Py, Hm, (Ccp)	Gneissic, felsic and mafic banding.	Py	100-500 μm	Several dominating Py clusters in a corner, subhedral-euhedral.	n/a	n/a	n/a	Py varies from highly weathered to completely intact with crystal faces. 500-1500 μm Hm laths are disseminated. Bt appear in the two described ways.

C Accessory mineralogy for Follo Line samples by 20 μ m AM mapping

Table 5: Accessory mineralogy for the Follo Line samples in wt% by 20 μ m Automated Mineralogy mapping. Blanks are less than 0,001 (10ppm).

	FB-A	FB-B	FB-C	FB-D	FB-E	FB-B2	FB-C2	FB-E2	FB-F	FB-G	FB-H	FB-I	FB-J	FB-K	Average
Chlorite	0,500	0,001	0,403	0,040	1,199	3,049	0,249	0,990	0,742	0,087	0,103	0,293	0,306	0,584	0,610
Apatite	0,303	0,462	0,342	0,423	0,323	0,224	0,231	0,388	0,393	0,193	0,488	0,475	0,293	0,629	0,369
Pyrite	0,309	0,102	0,001	0,100	0,168	0,258	0,105	0,112	0,451	0,062	0,126	0,090	0,149	0,424	0,176
Ilmenite	0,168	0,747	0,051	0,024	0,012	0,008	0,028	0,019	0,142	0,037	0,070	0,024	0,048	0,234	0,115
Calcite	0,757	0,004	0,001	0,005	0,004	0,042	0,002	0,162	0,582	0,001	0,001	0,003	0,017	0,003	0,113
Al silicate	0,149	0,089	0,285	0,071	0,272	0,036	0,067	0,110	0,037	0,066	0,039	0,044	0,041	0,099	0,100
Titanite	0,022		0,217	0,004	0,130	0,012	0,038	0,077	0,024	0,080	0,066	0,102	0,138	0,203	0,080
Carbonate	0,260	0,004		0,006	0,008	0,015	0,003	0,315	0,182	0,002	0,002	0,003	0,020	0,003	0,063
Amphibole	0,038	0,006	0,212	0,012	0,085	0,010	0,036	0,045	0,039	0,021	0,050	0,077	0,025	0,219	0,063
Zirkon						0,042	0,037	0,045	0,073	0,052	0,041	0,040	0,048	0,059	0,049
Ce-Monazite						0,028	0,006	0,026	0,011	0,042	0,052	0,015	0,018	0,017	0,024
P-Si-O phase	0,030	0,021	0,019	0,026	0,017										0,023
Rutile	0,009		0,003	0,005	0,007	0,081	0,002	0,011	0,003	0,003	0,004	0,003	0,005	0,003	0,010
Chalcopyrite	0,016	0,029		0,003	0,005	0,004	0,004	0,005	0,022	0,005	0,004	0,012	0,003	0,004	0,009
Pyrrhotite	0,006	0,022		0,002	0,006	0,005	0,004	0,002	0,007	0,001	0,003	0,004	0,015	0,005	0,006
Y-Monazite						0,001		0,001		0,002	0,003	0,002	0,003		0,001
Fe sulfate	0,004			0,001	0,001	0,001		0,001	0,003		0,002	0,001		0,001	0,001
Fe oxides	0,002	0,002	0,001		0,001	0,001	0,001	0,001		0,001	0,001	0,003	0,005		0,001
Sphalerite	0,005			0,001	0,001		0,001	0,001	0,004	0,001		0,001	0,001		0,001
Po rand effect	0,001	0,005			0,001	0,001			0,001				0,001		0,001
Ca sulfate		0,002	0,001	0,001					0,001						0,001
Pentlandite													0,001		

D Accessory mineralogy for Trois-Rivières samples by 20 μ m AM mapping

Table 6: Accessory mineralogy for the Trois-Rivières samples in wt% by 20 μ m Automated Mineralogy mapping. Blank space is less than 0,001 (10ppm).

	TR0,045/1mm	TR1/8mm	TR>8mm	TR<8mm	TR1/8mm(2)	Average
Pyrrhotite	0,291	0,430	0,915	0,717	0,666	0,604
Pyrite	0,397	0,630	0,336	0,650	0,968	0,596
Ilmenite	0,457	0,426	0,767	0,479	0,312	0,488
Apatite	0,346	0,236	0,413	0,397	0,369	0,352
Chlorite	0,285	0,435	0,182	0,103	0,378	0,277
Dolomite	0,140	0,393	0,279	0,293	0,260	0,273
Muscovite	0,177	0,061	0,034	0,184	0,375	0,166
Spinel	0,051	0,001		0,234	0,296	0,146
Fe-Mg oxide	0,126	0,139	0,135	0,099	0,193	0,138
Pentlandite	0,107	0,167	0,095	0,111	0,200	0,136
Po rand-effect	0,334	0,132	0,044	0,038	0,082	0,126
Fe-sulfate	0,151	0,103	0,033	0,030	0,072	0,078
Chalcopyrite	0,038	0,106	0,043	0,026	0,092	0,061
Rutile	0,061	0,068	0,015	0,070	0,028	0,048
TS-glass				0,114	0,055	0,042
Ca sulfate	0,185	0,004	0,001	0,003	0,002	0,039
Background		0,005	0,086			0,018
Al-oxide	0,002			0,006	0,062	0,014
Amphibole	0,014	0,018	0,008	0,008	0,016	0,013
Zircon	0,012	0,008	0,019	0,012	0,003	0,011
Sphalerite	0,001	0,006	0,016	0,013	0,004	0,008
Al-silicate	0,017	0,001		0,020	0,002	0,008
Pumpellyite	0,005	0,005	0,008	0,006	0,008	0,007
Titanite	0,001	0,001		0,002	0,001	0,001

E False color mineral maps from 20 μ m AM mapping on Follo Line sections

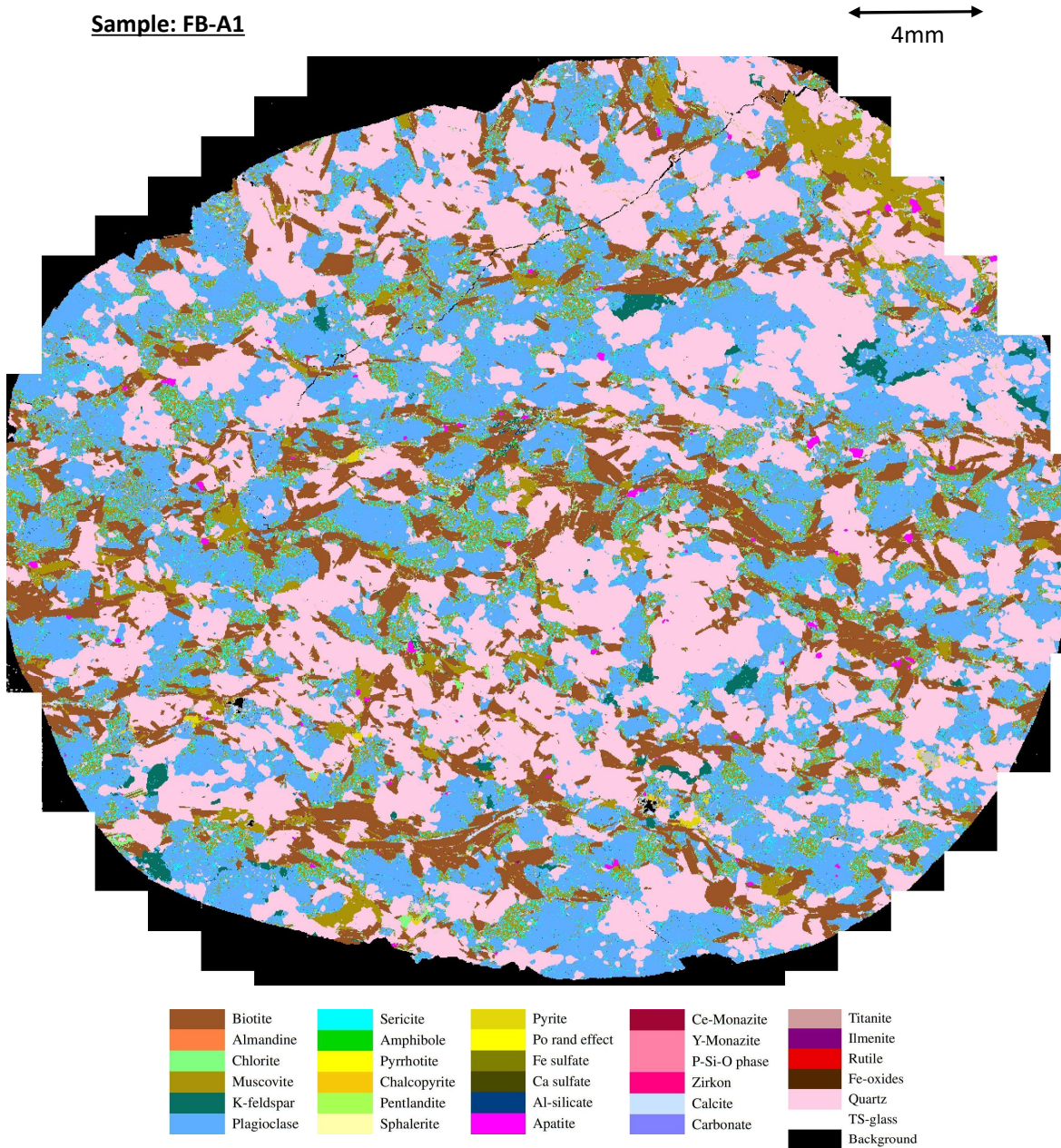


Figure 2: False color mineral map from 20 μ m AM mapping on the FB-A1 stub sample.

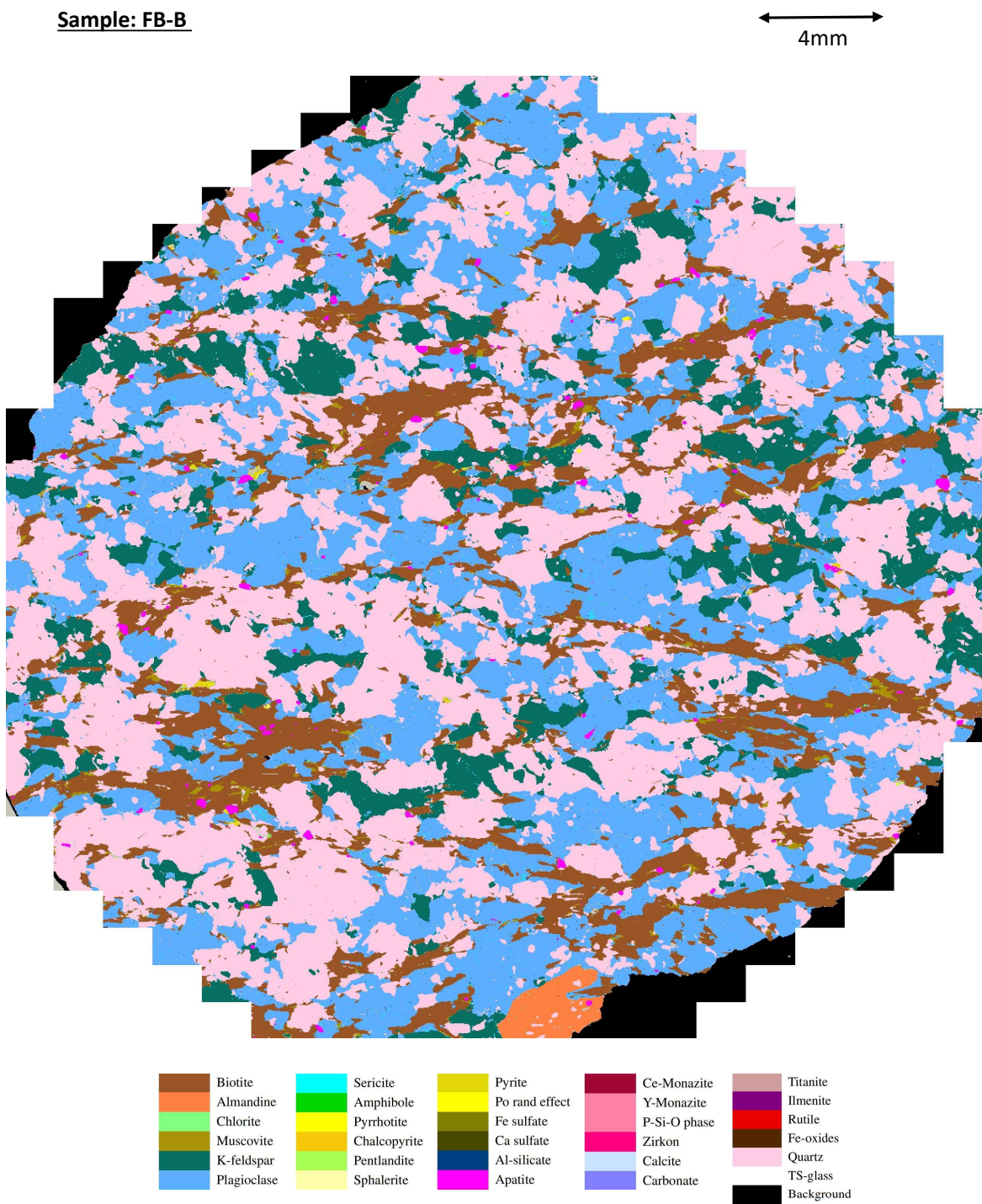


Figure 3: False color mineral map from 20 μ m AM mapping on the FB-B stub sample.

Sample: FB-C

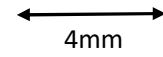
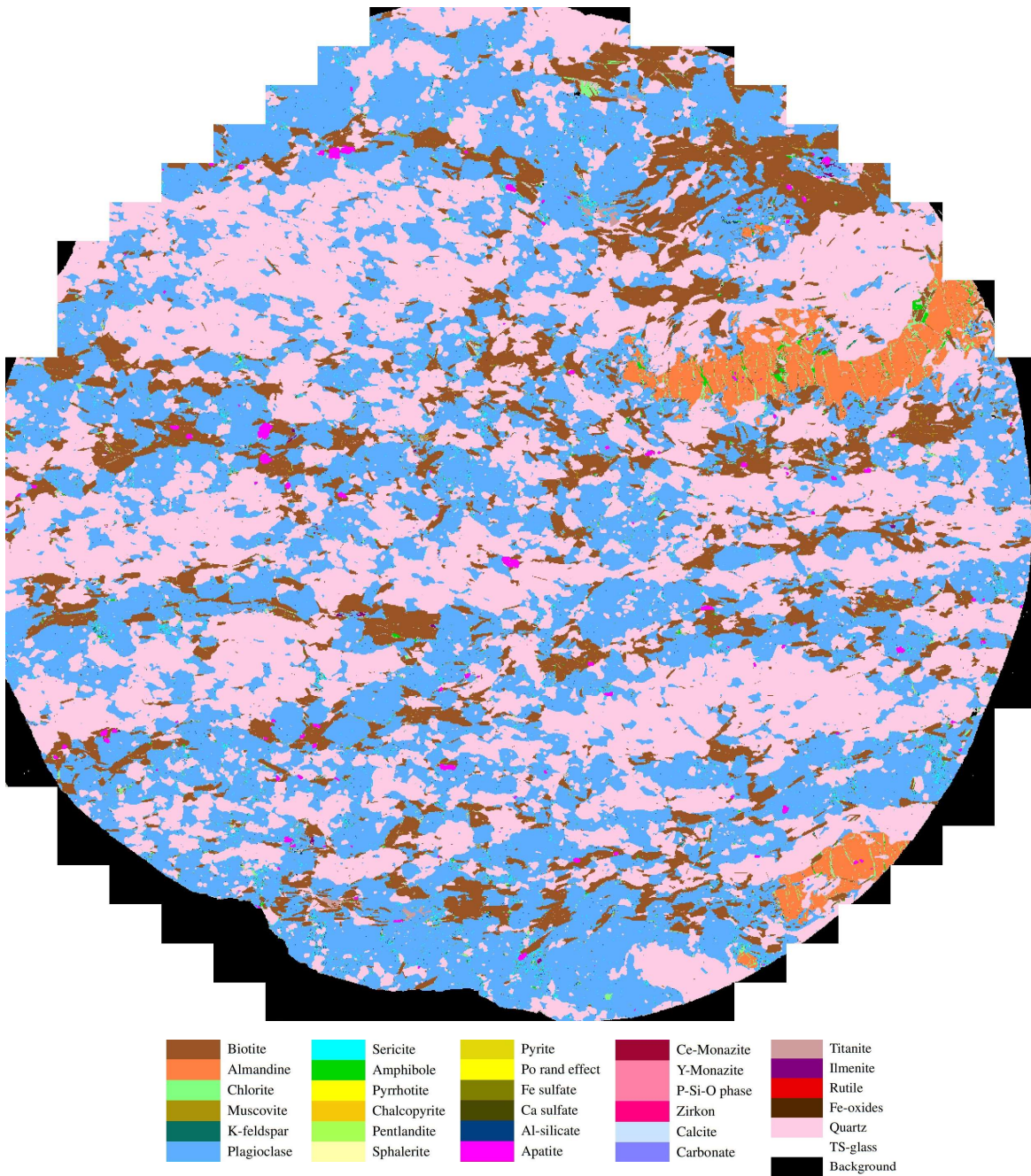

 A horizontal scale bar with arrows at both ends, labeled "4mm".


Figure 4: False color mineral map from 20 μ m AM mapping on the FB-C stub sample.

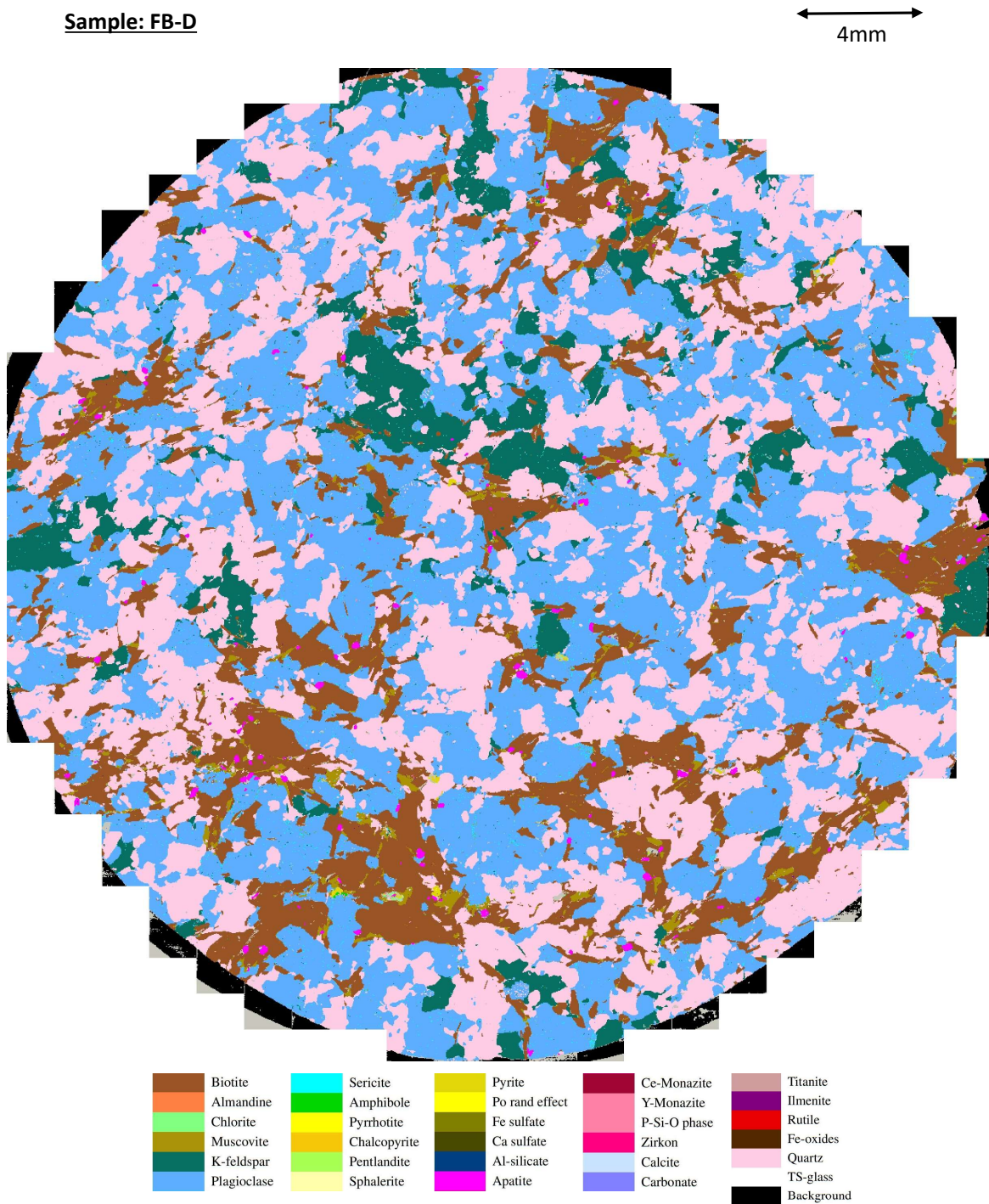


Figure 5: False color mineral map from 20 μ m AM mapping on the FB-D stub sample.

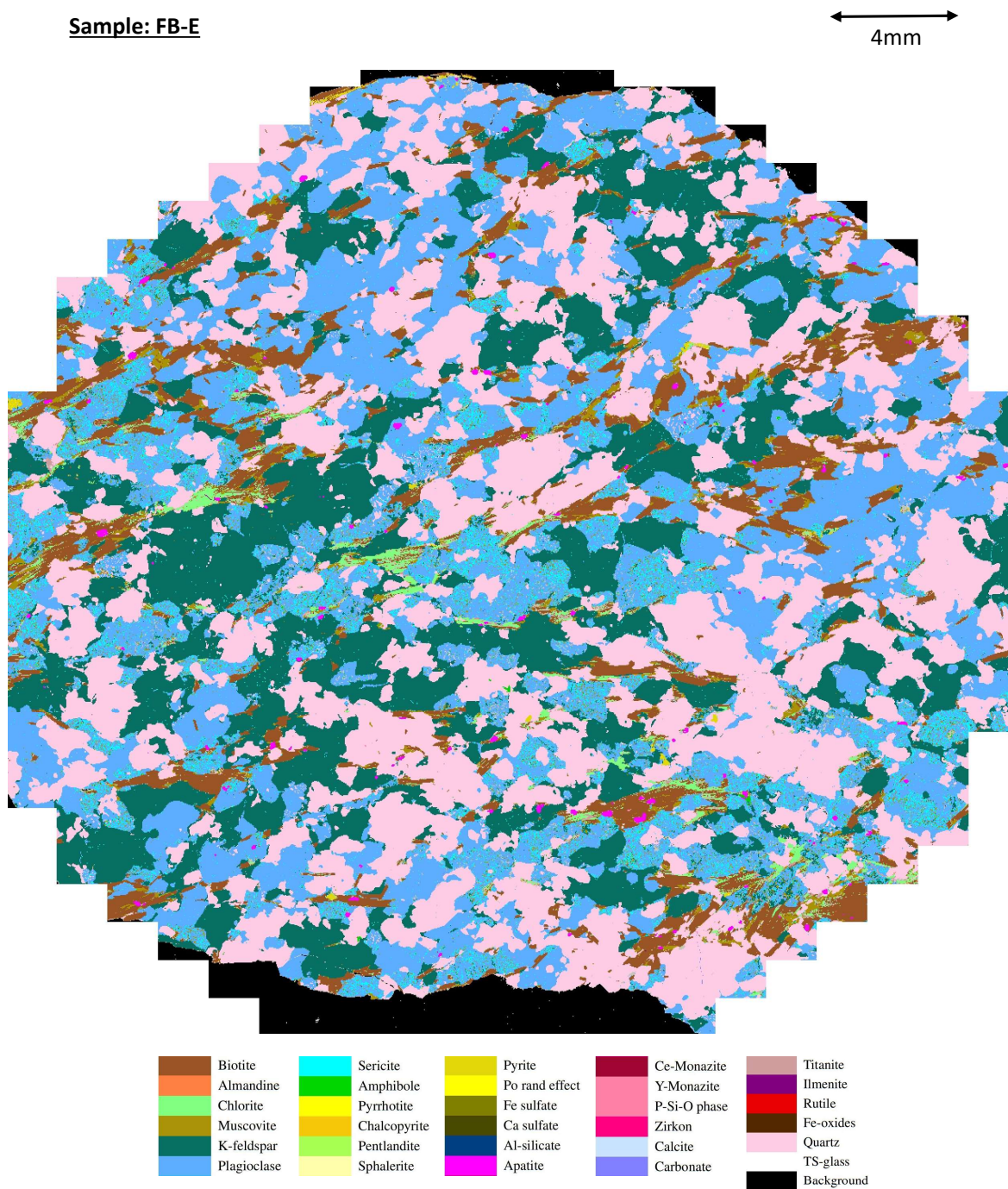



Figure 6: False color mineral map from 20 μ m AM mapping on the FB-E stub sample.

Sample: FB-B2



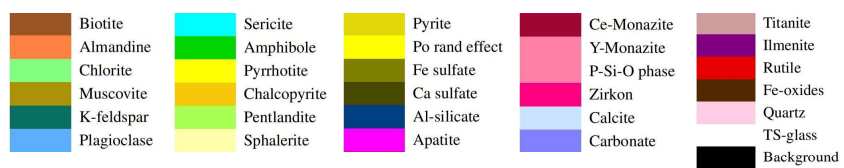
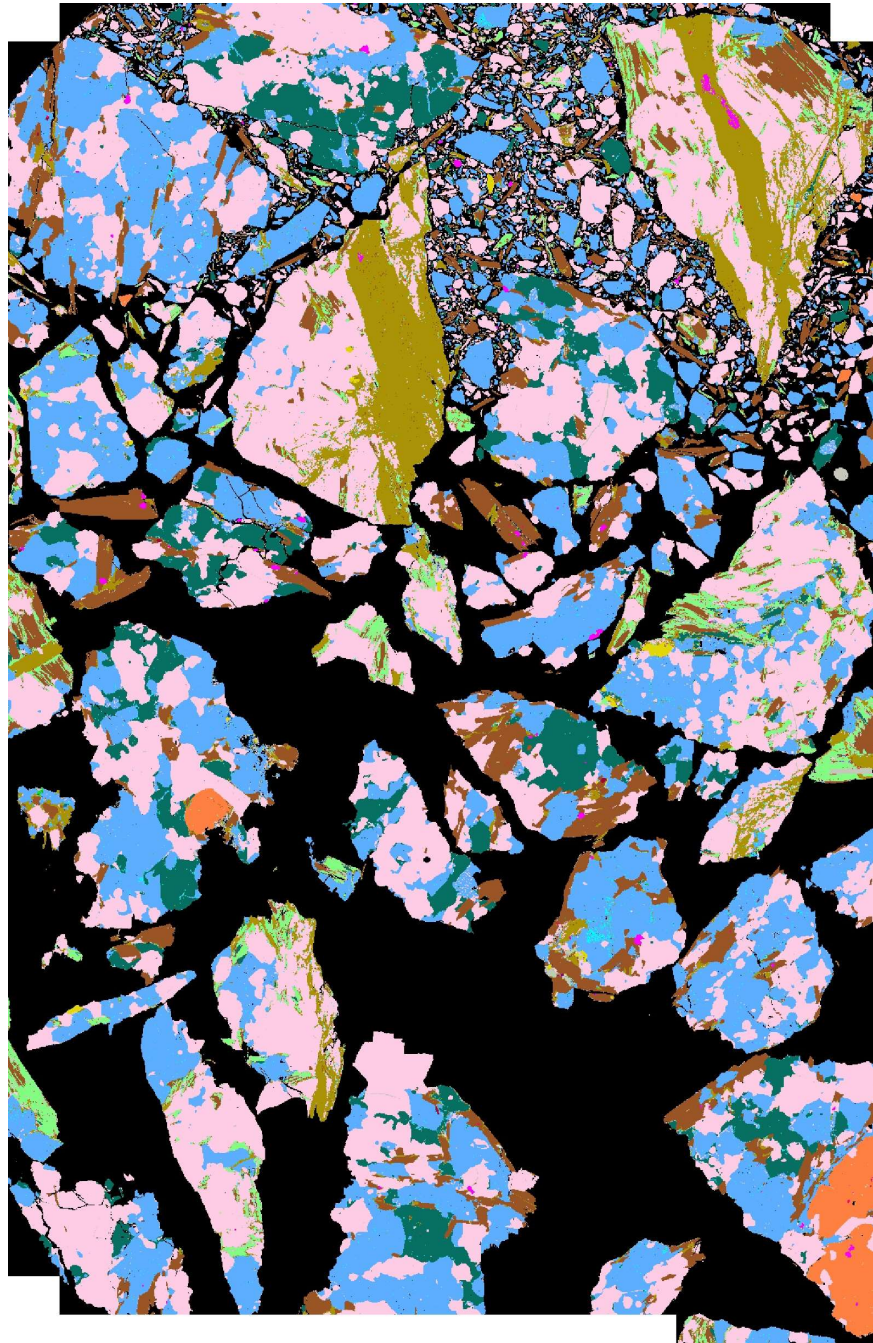

4mm


Figure 7: False color mineral map from 20 μ m AM mapping on the FB-B2 thin section.

Sample: FB-C2



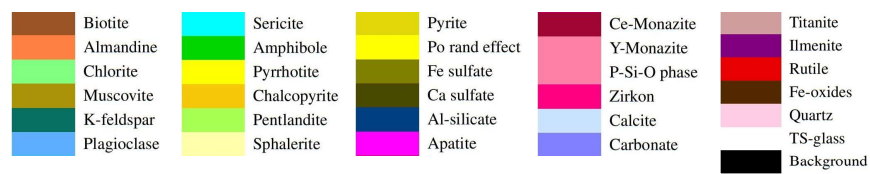
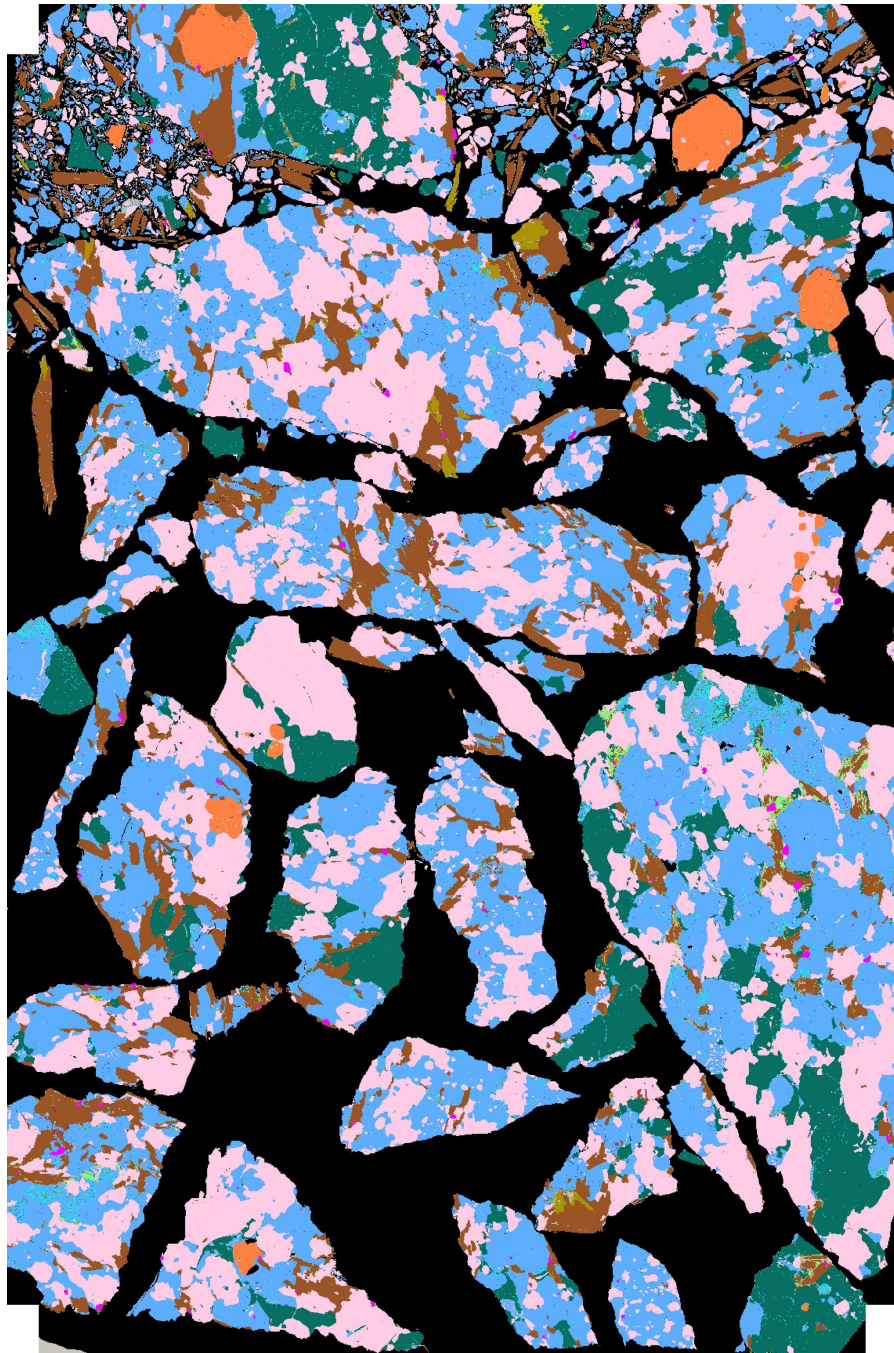
4mm


Figure 8: False color mineral map from 20 μ m AM mapping on the FB-C2 thin section.

Sample: FB-E2

4mm

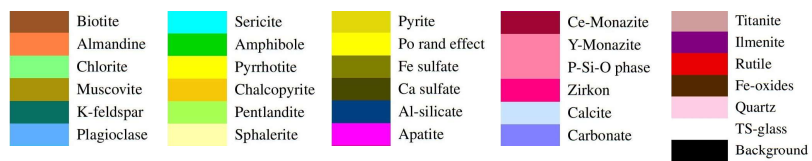
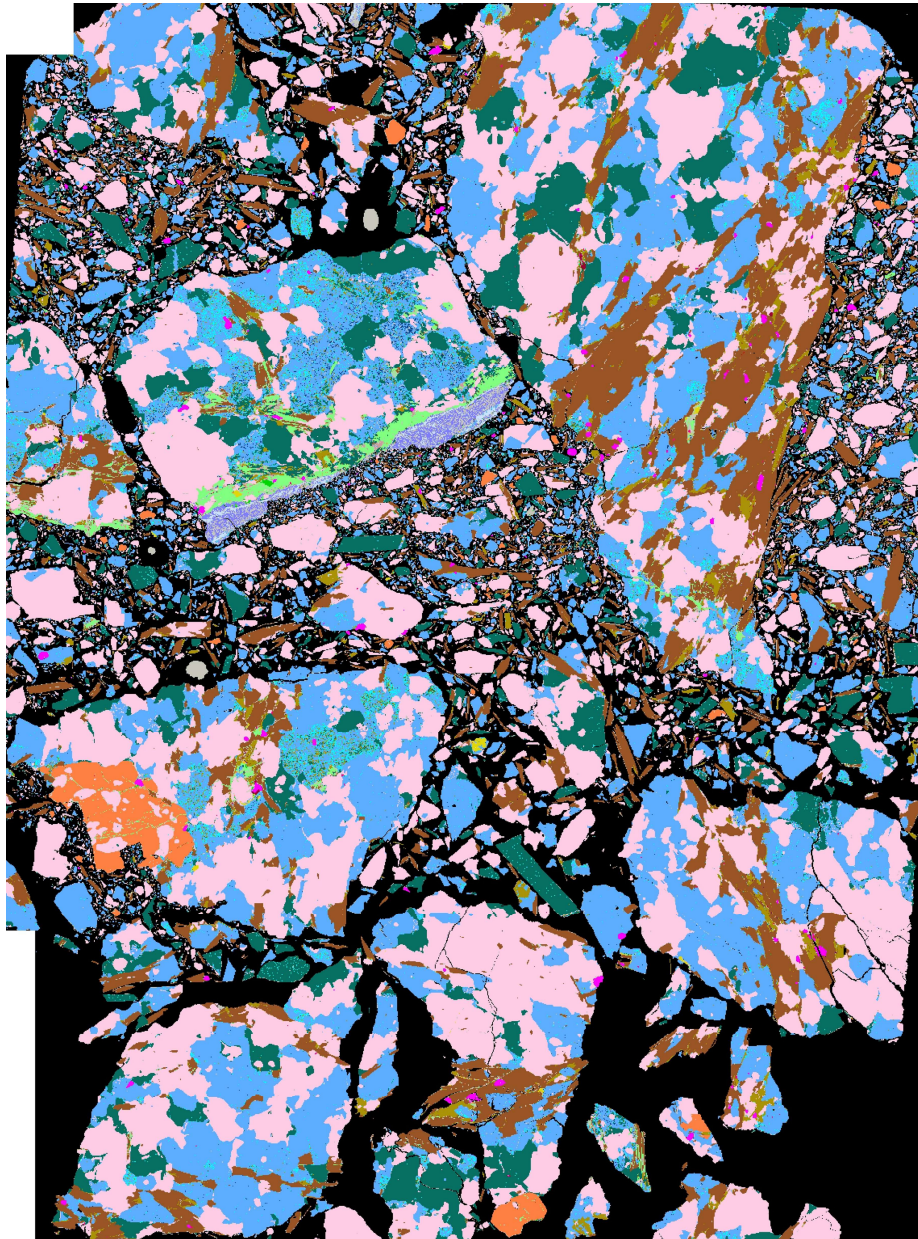


Figure 9: False color mineral map from 20 μ m AM mapping on the FB-E2 thin section.

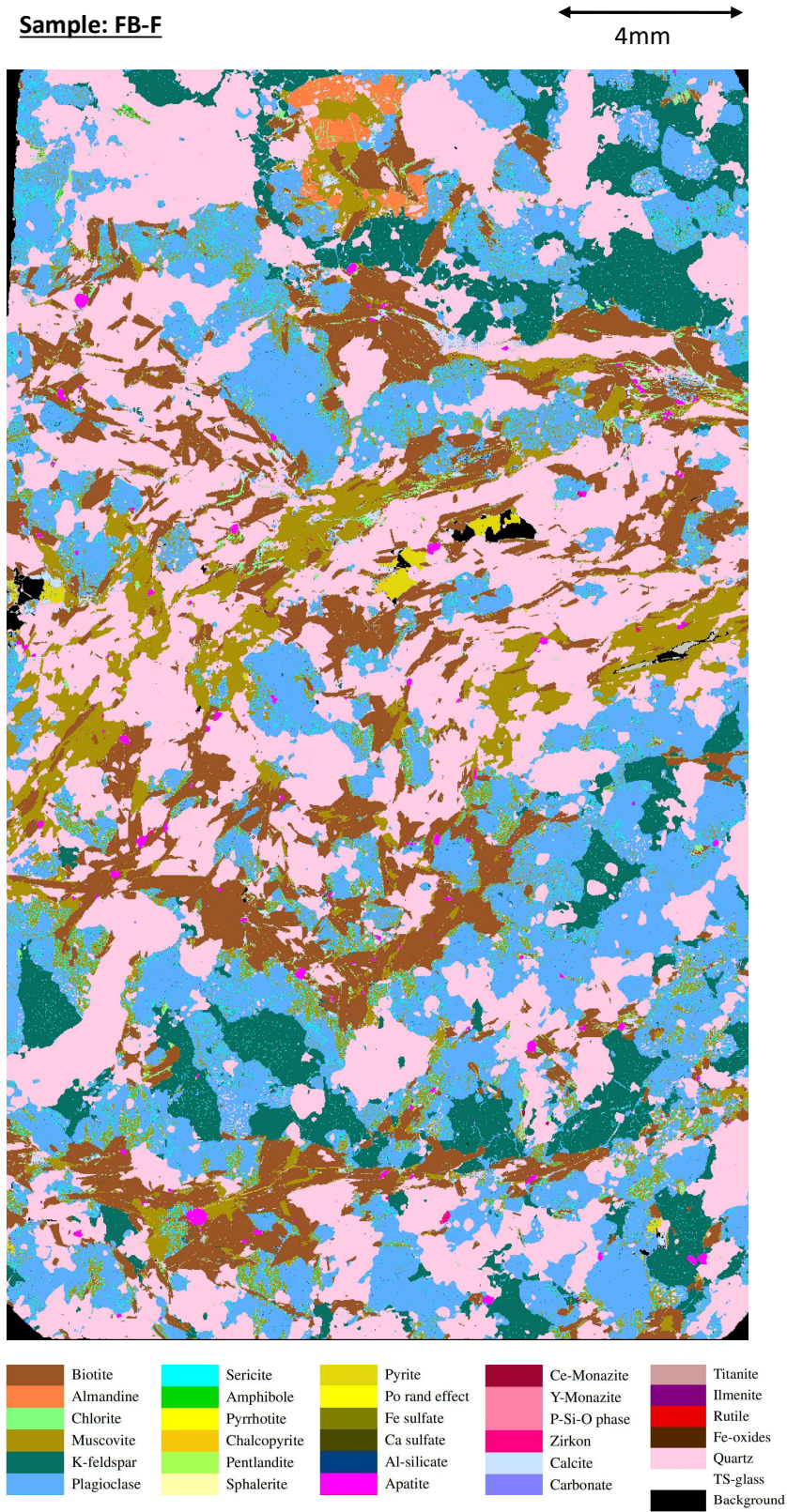


Figure 10: False color mineral map from 20 μ m AM mapping on the FB-F thin section.

Sample: FB-G

4mm

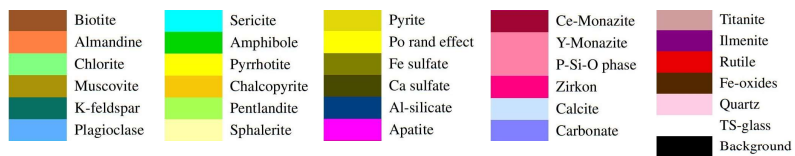
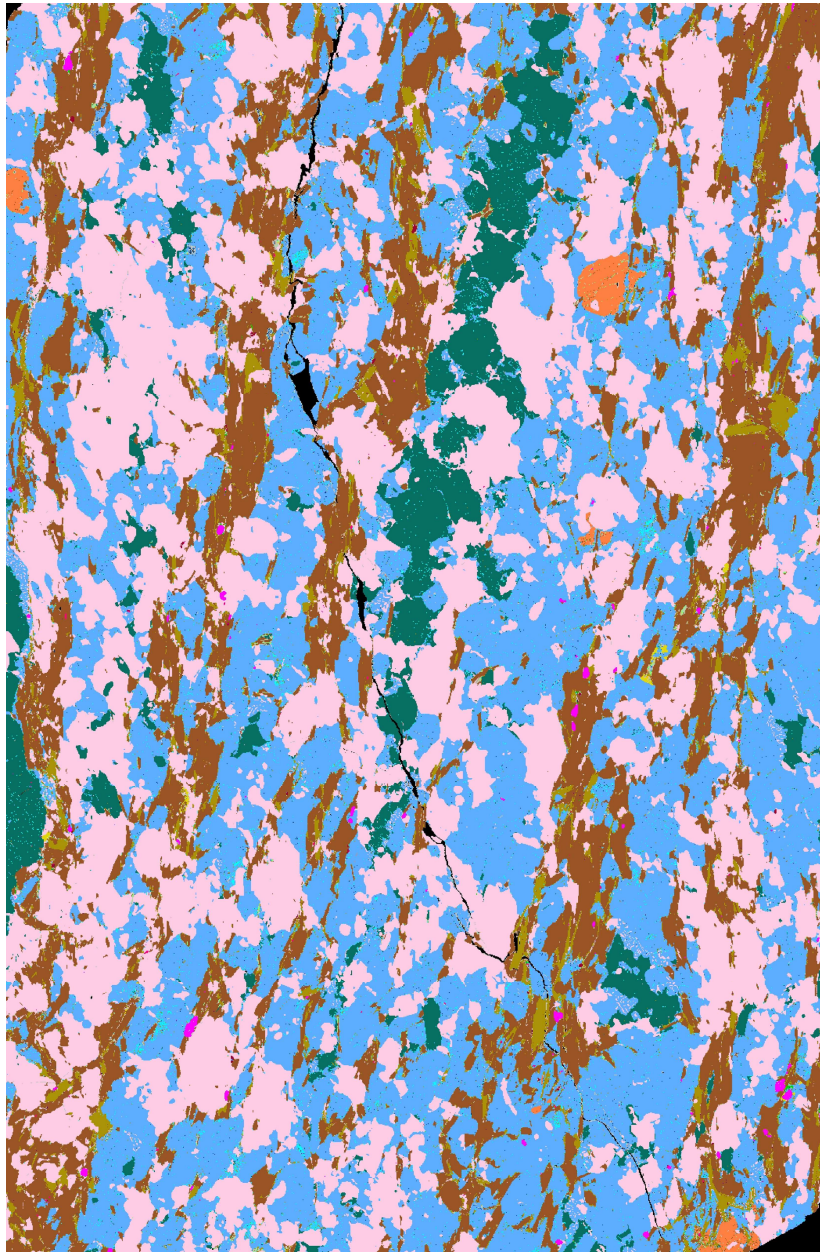


Figure 11: False color mineral map from 20 μ m AM mapping on the FB-G thin section.

Sample: FB-H

4mm

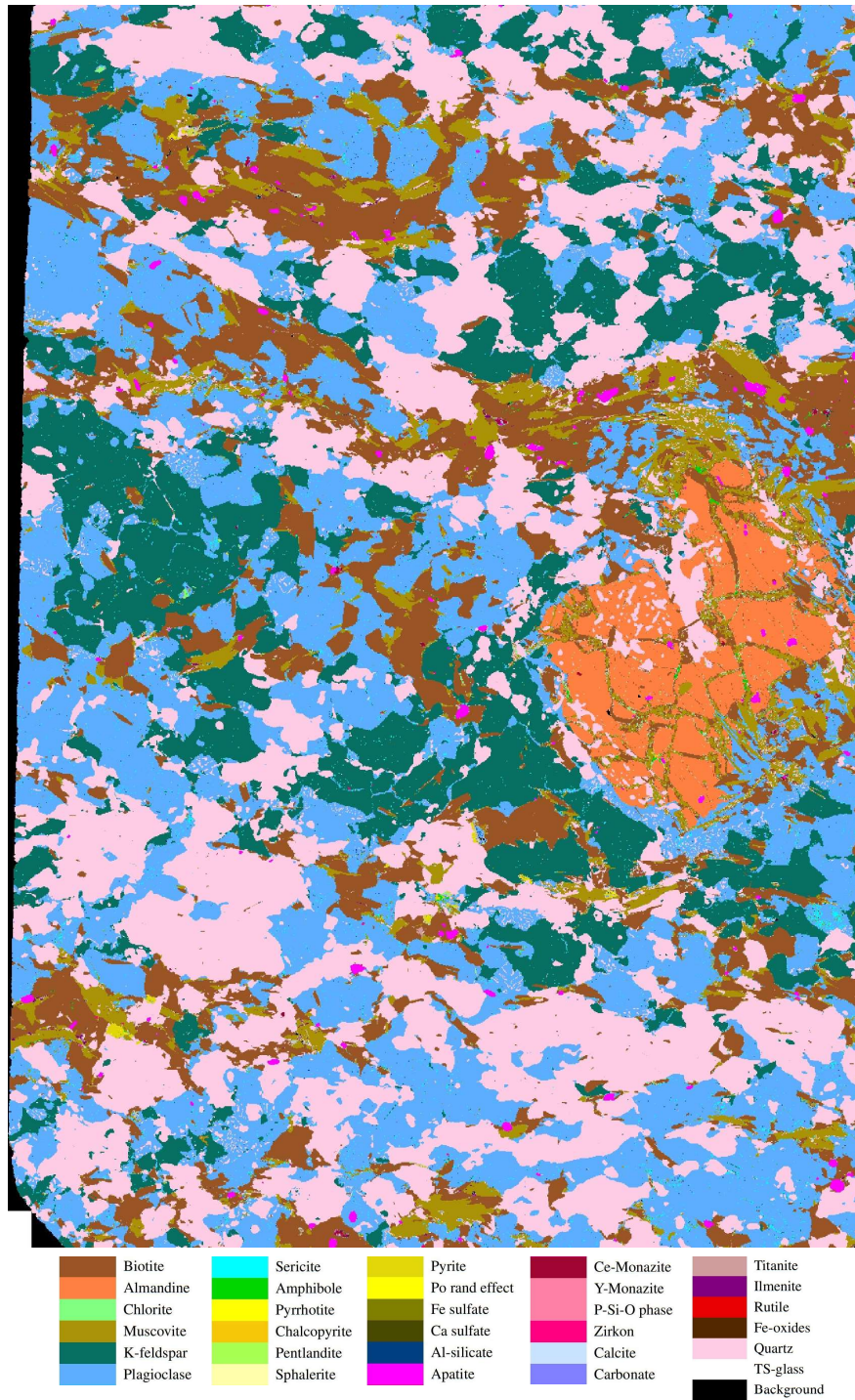


Figure 12: False color mineral map from 20 μ m AM mapping on the FB-H thin section.

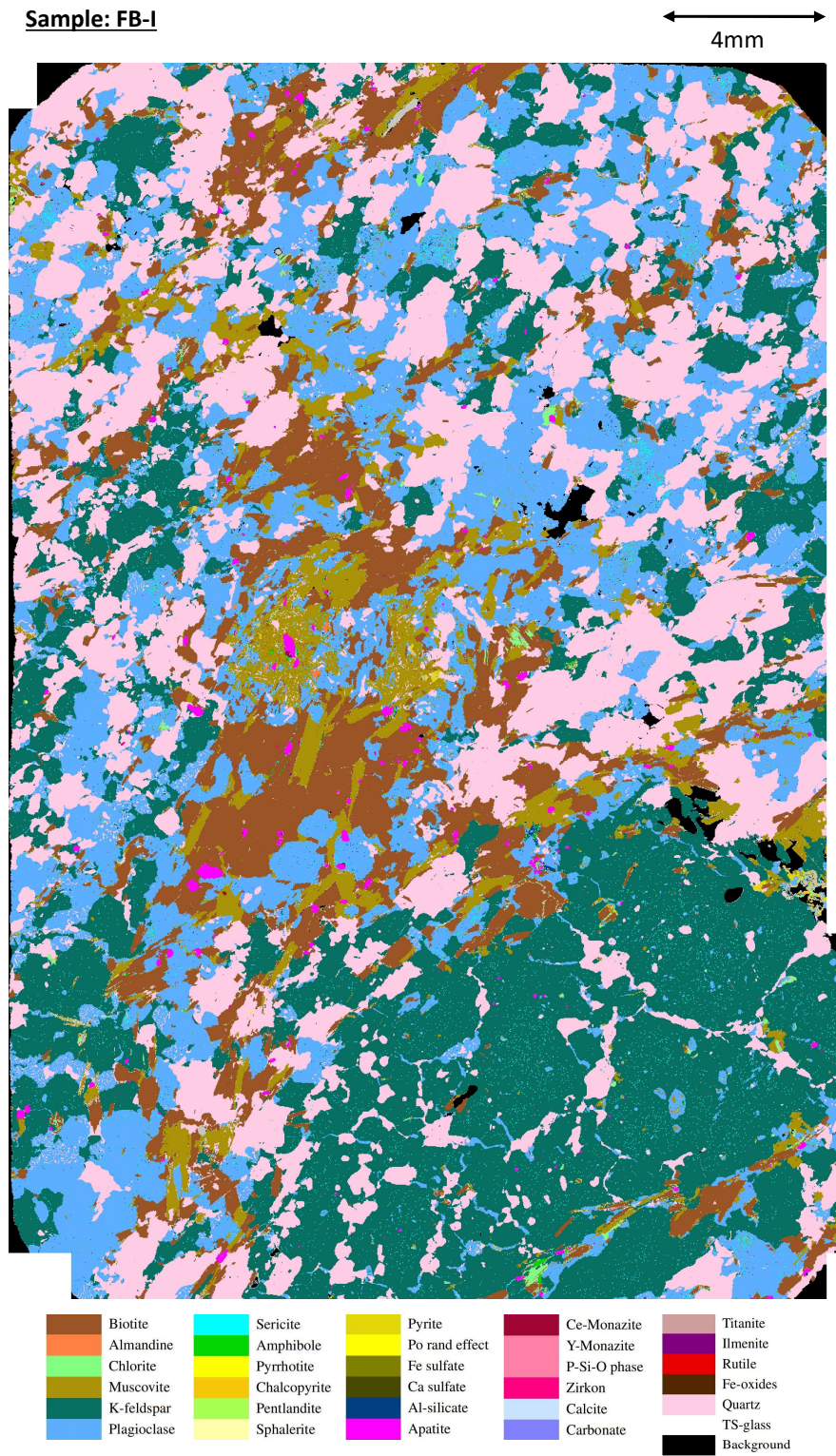


Figure 13: False color mineral map from 20 μ m AM mapping on the FB-I thin section.

Sample: FB-J

4mm

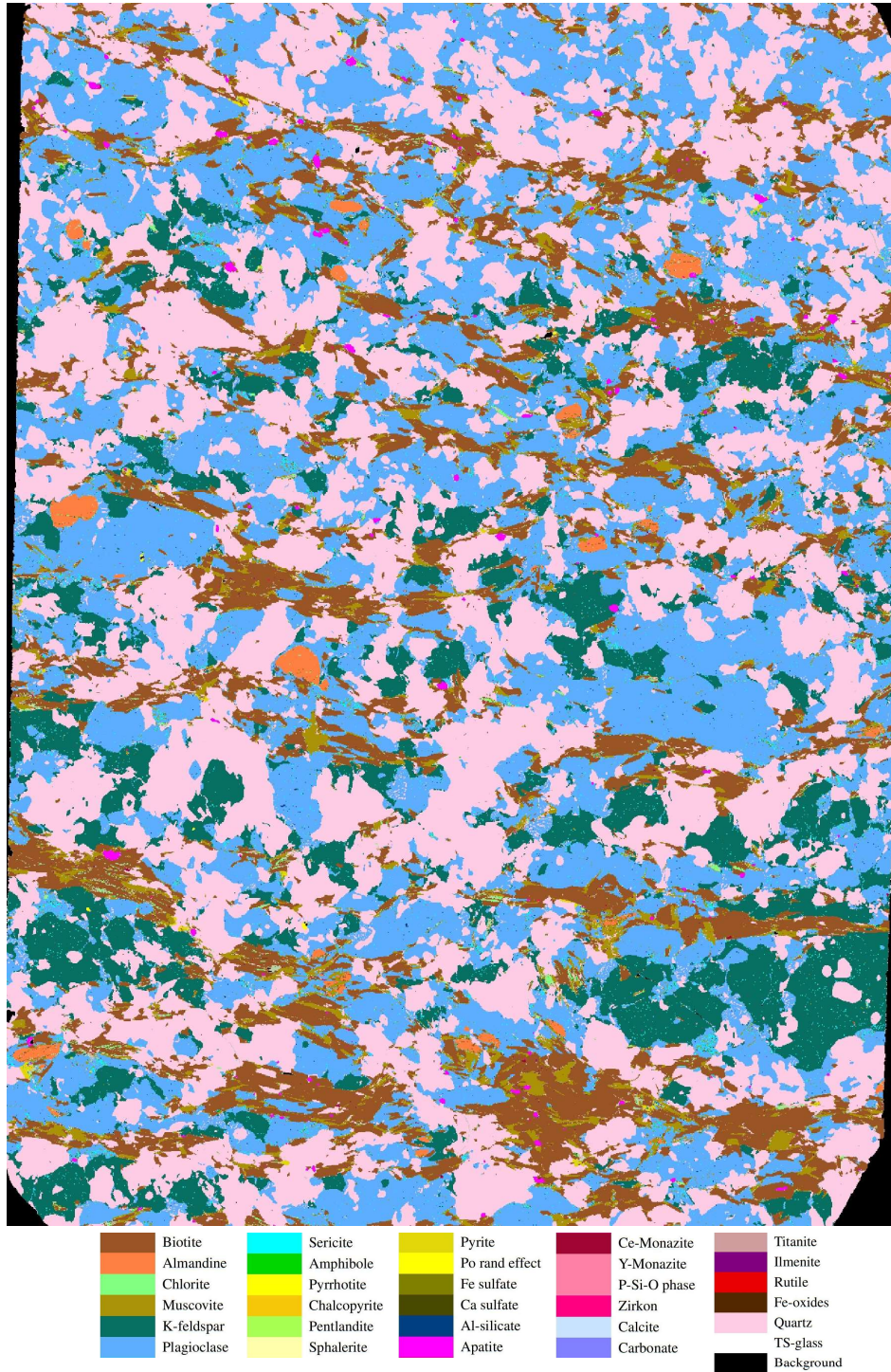


Figure 14: False color mineral map from 20µm AM mapping on the FB-J thin section.

Sample: FB-K

4mm

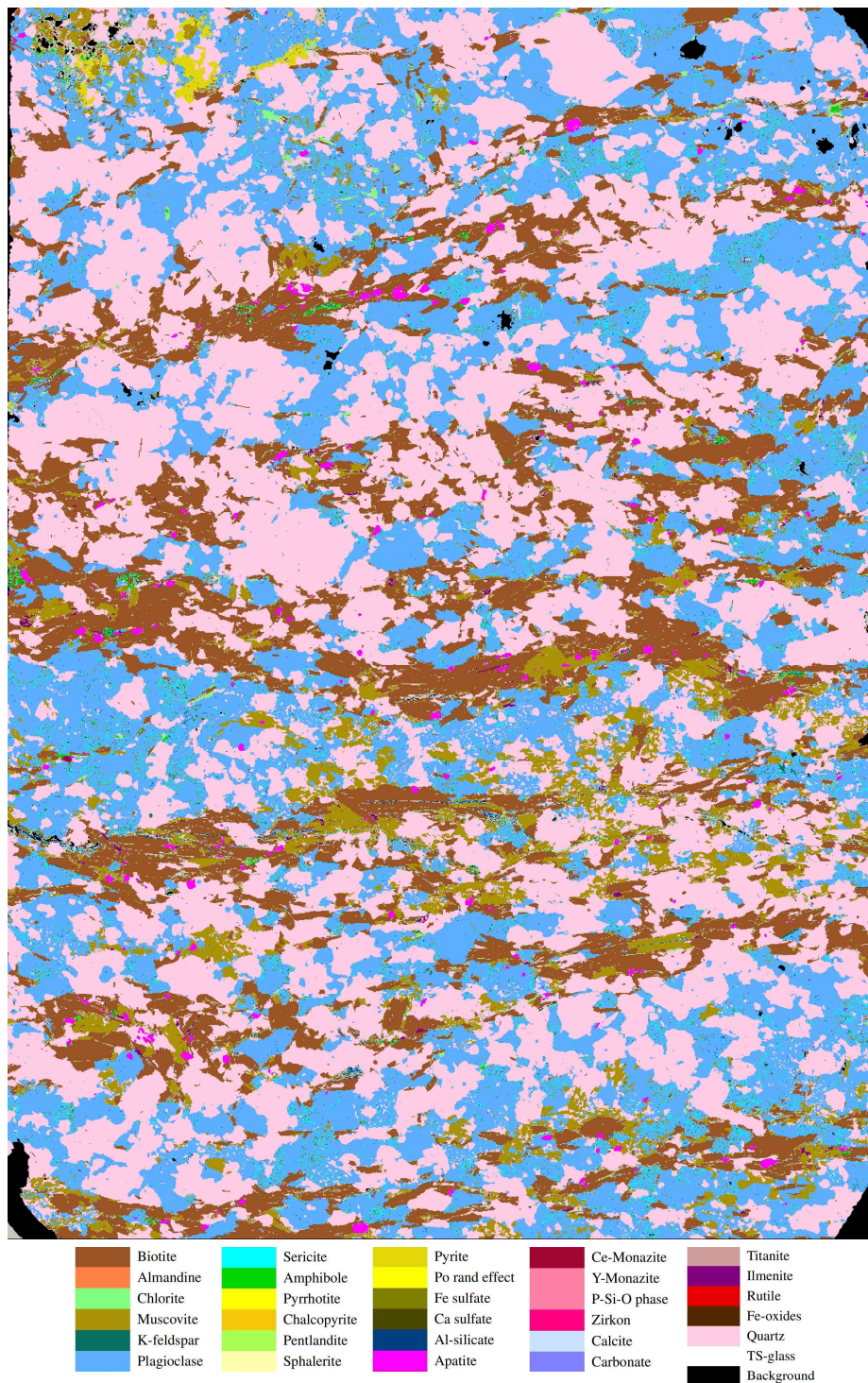


Figure 15: False color mineral map from 20 μ m AM mapping on the FB-K thin section.

F False color mineral maps from 20 μ m AM mapping on Trois-Rivières sections

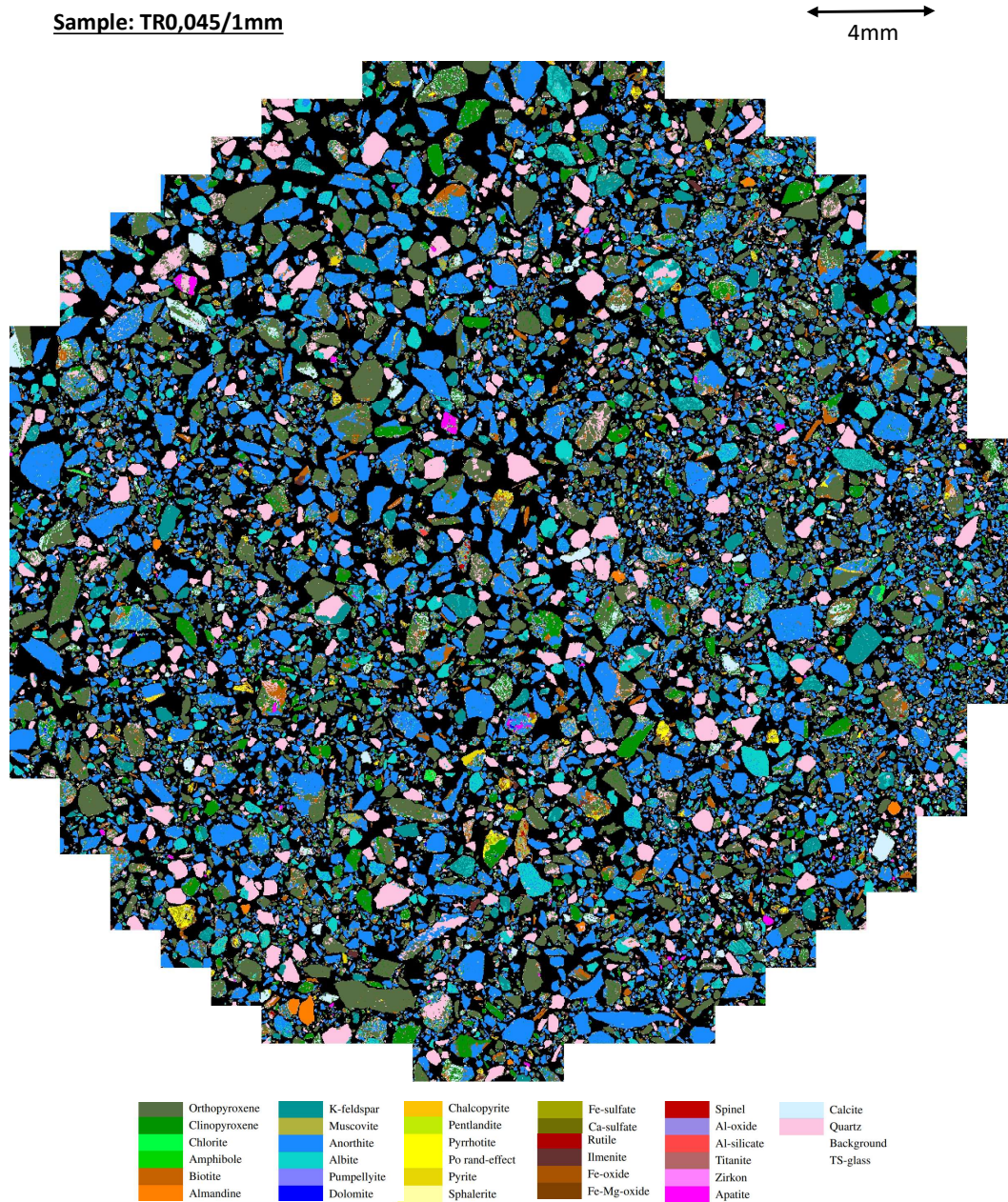


Figure 16: False color mineral map from 20 μ m AM mapping on the TR0,045/1mm stub sample.

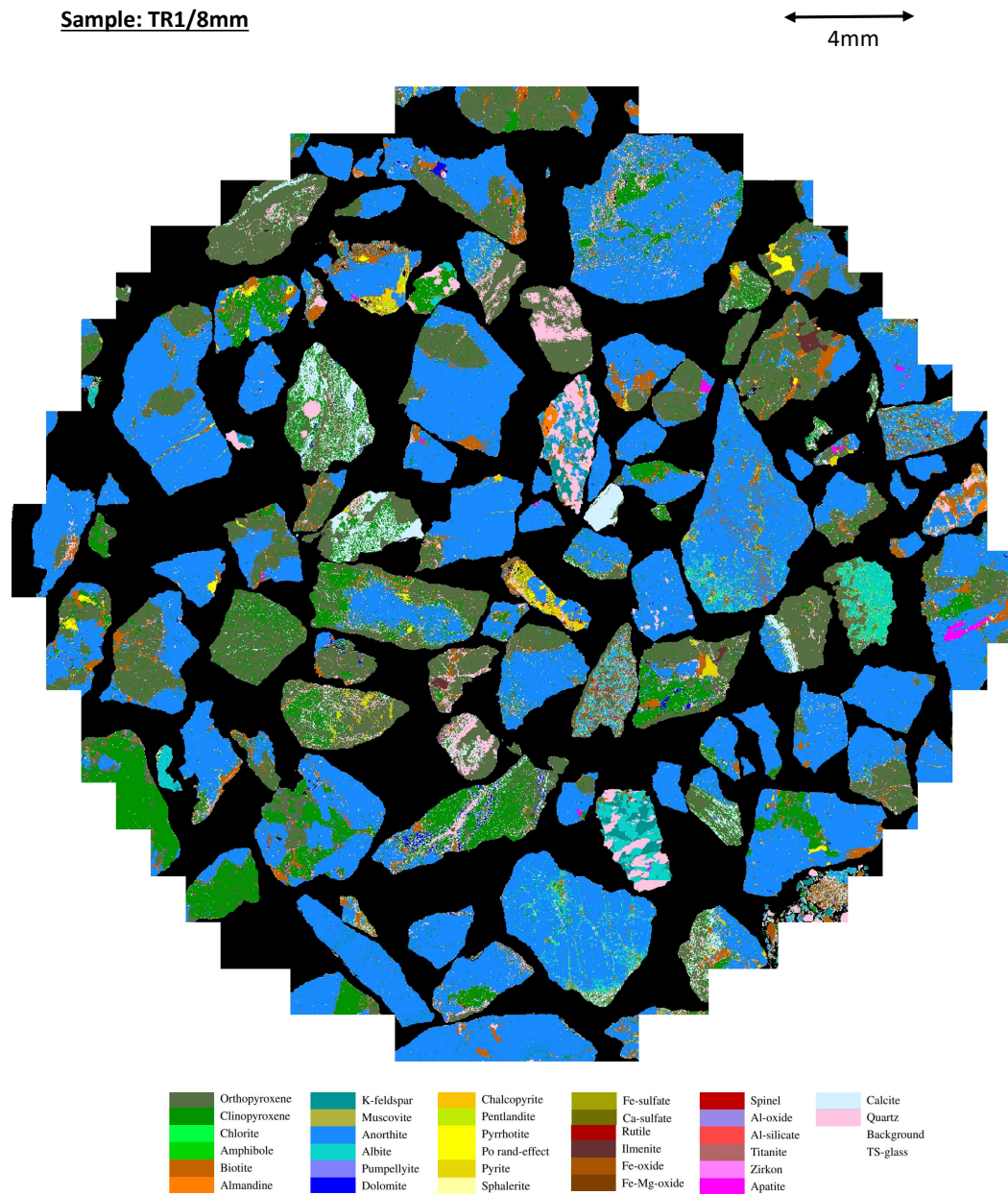


Figure 17: False color mineral map from 20 μ m AM mapping on the TR1/8mm stub sample.

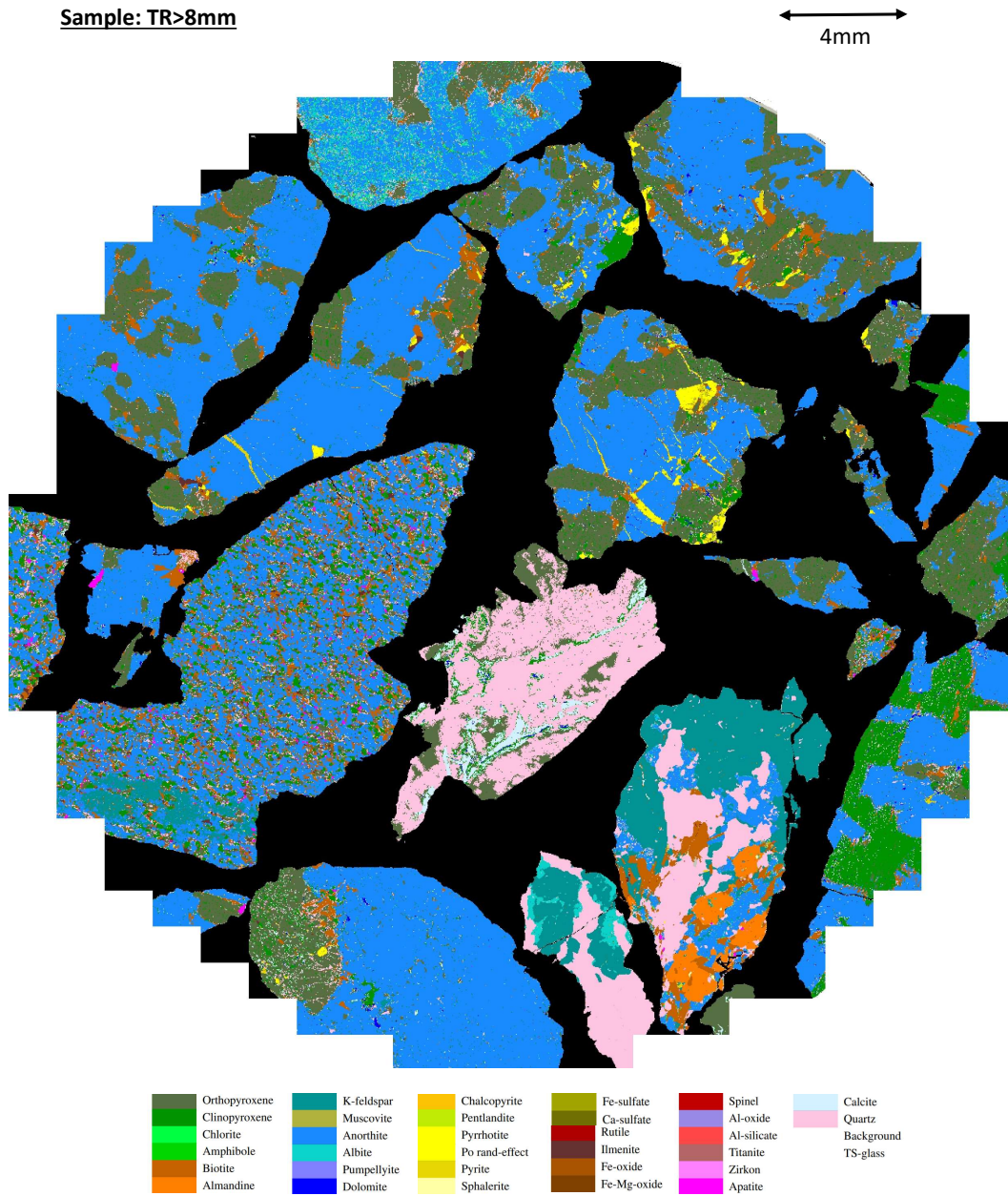


Figure 18: False color mineral map from 20 μ m AM mapping on the TR>8mm stub sample.

Sample: TR<8mm

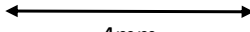
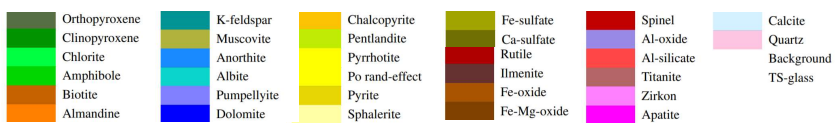
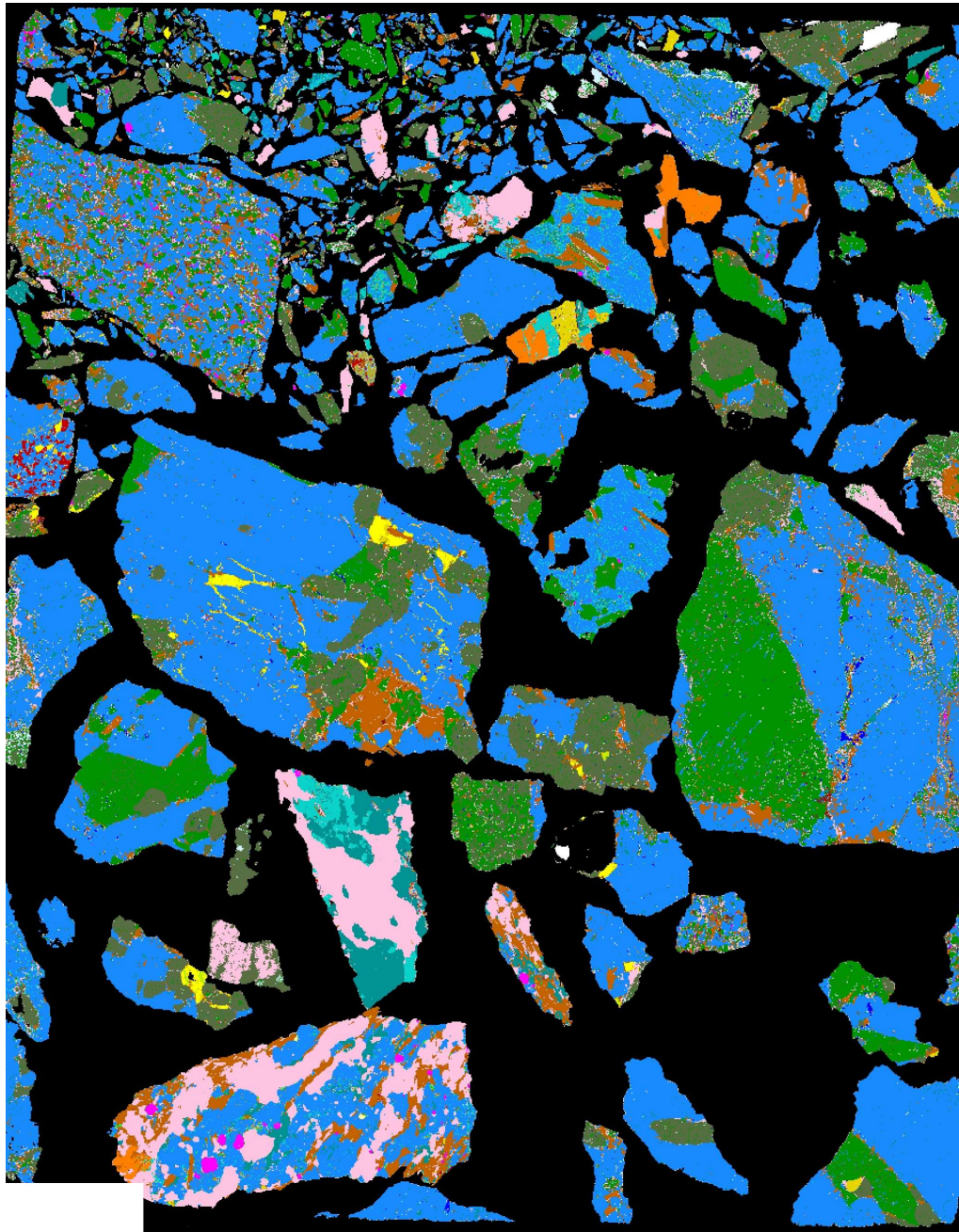

 4mm


Figure 19: False color mineral map from 20 μ m AM mapping on the TR<8mm thin section.

Sample: TR1/8mm

4mm

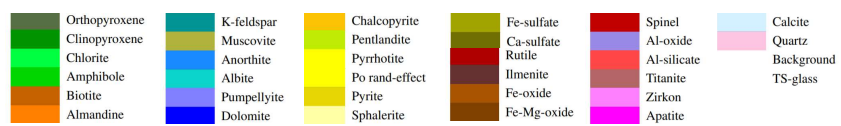
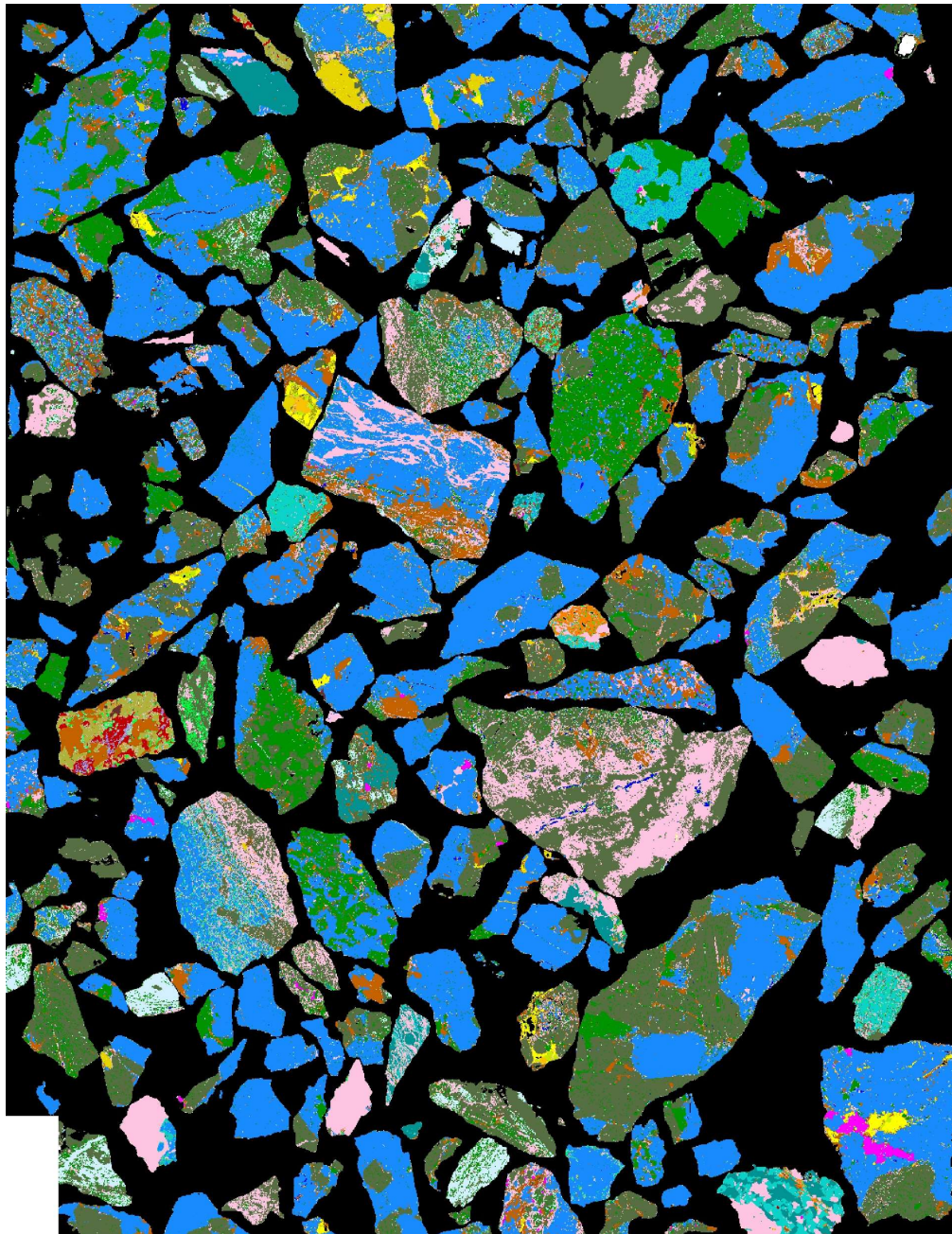


Figure 20: False color mineral map from 20 μ m AM mapping on the TR1/8mm thin section.

G Diffractograms from XRD analyses

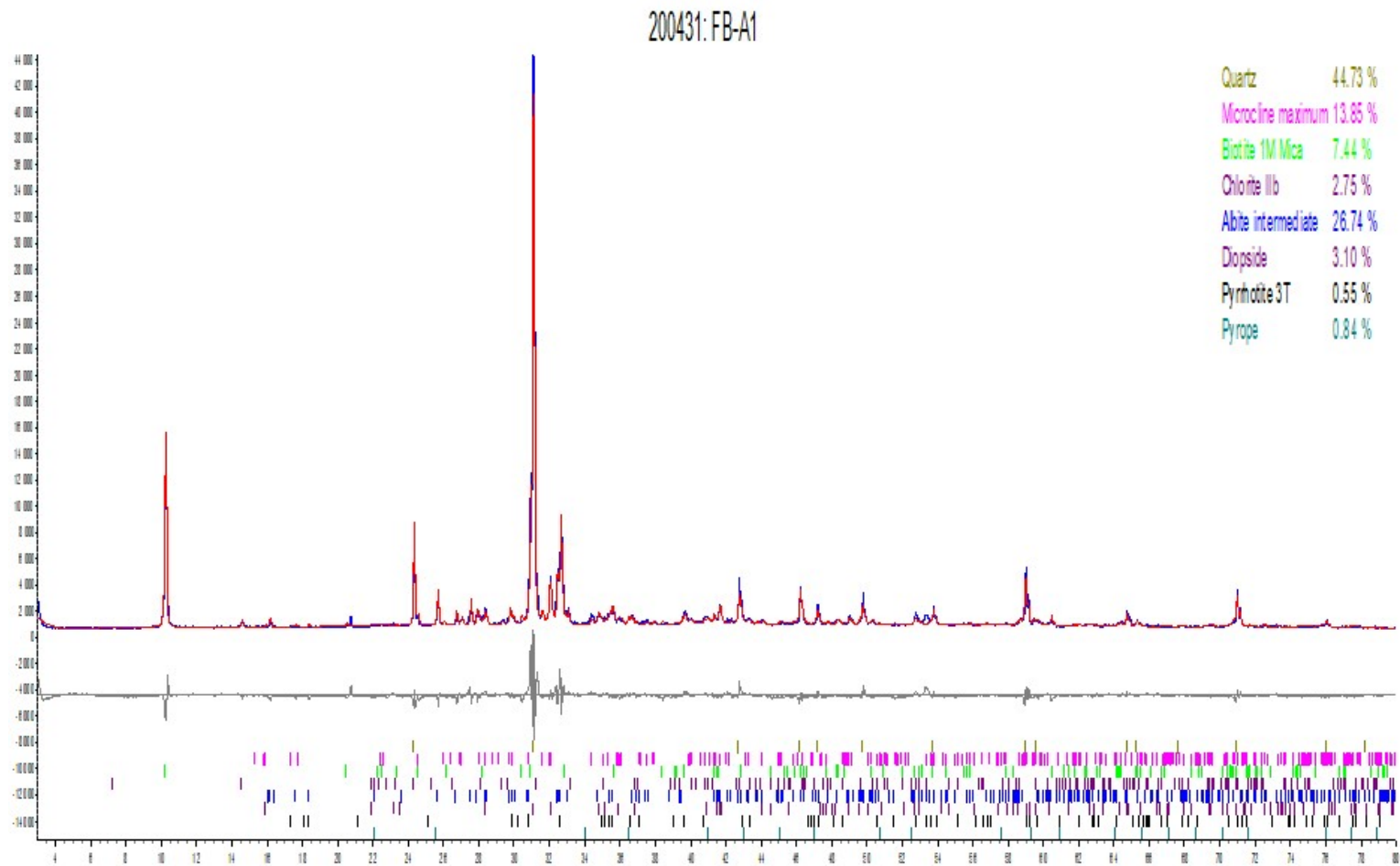


Figure 21: Diffractogram from XRD analysis on sample FB-A1.

200428: FB-B

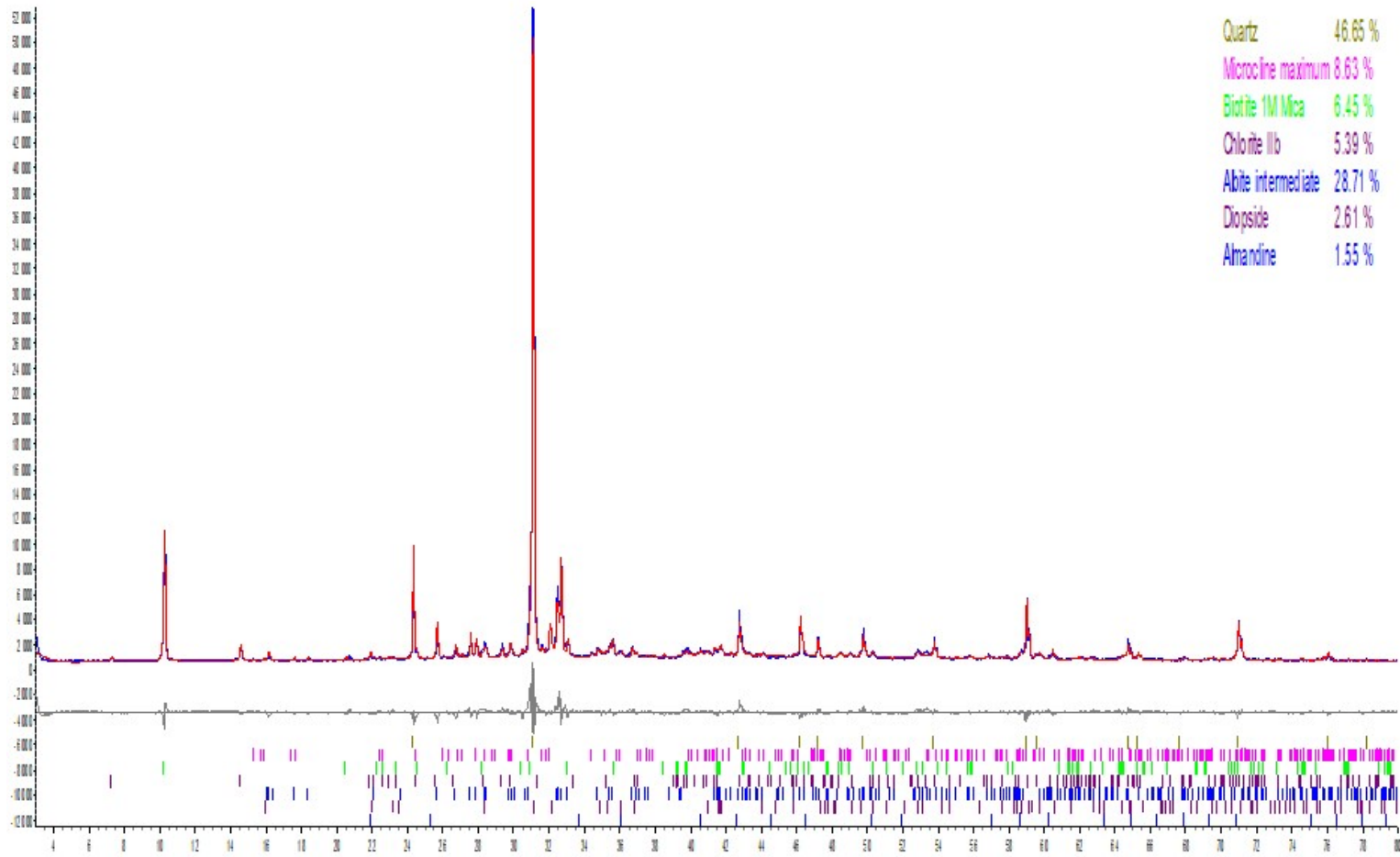


Figure 22: Diffractogram from XRD analysis on sample FB-B.

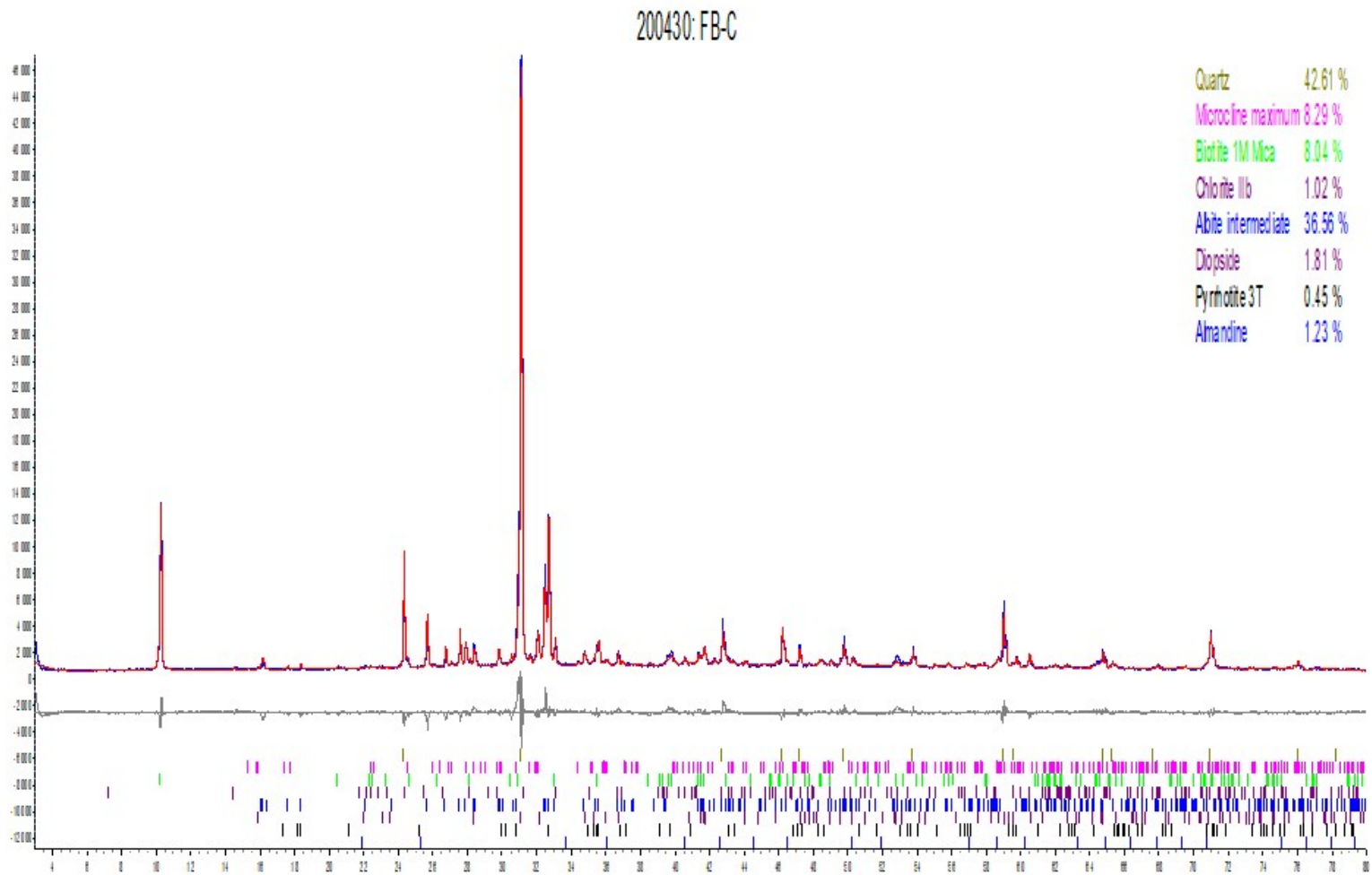


Figure 23: Diffractogram from XRD analysis on sample FB-C.

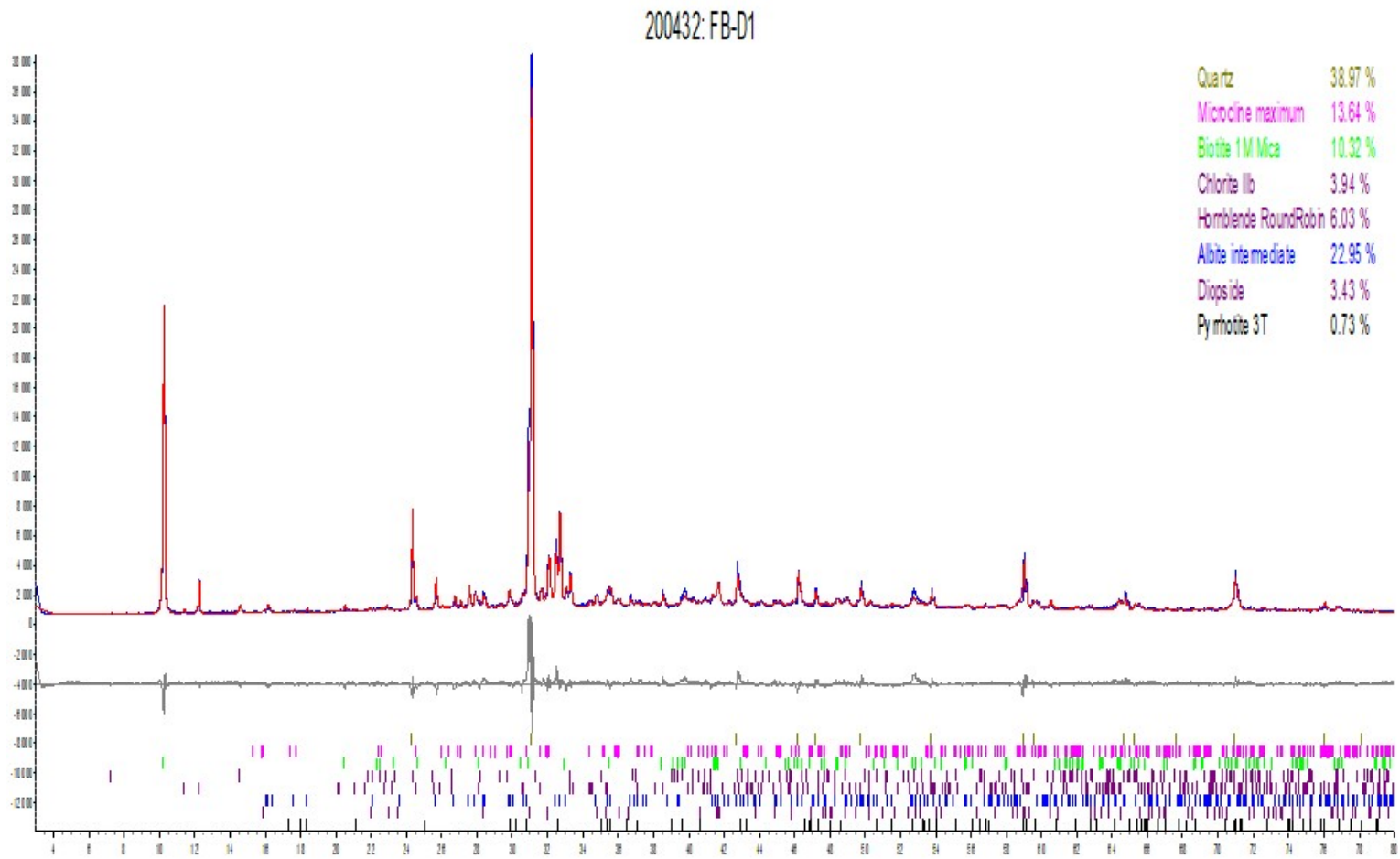


Figure 24: Diffractogram from XRD analysis on sample FB-D.

200429: FB-E

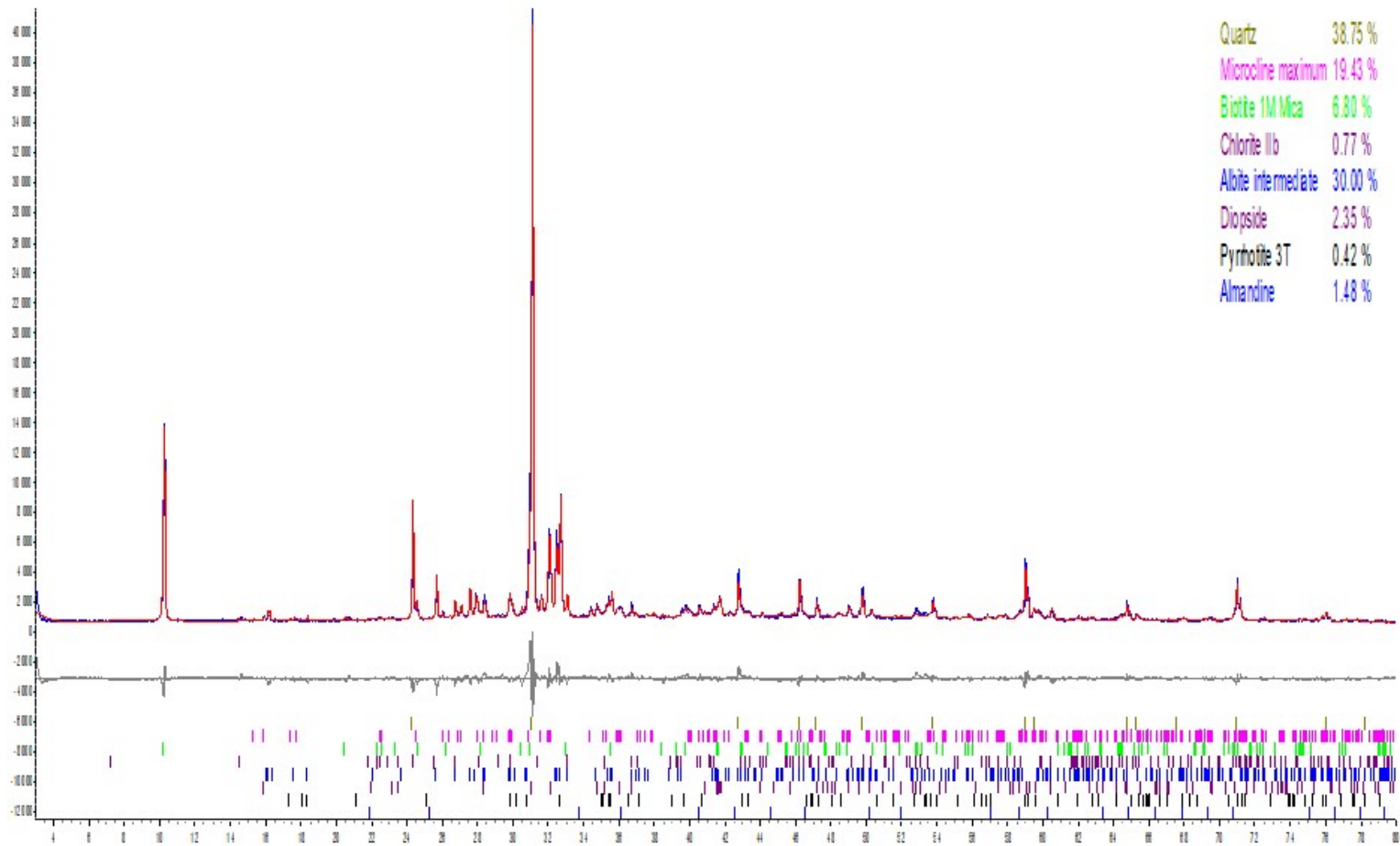


Figure 25: Diffractogram from XRD analysis on sample FB-E.

200433: TR1

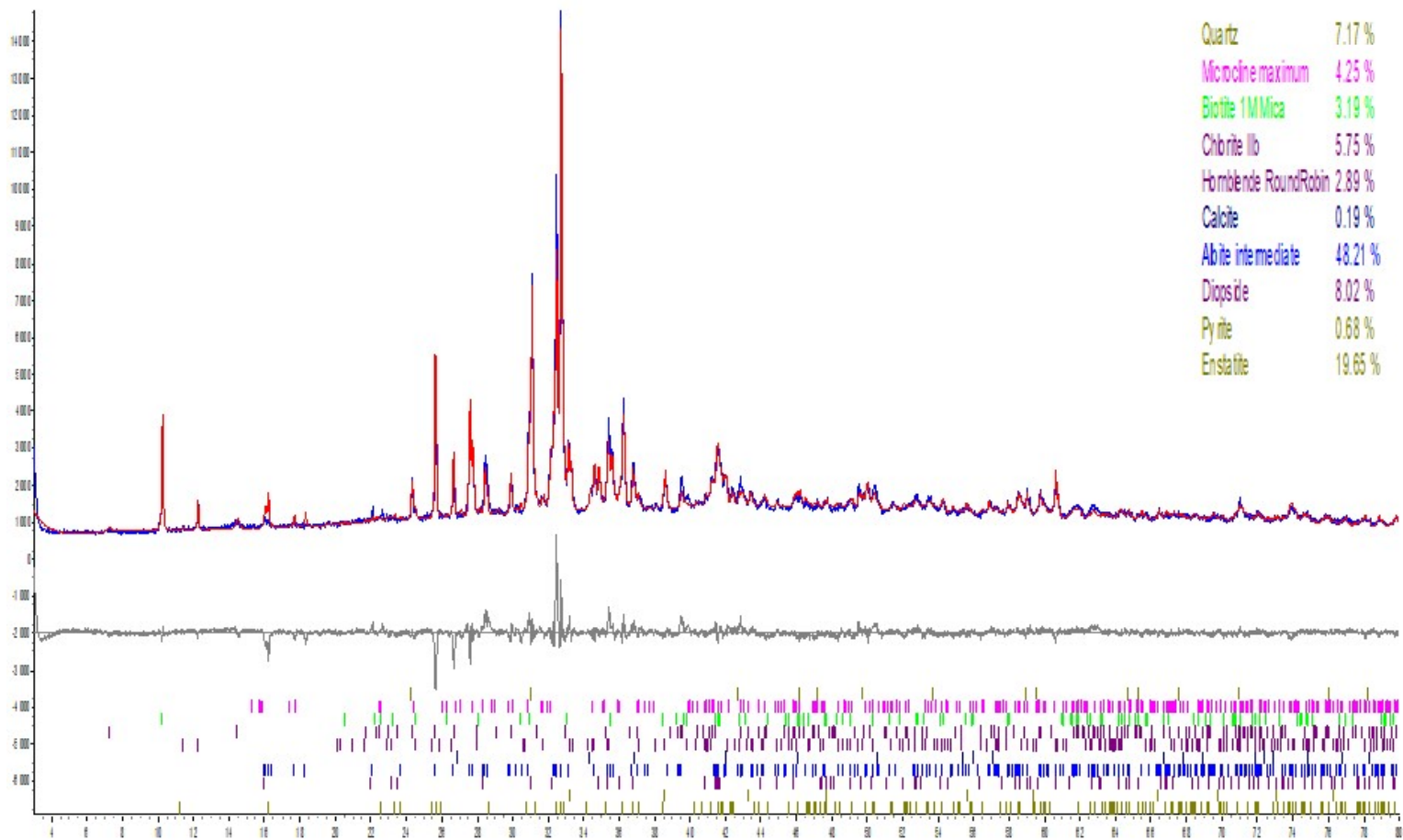


Figure 26: Diffractogram from XRD analysis on sample TR<8mm.

200434: TR2

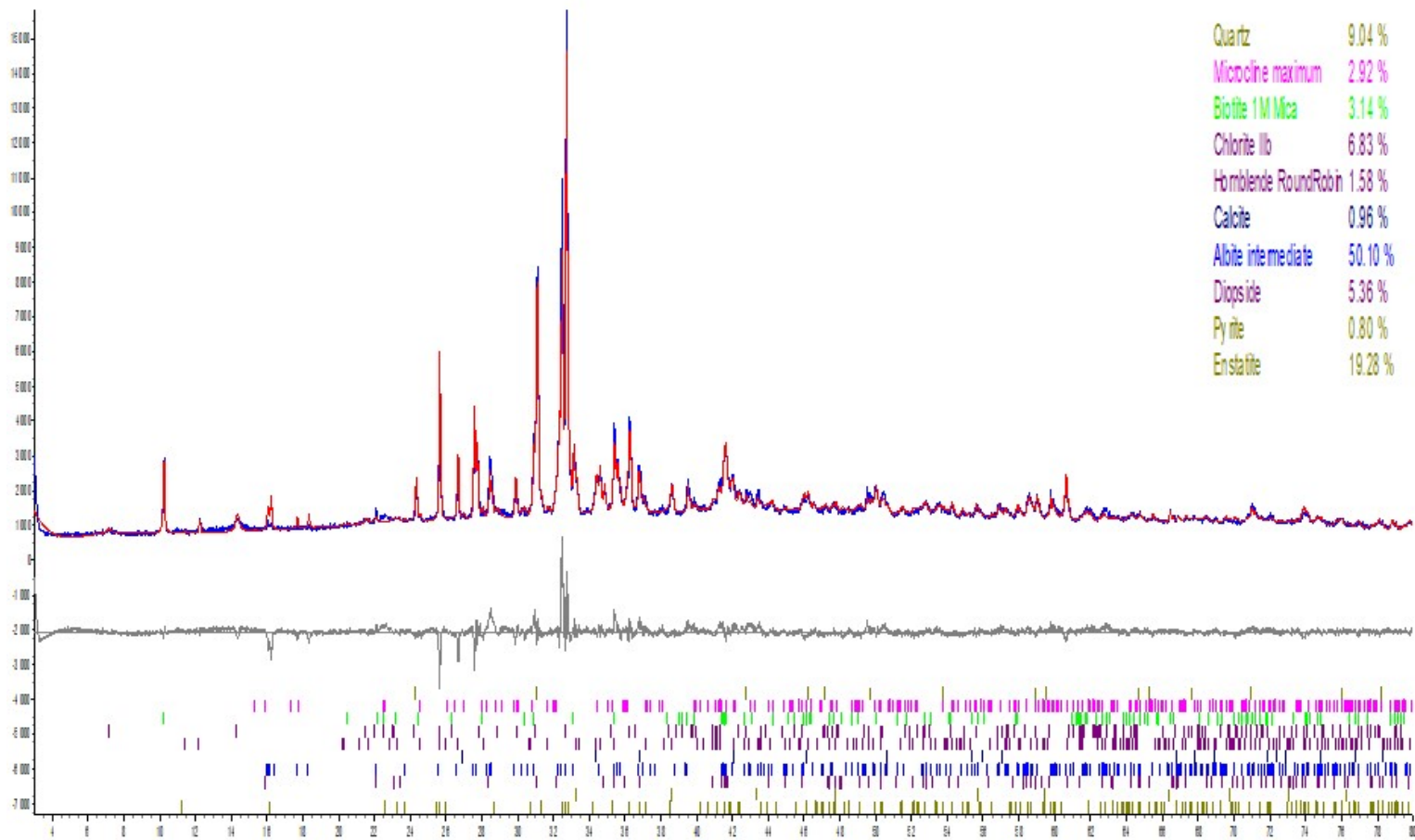


Figure 27: Diffractogram from XRD analysis on sample TR1/8mm.

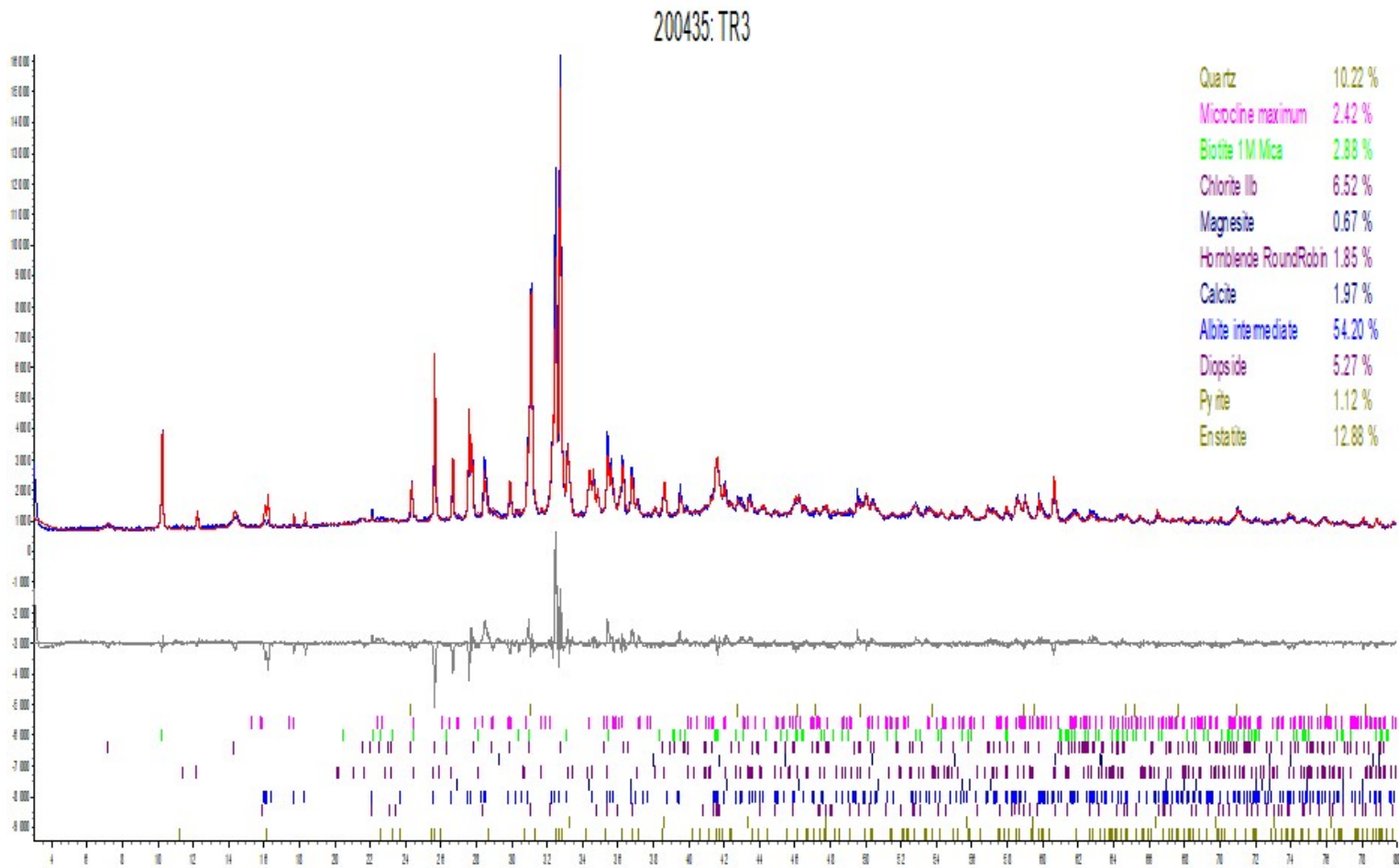


Figure 28: Diffractogram from XRD analysis on sample TR>8mm.

